

1 LEVERAGING MULTI-MESSENGER ASTROPHYSICS FOR DARK MATTER SEARCHES

By

Daniel Nicholas Salazar-Gallegos

A DISSERTATION

Submitted to
Michigan State University
in partial fulfillment of the requirements
for the degree of

Physics—Doctor of Philosophy
Computational Mathematics in Science and Engineering—Dual Major

Today

ABSTRACT

3 I did Dark Matter with HAWC and IceCube. I also used Graph Neural Networks

⁴ Copyright by

⁵ DANIEL NICHOLAS SALAZAR-GALLEGOS

⁶ Today

ACKNOWLEDGMENTS

8 I love my friends. Thanks to everyone that helped me figure this out. Amazing thanks to the people
9 at LANL who supported me. Eames, etc Dinner Parties Jenny and her child Kaydince Kirsten, Pat,
10 Andrea Family. You're so far but so critical to my formation. Unconditional love. Roommate

TABLE OF CONTENTS

12	LIST OF TABLES	vii
13	LIST OF FIGURES	ix
14	LIST OF ABBREVIATIONS	xviii
15	CHAPTER 1 INTRODUCTION	1
16	CHAPTER 2 DARK MATTER IN THE COSMOS	2
17	2.1 Introduction	2
18	2.2 Dark Matter Basics	3
19	2.3 Evidence for Dark Matter	4
20	2.4 Searching for Dark Matter: Particle DM	11
21	2.5 Sources for Indirect Dark Matter Searches	16
22	2.6 Multi-Messenger Dark Matter	18
23	CHAPTER 3 HIGH ALTITUDE WATER CHERENKOV (HAWC) OBSERVATORY	21
24	3.1 The Detector	21
25	3.2 Events Reconstruction and Data Acquisition	21
26	3.3 Remote Monitoring	21
27	CHAPTER 4 ICECUBE NEUTRINO OBSERVATORY	22
28	4.1 The Detector	22
29	4.2 Events Reconstruction and Data Acquisition	22
30	4.3 Northern Test Site	22
31	CHAPTER 5 GLORY DUCK: MULTI-WAVELENGTH SEARCH FOR DARK MATTER ANNIHILATION TOWARDS DWARF SPHEROIDAL GALAXIES	23
32	5.1 Introduction	23
33	5.2 Dataset and Background	25
34	5.3 Analysis	27
35	5.4 Likelihood Methods	31
36	5.5 HAWC Results	38
37	5.6 Glory Duck Combined Results	40
38	5.7 HAWC Systematics	45
39	5.8 J -factor distributions	47
40	5.9 Discussion and Conclusions	53
43	CHAPTER 6 MULTITHREADING HAWC ANALYSES FOR DARK MATTER SEARCHES	57
44	6.1 Introduction	57
45	6.2 Dataset and Background	57
46	6.3 Analysis	59

48	6.4 Likelihood Methods	63
49	6.5 Computational Methods: Multithreading	63
50	6.6 Analysis Results	69
51	6.7 Systematics	74
52	6.8 Conclusion and Discussion	74
53	CHAPTER 7 HEAVY DARK MATTER ANNIHILATION SEARCH WITH ICE-CUBE'S NORTH SKY TRACK DATA	76
55	7.1 Introduction	76
56	7.2 Dataset and Background	77
57	7.3 Analysis	78
58	7.4 Likelihood Methods	87
59	7.5 Background Simulation	87
60	7.6 Signal Recovery	88
61	7.7 Systematics	89
62	7.8 Conclusions	90
63	CHAPTER 8 NU DUCK	114
64	APPENDIX A MULTI-EXPERIMENT SUPPLEMENTARY FIGURES	115
65	APPENDIX B MULTITHREADING DARK MATTER ANALYSES SUPPLEMENTARY MATERIAL	116
67	B.1 Remaining Spectral Models	116
68	B.2 <code>mpu_analysis.py</code>	117
69	B.3 Comparison with Glory Duck	126
70	APPENDIX C ICECUBE HEAVY DARK MATTER ANALYSIS SUPPLEMENTARY MATERIAL	129
72	C.1 Docker Image for Oscillating Neutrino Spectra	129
73	C.2 Spline Fitting Statuses	132
74	C.3 Neutrino Composite Spectra	133
75	C.4 Segue 1 And Ursa Major II Signal Recovery	134
76	BIBLIOGRAPHY	135

LIST OF TABLES

<p>78 Table 5.1 Summary of the relevant properties of the dSphs used in the present work. Column 1 lists the dSphs. Columns 2 and 3 present their heliocentric distance and galactic coordinates, respectively. Columns 4 and 5 report the J-factors of each source given from the \mathcal{GS} and \mathcal{B} independent studies and their estimated $\pm 1\sigma$ uncertainties. The values $\log_{10} J$ (\mathcal{GS} set) [45] correspond to the mean J-factor values for a source extension truncated at the outermost observed star. The values $\log_{10} J$ (\mathcal{B} set) [49] are provided for a source extension at the tidal radius of each dSph. Bolded sources are within HAWC's field of view and provided to the Glory Duck analysis.</p> <p>87 Table 5.2 Summary of dSph observations by each experiment used in this work. A ‘-’ indicates the experiment did not observe the dSph for this study. For Fermi-LAT, the exposure at 1 GeV is given. For HAWC, $\Delta\theta$ is the absolute difference between the source declination and HAWC latitude. HAWC is more sensitive to sources with smaller $\Delta\theta$. For IACTs, we show the zenith angle range, the total exposure, the energy range, the angular radius θ of the signal or ON region, the ratio of exposures between the background-control (OFF) and signal (ON) regions (τ), and the significance of gamma-ray excess in standard deviations, σ.</p> <p>96 Table 6.1 Summary of the relevant properties of the dSphs used in the present work. Column 1 lists the dSphs. Columns 2 and 3 present their heliocentric distance and galactic coordinates, respectively. Column 4 reports the J-factors of each source given from the \mathcal{LS} studies and estimated $\pm 1\sigma$ uncertainties. The values $\log_{10} J$ (\mathcal{LS} set) [66] correspond to the mean J-factor values for a source extension truncated at 0.5°.</p> <p>102 Table 6.2 Timing summaries for analyses for serial and multithreaded processes. M tasks is the number of functional-parallel tasks ran for the computation. $T_{p,c}$ is a single run time in hours:minutes:seconds for runs utilizing p nodes and c threads. Runs are run interactively on the same computer to maximize consistency. Empty entries are indicated with ‘-’. (.) entries are estimated entries extrapolated from data earlier in the column.</p> <p>108 Table 6.3 Speed up summaries for analyses for serial and multithreaded processes. M tasks is the number of functional-parallel tasks ran for the computation. $S_{p,c}$ is a single speedup comparison for runs utilizing p nodes and c threads. [.] are the estimated speedups calculated from Tab. 6.2, Eq. (6.7), and Eq. (6.4). Empty entries are indicated with ‘-’.</p>	<p>32</p> <p>33</p> <p>63</p> <p>67</p> <p>69</p>
---	---

113	Table 7.1 Spline err tolerances used for input in particle physics component to Eq. (7.1).	
114	Column 1 is the DM annihilation channel being fit. Columns 2, 3, and 4	
115	are the tolerances for "GOOD" (pass), "OK" requires inspection, and "FAIL"	
116	(tune and refit) respectively. Column 5 has the X ranges over which the error	
117	is evaluated. MAX/MIN [·,·] takes the maximum or minimum of the two	
118	enclosed values.	84
119	Proof I know how to include	

LIST OF FIGURES

121	Figure 2.1	Rotation curve fit to NGC 6503 from [7]. Dashed line is the contribution 122 from visible matter. Dotted curves are from gas. Dash-dot curves are from 123 dark matter (DM). Solid line is the composite contribution from all matter 124 and DM sources. Data are indicated with bold dots with error bars. Data 125 agree strongly with a matter + DM composite prediction.	5
126	Figure 2.2	Light from distant galaxy is bent in unique ways depending on the distribution 127 of mass between the galaxy and Earth. Yellow dashed lines indicate where 128 the light would have gone if the matter were not present [8].	7
129	Figure 2.3	(left) Optical image of galactic cluster 1E0657-558. (right) X-ray image of the 130 cluster with redder meaning hotter and higher baryon density. (both) Green 131 contours are reconstruction of gravity contours from weak lensing. White 132 rings are the best fit mass maxima at 68.3%, 95.5%, and 99.7% confidence. 133 The matter maxima of the clusters are clearly separated from x-ray maxima. [9]	8
134	Figure 2.4	Plank CMB sky. Sky map features small variations in temperature in primor- 135 dial light. These anisotropies are used to make inferences about the universe's 136 energy budget and developmental history. [10]	9
137	Figure 2.5	Observed Cosmic Microwave Background power spectrum as a function of 138 multipole moment from Plank [10]. Blue line is best fit model from Λ CDM. 139 Red points and lines are data and error, respectively.	10
140	Figure 2.6	Predicted power spectra of CMB for different $\Omega_m h^2$ values for fixed baryon 141 density from [11]. (left) Low $\Omega_m h^2$ increases the prominence of first and 142 second peaks. (middle) $\Omega_m h^2$ is most similar to the observed power spectrum. 143 The second and third peaks are similar in height. (right) $\Omega_m h^2$ is large which 144 suppresses the first peak and raises the prominence of the third peak.	10
145	Figure 2.7	The Standard Model (SM) of particle physics. Figure taken from http://www.quantumdiaries.org/2014/03/14/the-standard-model-a-beautiful-but-flawed-theory/	12
148	Figure 2.8	Simplified Feynman diagram demonstrating with different ways DM can 149 interact with SM particles. The 'X's refer to the DM particles whereas the 150 SM refer to fundamental particles in the SM. The large circle in the center 151 indicates the vertex of interaction and is purposely left vague. The colored 152 arrows refer to different directions of time as well as their respective labels. 153 The arrows indicate the initial and final state of the DM -SM interaction in time.	13

154	Figure 2.9 A single jet event in ATLAS detector from 2017 [16]. Jet momentum was 155 observed to be 1.9 TeV. Missing transverse momentum was observed to be 156 1.9 TeV compared to the initial transverse momentum of the event was 0. 157 Implied MET is traced by a red dashed line in event display.	14
158	Figure 2.10 More detailed pseudo-Feynman diagram of particle cascade from dark matter 159 annihilation into 2 quarks. The quarks hadronize and down to stable particles 160 like γ or the anti-proton (p^-). Diagram pulled from ICRC 2021 presentation 161 on DM annihilation search [17].	15
162	Figure 2.11 Dark Matter (DM) decay spectrum for $b\bar{b}$ initial state and γ final state. Redder 163 spectra are for larger DM masses. Bluer spectra are light DM masses. x is a 164 unitless factor defined as the ratio of the mass of DM, m_χ , and the final state 165 particle energy E_γ . Figure from [19].	17
166	Figure 2.12 Different dark matter density profiles compared. Some models produce ex- 167 ceptionally large densities at small r [20].	18
168	Figure 2.13 The Milky Way Galaxy in photons (γ) and neutrinos (ν) [22]. The Galactic 169 center is at $l=0^\circ$ and is the brightest region in all panels. (top) An Optical 170 color image of the Milky Way galaxy seen from Earth. Clouds of gas and dust 171 obscure some light from stars. (2nd down) Integrated flux of γ -rays observed 172 by the Fermi-LAT telescope [23]. (middle) Expected neutrino emission 173 that corresponds with Fermi-LAT observations. (2nd up) Expected neutrino 174 emission profile after considering detector systematics of IceCube. (bottom) 175 Observed neutrino emission from region of the galactic plane. Substantial 176 neutrino emission was detected.	19
177	Figure 2.14 Dark Matter annihilation spectra for different final state particle and standard 178 model annihilation channels [24]. Photons (red), e^\pm (green), \bar{p} (blue), ν (black).	20
179	Figure 5.1 Sensitivities of five gamma-ray experiments compared to percentages of the 180 Crab nebula's emission and dark matter annihilation. Solid lines present 181 estimated sensitivities to power law spectra [FACT CHECK THIS] for each 182 experiment. Green lines are Fermi-LAT sensitivities where lighter green is 183 the sensitivity to the galactic center and dark green is its sensitivity to higher 184 declinations. Orange, red, and purple solid lines represent the MAGIC, HESS, 185 and VERITAS 50 hour sensitivities respectively. The maroon and brown lines 186 are the HAWC 1 year and 5 year sensitivities. Across four decades of gamma- 187 ray energy, these experiments have similar sensitivities on the order 10^{-12} 188 $\text{erg cm}^{-2}\text{s}^{-1}$. The dotted lines are estimated dark matter fluxes assuming 189 $m_\chi = 5 \text{ TeV}$ DM annihilating to bottom quarks (red), tau leptons (blue), 190 and W bosons (green). Faded gray lines outline percentage flux of the Crab 191 nebula. Figure is an augmented version of [25]	24

192	Figure 5.2	Effect of Electroweak (EW) corrections on expected DM annihilation spectrum for $\chi\chi \rightarrow W^-W^+$. Solid lines are spectral models that consider EW corrections. Dash-dot lines are spectral models without EW corrections. Red lines are models for $M_\chi = 1$ TeV. Blue lines represent models for $M_\chi = 100$ TeV. All models are sourced from the PPPC4DMID [44].	28
197	Figure 5.3	$\frac{dJ}{d\Omega}$ maps for Segue1 (top) and Coma Berenices (bottom). Origin is centered on the specific dwarf spheroidal galaxies (dSph). X and Y axes are the angular separation from the center of the dwarf. Profile is truncated at the scale radius. Plots of the remaining 11 dSph HAWC studied are linked in Fig. A.1.	30
201	Figure 5.4	Illustration of the combination technique showing a comparison between $-2 \ln \lambda$ provided by four instruments (colored lines) from the observation of the same dSph without any J nuisance and their sum, <i>i.e.</i> the resulting combined likelihood (thin black line). According to the test statistics of Equation (5.7), the intersection of the likelihood profiles with the line $-2 \ln \lambda = 2.71$ indicates the 95% C.L. upper limit on $\langle \sigma v \rangle$. The combined likelihood (thin black line) shows a smaller value of upper limit on $\langle \sigma v \rangle$ than those derived by individual instruments. We also show how the uncertainties on the J factor effects the combined likelihood and degrade the upper limit on $\langle \sigma v \rangle$ (thick black line). All likelihood profiles are normalized so that the global minimum $\widehat{\langle \sigma v \rangle}$ is 0. We note that each profile depends on the observational conditions in which a target object was observed. The sensitivity of a given instrument can be degraded and the upper limits less constraining if the observations are performed in non-optimal conditions such as a high zenith angle or a short exposure time.	36
216	Figure 5.5	39
217	Figure 5.6	HAWC TS values for best fit $\langle \sigma v \rangle$ versus m_χ for seven SM annihilation channels with J factors from \mathcal{GS} . The solid black line shows the combined best fit TS values. The colored, dashed lines are the TS values for each of the 13 sources HAWC studied.	40
221	Figure 5.7	HAWC Brazil bands at 95% confidence level on $\langle \sigma v \rangle$ versus DM mass for seven annihilation channels with J -factors from \mathcal{GS} [55]. The solid line represents the combined limit from 13 dSphs. The dashed line is the expected limit. The green band is the 68% containment. The yellow band is the 95% containment.	41

226	Figure 5.8	Upper limits at 95% confidence level on $\langle \sigma v \rangle$ in function of the DM mass for 227 eight annihilation channels, using the set of J factors from Ref. [55] (\mathcal{GS} set 228 in Table 5.1). The black solid line represents the observed combined limit, 229 the black dashed line is the median of the null hypothesis corresponding 230 to the expected limit, while the green and yellow bands show the 68% and 231 95% containment bands. Combined upper limits for each individual detector 232 are also indicated as solid, colored lines. The value of the thermal relic 233 cross-section in function of the DM mass is given as the red dotted-dashed 234 line [56].	42
235	Figure 5.9	Same as Fig. 5.8, using the set of J factors from Ref. [49, 57] (\mathcal{B} set in Table 5.1).	43
236	Figure 5.10	Comparisons of the combined limits at 95% confidence level for each of the 237 eight annihilation channels when using the J factors from Ref. [55] (\mathcal{GS} set in 238 Table 5.1), plain lines, and the J factor from Ref. [49, 57] (\mathcal{B} set in Table 5.1), 239 dashed lines. The cross-section given by the thermal relic is also indicated [56].	45
240	Figure 5.11	Comparisons of the combined limits at 95% confidence level for a point source 241 analysis and extended source using [55] \mathcal{GS} J-factor distributions and PPPC 242 [44] annihilation spectra. Shown are the limits for Segue1 which will have 243 the most significant impact on the combined limit. 6 of the 7 DM annihilation 244 channels are shown. Solid lines are extended source studies. Dashed lines 245 are point source studies. Overall, the extended source analysis improves the 246 limit by a factor of 2.	47
247	Figure 5.12	Same as Fig. 5.11 on Coma Berenices. This dSph also contributes signifi- 248 cantly to the limit. The limits are identical in this case.	48
249	Figure 5.13	Comparison of combined limits when correcting for HAWC's pointing sys- 250 tematic. All DM annihilation channels are shown. The solid black line is the 251 ratio between published limit to the declination corrected limit. The blue solid 252 line or "Combined_og" represented the limits computed for Glory Duck. The 253 solid orange line or "Combined_ad" represented the limits computed after 254 correcting for the pointing systematic.	49
255	Figure 5.14	Differential map of dJ/Ω from model built in Section 5.8.1 and profiles 256 provided directly from authors. (Top) Differential from Segue1. (bottom) 257 Differential from Coma Berenices. Note that their scales are not the same. 258 Segue1 shows the deepest discrepancies which is congruent with its large 259 uncertainties. Both models show anuli where unique models become apparent.	50

260	Figure 5.15 HAWC limits for Coma Berenices (top) and Segue1 (bottom) for two different 261 map sets. Blue lines are limits calculated on maps with poor model repre- 262 sentation. Orange lines are limits calculated on spatial profiles provided by 263 the authors of [45]. Black line is the ratio of the poor spatial model limits to 264 the corrected spatial models. The left y-axis measures $\langle \sigma v \rangle$ for the blue and 265 orange lines. The right y-axis measures the ratio and is unitless.	51
266	Figure 5.16 Comparisons between the J -factors versus the angular radius for the com- 267 putation of J factors from Ref. [55] (\mathcal{GS} set in Table 5.1) in blue and for 268 the computation from Ref. [49, 57] (\mathcal{B} set in Tab. 5.1) in orange. The solid 269 lines represent the central value of the J -factors while the shaded regions 270 correspond to the 1σ standard deviation.	53
271	Figure 5.17 Comparisons between the J -factors versus the angular radius for the computa- 272 tion of J factors from Ref. [55] (\mathcal{GS} set in Tab. 5.1) in blue and for the 273 computation from Ref. [49, 57] (\mathcal{B} set in Tab. 5.1) in orange. The solid 274 lines represent the central value of the J -factors while the shaded regions 275 correspond to the 1σ standard deviation.	54
276	Figure 6.1 Spectral hypotheses from PPPC [44] and HDM [65] for DM annihilation: 277 $\chi\chi \rightarrow W^-W^+$. Solid lines are spectral models with EW corrections from the 278 PPPC. Dash-dot lines are spectral models from HDM. Red lines are models 279 for $M_\chi = 1$ TeV. Blue lines represent models for $M_\chi = 100$ TeV.	59
280	Figure 6.2 Photon spectra for $\chi\chi \rightarrow \gamma\gamma$ (left) and $\chi\chi \rightarrow ZZ$ (right) after Gaussian 281 convolution of line features. Both spectra have δ -features at photon energies 282 equal to the DM mass. Bluer lines are annihilation spectra with lower DM 283 mass. Redder lines are spectra from larger DM mass. All spectral models are 284 sourced from the Heavy Dark Matter models [65]. Axes are drawn roughly 285 according to the energy sensitivity of HAWC.	60
286	Figure 6.3 $\frac{dJ}{d\Omega}$ maps for Coma Berenices, Draco, Segue1, and Sextans. Columns are 287 divided for the $\pm 1\sigma$ uncertainties in $dJ/d\Omega$ around the mean value from \mathcal{LS} 288 [66]. Origin is centered on the specific dwarf spheroidal galaxies (dSph). θ 289 and ϕ axes are the angular separation from the center of the dwarf. Profiles 290 are truncated at 1° and flattened beyond.	62
291	Figure 6.4 Infographic on how jobs and DM computation was organized in Section 5.3. 292 Jobs were built for each permutation of CHANS and SOURCES shown by the 293 left block in the figure. Each job, which took on the order 2 hrs to compute, 294 had the following work flow: 1. Import HAWC analysis software, 2 min to 295 run. 2. Load HAWC count maps, 5 min to run. 3. Load HAWC energy and 296 spatial resolutions, 4 min. 5. Load DM spatial source templates and spectral 297 models, less than 1 s. 6. Perform likelihood fit on data and model, about 8 298 min per DM mass. 7. Write results to file, less than 1s.	64

299	Figure 6.5	Graphic of Gustafson parallel coding pattern. f_s is the fraction of a program, 300 in time, spent on serial computation. f_p is the fraction of computing time 301 that is parallelizable. T_p is the total time for a parallel program to run. T_1 is 302 the total time for a parallel program to run if only 1 processor is allocated. 303 P_N is the N -th processor where it's row is the computation the processor 304 performs. The Gustafson pattern is most similar to what is implemented for 305 this analysis. Figure is pulled from [68].	65
306	Figure 6.6	Task chart for one multithreaded job developed for this project. Green blocks 307 indicate a shared resource across the threads AND computation performed 308 serially. Red blocks indicate functional parallel processing within each thread. 309 3 threads are represented here, yet many more can be employed during the 310 full analysis. Jobs are defined by the SOURCE as these require unique maps 311 to be loaded into the likelihood estimator. The m_χ , CHAN, and $\langle\sigma v\rangle$ variables 312 are entered into the thread pool and allocated as evenly as possible across the 313 threads.	67
314	Figure 6.7	HAWC upper limits at 95% confidence level on $\langle\sigma v\rangle$ versus m_χ for $\chi\chi \rightarrow b\bar{b}$, $t\bar{t}$, $u\bar{u}$, $d\bar{d}$, $s\bar{s}$, $c\bar{c}$, gg , W^+W^- , and hh . Limits are with \mathcal{LS} J-factors 315 [66]. The solid line represents the observed combined limit. Dashed lines 316 represent limits from individual dSphs.	70
318	Figure 6.8	HAWC upper limits at 95% confidence level on $\langle\sigma v\rangle$ versus m_χ for $\chi\chi \rightarrow \nu_e\bar{\nu}_e$, $\nu_\mu\bar{\nu}_\mu$, $\nu_\tau\bar{\nu}_\tau$, $e\bar{e}$, $\mu\bar{\mu}$, $\tau\bar{\tau}$, $\gamma\gamma$ and ZZ . Limits use \mathcal{LS} J-factors [66]. The 319 solid line represents the observed combined limit. Dashed lines represent 320 limits from individual dSphs.	71
322	Figure 6.9	HAWC TS values for best fit $\langle\sigma v\rangle$ versus m_χ for SM annihilation channels: 323 $\chi\chi \rightarrow b\bar{b}$, $t\bar{t}$, $u\bar{u}$, $d\bar{d}$, $s\bar{s}$, $c\bar{c}$, gg , W^+W^- , and hh . Limits use \mathcal{LS} J-factors. 324 The solid black line shows the combined best fit TS values. The colored, 325 dashed lines are the TS values from each dSph.	72
326	Figure 6.10	HAWC TS values for best fit $\langle\sigma v\rangle$ versus m_χ for SM annihilation channels: 327 $\chi\chi \rightarrow \nu_e\bar{\nu}_e$, $\nu_\mu\bar{\nu}_\mu$, $\nu_\tau\bar{\nu}_\tau$, $e\bar{e}$, $\mu\bar{\mu}$, $\tau\bar{\tau}$, $\gamma\gamma$ and ZZ . Limits use \mathcal{LS} J-factors. 328 The solid black line shows the combined best fit TS values. The colored, 329 dashed lines are the TS values from each dSph.	73
330	Figure 6.11	Comparison of HAWC limits from this analysis to Glory Duck (Fig. 5.5) 331 for 3 dSphs and 3 DM annihilation channels: $b\bar{b}$, $\tau\bar{\tau}$, and $e\bar{e}$. Each sector 332 shows the 95% confidence limit from Glory Duck (blue line) and this analysis 333 (orange line) in the top plot. The lower plot features the ratio in log scale of 334 Glory Duck to this analysis in a red solid line. Horizontal dashed lines are 335 for ratios of 1.0 (black) and $\sqrt{2}$ (blue). Ratios larger than 1.0 are for limits 336 smaller, or stricter, than Glory Duck. Ratios larger than $\sqrt{2}$ indicates limits 337 are stricter than a simple doubling of the Glory Duck data.	75

338	Figure 7.1	Neutrino spectra at production (left panels) and after oscillation at Earth 339 (right panels). Blue, orange, and green lines are the ν_e , ν_μ , and ν_τ spectra 340 respectively. Top panels show the spectra in $\frac{dN}{dE}$. Lower panels plot the flavor 341 ratio to $\nu_e + \nu_\mu + \nu_\tau$. SM annihilation channels $b\bar{b}$, $\tau\bar{\tau}$, and $\nu_\mu\bar{\nu}_\mu$ are shown 342 for $M_\chi = 1$ PeV, TeV, and EeV.	80
343	Figure 7.2	Signal recovery for 100 TeV DM annihilation into $\nu_\mu\bar{\nu}_\mu$ for a source at Dec 344 = 16.06°. n_{inj} is the number of injected signal events in simulation. n_s is 345 the number of reconstructed signal events from the simulation. Although 346 the uncertainties are small and tight, the reconstructed n_s are systematically 347 underestimated.	81
348	Figure 7.3	Left panel shows the two kernels overlaying the original spectrum from 349 χ arony after propagation to Earth [71]. The vertical red line indicates where 350 the original neutrino line is maximized. Blue line is the output from χ aroy. 351 Green line is the spectrum after convolution with a flat kernel. Orange line 352 is the spectrum after Gaussian convolution. Right panel shows the signal 353 recovery of the spectral model using the Gaussian kernel with parameters 354 enumerated above.	82
355	Figure 7.4	Example spline that failed the fit. Failed splined are corrected on a case by 356 case basis unless the SM channel has a systematic problem fitting the splines. 357 In this case, I made a bookkeeping error and loaded the incorrect spectral model	84
358	Figure 7.5	Summary of input spectral models that were smoothed with Gaussian kernel. 359 Spectral models are for $\chi\chi \rightarrow e\bar{e}$, $\mu\bar{\mu}\tau\bar{\tau}$, $\nu_e\bar{\nu}_e$, $\nu_\mu\bar{\nu}_\mu$, and $\nu_\tau\bar{\nu}_\tau$. These spectra 360 are the composite ($\nu_\mu + \nu_\tau$) of neutrino flavors. Every spectral model used for 361 this analysis is featured as a colored solid line. Bluer lines are for lower DM 362 mass spectral models. DM masses range from 681 GeV to 100 PeV. HDM 363 [65], χ aroy [71], and Photospline [75] are used to generate these spectra. 364 Energy (x-axis) was chosen to roughly represent the energy sensitivity of NST. .	85
365	Figure 7.6	Test statistic (TS) distributions for Segue 1 and $\chi\chi \rightarrow b\bar{b}$. Each subplot, 366 except the final, is the TS distribution for a specific DM mass listed in the 367 subplot. Orange dashed lines are the traces for a χ^2 distribution with 1 degree 368 of freedom. $\epsilon[\cdot]$ is the fraction of trials smaller than the bracketed value. The 369 final subplot plots the all DM spectral models, similar to Fig. 7.5, used as 370 input for the TS distributions.	91
371	Figure 7.7	Same as Fig. 7.6 for Segue 1 $\chi\chi \rightarrow \tau\bar{\tau}$	92
372	Figure 7.8	Same as Fig. 7.6 for Segue 1 $\chi\chi \rightarrow \nu_\mu\bar{\nu}_\mu$	93
373	Figure 7.9	Same as Fig. 7.6 for Ursa Major II 1 $\chi\chi \rightarrow b\bar{b}$	94
374	Figure 7.10	Same as Fig. 7.6 for Ursa Major II 1 $\chi\chi \rightarrow \tau\bar{\tau}$	95

375	Figure 7.11 Same as Fig. 7.6 for Ursa Major II 1 $\chi\chi \rightarrow \nu_\mu\bar{\nu}_\mu$	96
376	Figure 7.12 Same as Fig. 7.6 for 15, \mathcal{GS} J -factor, stacked sources and $\chi\chi \rightarrow b\bar{b}$	97
377	Figure 7.13 Same as Fig. 7.6 for 15, \mathcal{GS} J -factor, stacked sources and $\chi\chi \rightarrow t\bar{t}$	98
378	Figure 7.14 Same as Fig. 7.6 for 15, \mathcal{GS} J -factor, stacked sources and $\chi\chi \rightarrow u\bar{u}$	99
379	Figure 7.15 Same as Fig. 7.6 for 15, \mathcal{GS} J -factor, stacked sources and $\chi\chi \rightarrow d\bar{d}$	100
380	Figure 7.16 Same as Fig. 7.6 for 15, \mathcal{GS} J -factor, stacked sources and $\chi\chi \rightarrow e\bar{e}$	101
381	Figure 7.17 Same as Fig. 7.6 for 15, \mathcal{GS} J -factor, stacked sources and $\chi\chi \rightarrow \mu\bar{\mu}$	102
382	Figure 7.18 Same as Fig. 7.6 for 15, \mathcal{GS} J -factor, stacked sources and $\chi\chi \rightarrow \tau\bar{\tau}$	103
383	Figure 7.19 Same as Fig. 7.6 for 15, \mathcal{GS} J -factor, stacked sources and $\chi\chi \rightarrow W^+W^-$	104
384	Figure 7.20 Same as Fig. 7.6 for 15, \mathcal{GS} J -factor, stacked sources and $\chi\chi \rightarrow ZZ$	105
385	Figure 7.21 Same as Fig. 7.6 for 15, \mathcal{GS} J -factor, stacked sources and $\chi\chi \rightarrow \nu_e\bar{\nu}_e$	106
386	Figure 7.22 Same as Fig. 7.6 for 15, \mathcal{GS} J -factor, stacked sources and $\chi\chi \rightarrow \nu_\mu\bar{\nu}_\mu$	107
387	Figure 7.23 Signal Recovery study for an analysis with 15 stacked sources using the \mathcal{GS} J -factors [45]. Each panel block represents 14 studies for DM mass ranging between 1 TeV and 20 PeV and one annihilation channel. Panel block is for $t\bar{t}$. Each panel block features every spectral model used as input in the bottom-right subpanel. The remaining panels show n_{inj} as the number of signal events injected into background simulation. Whereas, n_s is the number of signal events recovered from analyzing the injected simulation. Blue line represents the median values of 100 simulations. Light blue bands show the 1σ statistical uncertainty around the median.	108
396	Figure 7.24 Same as Fig. 7.23 but for $\chi\chi \rightarrow b\bar{b}$ (top) and $\nu_\mu\bar{\nu}_\mu$ (bottom).	109
397	Figure 7.25 Words. I predict Icecube Sensitivities weeee	110
398	Figure 7.26 Words. I predict Icecube Sensitivities weeee	111
399	Figure 7.27 TODO: Earth attenuation diagram.[NEEDS A SOURCE][FACT CHECK THIS]	112
400	Figure 7.28 TODO: Declination sensitivity plot[NEEDS A SOURCE][FACT CHECK THIS]	113
401	Figure A.1 Sister figure to Figure 5.3. Sources in the first row from left to right: Bootes I, Canes Venatici I, II. In second row: Draco, Hercules, Leo I. In the first row: Leo II, Leo IV, Sextans. In the final row: Ursa Major I, Ursa Major II.	115

404	Figure B.1 Sister figure to Figure 6.2 for remaining SM primary annihilation channels 405 studied for this thesis. These did not require any post generation smoothing 406 and so are directly pulled from [65] with a binning scheme most helpful for a 407 HAWC analysis.	116
408	Figure B.2 TODO: fill this out	126
409	Figure B.3 TODO: fill this out	127
410	Figure B.4 TODO: fill this out	128
411	Figure C.1 Current status of spline tables according to constraints defined by Tab. 7.1. 412 Green splines are splines that passed under the GOOD tolerance. Yellow 413 are splines that are OK. Red are splines that FAIL. All yellow splines were 414 inspected individually before running the analysis. Splines were made for the 415 μ (PID 14; top panel) flavor and τ (PID 16; bottom panel) neutrino flavors.	132
416	Figure C.2 Sister figure to Fig. 7.5 for annihilation channels that did not require kernel 417 smoothing. These spectra are the composite ($\nu_\mu + \nu_\tau$) of neutrino flavors. 418 Every spectral model used for this analysis is featured as a colored solid line. 419 Bluer lines are for lower DM mass spectral models. DM masses range from 420 681 GeV to 100 PeV.	133
421	Figure C.3 TODO: Fill this out eventually. I think I want all the plots generated 422 first[NEEDS A SOURCE][FACT CHECK THIS]	134

LIST OF ABBREVIATIONS

- 424 **MSU** Michigan State University
425 **LANL** Los Alamos National Laboratory
426 **DM** Dark Matter
427 **SM** Standard Model
428 **HAWC** High Altitude Water Cherenkov Observatory
429 **dSph** Dwarf Spheroidal Galaxy

430

CHAPTER 1

INTRODUCTION

431 Is the text not rendering right? Ah ok it knows im basically drafting the doc still

CHAPTER 2

432

DARK MATTER IN THE COSMOS

433 **2.1 Introduction**

434 The dark matter problem can be summarized in part by the following thought experiment.

435 Let us say you are the teacher for an elementary school classroom. You take them on a field
436 trip to your local science museum and among the exhibits is one for mass and weight. The exhibit
437 has a gigantic scale, and you come up with a fun problem for your class.

438 You ask your class, "What is the total weight of the classroom? Give your best estimation to
439 me in 30 minutes, and then we'll check your guess on the scale. If your guess is within 10% of the
440 right answer, we will stop for ice cream on the way back."

441 The students are ecstatic to hear this, and they get to work. The solution is some variation of
442 the following strategy. The students should give each other their weight or best guess if they do
443 not know. Then, all they must do is add each student's weight and get a grand total for the class.

444 The measurement on the giant scale should show the true weight of the class. When comparing
445 the measured weight to your estimation, multiply the measurement by 1.0 ± 0.1 to get the $\pm 10\%$
446 tolerances for your estimation.

447 Two of your students, Sandra and Mario, return to you with a solution.

448 They say, "We weren't sure of everyone's weight. We used 65 lbs. for the people we didn't
449 know and added everyone who does know. There are 30 of us, and we got 2,000 lbs.! That's a ton!"

450 You estimated 1,900 lbs. assuming the average weight of a student in your class was 60 lbs.
451 So, you are pleased with Sandra's and Mario's answer. You instruct your students to all gather on
452 the giant scale and read off the weight together. To all your surprise, the scale reads *10,000 lbs.*!
453 10,000 is significantly more than a 10% error from 2,000. In fact, it is approximately 5 times more
454 massive than either your or your students' estimates. You think to yourself and conclude there
455 must be something wrong with the scale. You ask an employee to check the scale and verify it is
456 well calibrated. They confirm that the scale is in working order. You weigh a couple of students
457 individually to assess that the scale is well calibrated. Sandra weighs 59 lbs., and Mario weighs

458 62 lbs., typical weights for their age. You then weigh each student individually and see that their
459 weights individually do not deviate greatly from 60 lbs. So, where does all the extra weight come
460 from?

461 This thought experiment serves as an analogy to the Dark Matter problem. The important
462 substitution to make however is to replace the students with stars and the classroom with a galaxy,
463 say the Milky Way. Individually the mass of stars is well measured and defined with the Sun as our
464 nearest test case. However, when we set out to measure the mass of a collection of stars as large as
465 galaxies, our well-motivated estimation is wildly incorrect. There simply is no way to account for
466 this discrepancy except without some unseen, or dark, contribution to mass and matter in galaxies.
467 I set out in my thesis to narrow the possibilities of what this Dark Matter could be.

468 This chapter is organized like the following... **TODO: Text should look like ... Chapter x has**
469 **blah blah blah.**

470 2.2 Dark Matter Basics

471 Presently, a more compelling theory of cosmology that includes Dark Matter (DM) in order
472 to explain a variety of observations is Λ Cold Dark Matter, or Λ CDM. I present the evidence
473 supporting Λ CDM in Section 2.3 yet discuss the conclusions of the Λ CDM model here. According
474 to Λ CDM fit to observations on the Cosmic Microwave Background (CMB), DM is 26.8% of the
475 universe's current energy budget. Baryonic matter, stuff like atoms, gas, and stars, contributes to
476 4.9% of the universe's current energy budget [1, 2, 3].

477 DM is dark; it does not interact readily with light at any wavelength. DM also does not interact
478 noticeably with the other standard model forces (Strong and Weak) at a rate that is readily observed
479 [3]. DM is cold, which is to say that the average velocity of DM is below relativistic speeds [1].
480 'Hot' DM would not likely manifest the dense structures we observe like galaxies, and instead
481 would produce much more diffuse galaxies than what is observed [3, 1]. DM is old; it played a
482 critical role in the formation of the universe and the structures within it [1, 2].

483 Observations of DM have so far been only gravitational. The parameter space available to what
484 DM could be therefore is extremely broad. The broad DM parameter space is iteratively tested in

485 DM searches by supposing a hypothesis that has not yet been ruled out and performing observations
486 to test them. When the observations yield a null result, the parameter space is constrained further.
487 I present some approaches for DM searches in Section 2.4.

488 **2.3 Evidence for Dark Matter**

489 Dark Matter (DM) has been a looming problem in physics for almost 100 years. Anomalies
490 have been observed by astrophysicists in galactic dynamics as early as 1933 when Fritz Zwicky
491 noticed unusually large velocity dispersion in the Coma cluster. Zwicky's measurement was the
492 first recorded to use the Virial theorem to measure the mass fraction of visible and invisible matter
493 in celestial bodies [4]. From Zwicky in [5], "*If this would be confirmed, we would get the surprising*
494 *result that dark matter is present in much greater amount than luminous matter.*" Zwicky's and
495 others' observation did not instigate a crisis in astrophysics because the measurements did not
496 entirely conflict with their understanding of galaxies [4]. In 1978, Rubin, Ford, and Norbert
497 measured rotation curves for ten spiral galaxies [6]. Rubin et al.'s 1978 publication presented a
498 major challenge to the conventional understanding of galaxies that could no longer be dismissed by
499 measurement uncertainties. Evidence has been mounting ever since for this exotic form of matter.
500 The following subsections provide three compelling pieces of evidence in support of the existence
501 of DM.

502 **2.3.1 First Clues: Stellar Velocities**

503 Zwicky, and later Rubin, measured the stellar velocities of various galaxies to estimate their
504 virial mass. The Virial Theorem upon which these observations are interpreted is written as

$$2T + V = 0. \quad (2.1)$$

505 Where T is the kinetic energy and V is the potential energy in a self-gravitating system. The
506 classical Newton's law of gravity from stars and gas was used for gravitational potential modeled in
507 the observed galaxies:

$$V = -\frac{1}{2} \sum_i \sum_{j \neq i} \frac{m_i m_j}{r_{ij}}. \quad (2.2)$$

508 Zwicky et al. measured just the velocities of stars apparent in optical wavelengths [5]. Rubin et al.
 509 added by measuring the velocity of the hydrogen gas via the 21 cm emission line of Hydrogen [6].
 510 The velocities of the stars and gas are used to infer the total mass of galaxies and galaxy clusters
 511 via Equation (2.1). An inferred mass is obtained from the luminosity of the selected sources. The
 512 two inferences are compared to each other as a luminosity to mass ratio which typically yielded [1]

$$\frac{M}{L} \sim 400 \frac{M_{\odot}}{L_{\odot}} \quad (2.3)$$

513 M_{\odot} and L_{\odot} referring to stellar mass and stellar luminosity, respectively. These ratios clearly indicate
 514 a discrepancy in apparent light and mass from stars and gas and their velocities.

515 Rubin et al. [6] demonstrated that the discrepancy was unlikely to be an underestimation of
 516 the mass of the stars and gas. The inferred "dark" mass was up to 5 times more than the luminous
 517 mass. This dark mass also needed to extend well beyond the extent of the luminous matter.

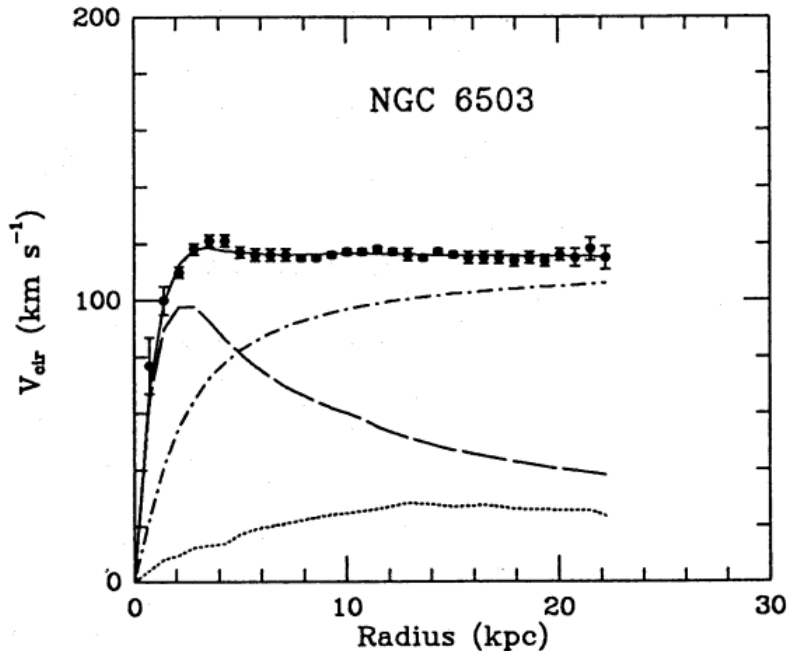


Figure 2.1 Rotation curve fit to NGC 6503 from [7]. Dashed line is the contribution from visible matter. Dotted curves are from gas. Dash-dot curves are from dark matter (DM). Solid line is the composite contribution from all matter and DM sources. Data are indicated with bold dots with error bars. Data agree strongly with a matter + DM composite prediction.

518 Figure 2.1 features one of many rotation curves plotted from the stellar velocities within galaxies.

519 The measured rotation curves mostly feature a flattening of velocities at higher radius which is not
520 expected if the gravity was only coming from gas and luminous matter. The extension of the
521 flat velocity region also indicates that the DM is distributed far from the center of the galaxy.
522 Modern velocity measurements include significantly larger objects, galactic clusters, and smaller
523 objects, dwarf galaxies. Yet, measurements along this regime are leveraging the Virial theorem
524 with Newtonian potential energies. We know Newtonian gravity is not a comprehensive description
525 of gravity. New observational techniques have been developed since 1978, and those are discussed
526 in the following sections.

527 **2.3.2 Evidence for Dark Matter: Gravitational Lensing**

528 Modern evidence for dark matter comes from new avenues beyond stellar velocities. Grav-
529 itational lensing from DM is a new channel from general relativity. General relativity predicts
530 aberrations in light caused by massive objects. In recent decades we have been able to measure the
531 lensing effects from compact objects and DM halos. Figure 2.2 shows how different massive ob-
532 jects change the final image of a faraway galaxy resulting from gravitational lensing. Gravitational
533 lensing developed our understanding of dark matter in two important ways.

534 Gravitational lensing provides additional compelling evidence for DM. The observation of two
535 merging galactic clusters in 2006, shown in Figure 2.3, provided a compelling argument for DM
536 outside the Standard Model. These clusters merged recently in astrophysical time scales. Galaxies
537 and star cluster have mostly passed by each other as the likelihood of their collision is low. Therefore,
538 these massive objects will mostly track the highest mass, dark and/or baryonic, density. Yet, the
539 intergalactic gas is responsible for the majority of the baryonic mass in the systems [4]. These gas
540 bodies will not phase through and will heat up as they collide together. The hot gas is located via
541 x-ray emission from the cluster. Two observations of the clusters were performed independently of
542 each other.

543 The first was the lensing of light around the galaxies due to their gravitational influences.
544 When celestial bodies are large enough, the gravity they exert bends space and time itself. The
545 warped space-time lenses light and will deflect in an analogous way to how glass lenses will bend

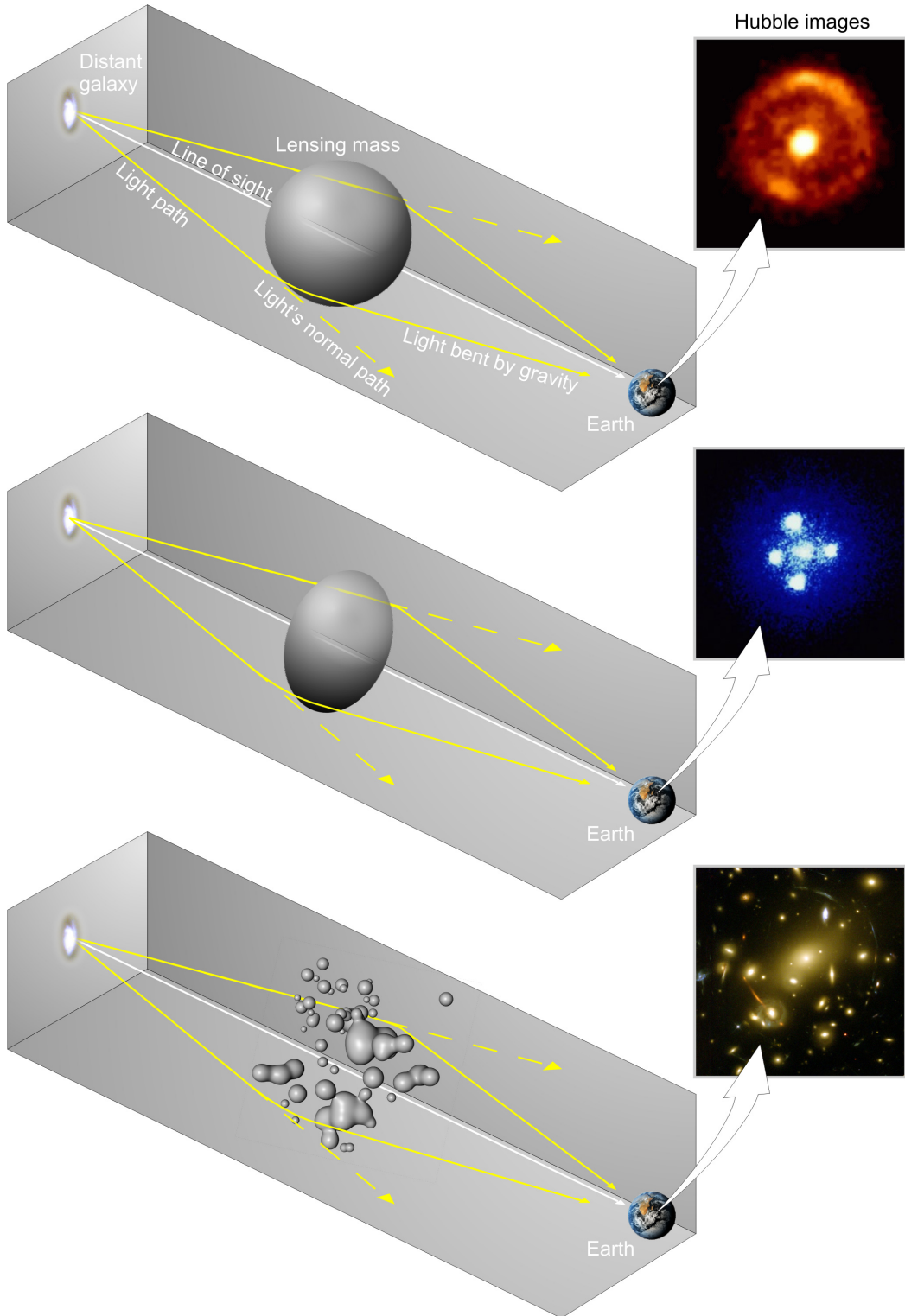


Figure 2.2 Light from distant galaxy is bent in unique ways depending on the distribution of mass between the galaxy and Earth. Yellow dashed lines indicate where the light would have gone if the matter were not present [8].

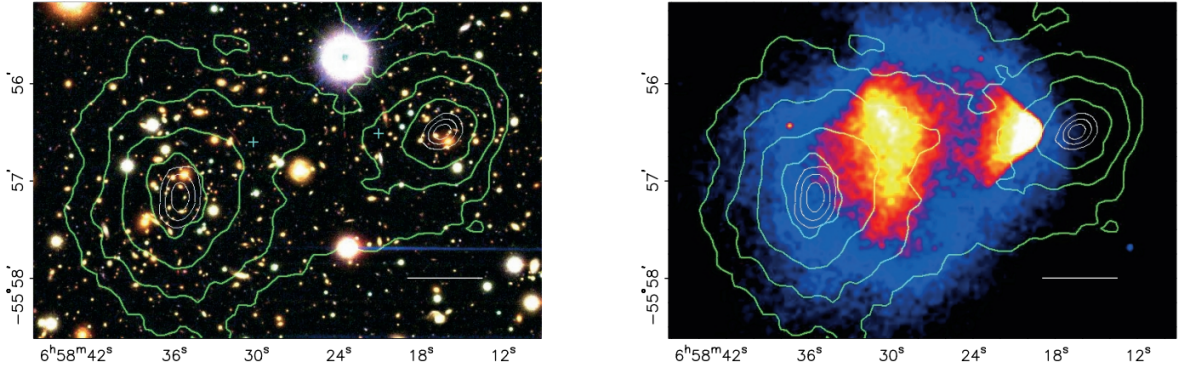


Figure 2.3 (left) Optical image of galactic cluster 1E0657-558. (right) X-ray image of the cluster with redder meaning hotter and higher baryon density. (both) Green contours are reconstruction of gravity contours from weak lensing. White rings are the best fit mass maxima at 68.3%, 95.5%, and 99.7% confidence. The matter maxima of the clusters are clearly separated from x-ray maxima. [9]

546 light, see Figure 2.2. With a sufficient understanding of light sources behind a massive object, we
 547 can reconstruct the contours of the gravitational lenses. The gradient of the contours shown in
 548 Figure 2.3 then indicates how dense the matter is and where it is.

549 The x-ray emission can then be observed from the clusters. Since these galaxies are mostly gas
 550 and are merging, then the gas should be getting hotter. If they are merging, the x-ray emissions
 551 should be the strongest where the gas is mostly moving through each other. Hence, X-ray emission
 552 maps out where the gas is in the merging galaxy cluster.

553 The lensing and x-ray observations were done on the Bullet cluster featured on Figure 2.3.
 554 The x-ray emissions do not align with the gravitational contours from lensing. The incongruence
 555 in mass density and baryon density suggests that there is a lot of matter somewhere that does
 556 not interact with light. Moreover, this dark matter cannot be baryonic [9]. The Bullet Cluster
 557 measurement did not really tell us what DM is exactly, but it did give the clue that DM also does
 558 not interact with itself very strongly. If DM did interact strongly with itself, then it would have been
 559 more aligned with the x-ray emission [9]. There have been follow-up studies of galaxy clusters with
 560 similar results. The Bullet Cluster and others like it provide a persuasive case against something
 561 possibly amiss in our gravitational theories.

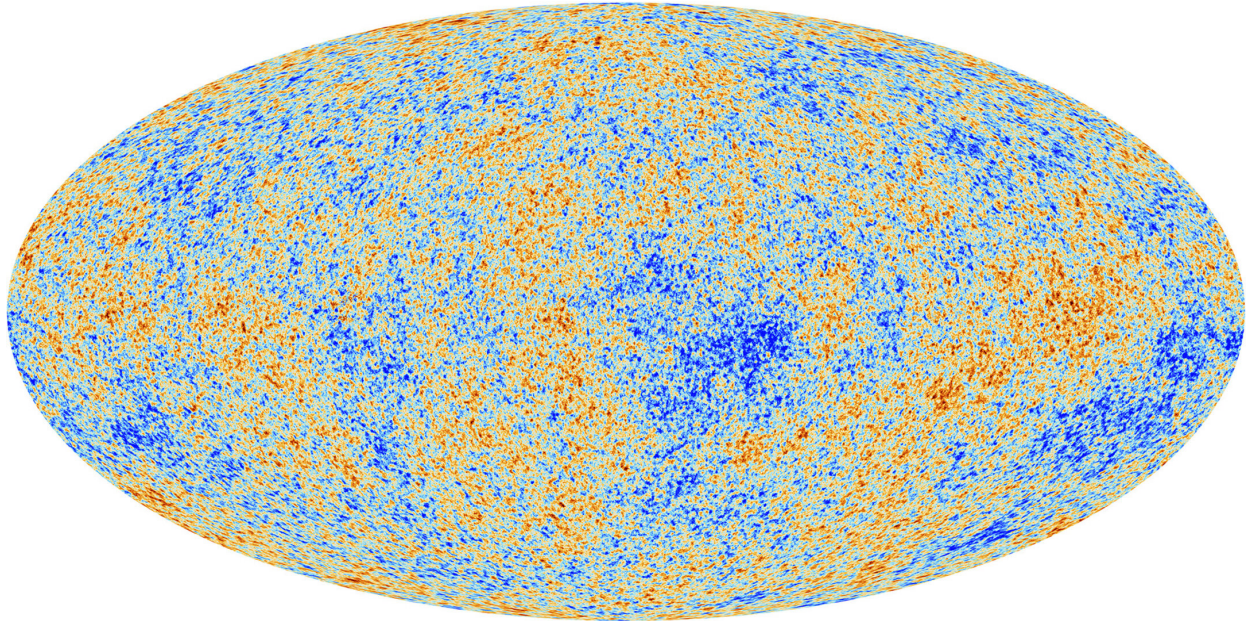


Figure 2.4 Plank CMB sky. Sky map features small variations in temperature in primordial light. These anisotropies are used to make inferences about the universe's energy budget and developmental history. [10]

562 **2.3.3 Evidence for Dark Matter: Cosmic Microwave Background**

563 The Cosmic Microwave Background (CMB) is the primordial light from the early universe
564 when Hydrogen atoms formed from the free electron and proton soup in the early universe. The
565 CMB is the earliest light we can observe; released when the universe was about 380,000 years old.
566 Then we look at how the simulated universes look like compared to what we see. Figure 2.4 is the
567 most recent CMB image from the Plank satellite after subtracting the average value and masking the
568 galactic plane [10]. Redder regions indicate a slightly hotter region in the CMB, and blue indicates
569 colder. The intensity variations are on the order of 1 in 1000 with respect to the average value.

570 The Cosmic Microwave Background shows that the universe had DM in it from an incredibly
571 early stage. To measure the DM, Dark Energy, and matter fractions of the universe from the CMB,
572 the image is analyzed into a power spectrum, which shows the amplitude of the fluctuations as
573 a function of spherical multipole moments. Λ CDM provides the best fit to the power spectra of
574 the CMB as shown in Figure 2.5. The CMB power spectrum is quite sensitive to the fraction
575 of each energy contribution in the early universe. Low l modes are dominated by variations
576 in gravitational potential. Intermediate l emerge from oscillations in photon-baryon fluid from

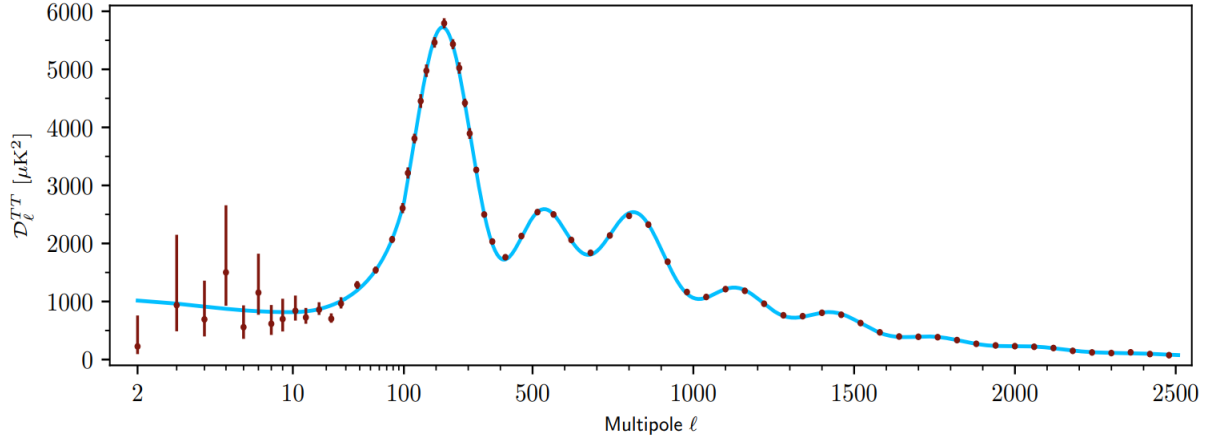


Figure 2.5 Observed Cosmic Microwave Background power spectrum as a function of multipole moment from Plank [10]. Blue line is best fit model from Λ CDM. Red points and lines are data and error, respectively.

577 competing baryon pressures and gravity. High l is a damped region from the diffusion of photons
 578 during electron-proton recombination. [1]

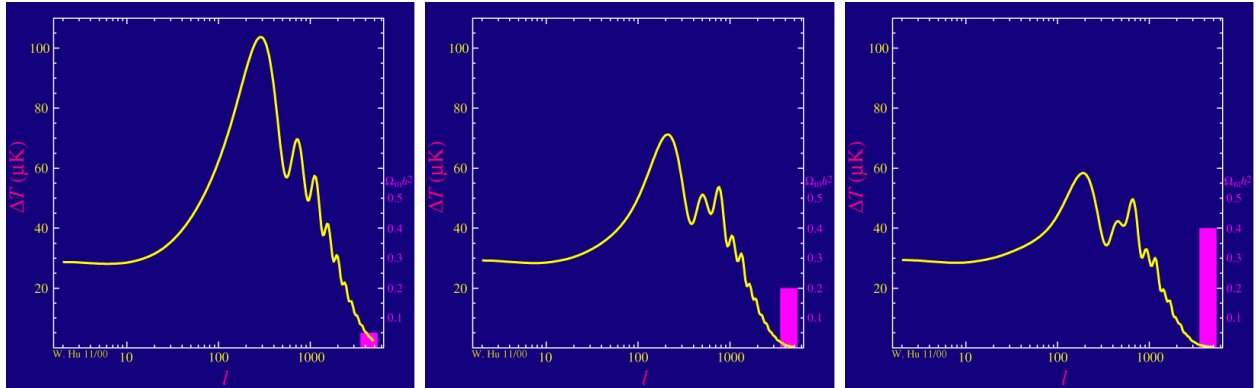


Figure 2.6 Predicted power spectra of CMB for different $\Omega_m h^2$ values for fixed baryon density from [11]. (left) Low $\Omega_m h^2$ increases the prominence of first and second peaks. (middle) $\Omega_m h^2$ is most similar to the observed power spectrum. The second and third peaks are similar in height. (right) $\Omega_m h^2$ is large which suppresses the first peak and raises the prominence of the third peak.

579 The harmonics would look quite different for a universe with less DM. Figure 2.6 demonstrates
 580 the effect $\Omega_m h^2$ has on the expected power spectrum for fixed baryon matter density. [11] Sweeping
 581 $\Omega_m h^2$ in this way clearly shows the effect dark matter has on the CMB power spectrum. The
 582 observations fit well with the Λ CDM model, and the derived fractions are as follows. The matter
 583 fraction: $\Omega_m = 0.3153$; and the baryon fraction: $\Omega_b = 0.04936$ [10]. Plank's observations also
 584 provide a measure of the Hubble constant, H_0 . H_0 especially has seen a growing tension in the

585 past decade that continues to deepened with observations from instruments like the James Webb
586 Telescope [12, 13]. As Hubble tensions deepen, we may find that perhaps Λ **CDM**, despite its
587 successes, is missing some critical physics.

588 Overall, the Newtonian motion of stars in galaxies, weak lensing from galactic clusters, and
589 power spectra from primordial light form a compelling body of research in favor of dark matter.
590 It takes another leap of theory and experimentation to make observations of DM that are non-
591 gravitational in nature. In Section 2.3, the evidence for DM implies strongly that the DM is matter
592 and not a lost parameter in the gravitational fields between massive objects. Finally, if we take one
593 axiom: that this matter has quantum behavior, such as being described by some Bohr wavelength
594 and abiding by some fermion or boson statistics; then we arrive at particle dark matter. One particle
595 DM hypothesis is the Weakly Interacting Massive Particle (WIMP). This DM candidate theory is
596 discussed further in the next section and is the focus of this thesis.

597 2.4 Searching for Dark Matter: Particle DM

598 Section 2.4 shows the Standard Model of particle physics and is currently the most accurate
599 model for the dynamics of fundamental particles like electrons and photons. The current status
600 of the SM does not have a viable DM candidate. When looking at the standard model, we can
601 immediately exclude any charged particle because charged particles interact strongly with light.
602 Specifically, this will rule out the following charged, fundamental particles: $e, \mu, \tau, W, u, d, s, c, t, b$
603 and their corresponding antiparticles. Recalling from Section 2.2 that DM must be long-lived and
604 stable over the age of the universe which excludes all SM particles with decay half-lives at or shorter
605 than the age of the universe. The lifetime constraint additionally eliminates the Z and H bosons.
606 Finally, the candidate DM needs to be somewhat massive. Recall from Section 2.2 that DM is cold
607 or not relativistic through the universe. This eliminates the remaining SM particles: $\nu_{e,\mu,\tau}, g, \gamma$ as
608 DM candidates. Because there are no DM candidates within the SM, the DM problem strongly
609 hints to physics beyond the SM (BSM).

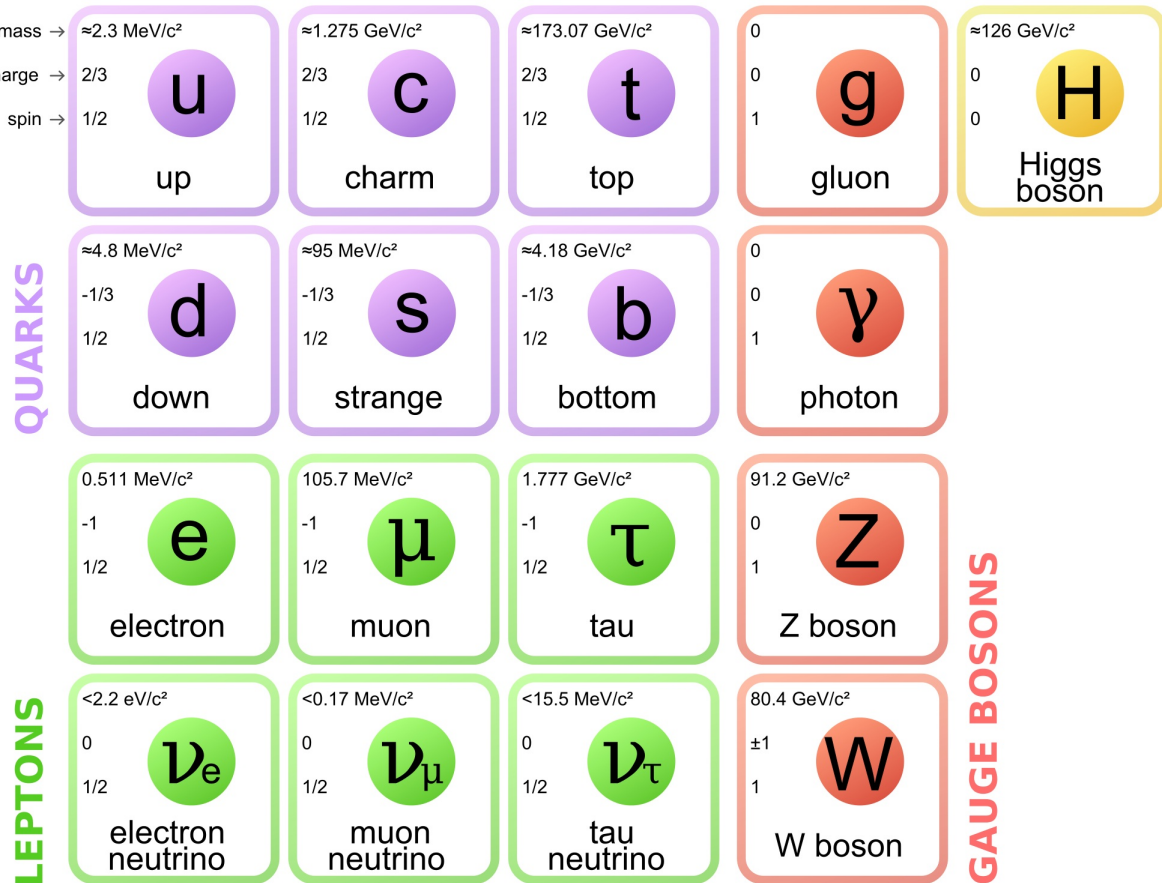


Figure 2.7 The Standard Model (SM) of particle physics. Figure taken from <http://www.quantumdiaries.org/2014/03/14/the-standard-model-a-beautiful-but-flawed-theory/>

610 2.4.1 Shake it, Break it, Make it

611 When considering DM that couples in some way with the SM, the interactions are roughly
 612 demonstrated by interaction demonstrated in Figure 2.8. The figure is a simplified Feynman
 613 diagram where the arrow of time represents the interaction modes of: **Shake it, Break it, Make it**.

614 **Shake it** refers to the direct detection of dark matter. Direct detection interactions start with
 615 a free DM particle and an SM particle. The DM and SM interact via elastic or inelastic collision
 616 and recoil away from each other. The DM remains in the dark sector and imparts some momentum
 617 onto the SM particle. The hope is that the momentum imparted onto the SM particle is sufficiently
 618 high enough to pick up with extremely sensitive instruments. Because we cannot create the DM in
 619 the lab, a direct detection experiment must wait until DM is incident on the detector. Most direct
 620 detection experiments are therefore placed in low-background environments with inert detection

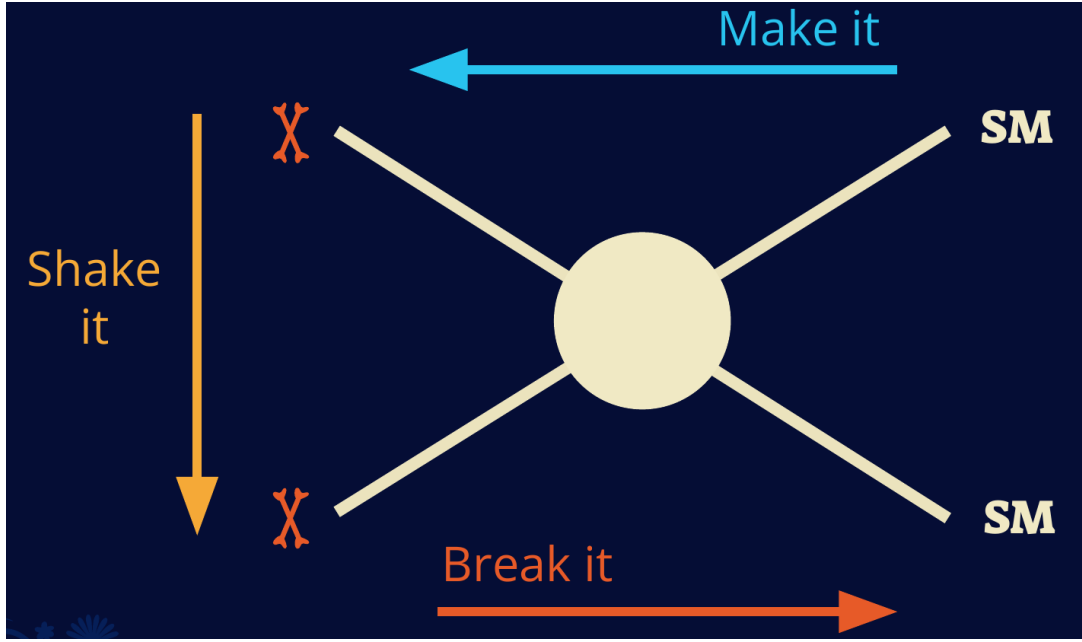


Figure 2.8 Simplified Feynman diagram demonstrating different ways DM can interact with SM particles. The 'X's refer to the DM particles whereas the SM refer to fundamental particles in the SM. The large circle in the center indicates the vertex of interaction and is purposely left vague. The colored arrows refer to different directions of time as well as their respective labels. The arrows indicate the initial and final state of the DM -SM interaction in time.

621 media like the noble gas Xenon. [14]

622 **Make it** refers to the production of DM from SM initial states. The experiment starts with
 623 particles in the SM. These SM particles are accelerated to incredibly high energies and then collide
 624 with each other. In the confluence of energy, DM hopefully emerges as a byproduct of the SM
 625 annihilation. Often it is the collider experiments that are energetic enough to hypothetically produce
 626 DM. These experiments include the world-wide collaborations ATLAS and CMS at CERN where
 627 proton collide together at extreme energies. The DM searches, however, are complex. DM likely
 628 does not interact with the detectors and lives long enough to escape the detection apparatus of
 629 CERN's colliders. This means any DM production experiment searches for an excess of events
 630 with missing momentum or energy in the events. An example event with missing transverse
 631 momentum is shown in Figure 2.9. The missing momentum with no particle tracks implies a
 632 neutral particle carried the energy out of the detector. However, there are other neutral particles
 633 in the SM, like neutrons or neutrinos, so any analysis has to account for SM signatures of missing

634 momentum. [15]

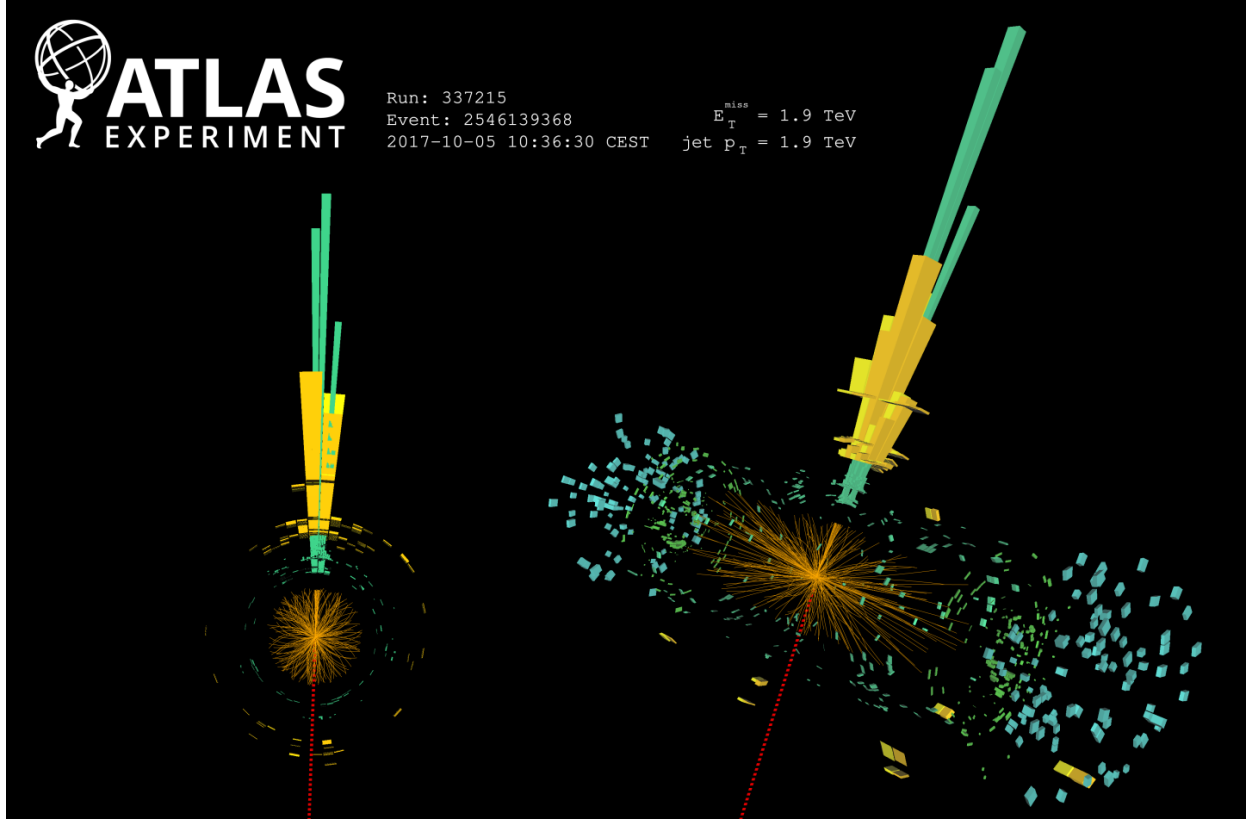


Figure 2.9 A single jet event in ATLAS detector from 2017 [16]. Jet momentum was observed to be 1.9 TeV. Missing transverse momentum was observed to be 1.9 TeV compared to the initial transverse momentum of the event was 0. Implied MET is traced by a red dashed line in event display.

635 2.4.2 Break it: Standard Model Signatures of Dark Matter through Indirect Searches

636 **Break it** refers to the creation of SM particles from the dark sector, and it is the primary focus
637 of this thesis. The interaction begins with DM or in the dark sector. The hypothesis is that this
638 DM will either annihilate with itself or decay and produce an SM byproduct. This method is
639 often referred to as the Indirect Detection of DM because we have no lab to directly control or
640 manipulate the DM. Therefore, most indirect DM searches are performed using observations of
641 known DM densities among the astrophysical sources. The strength is that we have the whole of the
642 universe and its 13.6-billion-year lifespan to use as a detector and particle accelerator. Additionally,
643 locations of dark matter are well cataloged since it was astrophysical observations that presented

644 the problem of DM in the first place.

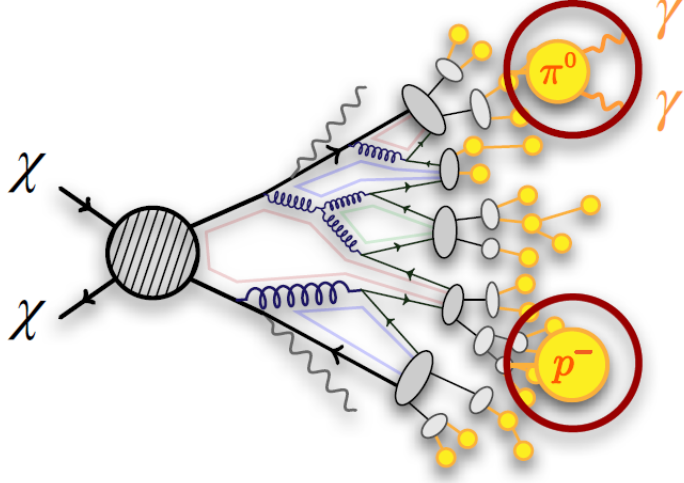


Figure 2.10 More detailed pseudo-Feynman diagram of particle cascade from dark matter annihilation into 2 quarks. The quarks hadronize and down to stable particles like γ or the anti-proton (p^-). Diagram pulled from ICRC 2021 presentation on DM annihilation search [17].

645 However, anything can happen in the universe. There are many difficult to deconvolve back-
646 grounds when searching for DM. One prominent example is the galactic center. We know the
647 galactic center has a large DM content because of stellar kinematics in our Milky Way and DM halo
648 simulations. Yet, any signal from the galactic center is challenging to parse apart from the extreme
649 environment of our supermassive black hole, unresolved sources, and diffuse emission from the
650 interstellar medium [18]. Despite the challenges, any DM model that yields evidence in the other
651 two observation methods, **Shake it or Make it** must be corroborated with indirect observations of
652 the known DM sources. Without corroborating evidence, DM observation in the lab is hard-pressed
653 to demonstrate that it is the model contributing to the DM seen at the universal scale.

654 In the case of WIMP DM, signals are described in terms of primary SM particles produced
655 from DM decay or annihilation. The SM initial state particles are then simulated down to stable
656 final states such as the γ , ν , p , or e which can traverse galactic lengths to reach Earth.

657 Figure 2.10 shows the quagmire of SM particles that emerges from SM initial states that are not
658 stable [17]. There are many SM particles with varying energies that can be produced in such an

659 interaction. For any arbitrary DM source and stable SM particle, the SM flux from DM annihilating
 660 to a neutral particle in the SM, ϕ , from a region in the sky is described by the following.

$$\frac{d\Phi_\phi}{dE_\phi} = \frac{\langle\sigma v\rangle}{8\pi m_\chi^2} \frac{dN_\phi}{dE_\phi} \times \int_{\text{source}} d\Omega \int_{l.o.s} \rho_\chi^2 dl(r, \theta') \quad (2.4)$$

661 In Equation (7.1), $\langle\sigma v\rangle$ is the velocity-weighted annihilation cross-section of DM to the SM. m_χ
 662 refers to the mass of DM, noted with Greek letter χ . $\frac{dN_\phi}{dE_\phi}$ is the N particle flux weighted by the
 663 particle energy. An example is provided in Figure 2.11 for the γ final state. The integrated terms
 664 are performed over the solid angle, $d\Omega$, and line of sight, l.o.s. ρ is the density of DM for a
 665 location (r, θ') in the sky. The terms left of the '×' are often referred to as the particle physics
 666 component. The terms on the right are referred to as the astrophysical component. For decaying
 667 DM, the equation changes to...

$$\frac{d\Phi_\phi}{dE_\phi} = \frac{1}{4\pi\tau m_\chi} \frac{dN_\phi}{dE_\phi} \times \int_{\text{source}} d\Omega \int_{l.o.s} \rho_\chi dl(r, \theta') \quad (2.5)$$

668 In Equation (2.5), τ is the decay lifetime of the DM. Just as in Equation (7.1), the left and right
 669 terms are the particle physics and the astrophysical components respectively. The integrated
 670 astrophysical component of Equation (7.1) is often called the J-Factor. Whereas the integrated
 671 astrophysical component of Equation (2.5) is often called the D-Factor.

672 Exact DM $\text{DM} \rightarrow \text{SM SM}$ branching ratios are not known, so it is usually assumed to go 100%
 673 into an SM particle/anti-particle. Additionally, when a DM annihilation or decay produces one of
 674 the neutral, long-lived SM particles (ν or γ), the particle is traced back to a DM source. For DM
 675 above GeV energies, there are very few SM processes that can produce particles with such a high
 676 energy. Seeing such a signal would almost certainly be an indication of the presence of dark matter.
 677 Fortunately, the universe provides us with the largest volume and lifetime ever for a particle physics
 678 experiment.

679 2.5 Sources for Indirect Dark Matter Searches

680 The first detection of DM relied on optical observations. Since then, we have developed new
 681 techniques to find DM dense regions. As described in Section 2.3.1, many DM dense regions were
 682 through observing galactic rotation curves. Our Milky Way galaxy is among DM dense regions

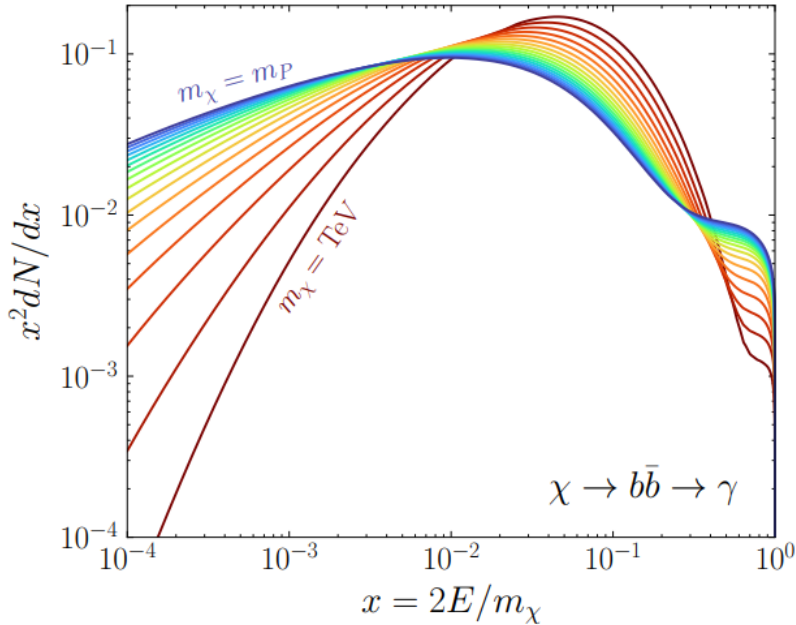


Figure 2.11 Dark Matter (DM) decay spectrum for $b\bar{b}$ initial state and γ final state. Redder spectra are for larger DM masses. Bluer spectra are light DM masses. x is a unitless factor defined as the ratio of the mass of DM, m_χ , and the final state particle energy E_γ . Figure from [19].

discovered, and it is the largest nearby DM dense region to look at. Additionally, the DM halo surrounding the Milky Way is clumpy [18]. There are regions in the DM halo of the Milky Way that have more DM than others that have captured gas over time. These sub-halos were dense enough collapse gas and form stars. These apparent sub galaxies are known as dwarf spheroidal galaxies and are the main sources studied in this thesis. Each source type comes with different trade-offs. Galactic Center studies will be very sensitive to the assumed distribution of DM. The central DM density can vary substantially as demonstrated in Figure 2.12. At distances close to the center of the galaxy, or small r , the differences in DM densities can be 3-4 orders of magnitude. Searches toward the galactic center will therefore be quite sensitive to the assumed DM distribution.

Searches toward Dwarf Spheroidal Galaxies (dSph's) suffer from uncertainties in the DM density less than the galactic center studies. This is mostly from their diminutive size being smaller than the angular resolution of most γ -ray observatories [18]. The DM content dSph's are typically determined with the Virial theorem, Equation (2.1), and are usually majority DM [18] in mass. DSph's tend to be ideal sources to look at for DM searches. Their environments are quiet with little

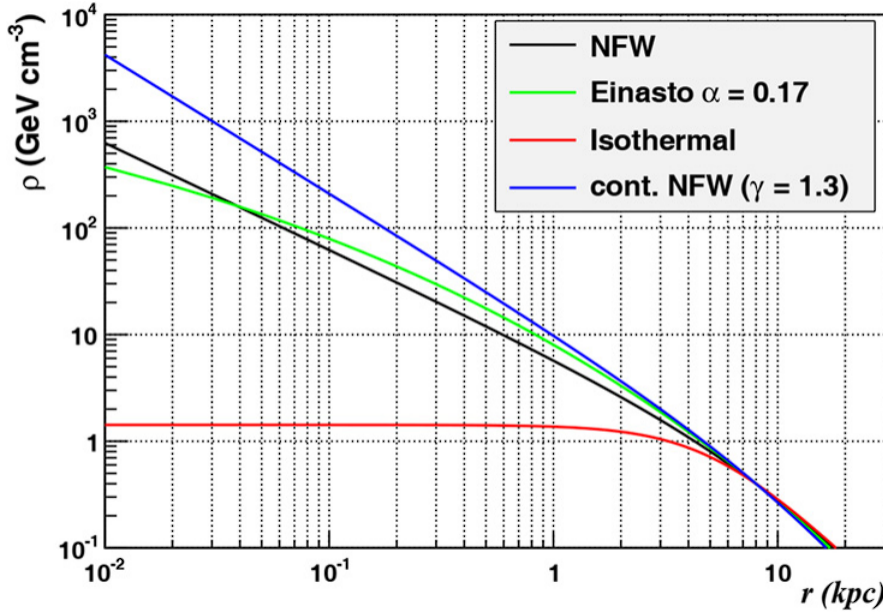


Figure 2.12 Different dark matter density profiles compared. Some models produce exceptionally large densities at small r [20].

697 astrophysical background. Unlike the galactic center, the most active components of dSph's are the
 698 stars within them versus a violent accretion disc around a black hole. All this together means that
 699 dSph's are among the best sources to look at for indirect DM searches. dSph's are the targets of
 700 focus for this thesis.

701 2.6 Multi-Messenger Dark Matter

702 Astrophysics entered a new phase in the past few decades that leverages our increasing sensitivity
 703 to SM channels and general relativity (GR). Up until the 21st century, astrophysical observations
 704 were performed with photons (γ) only. Astrophysics with this 'messenger' is fairly mature now.
 705 Novel observations of the universe have since only adjusted the sensitivity of the wavelength of
 706 light that is observed except at MeV energies. Gems like the CMB [10], and more have ultimately
 707 been observations of different wavelengths of light. Multi-messenger astrophysics proposes using
 708 other SM particles such the p^{+-} , or ν or gravitation waves predicted by general relativity.

709 The experiment LIGO had a revolutionary discovery in 2016 with the first detection of a binary
 710 black hole merger [21]. This opened the collective imagination to observing the universe through
 711 gravitational waves. There has also been a surge of interest in the neutrino (ν) sector. IceCube

712 demonstrated that we are sensitive to neutrinos in regions that correlate with significant photon
 713 emission like the galactic plane [22]. Neutrinos, like gravitational waves and light, travel mostly
 714 unimpeded from their source to our observatories. This makes pointing to the originating source
 715 of these messengers much easier than it is for cosmic rays which are deflected from their source by
 716 magnetic fields.

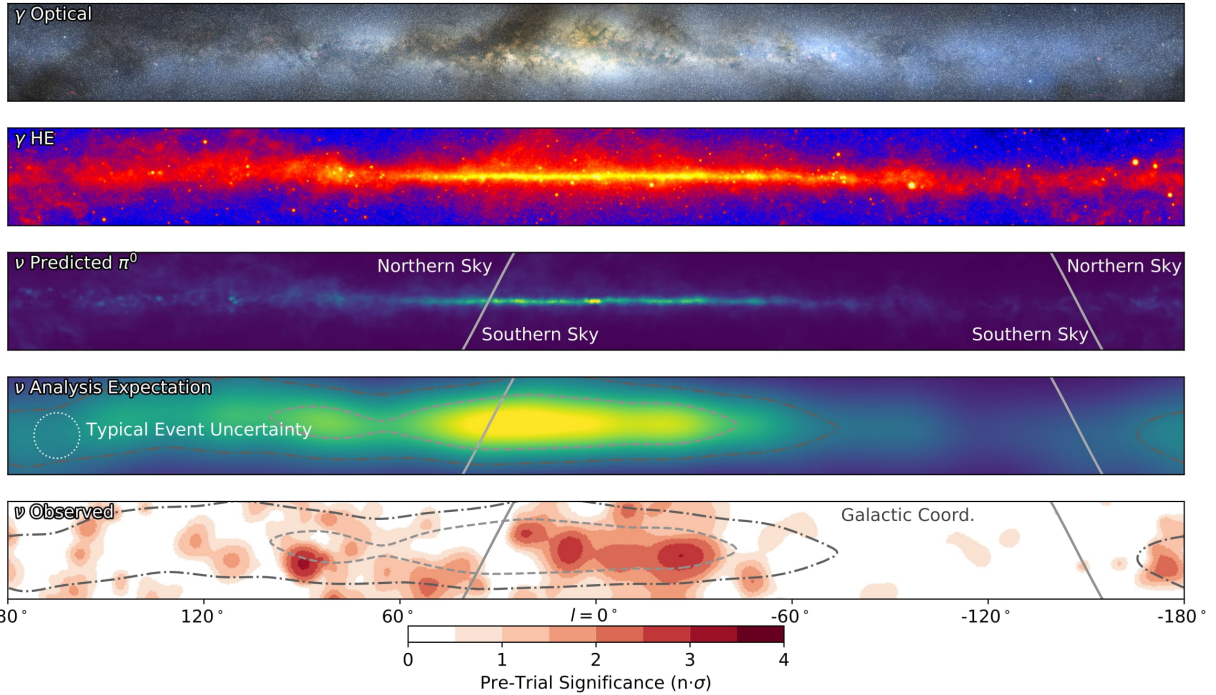


Figure 2.13 The Milky Way Galaxy in photons (γ) and neutrinos (ν) [22]. The Galactic center is at $l=0^\circ$ and is the brightest region in all panels. (top) An Optical color image of the Milky Way galaxy seen from Earth. Clouds of gas and dust obscure some light from stars. (2nd down) Integrated flux of γ -rays observed by the Fermi-LAT telescope [23]. (middle) Expected neutrino emission that corresponds with Fermi-LAT observations. (2nd up) Expected neutrino emission profile after considering detector systematics of IceCube. (bottom) Observed neutrino emission from region of the galactic plane. Substantial neutrino emission was detected.

717 The IceCube collaboration recently published a groundbreaking result of the Milky Way in
 718 neutrinos. The recent result from IceCube, shown in Figure 2.13, proves that we can make
 719 observations under different messenger regimes. The top two panels show the appearance of the
 720 galactic plane to different wavelengths of light. Some sources are more apparent in some panels,
 721 while others are not. This new channel is powerful because neutrinos are readily able to penetrate
 722 through gas and dust in the Milky Way. This new image also refines our understanding of how high

723 energy particles are produced. For example, the fit to IceCube data prefers neutrino production
 724 from the decay of π^0 [22].

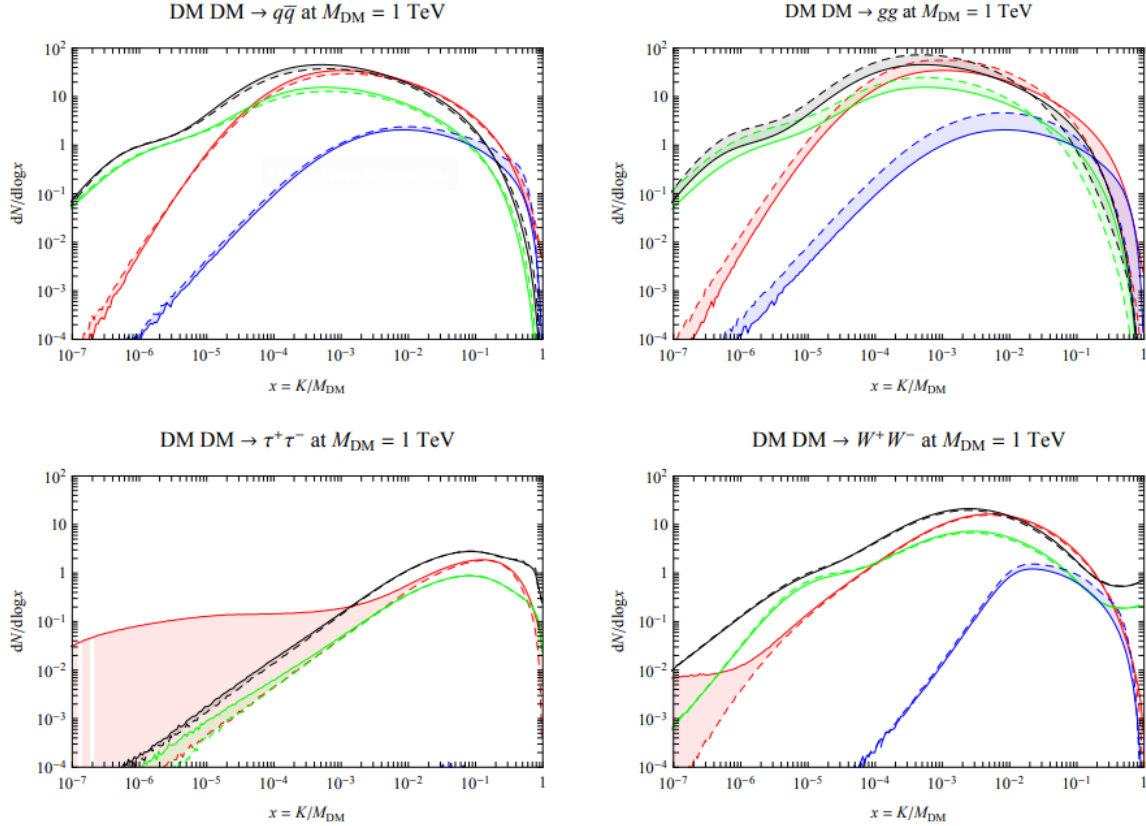


Figure 2.14 Dark Matter annihilation spectra for different final state particle and standard model annihilation channels [24]. Photons (red), e^\pm (green), \bar{p} (blue), ν (black).

725 Exposing our observations to more cosmic messengers greatly increases our sensitivity to
 726 rare processes. In the case of DM, Figure 2.14, there are many SM particles produced in DM
 727 annihilation. Among the final state fluxes are gammas and neutrinos. Charged particles are also
 728 produced however they would not likely make it to Earth since they will be deflected by magnetic
 729 fields between the source and Earth. This means observatories that can see the neutral messengers
 730 are especially good for DM searches and for combining data for a multi-messenger DM search.

CHAPTER 3

731 **HIGH ALTITUDE WATER CHERENKOV (HAWC) OBSERVATORY**

732 **3.1 The Detector**

733 **3.2 Events Reconstruction and Data Acquisition**

734 **3.2.1 G/H Discrimination**

735 **3.2.2 Angle**

736 **3.2.3 Energy**

737 **3.3 Remote Monitoring**

738 **3.3.1 ATHENA Database**

739 **3.3.2 HOMER**

740

CHAPTER 4

ICECUBE NEUTRINO OBSERVATORY

741 **4.1 The Detector**

742 **4.2 Events Reconstruction and Data Acquisition**

743 **4.2.1 Angle**

744 **4.2.2 Energy**

745 **4.3 Northern Test Site**

746 **4.3.1 PIgeon remote dark rate testing**

747 **4.3.2 Bulkhead Construction**

CHAPTER 5

GLORY DUCK: MULTI-WAVELENGTH SEARCH FOR DARK MATTTER ANNIHILATION TOWARDS DWARF SPHEROIDAL GALAXIES

5.1 Introduction

The field of astrophysics now has several instruments and observatories sensitive to high energy gamma-rays. The energy sensitivity for the modern gamma-ray program spans many orders of magnitude. Figure 5.1 demonstrates these comparable sensitivities across energies for the five experiments: Fermi-LAT, HAWC, HESS, MAGIC, and VERITAS.

Each of the five experiments featured in Figure 5.1 have independently searched for DM annihilation from dwarf spheroidal galaxies (dSph) and set limits on annihilation cross-section of WIMPs. Intriguingly, there are regions of substantial overlap in their energy sensitivities. This clearly motivates an analysis that combines data from these five. Each experiment has unique gamma-ray detection methods and their weaknesses and strengths can be leveraged with each other. The HAWC gamma-ray observatory is extensively introduced in chapter 3, so it is not introduced here. A brief description of the remaining experiments are in the following paragraphs.

The Large Area Telescope (LAT) is a pair conversion telescope mounted on the NASA Fermi satellite in orbit \sim 550 km above the Earth [26]. LAT's field of view covers about 20% of the whole sky, and it sweeps the whole sky approximately every 3 hours. LAT's gamma-ray energy sensitivity ranges from 20 MeV up to 1 TeV. Previous DM searches towards dSphs using Fermi-LAT are published in [27] and [28].

The High Energy Spectroscopic System (HESS), Major Atmospheric Gamma Imaging Cherenkov (MAGIC), and Very Energetic Radiation Imaging Telescope Array System (VERITAS) are arrays of Imaging Atmospheric Cherenkov Telescopes (IACT). These telescopes observe the Cherenkov light emitted from gamma-ray showers in the Earth's atmosphere. The field of view for these telescopes is no larger than 5° with energy sensitivities ranging from 30 GeV up to 100 TeV [29, 30, 31]. IACTs are able to make precise observations in selected regions of the sky, however can only be operated in ideal dark conditions. HESS's observations of the dwarves

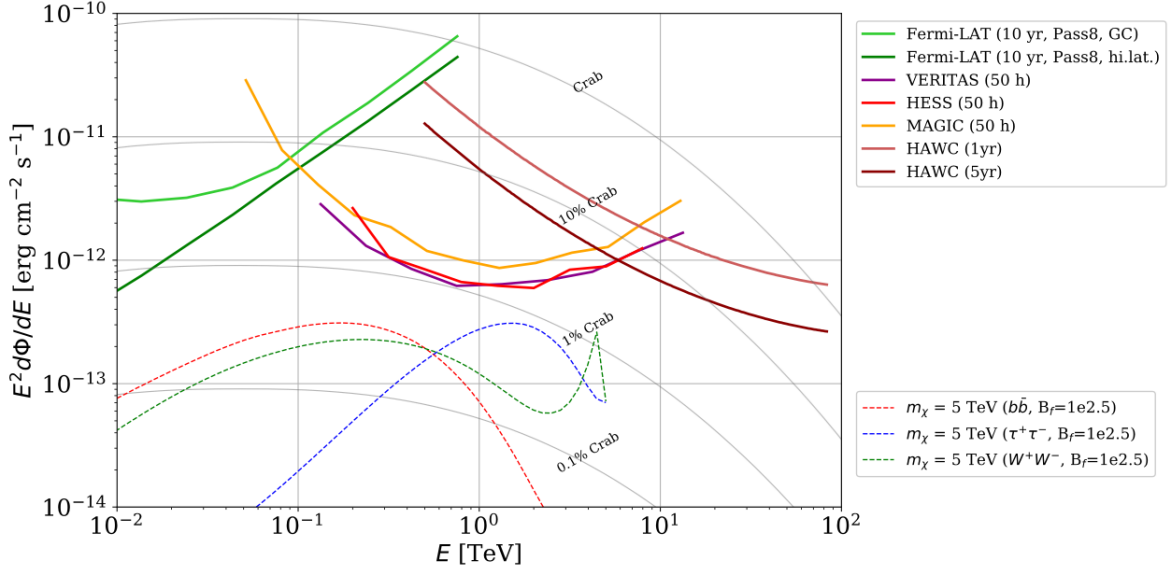


Figure 5.1 Sensitivities of five gamma-ray experiments compared to percentages of the Crab nebula’s emission and dark matter annihilation. Solid lines present estimated sensitivities to power law spectra [FACT CHECK THIS] for each experiment. Green lines are Fermi-LAT sensitivities where lighter green is the sensitivity to the galactic center and dark green is its sensitivity to higher declinations. Orange, red, and purple solid lines represent the MAGIC, HESS, and VERITAS 50 hour sensitivities respectively. The maroon and brown lines are the HAWC 1 year and 5 year sensitivities. Across four decades of gamma-ray energy, these experiments have similar sensitivities on the order 10^{-12} erg $\text{cm}^{-2}\text{s}^{-1}$. The dotted lines are estimated dark matter fluxes assuming $m_\chi = 5$ TeV DM annihilating to bottom quarks (red), tau leptons (blue), and W bosons (green). Faded gray lines outline percentage flux of the Crab nebula. Figure is an augmented version of [25]

774 Sculptor and Carina were between January 2008 and December 2009. HESS’s observations of
 775 Coma Berenices were taken from 2010 to 2013, and Fornax was observed in 2010 [32, 33, 34].
 776 MAGIC provided deep observations of Segue1 between 2011 and 2013 [35]. MAGIC also provides
 777 data for three additional dwarves: Coma Berenices, Draco, and Ursa Major II where observations
 778 were made in: January - June 2019 [36], March - September 2018 [36], and 2014 - 2016 [37]
 779 respectively. VERITAS provided data for Boötes I, Draco, Segue 1, and Ursa Minor from 2009 to
 780 2016 [38].

781 This chapter presents the Glory Duck analysis, the name given for the search for dark matter
 782 annihilation from dSph by combining data from the five gamma-ray observatories: Fermi-LAT,
 783 HAWC, HESS, MAGIC, and VERITAS. Specifically, the methods in analysis and modeling are
 784 presented for the HAWC gamma-ray observatory. This work will be published in the Journal of

785 Cosmology and Astroparticle Physics and presented at the International Cosmic Ray Conference
786 in 2019, 2021, and 2023 [39, 40, 41] and others.

787 **5.2 Dataset and Background**

788 This section enumerates the data analysis and background estimation methods used for HAWC's
789 study of dSphs. Section 5.2.1 and Section 5.2.2 are most useful for fellow HAWC collaborators
790 looking to replicate the Glory Duck analysis.

791 **5.2.1 Itemized HAWC files**

792 These files are only available withing HAWC's internal documentation and collaborators. They
793 are not meant for public access, and are presented here so that HAWC collaborators can reproduce
794 results accurately.

- 795 • Detector Response: `response_aerie_svn_27754_systematics_best_mc_test_noBr`
796 `oadpulse\10pctlogchargesmearing_0.63qe_25kHzNoise_run5481_curvature`
797 `0_index3.root`
- 798 • Data Map: `maps-20180119/liff/maptree_1024.root`
- 799 • Spectral Dictionary: `DM_CirrelliSpectrum_dict_gammas.npy`
- 800 • Analysis wiki: https://private.hawc-observatory.org/wiki/index.php/Glory_Duck_Multi-Experiment_Dark_Matter_Search

802 **5.2.2 Software Tools and Development**

803 This analysis was performed using HAL and 3ML [42, 43] in Python version 2. I built software
804 to implement the *A Poor Particle Physicist Cookbook for Dark Matter Indirect Detection* (PPPC)
805 [44] DM spectral model and dSphs spatial model from [45] for HAWC analysis. A NumPy version
806 of this dictionary was made for both Py2 and Py3. The code base for creating this dictionary is
807 linked on my GitLab sandbox:

- 808 • Py2: [Dictionary Generator \(Deprecated\)](#)

- 809 • Py3: [PPPC2Dict](#)

810 The analysis was performed using the f_{hit} framework as used and described in the HAWC Crab
811 paper [42]. The Python2 NumPy dictionary file for gamma-ray final states is `dmCirSpecDict.npy`.
812 The corresponding Python3 file is `DM_CirrelliSpectrum_dict_gammas.npy`. These files can
813 also be used for decay channels and the PPPC describes how [44]. All other software used for data
814 analysis, DM profile generation, and job submission to SLURM are also kept in my sandbox for
815 [the Glory Duck](#) project.

816 **5.2.3 Data Set and Background Description**

817 The HAWC data maps used for this analysis contain 1017 days of data between runs 2104
818 (2014-11-26) and 7476 (2017-12-20). They were generated from pass 4.0 reconstruction. The
819 analysis is performed using the f_{hit} energy binning scheme with bins (1-9) similar to what was done
820 for the Crab and previous HAWC dSph analysis [42, 46]. Bin 0 was excluded as it has substantial
821 hadronic contamination and poor angular resolution.

822 This analysis was done on dSphs because of their large DM mass content relative to baryonic
823 mass. We consider the following to estimate the background to this study.

- 824 • The dSphs' angular extent are small relative to HAWC's spatial resolution, so the analysis is
825 not sensitive to large or small scale anisotropies.
- 826 • The dSphs used in this analysis are off the galactic plane and therefore not contaminated by
827 diffuse emission from the galaxy.
- 828 • The dSphs are baryonically faint relative to their expected dark matter content and are not
829 expected to contain high energy gamma-ray sources.

830 Therefor we make no additional assumptions on the background from our sources and use
831 HAWC's standard direct integration method for background estimation [42]. The largest background
832 under this consideration is from an isotropic flux of cosmic rays. The contamination of this hadronic
833 flux is worse at lower energies where HAWC's gamma/hadron discrimination worse. It is possible

834 for gamma rays from DM annihilation to scatter in transit to HAWC via Inverse Compton Scattering
835 (ICS). This was investigated and its impact on the flux is negligible. Supporting information on
836 this is in Section 5.7.1

837 **5.3 Analysis**

838 The expected differential photon flux from DM-DM annihilation to standard model particles,
839 $d\Phi_\gamma/dE_\gamma$, over solid angle, Ω , is described by the familiar equation.

$$\frac{d\Phi_\gamma}{dE_\gamma} = \frac{\langle\sigma v\rangle}{8\pi m_\chi^2} \frac{dN_\gamma}{dE_\gamma} \times \int_{\text{source}} d\Omega \int_{l.o.s} dl \rho_\chi^2 J(r, \theta') \quad (5.1)$$

840 Where $\langle\sigma v\rangle$ is the velocity weighted annihilation cross-section. $\frac{dN}{dE}$ is the expected differential
841 number of photons produced at each energy per annihilation. m_χ is the rest mass of the supposed
842 DM particle. ρ_χ is the DM density. J is the astrophysical J-factor and is defined as

$$J = \int d\Omega \int_{l.o.s} dl \rho_\chi^2(r, \theta') \quad (5.2)$$

843 l is the distance to the source from Earth. r is the radial distance from the center of the source. θ' is
844 the half angle defining a cone containing the DM source. How each component is synthesized and
845 considered for HAWC's analysis is presented in the following sections. Section 5.3.1 presents the
846 particle physics model for DM annihilation. Section 5.3.2 presents the spatial distributions built
847 for each dSph.

848 **5.3.1 $\frac{dN_\gamma}{dE_\gamma}$ - Particle Physics Component**

849 For these spectra, we import the PPPC with Electroweak (EW) corrections [44]. Public versions
850 of the imported tables are provided by the [authors online](#). The spectrum is implemented as a model
851 script in astromodels for 3ML. The EW corrections were previously not considered for HAWC and
852 are significant for DM annihilating to EW coupled SM particles such as all leptons, and the γ ,
853 Z , and W bosons [46]. Figure 5.2 demonstrates the significance of EW corrections for W boson
854 annihilation. Across EW SM channels, the gamma-ray spectra become harder than spectra without
855 EW corrections. Tables from the PPPC were reformatted into Python NumPy dictionaries for
856 collaboration-wide use. A class in astromodels was developed to include the EW correction from
857 the PPPC and is aptly named `PPPCSpectra` within `DM_models.py`.

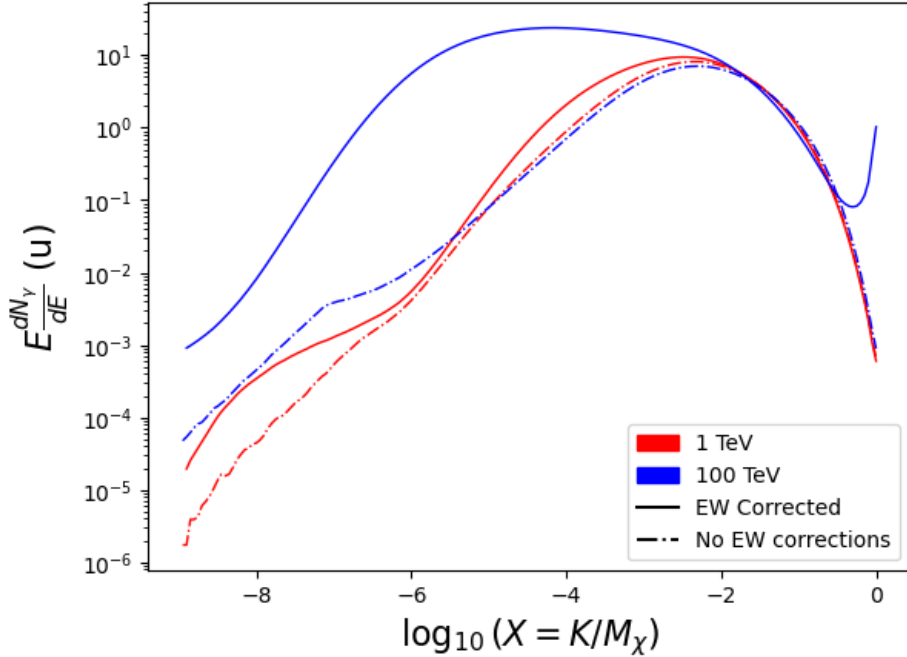


Figure 5.2 Effect of Electroweak (EW) corrections on expected DM annihilation spectrum for $\chi\chi \rightarrow W^-W^+$. Solid lines are spectral models that consider EW corrections. Dash-dot lines are spectral models without EW corrections. Red lines are models for $M_\chi = 1$ TeV. Blue lines represent models for $M_\chi = 100$ TeV. All models are sourced from the PPPC4DMID [44].

858 5.3.2 J- Astrophysical Component

859 The J-factor profiles for each source are imported from Geringer-Sameth (referred to with \mathcal{GS})
 860 [45]. \mathcal{GS} fits the Zhao DM profile to the dSphs which has a DM density described as [47]

$$\rho(r) = \frac{\rho_0}{(r/R_s)^\gamma (1 + (r/R_s)^\alpha)^{(\beta-\gamma)}}. \quad (5.3)$$

861 R_s is the scale radius and free parameter in the model. γ is the logarithmic slope in the region
 862 $r \ll R_s$. β is the logarithmic slope in the region $r \gg R_s$. α is known as the sharpness of transition
 863 where $r \approx R_s$. The classic Navarro-Frenk-White [48] (NFW) can be retrieved from Zhao by fixing
 864 $(\alpha, \beta, \gamma) = (1, 3, 1)$.

865 \mathcal{GS} best fits were pulled from the publication as $J(\theta)$, where θ is the angular separation from
 866 the center of the source. HAWC requires maps in terms of $\frac{dJ}{d\Omega}$, so the conversion from the maps
 867 was done in the following way...

868 First, convert the angular distances to solid angles

$$\Omega = 2 \cdot \pi(1 - \cos(\theta)) \quad (5.4)$$

869 which reduces with a small angle approximation to $\pi\theta^2$. Next, the central difference for both the
870 ΔJ and $\Delta\Omega$ value were calculated from the discretized $J(\theta)$ with the central difference stencil:

$$\Delta\phi_i = \phi_{i+1} - \phi_{i-1} \quad (5.5)$$

871 Where ϕ is either Ω or J . These were done separately in case the grid spacing in θ was not uniform.
872 Finally, these lists are divided so that we are left with an approximation of the $dJ/d\Omega$ profile that
873 is a function of θ . Admittedly, this is an approximation method for the map which introduces small
874 errors compared to the true profile estimate. This was checked as a systematic against the author's
875 profiling of the spatial distribution and is documented in Section 5.8.1.

876 With $\frac{dJ}{d\Omega}(\theta)$, a map is generated, first by filling in the north-east quadrant of the map. This
877 quadrant is then reflected twice, vertically then horizontally, to fill the full map. Maps are then
878 normalized by dividing the discrete 2D integral of the map. The 2D integral was a simple height
879 of bins, Newton's integral:

$$p^2 \cdot \sum_{i,j=0}^{N,M} \frac{dJ}{d\Omega}(\theta_{i,j}, \phi_{i,j}) \quad (5.6)$$

880 These maps are HEALpix maps with NSIDE 16384 and saved in the .fits format. The hyper fine
881 resolution was selected to better preserve the total expected counts after integrating Eq. (7.1) with
882 the detector response.

883 Another DM spatial distribution model from Bonnivard (\mathcal{B}) [49] was used for the Glory Duck
884 study. However, to save computational time, limits from \mathcal{GS} were scaled to \mathcal{B} instead of each
885 experiment performing a full study a second time. How these models compare is demonstrated
886 for each dSph in Figure 5.16 and Figure 5.17 Plots of these maps are provided for each source
887 in chapter A Examples of the two most impactful dSphs derived from \mathcal{GS} , Segue1 and Coma
888 Berenices are featured in Figure 5.3

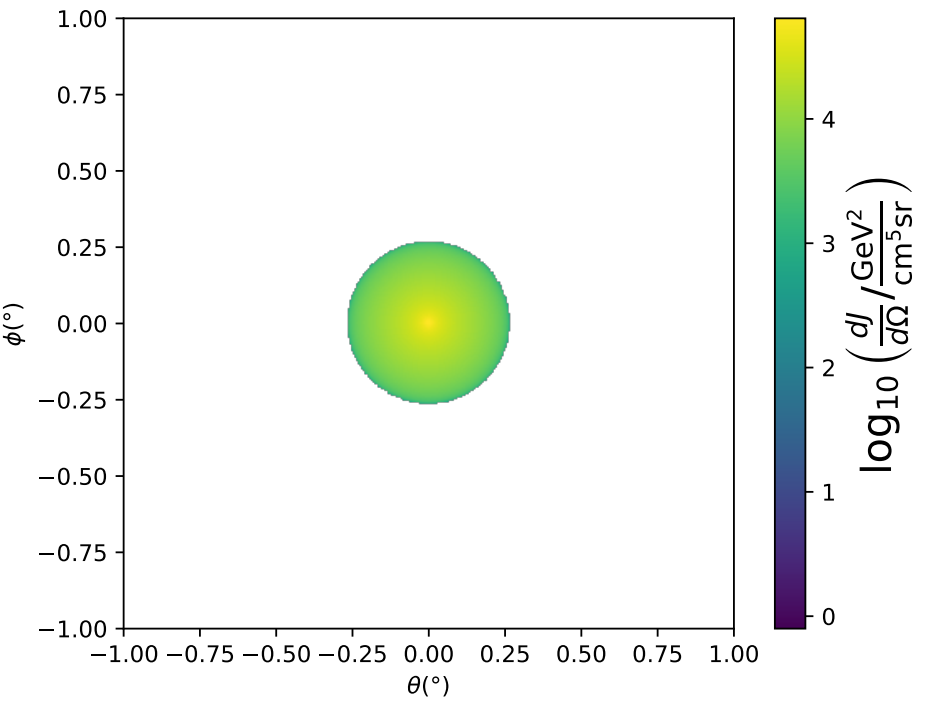
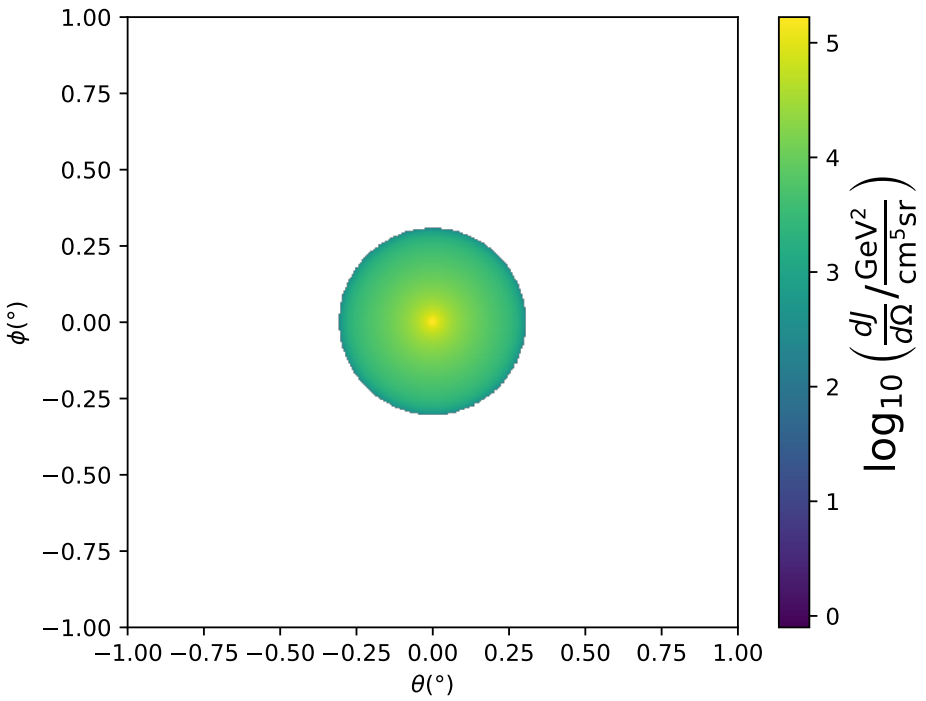


Figure 5.3 $\frac{dJ}{d\Omega}$ maps for Segue1 (top) and Coma Berenices (bottom). Origin is centered on the specific dwarf spheroidal galaxies (dSph). X and Y axes are the angular separation from the center of the dwarf. Profile is truncated at the scale radius. Plots of the remaining 11 dSph HAWC studied are linked in Fig. A.1.

889 **5.3.3 Source Selection and Annihilation Channels**

890 We use many of the dSphs presented in HAWC’s previous dSph DM search [46]. HAWC’s
891 sources for Glory Duck include Boötes I, Coma Berenices, Canes Venatici I + II, Draco, Hercules,
892 Leo I, II, + IV, Segue 1, Sextans, and Ursa Major I + II. A full description of all sources used
893 in Glory Duck is found in Table 5.1. Triangulum II was excluded from the Glory Duck analysis
894 because of large uncertainties in its J factor. Ursa Minor was excluded from HAWC’s contribution
895 to the combination because the source extension model extended Ursa Minor beyond HAWC’s field
896 of view. Ursa Minor was not expected to contribute significantly to the combined limit, so work
897 was not invested in a solution to include Ursa Minor.

898 This analysis improves on the previous HAWC dSph paper [46] in the following ways. Pre-
899 viously, the dSphs were treated and implemented as point sources. For this analysis, dSphs are
900 modeled and treated as extended source. The impact of this change with respect to the upper limit
901 is source dependent and is explored in Section 5.7.2. Previously, the particle physics model used for
902 gamma-ray spectra from DM annihilation did not have EW corrections where the PPPC includes
903 them. Finally, the gamma-ray ray dataset is much larger. The study performed here analyzes over
904 1000 days of data compared to 507.

905 The SM annihilation channels probed for the Glory Duck combination include $b\bar{b}$, $e\bar{e}$, $\mu\bar{\mu}$, $\tau\bar{\tau}$,
906 $t\bar{t}$, W^+W^- , and ZZ . A summary of all sources, with a description of each experiments’ sensitivity
907 to the source, is provided in Table 5.2.

908 **5.4 Likelihood Methods**

909 **5.4.1 HAWC Likelihood**

910 For every analysis bin in energy, f_{hit} bins (1-9), and location, we can expect N signal events and
911 B background events. The expected number of excess signal events from dark matter annihilation,
912 S , is estimated by convolving Equation (7.1) with HAWC’s energy response and pixel point spread
913 functions. I then compute the test statistic (TS) with the log-likelihood ratio test,

$$TS_{max} = -2 \ln \left(\frac{\mathcal{L}_0}{\mathcal{L}^{max}} \right) \quad (5.7)$$

Table 5.1 Summary of the relevant properties of the dSphs used in the present work. Column 1 lists the dSphs. Columns 2 and 3 present their heliocentric distance and galactic coordinates, respectively. Columns 4 and 5 report the J -factors of each source given from the \mathcal{GS} and \mathcal{B} independent studies and their estimated $\pm 1\sigma$ uncertainties. The values $\log_{10} J$ (\mathcal{GS} set) [45] correspond to the mean J -factor values for a source extension truncated at the outermost observed star. The values $\log_{10} J$ (\mathcal{B} set) [49] are provided for a source extension at the tidal radius of each dSph. **Bolded sources are within HAWC's field of view and provided to the Glory Duck analysis.**

Name	Distance (kpc)	l, b ($^{\circ}$)	$\log_{10} J$ (\mathcal{GS} set) $\log_{10}(\text{GeV}^2\text{cm}^{-5}\text{sr})$	$\log_{10} J$ (\mathcal{B} set) $\log_{10}(\text{GeV}^2\text{cm}^{-5}\text{sr})$
Boötes I	66	358.08, 69.62	$18.24^{+0.40}_{-0.37}$	$18.85^{+1.10}_{-0.61}$
Canes Venatici I	218	74.31, 79.82	$17.44^{+0.37}_{-0.28}$	$17.63^{+0.50}_{-0.20}$
Canes Venatici II	160	113.58, 82.70	$17.65^{+0.45}_{-0.43}$	$18.67^{+1.54}_{-0.97}$
Carina	105	260.11, -22.22	$17.92^{+0.19}_{-0.11}$	$18.02^{+0.36}_{-0.15}$
Coma Berenices	44	241.89, 83.61	$19.02^{+0.37}_{-0.41}$	$20.13^{+1.56}_{-1.08}$
Draco	76	86.37, 34.72	$19.05^{+0.22}_{-0.21}$	$19.42^{+0.92}_{-0.47}$
Fornax	147	237.10, -65.65	$17.84^{+0.11}_{-0.06}$	$17.85^{+0.11}_{-0.08}$
Hercules	132	28.73, 36.87	$16.86^{+0.74}_{-0.68}$	$17.70^{+1.08}_{-0.73}$
Leo I	254	225.99, 49.11	$17.84^{+0.20}_{-0.16}$	$17.93^{+0.65}_{-0.25}$
Leo II	233	220.17, 67.23	$17.97^{+0.20}_{-0.18}$	$18.11^{+0.71}_{-0.25}$
Leo IV	154	265.44, 56.51	$16.32^{+1.06}_{-1.70}$	$16.36^{+1.44}_{-1.65}$
Leo V	178	261.86, 58.54	$16.37^{+0.94}_{-0.87}$	$16.30^{+1.33}_{-1.16}$
Leo T	417	214.85, 43.66	$17.11^{+0.44}_{-0.39}$	$17.67^{+1.01}_{-0.56}$
Sculptor	86	287.53, -83.16	$18.57^{+0.07}_{-0.05}$	$18.63^{+0.14}_{-0.08}$
Segue I	23	220.48, 50.43	$19.36^{+0.32}_{-0.35}$	$17.52^{+2.54}_{-2.65}$
Segue II	35	149.43, -38.14	$16.21^{+1.06}_{-0.98}$	$19.50^{+1.82}_{-1.48}$
Sextans	86	243.50, 42.27	$17.92^{+0.35}_{-0.29}$	$18.04^{+0.50}_{-0.28}$
Ursa Major I	97	159.43, 54.41	$17.87^{+0.56}_{-0.33}$	$18.84^{+0.97}_{-0.43}$
Ursa Major II	32	152.46, 37.44	$19.42^{+0.44}_{-0.42}$	$20.60^{+1.46}_{-0.95}$
Ursa Minor	76	104.97, 44.80	$18.95^{+0.26}_{-0.18}$	$19.08^{+0.21}_{-0.13}$

Table 5.2 Summary of dSph observations by each experiment used in this work. A ‘-’ indicates the experiment did not observe the dSph for this study. For Fermi-LAT, the exposure at 1 GeV is given. For HAWC, $|\Delta\theta|$ is the absolute difference between the source declination and HAWC latitude. HAWC is more sensitive to sources with smaller $|\Delta\theta|$. For IACTs, we show the zenith angle range, the total exposure, the energy range, the angular radius θ of the signal or ON region, the ratio of exposures between the background-control (OFF) and signal (ON) regions (τ), and the significance of gamma-ray excess in standard deviations, σ .

Source name	Fermi-LAT	HAWC	H.E.S.S, MAGIC, VERITAS						
	Exposure (10^{11} s m 2)	$ \Delta\theta $ ($^\circ$)	IACT	Zenith ($^\circ$)	Exposure (h)	Energy range (GeV)	θ ($^\circ$)	τ	S (σ)
Boötes I	2.6	4.5	VERITAS	15 – 30	14.0	100–41000	0.10	8.6	-1.0
Canes Venatici I	2.9	14.6	–	–	–	–	–	–	–
Canes Venatici II	2.9	15.3	–	–	–	–	–	–	–
Carina	3.1	–	H.E.S.S.	27 – 46	23.7	310 – 70000	0.10	18.0	-0.3
Coma Berenices	2.7	4.9	H.E.S.S.	47 – 49	11.4	550 – 70000	0.10	14.4	-0.4
			MAGIC	5 – 37	49.5	60 – 10000	0.17	1.0	–
			MAGIC	29 – 45	52.1	70 – 10000	0.22	1.0	–
Draco	3.8	38.1	VERITAS	25 – 40	49.8	120 – 70000	0.10	9.0	-1.0
Fornax	2.7	–	H.E.S.S.	11 – 25	6.8	230 – 70000	0.10	45.5	-1.5
Hercules	2.8	6.3	–	–	–	–	–	–	–
Leo I	2.5	6.7	–	–	–	–	–	–	–
Leo II	2.6	3.1	–	–	–	–	–	–	–
Leo IV	2.4	19.5	–	–	–	–	–	–	–
Leo V	2.4	–	–	–	–	–	–	–	–
Leo T	2.6	–	–	–	–	–	–	–	–
Sculptor	2.7	–	H.E.S.S.	10 – 46	11.8	200 – 70000	0.10	19.8	-2.2
Segue I	2.5	2.9	MAGIC	13 – 37	158.0	60 – 10000	0.12	1.0	-0.5
			VERITAS	15 – 35	92.0	80 – 50000	0.10	7.6	0.7
Segue II	2.7	–	–	–	–	–	–	–	–
Sextans	2.4	20.6	–	–	–	–	–	–	–
Ursa Major I	3.4	32.9	–	–	–	–	–	–	–
Ursa Major II	4.0	44.1	MAGIC	35 – 45	94.8	120 – 10000	0.30	1.0	-2.1
Ursa Minor	4.1	–	VERITAS	35 – 45	60.4	160 – 93000	0.10	8.4	-0.1

914 where \mathcal{L}_0 is the null hypothesis, or no DM emission, likelihood. \mathcal{L}^{\max} is the best fit signal
 915 hypothesis where $\langle\sigma v\rangle$ maximizes the likelihood. We calculate the likelihood of each source and
 916 model, assuming events are Poisson distributed, with

$$\mathcal{L} = \prod_i \frac{(B_i + S_i)^{N_i} e^{-(B_i + S_i)}}{N_i!} \quad (5.8)$$

918 where S_i is the sum of expected number of signal counts. B_i is the number of background counts
 919 observed. N_i is the total number of counts.

920 I also calculate an upper limit on $\langle\sigma v\rangle$ by calculating the 95% confidence level (CL). For the
 921 CL, we define a parameter, TS_{95} , as

$$TS_{95} \equiv \sum_{\text{bins}} \left[2N \ln \left(1 + \frac{\epsilon S_{\text{ref}}}{B} \right) - 2\epsilon S_{\text{ref}} \right] \quad (5.9)$$

922 where the expected signal counts from a dSph is scaled by ϵ . S_{ref} is the expected number of excess
 923 counts in a bin from DM emission from a dSph with a corresponding annihilation cross-section,
 924 $\langle\sigma v\rangle$. We scan ϵ such that

$$2.71 = TS_{\max} - TS_{95} \quad (5.10)$$

925 HAWC's exclusive results are provided in Section 5.5.

926 5.4.2 Glory Duck Joint Likelihood

927 The joint likelihood for the 5-experiment combination was done similarly as Section 5.4.1. We
 928 calculate upper limits on $\langle\sigma v\rangle$ from the TS, Eq. (5.7), and define the likelihood ratio more generally

$$\lambda(\langle\sigma v\rangle | \mathcal{D}_{\text{dSphs}}) = \frac{\mathcal{L}(\langle\sigma v\rangle; \hat{\nu} | \mathcal{D}_{\text{dSphs}})}{\mathcal{L}(\widehat{\langle\sigma v\rangle}; \hat{\nu} | \mathcal{D}_{\text{dSphs}})} \quad (5.11)$$

929 $\mathcal{D}_{\text{dSphs}}$ is the totality of observations across experiments and dSphs. ν are the nuisance parameters
 930 which are the J factors in this study. $\widehat{\langle\sigma v\rangle}$ and $\hat{\nu}$ are the respective estimate that maximize \mathcal{L}
 931 globally. Finally, $\hat{\nu}$ is the set of nuisance parameters that maximize \mathcal{L} for a fixed value of $\langle\sigma v\rangle$.

932 The *complete* joint likelihood, \mathcal{L} that encompasses all observations from all instruments and
 933 dSphs can be factorized into *partial* functions for each dSph l (with $\mathcal{L}_{\text{dSph},l}$) and its J factor (\mathcal{J}_l):

$$\mathcal{L}(\langle\sigma v\rangle; \nu | \mathcal{D}_{\text{dSphs}}) = \prod_{l=1}^{N_{\text{dSphs}}} \mathcal{L}_{\text{dSph},l}(\langle\sigma v\rangle; J_l, \nu_l | \mathcal{D}_l) \times \mathcal{J}_l(J_l | J_{l,\text{obs}}, \sigma_{\log J_l}). \quad (5.12)$$

934 For this study, $N_{\text{dSphs}} = 20$ is the number of dSphs studied. \mathcal{D}_l are the gamma-ray observations
 935 of dSph, l . ν_l are the nuisance parameters modifying the gamma-ray observations of dSph, l ,
 936 but excludes \mathcal{J}_l . \mathcal{J}_l is the J factor for dSph, l , as defined in Equation (5.2), and it is a nuisance
 937 parameter whose value is unknown. $\log_{10} J_{l,\text{obs}}$ and $\sigma_{\log J_l}$ are obtained by fitting a log-normal
 938 function of $J_{l,\text{obs}}$ to the posterior distribution of J_l [50]. $\log_{10} J_{l,\text{obs}}$ and $\sigma_{\log J_l}$ values are provided
 939 in Table 5.1. The term \mathcal{J}_l constraining J_l is written as:

$$\mathcal{J}_l(J_l | J_{l,\text{obs}}, \sigma_{\log J_l}) = \frac{1}{\ln(10)J_{l,\text{obs}}\sqrt{2\pi}\sigma_{\log J_l}} \exp\left(-\frac{(\log_{10} J_l - \log_{10} J_{l,\text{obs}})^2}{2\sigma_{\log J_l}^2}\right). \quad (5.13)$$

940 Both the \mathcal{GS} and \mathcal{B} , displayed in Table 5.1, sets of J factors are used in this analysis. Equation (5.13)
 941 is also normalized, so it can also be interpreted as a probability density function (PDF) for $J_{l,\text{obs}}$.
 942 From Equation (7.1), we can also see that $\langle\sigma v\rangle$ and J_l are degenerate when computing $\mathcal{L}_{\text{dSph},l}$.
 943 Therefore, as noted in [51], it is sufficient to compute $\mathcal{L}_{\text{dSph},l}$ versus $\langle\sigma v\rangle$ for a fixed value of J_l .
 944 We used $J_{l,\text{obs}}(\mathcal{GS})$ reported in Tab. 5.1, in order to perform the profile of \mathcal{L} with respect to J_l .
 945 The degeneracy implies that for any $J'_l \neq J_{l,\text{obs}}$ (in practice in our case we used $J'_l = J_{l,\text{obs}}(\mathcal{B})$ to
 946 compute results from a different set of J factors):

$$\mathcal{L}_{\text{dSph},l}(\langle\sigma v\rangle; J'_l, \nu_l | \mathcal{D}_l) = \mathcal{L}_{\text{dSph},l}\left(\frac{J'_l}{J_{l,\text{obs}}} \langle\sigma v\rangle; J_{l,\text{obs}}, \nu_l | \mathcal{D}_l\right), \quad (5.14)$$

947 which is a straightforward rescaling operation that reduces the computational needs of the profiling
 948 operation since:

$$\mathcal{L}(\langle\sigma v\rangle; \hat{\nu} | \mathcal{D}_{\text{dSphs}}) = \prod_{l=1}^{N_{\text{dSphs}}} \max_{J_l} \left[\mathcal{L}_{\text{dSph},l}(\langle\sigma v\rangle; J_l, \hat{\nu}_l | \mathcal{D}_l) \times \mathcal{J}_l(J_l | J_{l,\text{obs}}, \sigma_{\log J_l}) \right]. \quad (5.15)$$

949 In addition, Eq. (5.14) enables the combination of data from different gamma-ray instruments and
 950 observed dSphs via tabulated values of $\mathcal{L}_{\text{dSph},l}$, or equivalently of λ from Eq. (5.11) as was done in
 951 this work, versus $\langle\sigma v\rangle$. $\mathcal{L}_{\text{dSph},l}$ is computed for a fixed value of J_l and profiled with respect to all
 952 instrumental nuisance parameters ν_l , these nuisance parameters are discussed in more detail below.
 953 These values are produced by each detector independently and therefore there is no need to share
 954 sensitive low-level information used to produce them, such as event lists. Figure 5.4 illustrates the
 955 multi-instrument combination technique used in this study with a comparison of the upper limit

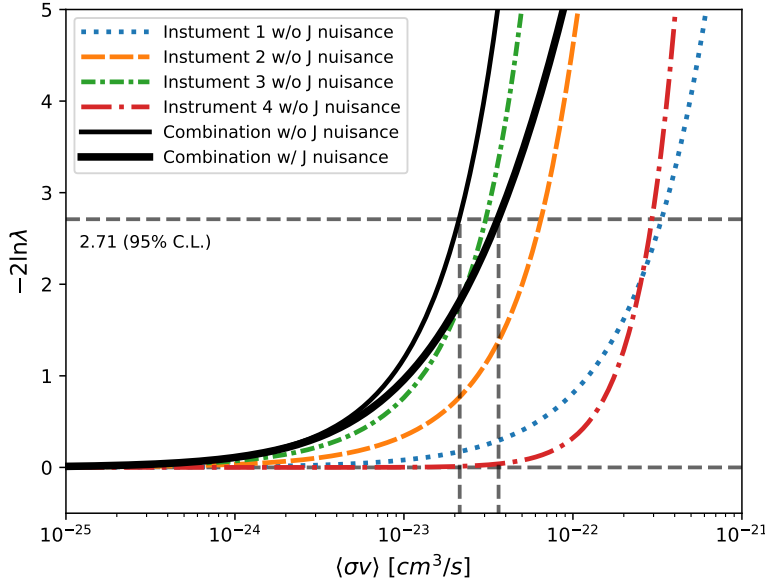


Figure 5.4 Illustration of the combination technique showing a comparison between $-2 \ln \lambda$ provided by four instruments (colored lines) from the observation of the same dSph without any J nuisance and their sum, *i.e.* the resulting combined likelihood (thin black line). According to the test statistics of Equation (5.7), the intersection of the likelihood profiles with the line $-2 \ln \lambda = 2.71$ indicates the 95% C.L. upper limit on $\langle\sigma v\rangle$. The combined likelihood (thin black line) shows a smaller value of upper limit on $\langle\sigma v\rangle$ than those derived by individual instruments. We also show how the uncertainties on the J factor effects the combined likelihood and degrade the upper limit on $\langle\sigma v\rangle$ (thick black line). All likelihood profiles are normalized so that the global minimum $\widehat{\langle\sigma v\rangle}$ is 0. We note that each profile depends on the observational conditions in which a target object was observed. The sensitivity of a given instrument can be degraded and the upper limits less constraining if the observations are performed in non-optimal conditions such as a high zenith angle or a short exposure time.

956 on $\langle\sigma v\rangle$ obtained from the combination of the observations of four experiments towards one dSph
 957 versus the upper limit from individual instruments. It also shows graphically the effect of the
 958 J -factor uncertainty on the combined observations.

959 The *partial* joint likelihood function for gamma-ray observations of each dSph ($\mathcal{L}_{dSph,l}$) is
 960 written as the product of the likelihood terms describing the $N_{exp,l}$ observations performed with
 961 any of our observatories:

$$\mathcal{L}_{dSph,l} (\langle\sigma v\rangle; J_l, \nu_l | \mathcal{D}_l) = \prod_{k=1}^{N_{exp,l}} \mathcal{L}_{lk} (\langle\sigma v\rangle; J_l, \nu_{lk} | \mathcal{D}_{lk}), \quad (5.16)$$

962 where each \mathcal{L}_{lk} term refers to an observation of the l -th dSph with associated k -th instrument

963 responses. $N_{\text{exp},l}$ varies from dSph to dSph and can be inferred from Table 5.2.

964 Each collaboration separately analyzes their data for \mathcal{D}_{lk} corresponding to dSph l and gamma-
965 ray detector k , using as many common assumptions as possible in the analysis. HAWC's treatment
966 was described earlier in Section 5.4.1 whereas the specifics of the remaining experiments is left to
967 the publication. We compute the values for the likelihood functions \mathcal{L}_{lk} (see Eq. (5.16)) for a fixed
968 value of J_l and profile over the rest of the nuisance parameters ν_{lk} . Then, values of λ from Eq. (5.11)
969 are computed as a function of $\langle \sigma v \rangle$, and shared using a common format. Results are computed for
970 seven annihilation channels, W^+W^- , ZZ , $b\bar{b}$, $t\bar{t}$, e^+e^- , $\mu^+\mu^-$, and $\tau^+\tau^-$ over 62 m_χ values between
971 5 GeV and 100 TeV provided in [44]. The $\langle \sigma v \rangle$ range is defined between 10^{-28} and $10^{-18} \text{cm}^3 \cdot \text{s}^{-1}$,
972 with 1001 logarithmically spaced values. The likelihood combination, i.e. Equation (5.12), and
973 profile over the J -factor to compute the profile likelihood ratio λ , Equation (5.11), are carried out
974 with two different public analysis software packages, namely `gLike` [52] and `LklCom` [53], that
975 provide the same results [54].

976 As mentioned previously, each experiment computes the \mathcal{L}_{lk} from Equation (5.11) differently.
977 The remainder of this section highlights the differences in this calculation across the experiments.
978 Four experiments, namely *Fermi*-LAT, H.E.S.S., HAWC and MAGIC, use a binned likelihood to
979 compute the \mathcal{L}_{lk} . For these experiments, for each observation \mathcal{D}_{lk} of a given dSph l carried out
980 using a given gamma-ray detector k , the binned likelihood function is:

$$\mathcal{L}_{lk} (\langle \sigma v \rangle; J_l, \nu_{lk} | \mathcal{D}_{lk}) = \prod_{i=1}^{N_E} \prod_{j=1}^{N_P} \left[\mathcal{P}(s_{lk,ij}(\langle \sigma v \rangle, J_l, \nu_{lk}) + b_{lk,ij}(\nu_{lk}) | N_{lk,ij}) \right] \times \mathcal{L}_{lk,\nu} (\nu_{lk} | \mathcal{D}_{\nu_{lk}}) \quad (5.17)$$

981 where N_E and N_P are the number of considered bins in reconstructed energy and arrival direction,
982 respectively; \mathcal{P} represents a Poisson PDF for the number of gamma-ray candidate events $N_{lk,ij}$
983 observed in the i -th bin in energy and j -th bin in arrival direction, when the expected number is
984 the sum of the expected mean number of signal events s_{ij} (produced by DM annihilation) and of
985 background events b_{ij} ; $\mathcal{L}_{lk,\nu}$ is the likelihood term for the extra ν_{lk} nuisance parameters that vary
986 from one instrument k to another. The expected counts for signal events s_{ij} for a given dSph l and

987 detector k is given by:

$$s_{ij}(\langle\sigma\nu\rangle, J) = \int_{E'_{\min,i}}^{E'_{\max,i}} dE' \int_{P'_{\min,j}}^{P'_{\max,j}} d\Omega' \int_0^\infty dE \int_{\Delta\Omega_{tot}} d\Omega \int_0^{T_{\text{obs}}} dt \frac{d^2\Phi(\langle\sigma\nu\rangle, J)}{dEd\Omega} \text{IRF}(E', P' | E, P, t) \quad (5.18)$$

988 where E' and E are the reconstructed and true energies, P' and P the reconstructed and true
989 arrival directions; $E'_{\min,i}$, $P'_{\min,j}$, $E'_{\max,i}$, and $P'_{\max,j}$ are their lower and upper limits of the i -th
990 energy bin and the j -th arrival direction bin; T_{obs} is the (dead-time corrected) total observation
991 time; t is the time along the observations; $d^2\Phi/dEd\Omega$ is the DM flux in the source region (see
992 Equation (7.1)); and $\text{IRF}(E', P' | E, P, t)$ is the IRF, which can be factorized as the product of the
993 effective collection area of the detector $A_{\text{eff}}(E, P, t)$, the PDFs for the energy estimator $f_E(E' | E, t)$,
994 and arrival direction $f_P(P' | E, P, t)$ estimators. Note that for Fermi-LAT, HAWC, MAGIC, and
995 VERITAS the effect of the finite angular resolution is taken into account through the convolution
996 of $d\Phi/dEd\Omega$ with f_P in Equation (5.18), whereas in the cases of H.E.S.S. f_P is approximated by a
997 delta function. This approximation has been made in order to maintain compatibility of the result
998 with what has been previously published. The difference introduced by this approximation is $< 5\%$
999 for all considered dSphs. A more comprehensive review of the differences between the analyses of
1000 different instruments can be found in [25].

1001 5.5 HAWC Results

1002 13 of the 20 dSphs considered for the Glory Duck analysis are within HAWC's field of view.
1003 These dSph are analyzed for emission from DM annihilation according to the likelihood method
1004 described in Section 5.4. The 13 likelihood profiles are then stacked to synthesize a combined
1005 limit on the dark matter cross-section, $\langle\sigma\nu\rangle$. This combination is done for the 7 SM annihilation
1006 channels used in the Glory Duck analysis. Figure 5.5 shows the combined limit for all annihilation
1007 channels with HAWC only observations. We also perform 300 studies of Poisson trials on the
1008 background. These trials are used to produce HAWC sensitivities with $\pm 1\sigma$ and $\pm 2\sigma$ uncertainty
1009 bands which were shared with the other collaborators for combination. The results on fitting to
1010 HAWC's Poisson trials of the DM hypothesis is shown in Figure 5.7 for all the DM annihilation
1011 channels studied for Glory Duck.

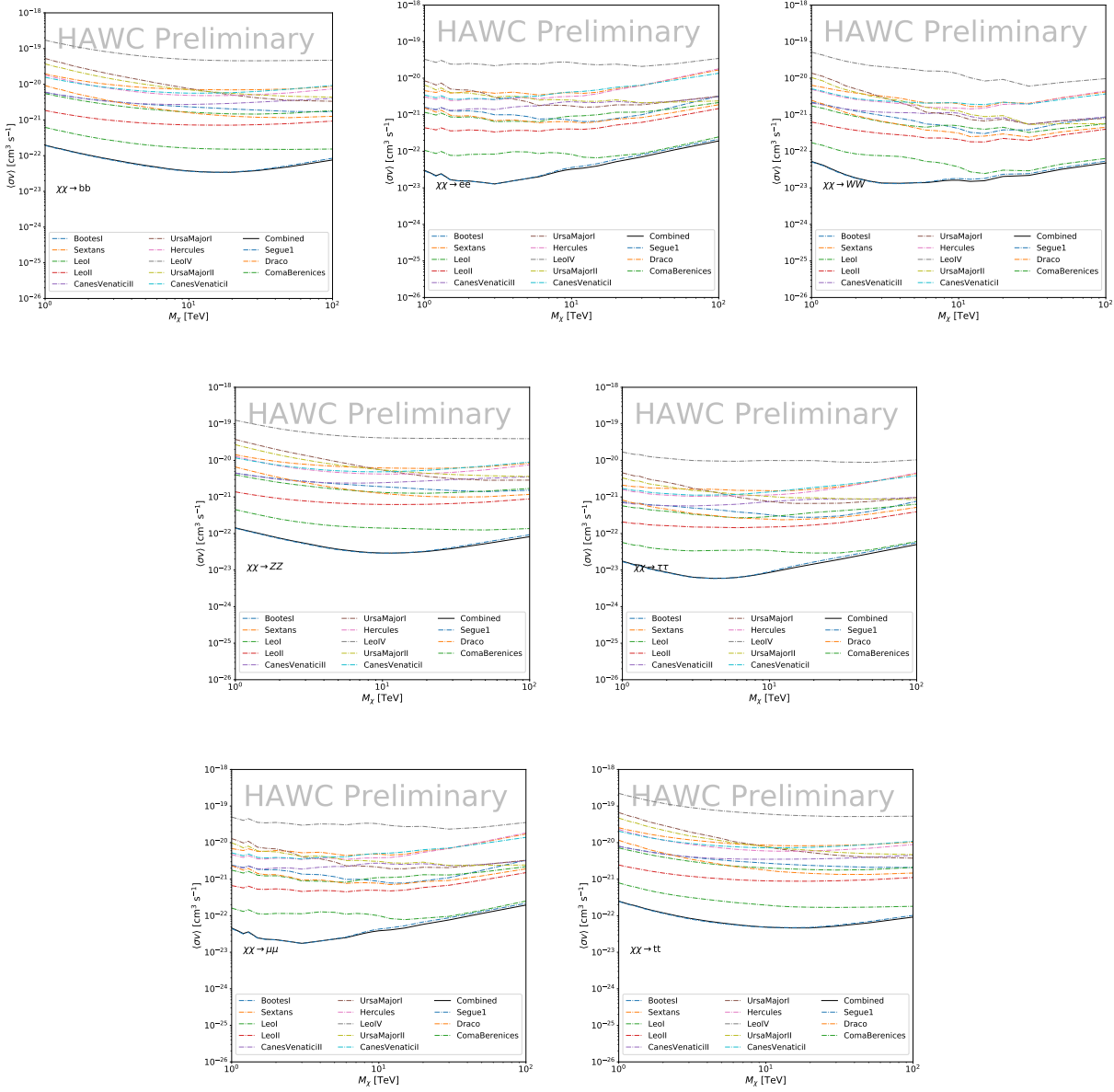


Figure 5.5

No DM was found in HAWC observations. HAWC's limits are dominated by the dSphs Segue1 and Coma Berenices. The remaining 11 dSphs do not contribute significantly to the limit because they are at high zenith and/or have much smaller J factors. Even though some remaining dSphs have large J factors, they are towards the edge of HAWC's field of view where HAWC analysis is less sensitive.

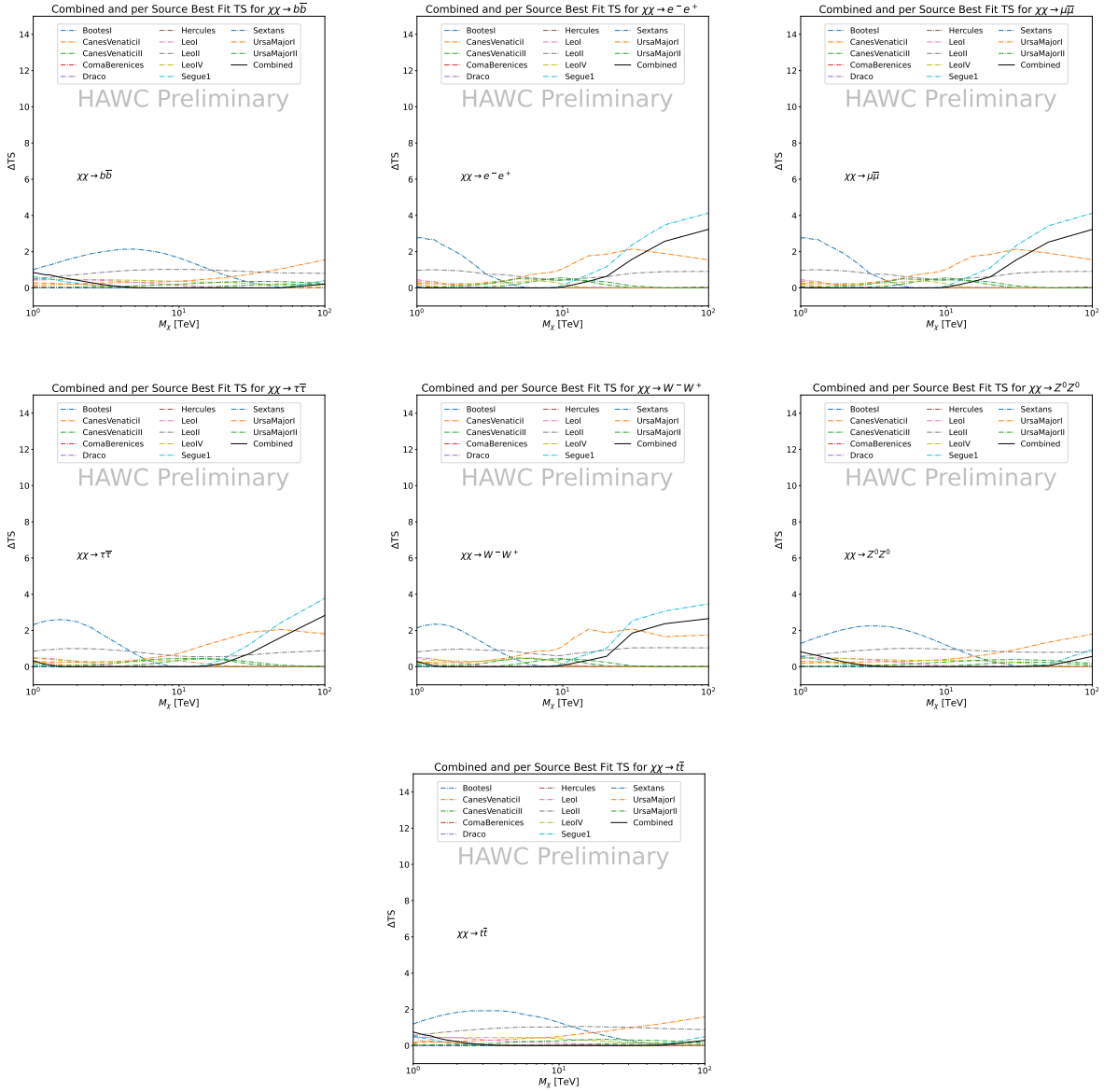


Figure 5.6 HAWC TS values for best fit $\langle\sigma v\rangle$ versus m_χ for seven SM annihilation channels with J factors from \mathcal{GS} . The solid black line shows the combined best fit TS values. The colored, dashed lines are the TS values for each of the 13 sources HAWC studied.

5.6 Glory Duck Combined Results

The crux of this analysis is that HAWC's results are combined with 4 other gamma-ray observa-

tories: Fermi-LAT, H.E.S.S., MAGIC, and VERITAS. No significant DM emission was observed by any of the five instruments. We present the upper limits on $\langle\sigma v\rangle$ assuming seven independent DM self annihilation channels, namely W^+W^- , Z^+Z^- , $b\bar{b}$, $t\bar{t}$, e^+e^- , $\mu^+\mu^-$, and $\tau^+\tau^-$. The 68%

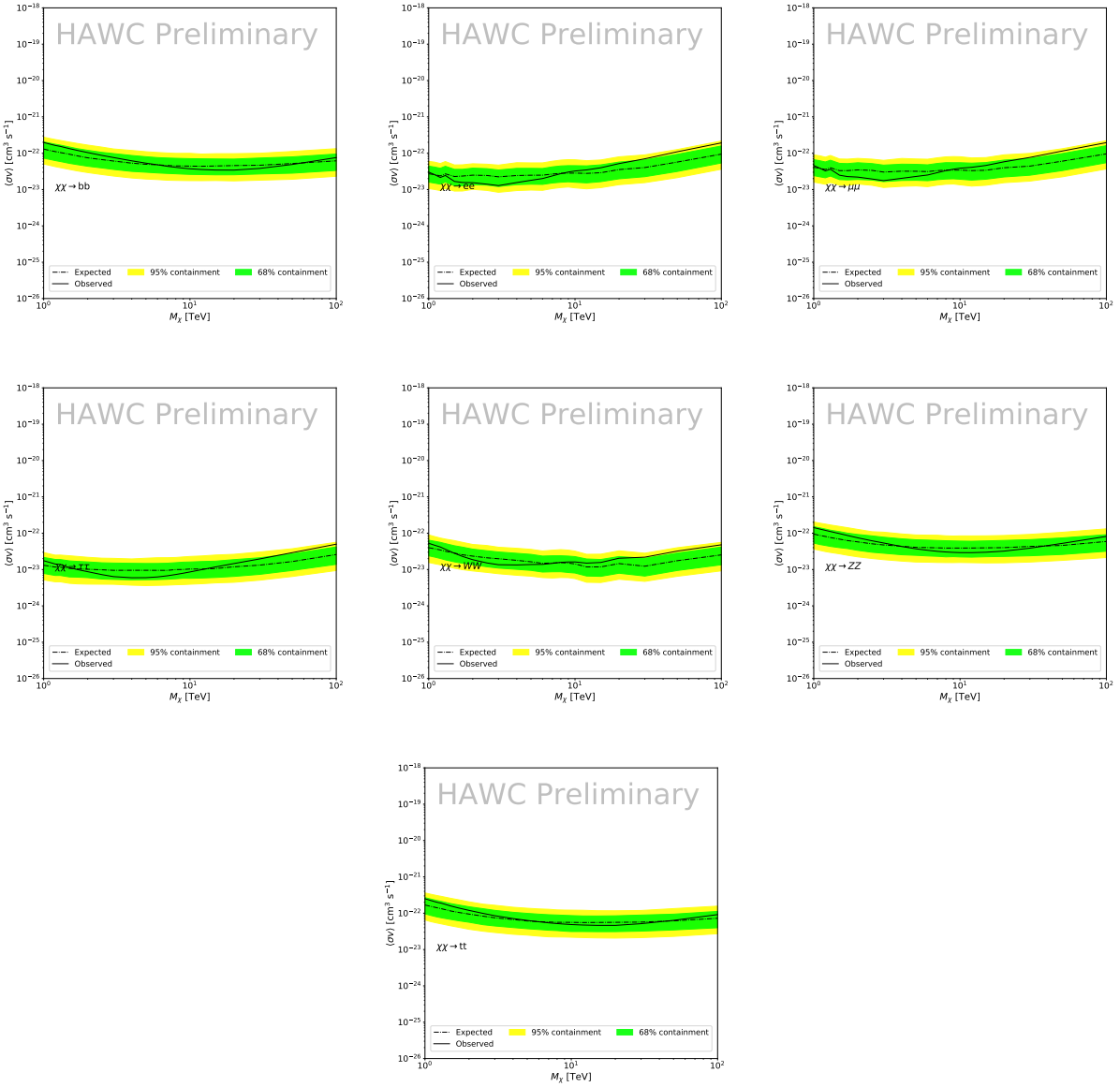


Figure 5.7 HAWC Brazil bands at 95% confidence level on $\langle\sigma v\rangle$ versus DM mass for seven annihilation channels with J -factors from \mathcal{GS} [55]. The solid line represents the combined limit from 13 dSphs. The dashed line is the expected limit. The green band is the 68% containment. The yellow band is the 95% containment.

and 95% containment bands are produced from 300 Poisson realizations of the null hypothesis corresponding to each of the combined datasets. These 300 realizations are combined identically to dSph observations. The containment bands and the median are extracted from the distribution of resulting limits on the null hypothesis. These 300 realizations are obtained either by fast simulations of the OFF observations, for H.E.S.S., MAGIC, VERITAS, and HAWC, or taken from real

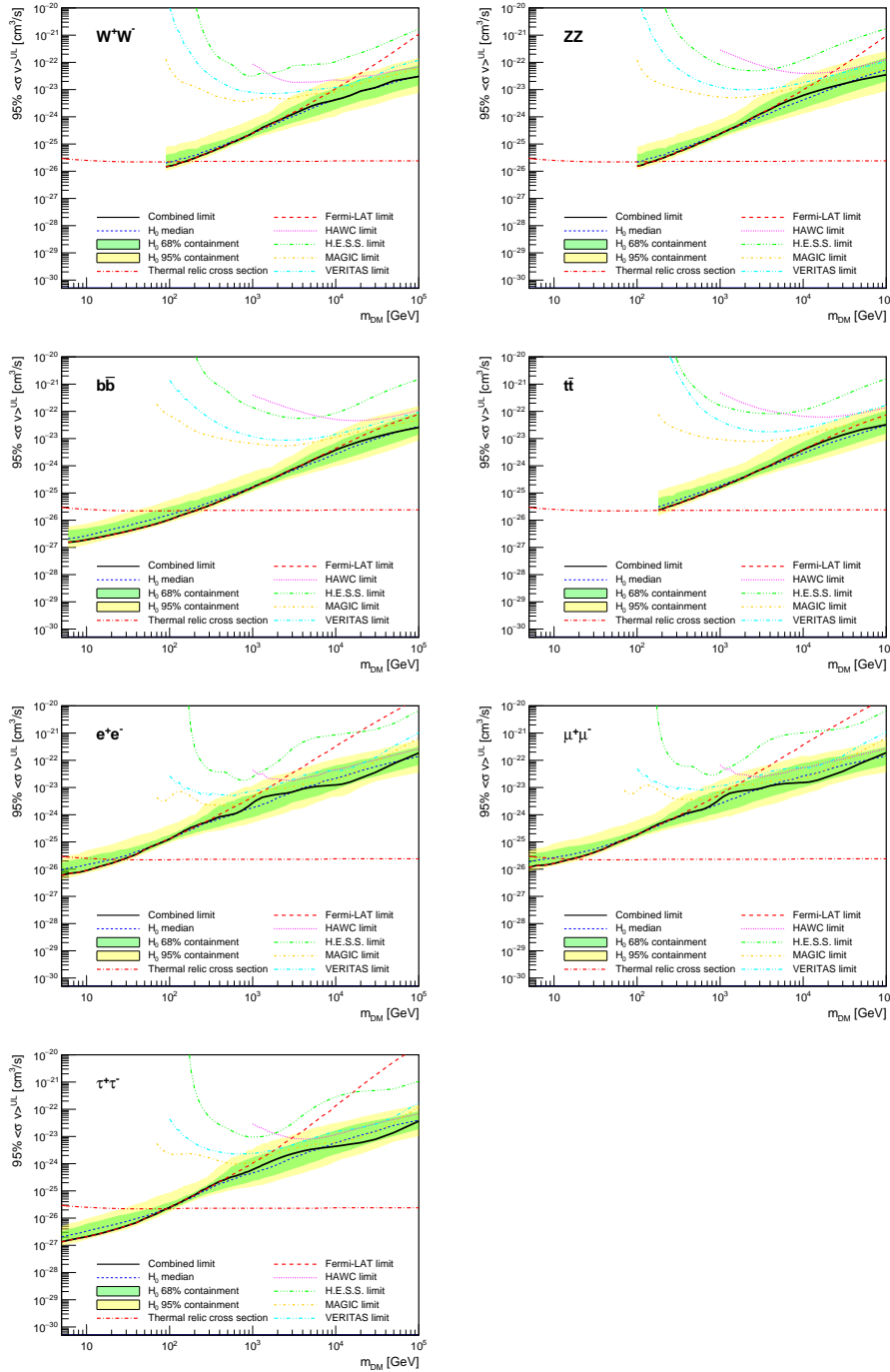


Figure 5.8 Upper limits at 95% confidence level on $\langle\sigma v\rangle$ in function of the DM mass for eight annihilation channels, using the set of J factors from Ref. [55] (\mathcal{GS} set in Table 5.1). The black solid line represents the observed combined limit, the black dashed line is the median of the null hypothesis corresponding to the expected limit, while the green and yellow bands show the 68% and 95% containment bands. Combined upper limits for each individual detector are also indicated as solid, colored lines. The value of the thermal relic cross-section in function of the DM mass is given as the red dotted-dashed line [56].

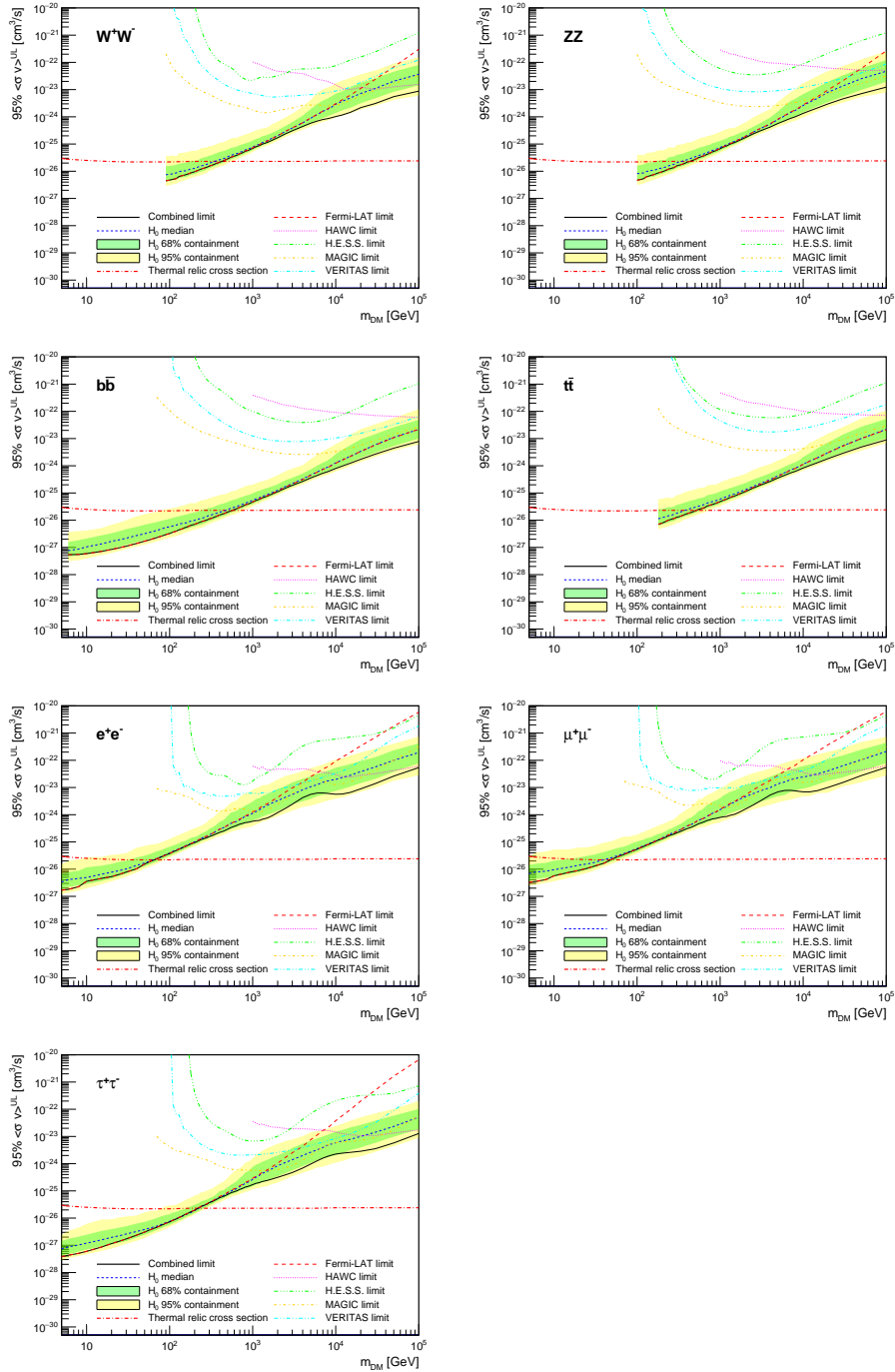


Figure 5.9 Same as Fig. 5.8, using the set of J factors from Ref. [49, 57] (\mathcal{B} set in Table 5.1).

1027 observations of empty fields of view in the case of Fermi-LAT [50, 58, 59].

1028 The obtained limits are shown in Figure 5.8 for the $\mathcal{G}\mathcal{S}$ set of J -factors [55] and in Figure 5.9
1029 for the \mathcal{B} set of J -factors [49, 57]. The combined limits are presented with their 68% and 95%
1030 containment bands, and are expected to be close to the median limit when no signal is present.

1031 We observe agreement with the null hypothesis for all channels, within 2σ standard deviations,
1032 between the observed limits and the expectations given by the median limits. Limits obtained from
1033 each detector are also indicated in the figures, where limits for all dSphs observed by the specific
1034 instrument have been combined.

1035 Below ~ 300 GeV, the *Fermi*-LAT dominates the DM limits for all annihilation channels. From
1036 ~ 300 GeV to ~ 2 TeV, *Fermi*-LAT continues to dominate for the hadronic and bosonic DM channels,
1037 yet the IACTs (H.E.S.S., MAGIC, and VERITAS) and *Fermi*-LAT all contribute to the limit for
1038 leptonic DM channels. For DM masses between ~ 2 TeV to ~ 10 TeV, the IACTs dominate leptonic
1039 DM annihilation channels, whereas both the *Fermi*-LAT and the IACTs dominate bosonic and
1040 hadronic DM annihilation channels. From ~ 10 TeV to ~ 100 TeV, both the IACTs and HAWC
1041 contribute significantly to the leptonic DM limit. For hadronic and bosonic DM, the IACTs and
1042 *Fermi*-LAT both contribute strongly.

1043 We notice that the limits computed using the \mathcal{B} set of J -factor are always better compared to the
1044 ones calculated with the \mathcal{GS} set. For the W^+W^- , Z^+Z^- , $b\bar{b}$, and $t\bar{t}$ channels, the ratio between the
1045 limits computed with the two sets of J -factor is varying between a factor of ~ 3 and ~ 5 depending
1046 on the energy, with the largest ratio around 10 TeV. For the channels e^+e^- , $\mu^+\mu^-$, and $\tau^+\tau^-$, the
1047 ratio lies between ~ 2 to ~ 6 , being maximum around 1 TeV. Examining Figure 5.16 and Figure 5.17
1048 in Section 5.8, these differences are explained by the fact that the \mathcal{B} set provides higher J -factors
1049 for the majority of the studied dSphs, with the notable exception of Segue I. The variation on the
1050 ratio of the limits for the two sets is due to different dSph dominating the limits depending on the
1051 energy. One set, \mathcal{B} , pushes the range of which thermal cross-section which can be excluded to
1052 higher mass. This comparison demonstrates the magnitude of systematic uncertainties associated
1053 with the choice of the J -factor calculation. The \mathcal{GS} and \mathcal{B} sets present a difference in the limits for
1054 all channels of about This difference is explained, see Figure 5.16 and Figure 5.17, by the fact that
1055 the \mathcal{B} set provides higher J -factors for all dSph except for Segue I.

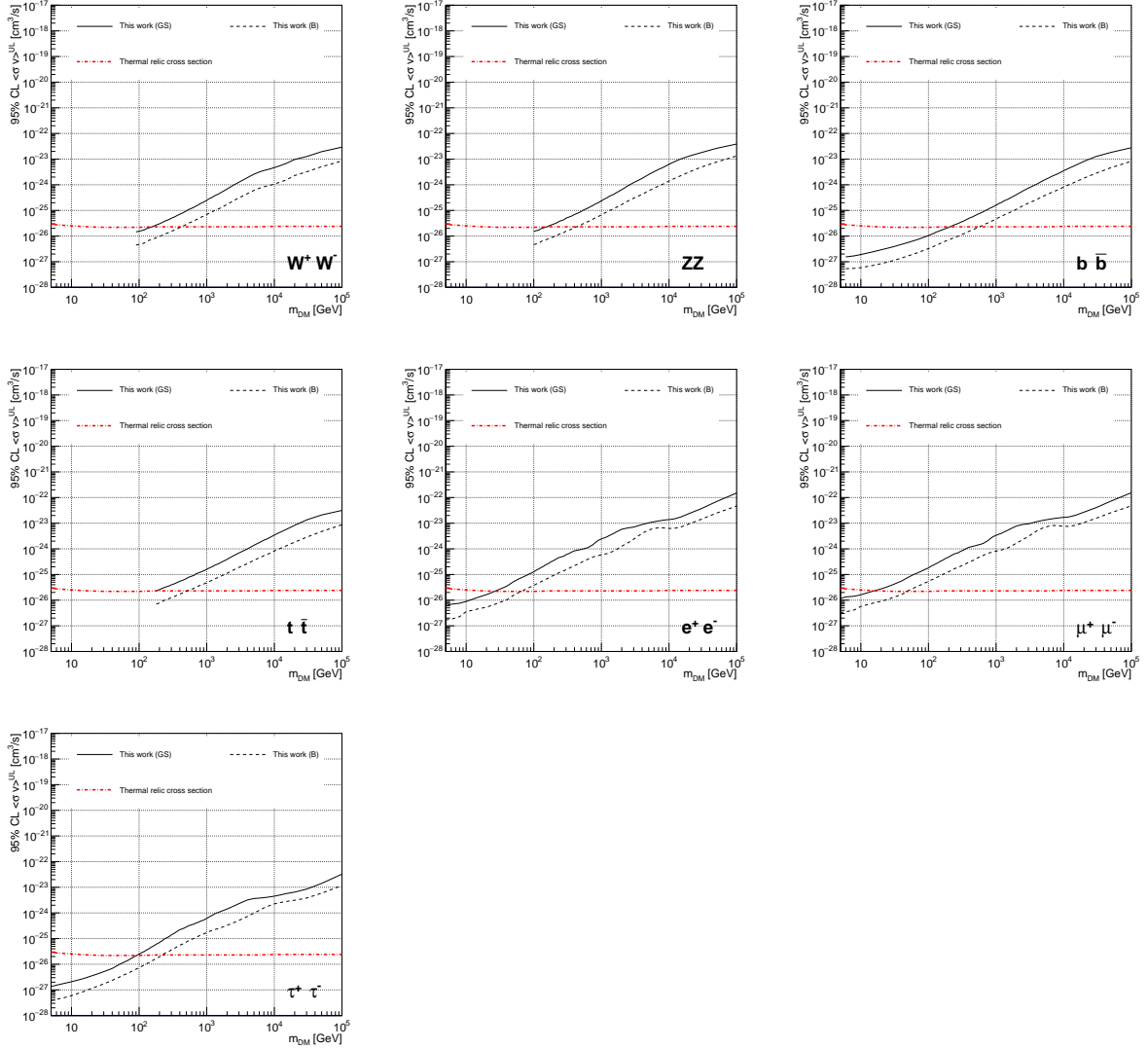


Figure 5.10 Comparisons of the combined limits at 95% confidence level for each of the eight annihilation channels when using the J factors from Ref. [55] (\mathcal{GS} set in Table 5.1), plain lines, and the J factor from Ref. [49, 57] (\mathcal{B} set in Table 5.1), dashed lines. The cross-section given by the thermal relic is also indicated [56].

1056 5.7 HAWC Systematics

1057 5.7.1 Inverse Compton Scattering

1058 The DM-DM annihilation channels produce many high energy electrons regardless of the
 1059 primary annihilation channel. These high energy electrons can produce high energy gamma-rays
 1060 through Inverse Compton Scattering (ICS). If this effect is strong, it would change the morphology
 1061 of the source and increase the total expected gamma-ray counts from any source. The PPPC [44]

1062 provides tools in Mathematica for calculating the impact of ICS for an arbitrary location in the
1063 sky for a specified annihilation channel. We calculated the change in gamma-ray counts for DM
1064 annihilation to primary $e\bar{e}$ for RA and Dec corresponding to Segue1 and Coma Berenices. These
1065 dSphs were chosen because they are the strongest contributors to the limit. $e\bar{e}$ was selected because
1066 it would have the largest number of high energy electrons. The effect was found to be on the order
1067 of 10^{-7} on the gamma-ray spectrum. As a result, this systematic is not considered in our analysis.

1068 **5.7.2 Point Source Versus Extended Source Limits**

1069 The previous DM search toward dSph approximated the dSphs as point sources [46]. In
1070 this analysis, the dSphs are implemented as extended with J-factor distributions following those
1071 produced by [55]. The resolution of the cited map is much finer than HAWC’s angular resolution.
1072 The vast majority of the J-factor distribution is represented on the central HAWC pixel of the dSph
1073 spatial map. However, the neighboring 8 pixels are not negligible and contribute to our limit.

1074 Figure 5.11 shows a substantial improvement to the limit for Segue1. Fig. 5.12 however showed
1075 identical limits. These disparities are best explained by the relative difference in their J-Factors.
1076 Both dSphs pass almost overhead the HAWC detector, however Segue1 has the larger J-Factor
1077 between the two. Adjacent pixels to the central pixel will therefore contribute to the limits. This is
1078 the case for other dSph that are closer to the zenith of the HAWC detector.

1079 Comparison plots for all sources and the combined limit can be found in the sandbox for the
1080 Glory Duck project.

1081 **5.7.3 Impact of Pointing Systematic**

1082 During the analysis it was discovered that directional reconstruction of gamma-rays had a
1083 systematic bias at large zenith angles. Slides describing this systematic can be found [here](#). Shown
1084 on the presentation is dependence on the pointing systematic on declination. New spatial profiles
1085 were generated for every dSph and limits were computed for the adjusted declination.

1086 Section 5.7.3 demonstrates the impact of this systematic for all DM annihilation channels
1087 studied by HAWC. The impact is a tiny improvement, yet mostly identical, to the combined limits.

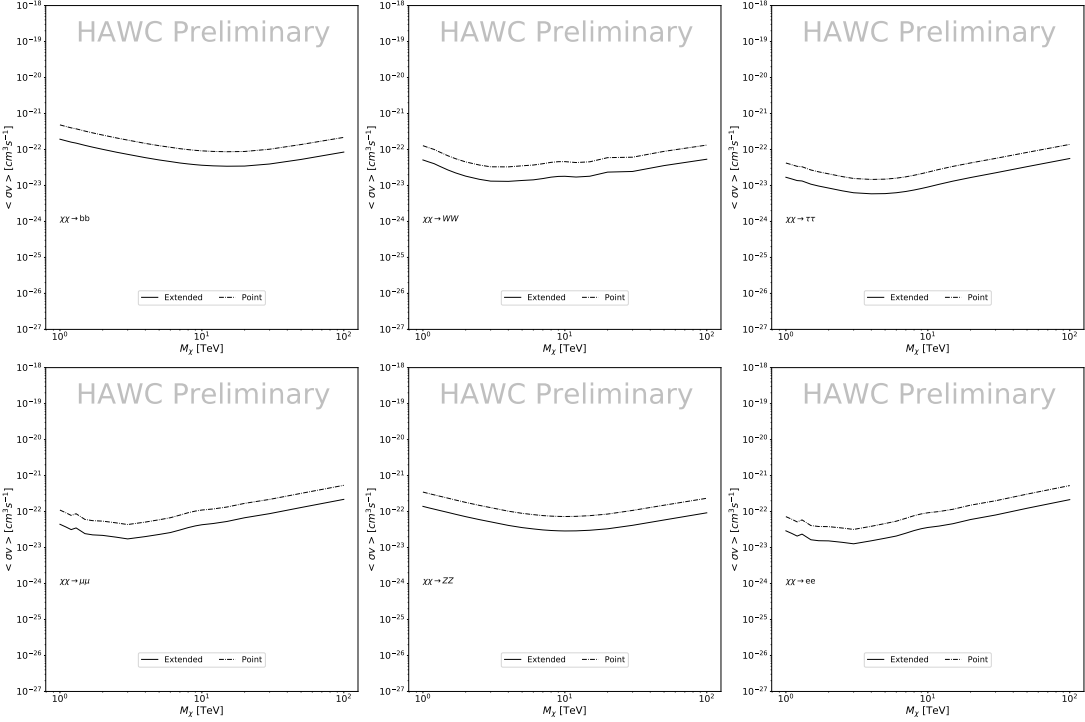


Figure 5.11 Comparisons of the combined limits at 95% confidence level for a point source analysis and extended source using [55] \mathcal{GS} J-factor distributions and PPPC [44] annihilation spectra. Shown are the limits for Segue1 which will have the most significant impact on the combined limit. 6 of the 7 DM annihilation channels are shown. Solid lines are extended source studies. Dashed lines are point source studies. Overall, the extended source analysis improves the limit by a factor of 2.

1088 5.8 J-factor distributions

1089 5.8.1 Numerical integration of \mathcal{GS} maps

1090 It was discovered well after the HAWC analysis was completed that the published tables from
 1091 \mathcal{GS} [45] quoted median J -factors were computed in a non-trivial manner. The assumption myself
 1092 and collaborators had been that the published tables represented the J -factor as a function of θ for
 1093 the best global fit model on a per-source basis. However, this is not the case. Instead, what is
 1094 published are the best fit model for each dwarf that only considers stars up to the angular separation
 1095 θ . Therefore, the model is changing for each value of θ for each dwarf. Yet, the introduced features
 1096 from unique models at each θ are much smaller than the angular resolution of HAWC. It is not
 1097 expected for these effects to impact the limits and TS greatly as a result.

1098 Median J -factor model profiles were provided by the authors. New maps were generated

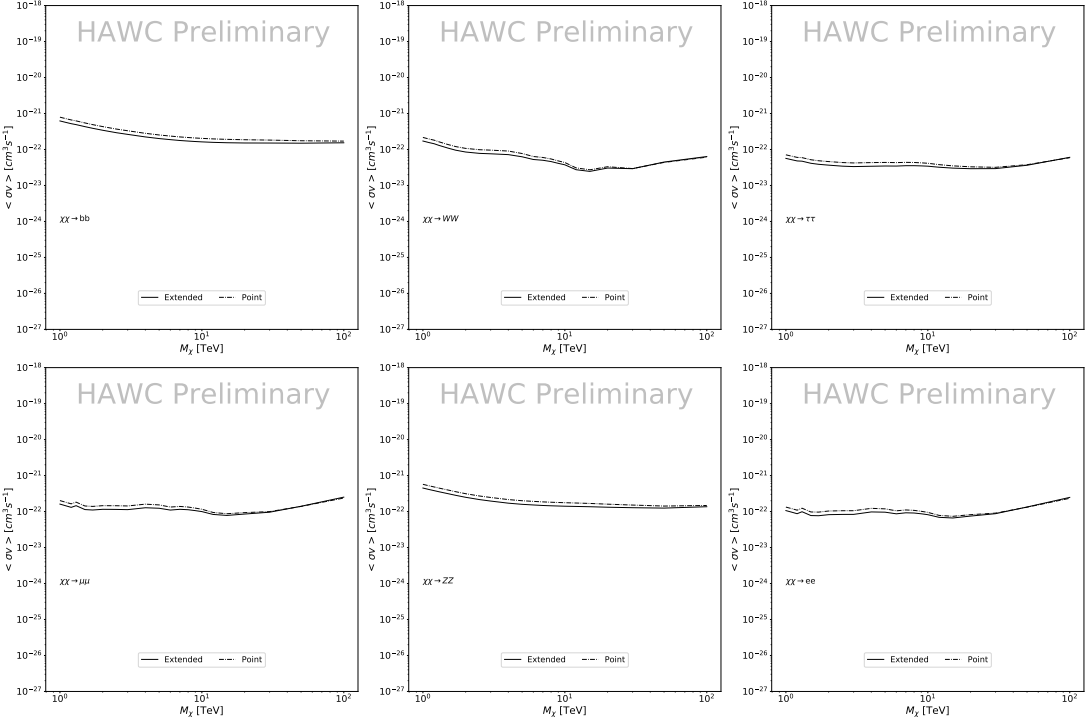


Figure 5.12 Same as Fig. 5.11 on Coma Berenices. This dSph also contributes significantly to the limit. The limits are identical in this case.

and analyzed for Segue1 and Coma Berenices. Figure 5.14 shows the differential between maps generated with the method from Section 5.8.1 and from the authors of [45]. These maps were reanalyzed for all SM DM annihilation channels. Upper limits for these channels are shown in Figure 5.15

From Figure 5.15, we can see that the impact of these model difference was no substantial. The observed impact was a fractional effect which is much smaller than the impact from selecting another DM spatial distribution model as was shown in Figure 5.10.

5.8.2 \mathcal{GS} Versus \mathcal{B} spatial models

We show in this appendix a comparison between the J -factors computed by Geringer-Sameth *et al.* [55] (the \mathcal{GS} set) and the ones computed by Bonnivard *et al.* [49, 57] (the \mathcal{B} set). The \mathcal{GS} J -factors are computed through a Jeans analysis of the kinematic stellar data of the selected dSphs, assuming a dynamic equilibrium and a spherical symmetry for the dSphs. They adopted the generalized DM density distribution, known as Zhao-Hernquist, introduced by [47], carrying

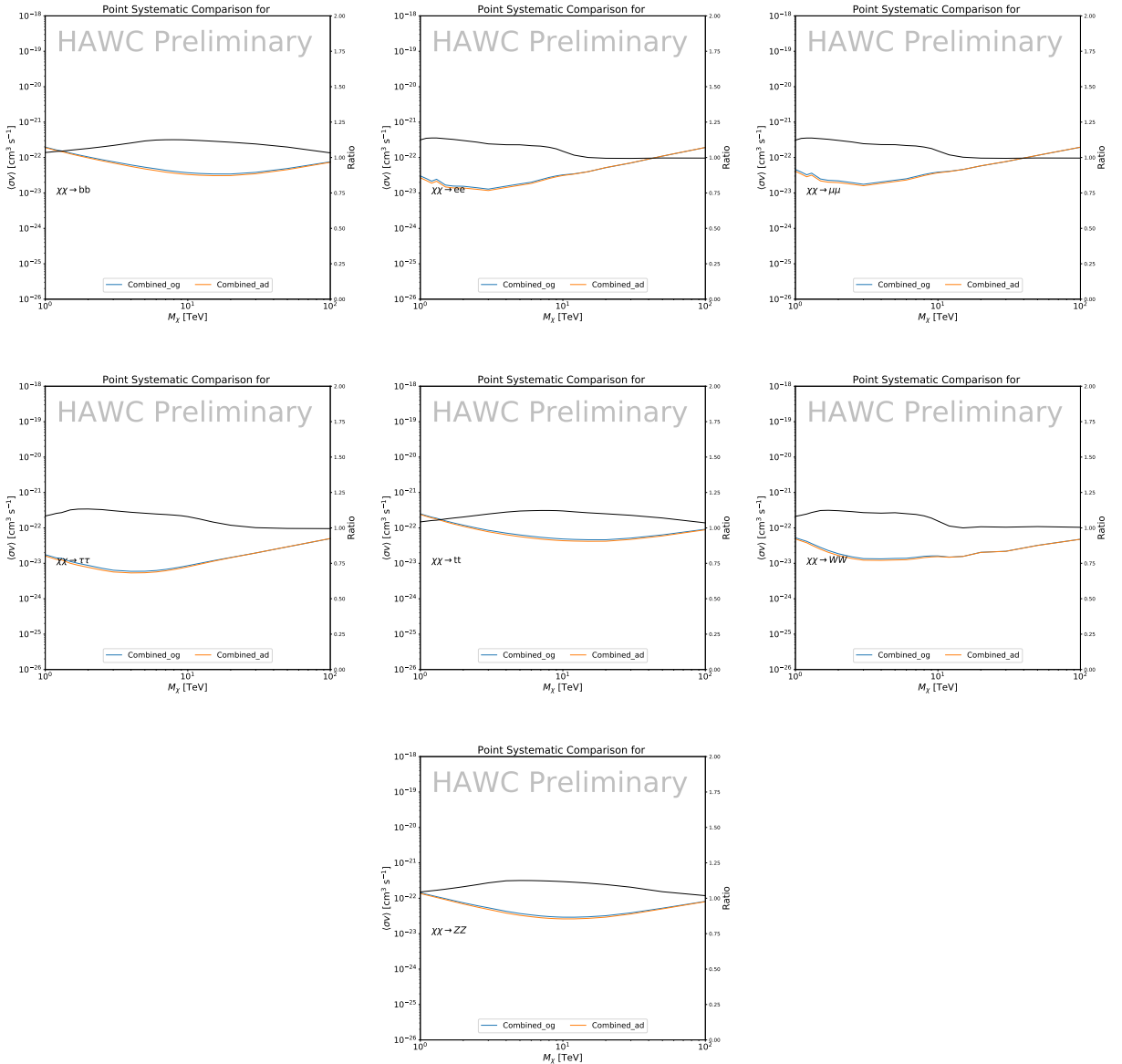


Figure 5.13 Comparison of combined limits when correcting for HAWC's pointing systematic. All DM annihilation channels are shown. The solid black line is the ratio between published limit to the declination corrected limit. The blue solid line or "Combined_og" represented the limits computed for Glory Duck. The solid orange line or "Combined_ad" represented the limits computed after correcting for the pointing systematic.

1112 three additional index parameters to describe the inner and outer slopes, and the break of the
 1113 density profile. Such a profile parametrization allows the reduction of the theoretical bias from
 1114 the choice of a specific radial dependency on the kinematic data. In other words, the increase of
 1115 free parameters with the use of the Zhao-Hernquist profile allows a better description of the mass

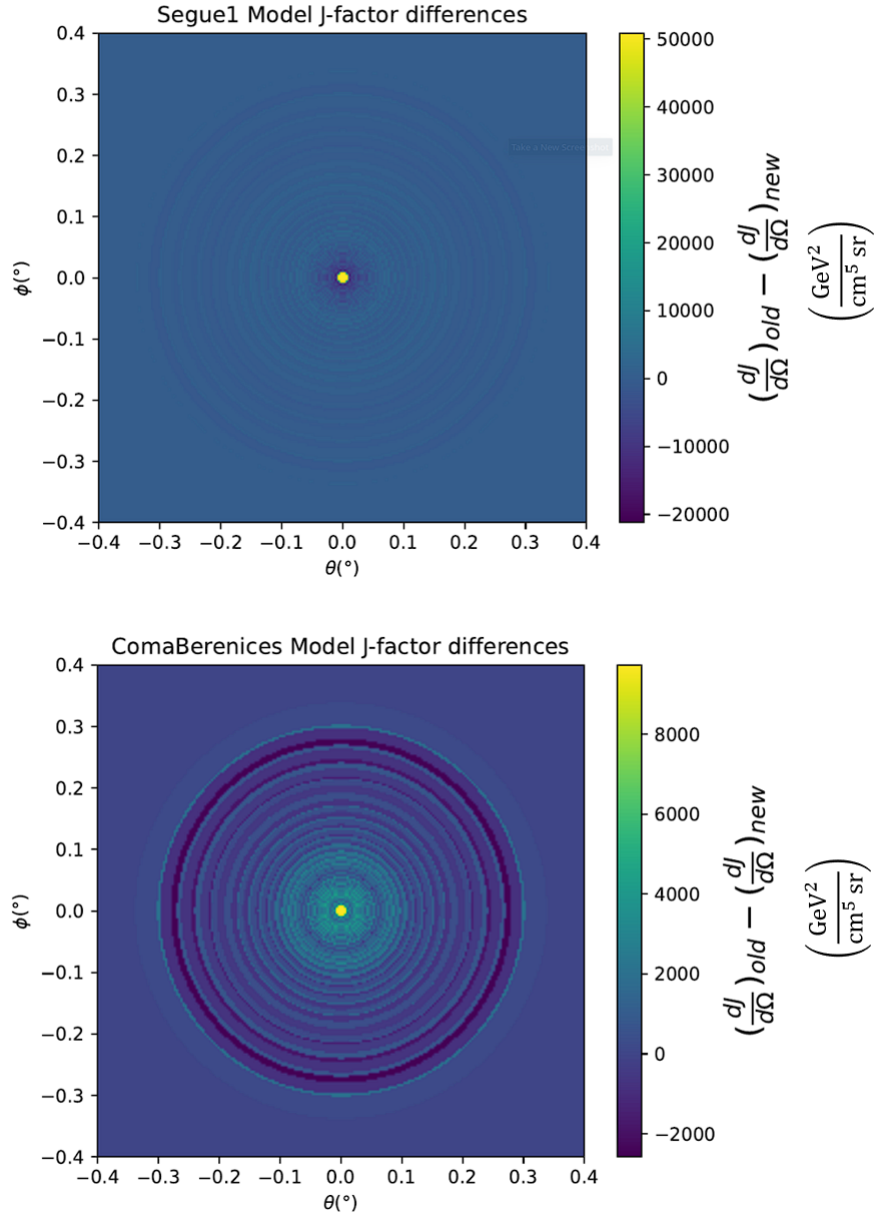


Figure 5.14 Differential map of dJ/Ω from model built in Section 5.8.1 and profiles provided directly from authors. (Top) Differential from Segue1. (bottom) Differential from Coma Berenices. Note that their scales are not the same. Segue1 shows the deepest discrepancies which is congruent with its large uncertainties. Both models show anuli where unique models become apparent.

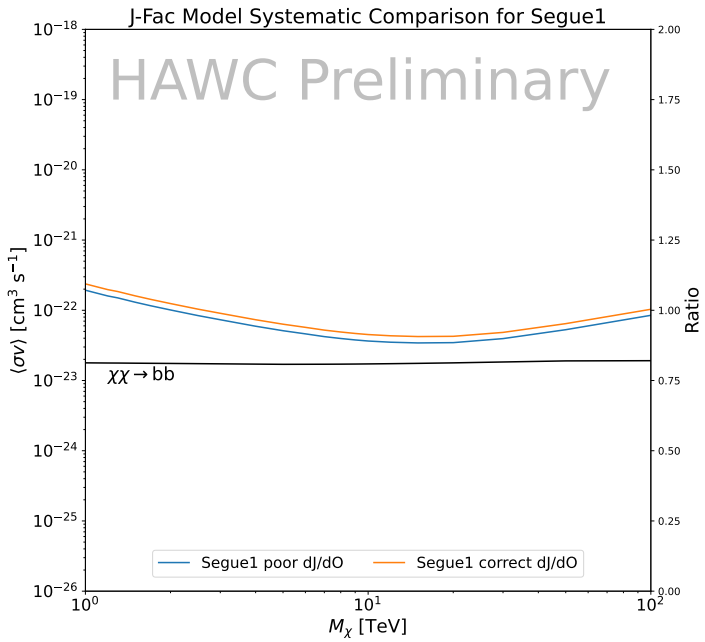
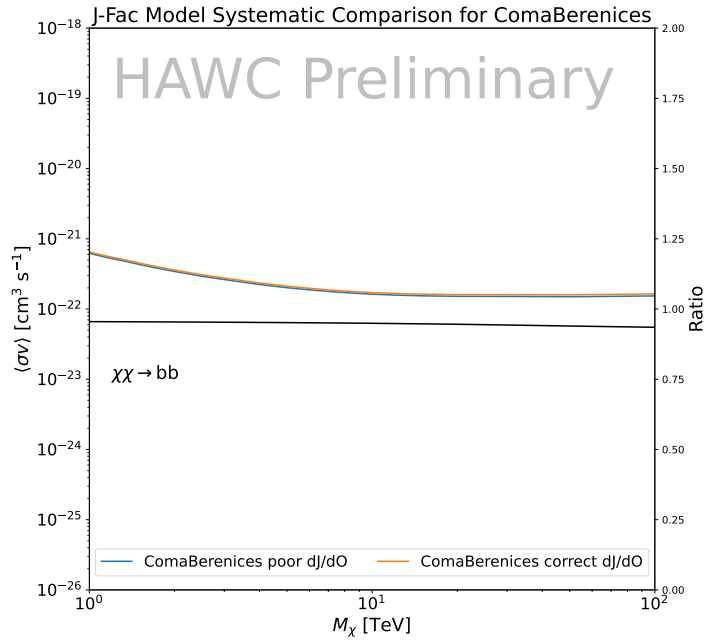


Figure 5.15 HAWC limits for Coma Berenices (top) and Segue1 (bottom) for two different map sets. Blue lines are limits calculated on maps with poor model representation. Orange lines are limits calculated on spatial profiles provided by the authors of [45]. Black line is the ratio of the poor spatial model limits to the corrected spatial models. The left y-axis measures $\langle \sigma v \rangle$ for the blue and orange lines. The right y-axis measures the ratio and is unitless.

1116 density distribution of dark matter.

1117 In addition, a constant velocity anisotropy profile and a Plummer light profile [60] for the stellar
1118 distribution were assumed. The velocity anisotropy profile depends on the radial and tangential
1119 velocity dispersion. However, its determination remains challenging since only the line-of-sight
1120 velocity dispersion can be derived from velocity measurements. Therefore, the parametrization of
1121 the anisotropy profile is obtained from simulated halos (see [61] for more details). They provide the
1122 values of the J -factors of regions extending to various angular radius up to the outermost member
1123 star.

1124 The \mathcal{B} J -factors were computed through a Jeans analysis taking into account the systematic
1125 uncertainties induced by the DM profile parametrization, the radial velocity anisotropy profile, and
1126 the triaxiality of the halo of the dwarf galaxies. They performed a more complete study of the dSph
1127 kinematics and dynamics than \mathcal{GS} for the determination of the J -factor. Conservative values of the
1128 J -factors where obtained using an Einasto DM density profile [62], a realistic anisotropy profile
1129 known as the Baes & Van Hese profile [63] which takes into account that the inner regions can be
1130 significantly non-isotropic, and a Zhao-Hernquist light profile [47].

1131 For both sets, J -factor values are provided for all dSphs as a function of the radius of the
1132 integration region [55, 49, 57]. Table 5.1 shows the heliocentric distance and Galactic coordinates
1133 of the twenty dSphs, together with the two sets of J -factor values integrated up to the outermost
1134 observed star for \mathcal{GS} and the tidal radius for \mathcal{B} . Both J -factor sets were derived through a Jeans
1135 analysis based on the same kinematic data, except for Draco where the measurements of [64] have
1136 been adopted in the computation of the \mathcal{B} value. The computations for producing the \mathcal{GS} and \mathcal{B}
1137 samples differ in the choice of the DM density, velocity anisotropy, and light profiles, for which the
1138 set \mathcal{B} takes into account some sources of systematic uncertainties.

1139 Figure 5.16 and Figure 5.17 show the comparisons for the J -factor versus the angular radius
1140 for each of the 20 dSphs used in this study. The uncertainties provided by the authors are also
1141 indicated in the figures. For the \mathcal{GS} set, the computation stops at the angular radius corresponding
1142 to the outermost observed star, while for the \mathcal{B} set, the computation stops at the angular radius

1143 corresponding to the tidal radius.

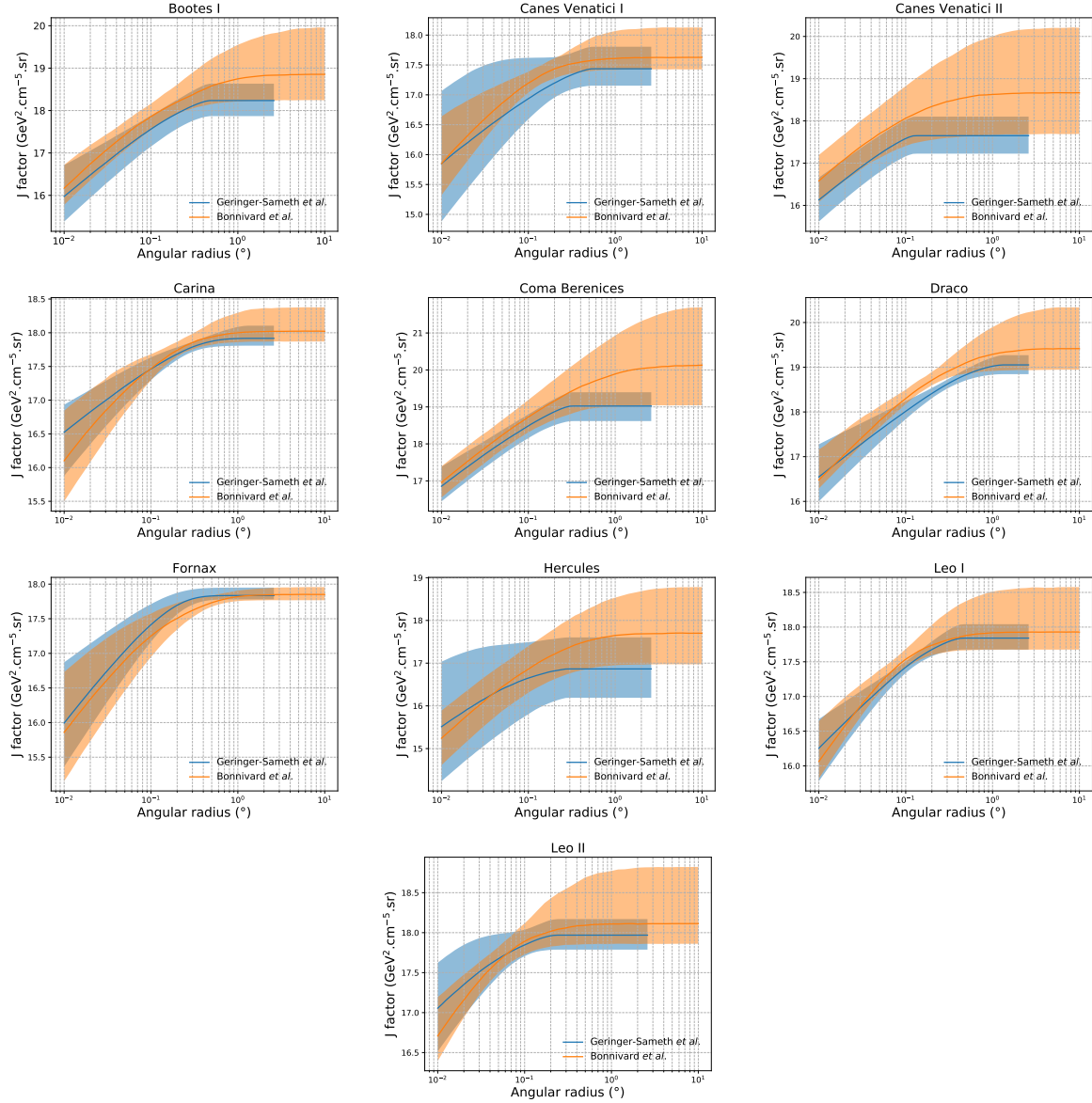


Figure 5.16 Comparisons between the J -factors versus the angular radius for the computation of J factors from Ref. [55] (\mathcal{GS} set in Table 5.1) in blue and for the computation from Ref. [49, 57] (\mathcal{B} set in Tab. 5.1). The solid lines represent the central value of the J -factors while the shaded regions correspond to the 1σ standard deviation.

1144 5.9 Discussion and Conclusions

1145 In this multi-instrument analysis, we have used observations of 20 dSphs from the gamma-ray
 1146 telescopes Fermi-LAT, H.E.S.S., MAGIC, VERITAS, and HAWC to perform a collective DM
 1147 search annihilation signals. The data were combined across sources and detectors to significantly

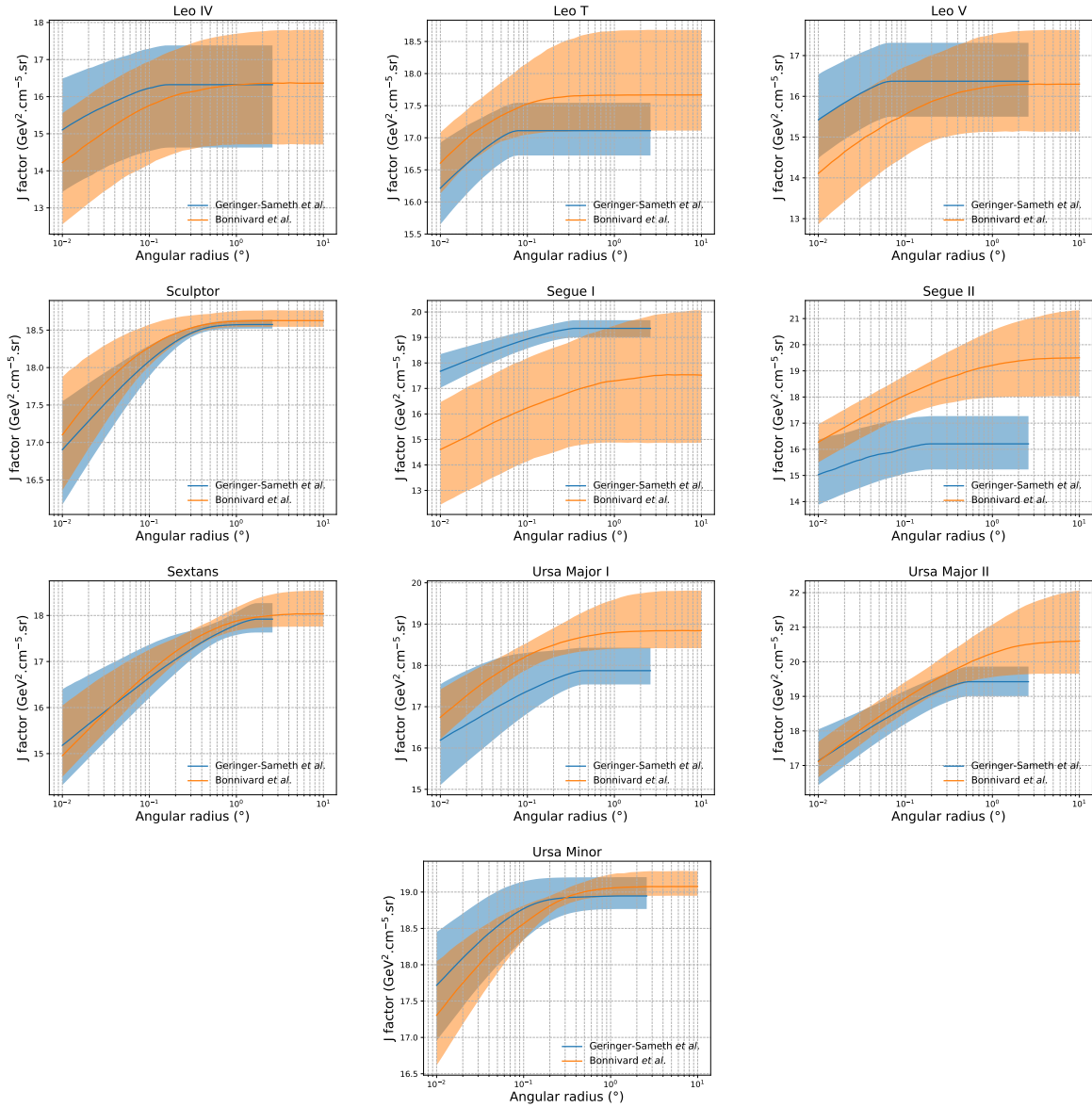


Figure 5.17 Comparisons between the J -factors versus the angular radius for the computation of J factors from Ref. [55] (\mathcal{GS} set in Tab. 5.1) in blue and for the computation from Ref. [49, 57] (\mathcal{B} set in Tab. 5.1) in orange. The solid lines represent the central value of the J -factors while the shaded regions correspond to the 1σ standard deviation.

increase the sensitivity of the search. We have observed no significant deviation from the null, no DM hypothesis, and so present our results in terms of upper limits on the annihilation cross-section for seven potential DM annihilation channels.

Fermi-LAT brings the most stringent constraints for continuum channels below approximately 1 TeV. The remaining detectors dominate at higher energies. Overall, for multi-TeV DM mass,

1153 the combined DM constraints from all five telescopes are 2-3 times stronger than any individual
1154 telescope for multi-TeV DM.

1155 Derived from observations of many dSphs, our results produce robust limits given the DM
1156 content of the dSphs is relatively well constrained. The obtained limits span the largest mass
1157 range of any WIMP DM search. Our combined analysis improves the sensitivity over previously
1158 published results from each detector which produces the most stringent limits on DM annihilation
1159 from dSphs. These results are based on deep exposures of the most promising known dSphs with
1160 the currently most sensitive gamma-ray instruments. Therefore, our results constitute a legacy of
1161 a generation of gamma-ray instruments on WIMP DM searches towards dSphs. Our results will
1162 remain the reference in the field until a new generation of more sensitive gamma-ray instruments
1163 begin operations, or until new dSphs with higher J -factors are discovered.

1164 This analysis serves as a proof of concept for future multi-instrument and multi-messenger
1165 combination analyses. With this collaborative effort, we have managed to sample over four orders
1166 in magnitude in gamma-ray energies with distinct observational techniques. Determining the nature
1167 of DM continues to be an elusive and difficult problem. Larger datasets with diverse measurement
1168 techniques could be essential to tackling the DM problem. A future collaboration using similar
1169 techniques as the ones described in this paper could grow even beyond gamma rays. The models we
1170 used for this study include annihilation channels with neutrinos in the final state. Advanced studies
1171 could aim to merge our results with those from neutrino observatories with large data sets. Efforts
1172 are already underway to add data from the IceCube, ANTARES, and KM3NeT observatories to
1173 these gamma-ray results.

1174 From this work, a selection of the best candidates for observations, according to the latest
1175 knowledge on stellar dynamics and modelling techniques for the derivation of the J -factors on
1176 the potential dSphs targets, is highly desirable at the time that new experiments are starting their
1177 dark matter programs using dSphs. Given the systematic uncertainty inherent to the derivation of
1178 the J -factors, an informed observational strategy would be to select both objects with the highest
1179 J -factors that could lead to DM signal detection, and objects with robust J -factor predictions, i.e.

1180 with kinematic measurements on many bright stars, which would strengthen the DM interpretation
1181 reliability of the observation outcome.

1182 This analysis combines data from multiple telescopes to produce strong constraints on astro-
1183 physical objects. From this perspective, these methods can be applied beyond just DM searches.
1184 Almost every astrophysical study can benefit from multi-telescope, multi-wavelength gamma-ray
1185 studies. We have enabled these telescopes to study the cosmos with greater precision and detail.
1186 Many astrophysical searches can benefit from multi-instrument gamma-ray studies, for which our
1187 analysis lays the foundation.

CHAPTER 6

MULTITHREADING HAWC ANALYSES FOR DARK MATTER SEARCHES

6.1 Introduction

HAWC's current software suite, plugins to 3ML and HAL [54, 42], do not fully utilize computational advancements of recent decades. Said advancements include the proliferation of Graphical Processing Units (GPUs), and multithreading on multicore processors. The analysis described in chapter 5 took up to 3 months of wall time waiting for the full gambit of data analysis and simulation of background to compute. Additionally, with the updated 2D energy binning scheme, f_{hit} and Neural Network (NN), the time needed to compute expected to grow. Although excessive computing time was, in part, from an intense use of a shared computing cluster, it was evident that there was room for improvement. In HAWC's next generation dSph DM search, I decided to develop codes that would utilize the multicore processors on modern high performance computing clusters. The results of this work are featured in this chapter and brought a human timing improvement to computation that scales approximately as $1/N$ where N is the number of threads.

6.2 Dataset and Background

This section enumerates the data and background methods used for HAWC's multithreaded study of dSphs. Section 6.2.1 and Section 6.2.2 are most useful for fellow HAWC collaborators looking to replicate a multithreaded dSph DM search.

6.2.1 Itemized HAWC files

These files are only available within HAWC's internal documentation and collaborators. They are not meant for public access, and are presented here so that HAWC collaborators can reproduce results accurately.

- Detector Resolution: `refit-Pass5-Final-NN-detRes-zenith-dependent.root`
- Data Map: `Pass5-Final-NN-maptree-ch103-ch1349-zenith-dependent.root`
- Spectral Dictionary: `HDMspectra_dict_gamma.npy`

1212 **6.2.2 Software Tools and Development**

1213 This analysis was performed using HAL and 3ML [42, 43] in Python3. I built software
1214 in collaboration with Michael Martin and Letrell Harris to implement the *Dark Matter Spectra*
1215 *from the Electroweak to the Planck Scale* (HDM) [65] and dSphs spatial model from [66] for
1216 HAWC analysis. A NumPy dictionary of HDM, `HDMspectra_dict_gamma.npy`, was made for
1217 portability within the collaboration. These dictionaries were generated from the [git repository](#) [65].
1218 The analysis was performed using the Neural Network energy estimator for Pass 5.F. A description
1219 of this estimator was provided in chapter 3. [TODO: Define a subsection when it's written](#), and its
1220 key, relevant improvements are an improved energy estimation and improved sensitivities at higher
1221 zenith angles. All other software used for data analysis, DM profile generation, and job submission
1222 to SLURM are also kept in my sandbox in the [Dark Matter HAWC](#) project. The above repository
1223 also incorporates the model inputs used previously in Glory Duck, described in chapter 5, so Glory
1224 Duck remains compatible with modern software.

1225 **6.2.3 Data Set and Background Description**

1226 The HAWC data maps used for this analysis contain 2565 days of data between runs 2104 and
1227 7476. They were generated from pass 5.f reconstruction. The analysis is performed using the NN
1228 energy estimator with bin list:

1229 `B1C0Ea, B1C0Eb, B1C0Ec, B1C0Ed, B1C0Ee, B2C0Ea, B2C0Eb, B2C0Ec, B2C0Ed, B2C0Ee,`
1230 `B3C0Ea, B3C0Eb, B3C0Ec, B3C0Ed, B3C0Ee, B3C0Ef, B4C0Eb, B4C0Ec, B4C0Ed, B4C0Ee,`
1231 `B4C0Ef, B5C0Ec, B5C0Ed, B5C0Ee, B5C0Ef, B5C0Eg, B6C0Ed, B6C0Ee, B6C0Ef, B6C0Eg,`
1232 `B6C0Eh, B7C0Ee, B7C0Ef, B7C0Eg, B7C0Eh, B7C0Ei, B8C0Ee, B8C0Ef, B8C0Eg, B8C0Eh,`
1233 `B8C0Ei, B8C0Ej, B9C0Ef, B9C0Eg, B9C0Eh, B9C0Ei, B9C0Ej, B10C0Eg, B10C0Eh,`
1234 `B10C0Ei, B10C0Ej, B10C0Ek, B10C0El`

1235 Bin 0 was excluded as it has substantial hadronic contamination and poor angular resolution.

1236 Background considerations and source selection was identical to Section 5.2.3, and no additional
1237 arguments are provided here. Many of the HAWC systematics explored in Section 5.7 also apply

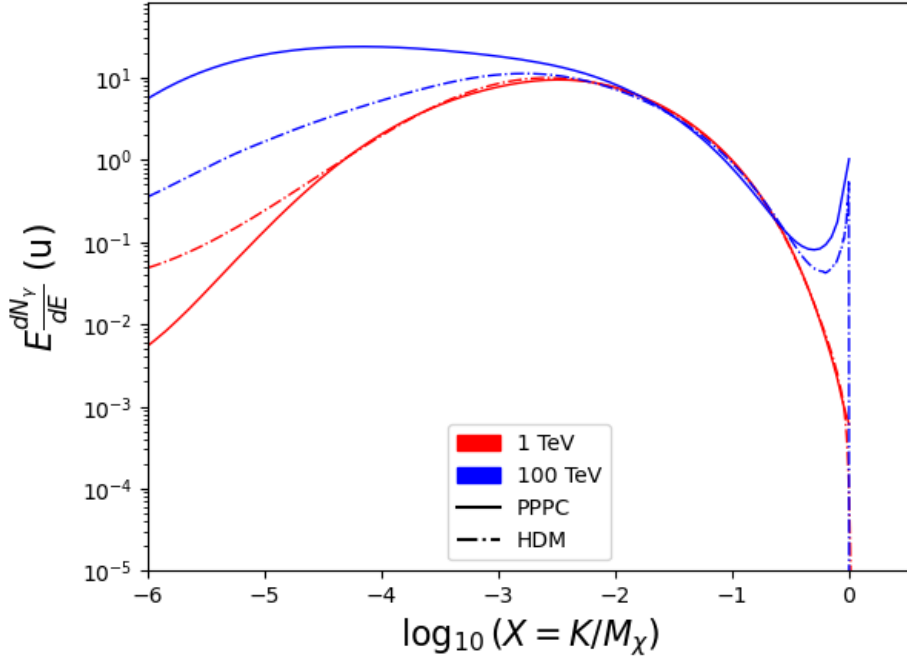


Figure 6.1 Spectral hypotheses from PPPC [44] and HDM [65] for DM annihilation: $\chi\chi \rightarrow W^-W^+$. Solid lines are spectral models with EW corrections from the PPPC. Dash-dot lines are spectral models from HDM. Red lines are models for $M_\chi = 1$ TeV. Blue lines represent models for $M_\chi = 100$ TeV.

1238 for this DM search and are not added upon here.

1239 6.3 Analysis

1240 The analysis and its systematics are almost identical to Section 5.3. Importantly, we use the
 1241 same **TODO: fix this ref** Equation (7.1) and Equation (5.2) for estimating the gamma-ray flux at
 1242 HAWC from our sources.

1243 6.3.1 $\frac{dN_\gamma}{dE_\gamma}$ - Particle Physics Component

1244 For these spectra, we import HDM with Electroweak (EW) corrections and additional correc-
 1245 tions for neutrinos above the EW scale [65]. The spectra are implemented as a model script in
 1246 astromodels for 3ML. A comprehensive description of EW corrections and neutrino considerations
 1247 are provided later in Sec. 8.

1248 Figure 6.1 demonstrates the impact of changes implemented in HDM on DM annihilation to W
 1249 bosons. A class in astromodels was developed to include HDM and is aptly named **HDMspectra**
 1250 within `DM_models.py`. The SM DM annihilation channels studied here are $\chi\chi \rightarrow:$

1251 e^+e^- , $\mu^+\mu^-$, $\tau^+\tau^-$, $b\bar{b}$, $t\bar{t}$, gg , W^+W^- , ZZ , $c\bar{c}$, $u\bar{u}$, $d\bar{d}$, $s\bar{s}$, $\nu_e\bar{\nu}_e$, $\nu_\mu\bar{\nu}_\mu$, $\nu_\tau\bar{\nu}_\tau$, $\gamma\gamma$, hh .

1252 For $\gamma\gamma$ and ZZ , a substantial fraction of the signal photons are expected to have $E_\gamma = m_\chi$ [65].
 1253 This introduces δ -function that is much narrower than the energy resolution of the HAWC detector.
 1254 To ensure that this feature is not lost in the likelihood fits, the 'line' feature is convolved with a
 1255 Gaussian kernel with a 1σ width of $0.05 \cdot m_\chi$ and total kernel window of $\pm 4\sigma$. This differs from
 1256 HAWC's previous line study where 30% of HAWC's energy resolution was used for the kernel [67].
 1257 The NN energy estimator's strength compared to f_{hit} at low gamma-ray energy enables narrower
 1258 kernels [65]. $\chi\chi \rightarrow \gamma\gamma$ and ZZ spectral hypotheses are shown in Figure 6.2. We did not explore
 1259 how well we reconstruct injected signal events for various kernels widths. This is a systematic
 1260 that should be tested before publication to journal. Spectral models for the remaining annihilation
 1261 channels are plotted for each m_χ in Figure B.1.

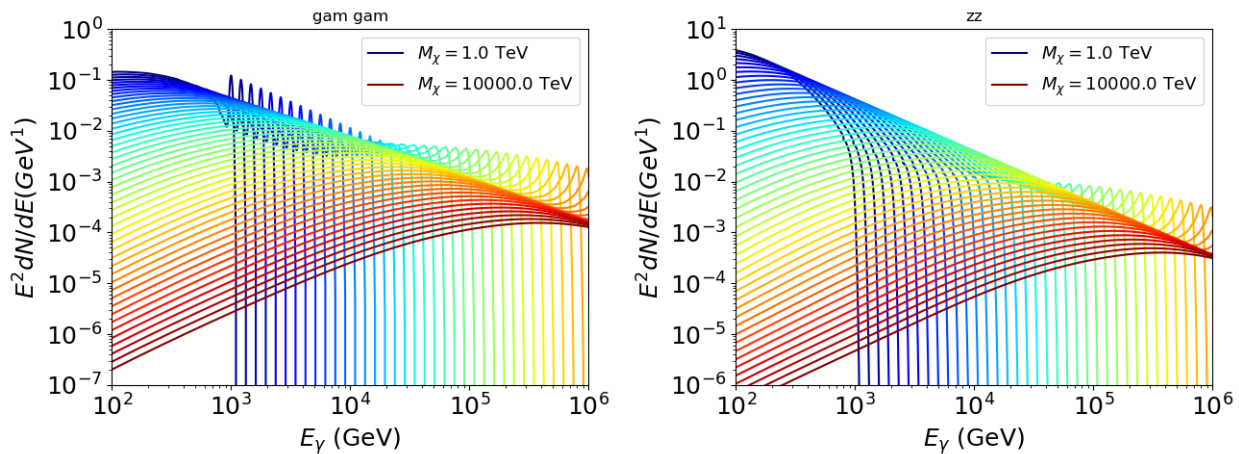


Figure 6.2 Photon spectra for $\chi\chi \rightarrow \gamma\gamma$ (left) and $\chi\chi \rightarrow ZZ$ (right) after Gaussian convolution of line features. Both spectra have δ -features at photon energies equal to the DM mass. Bluer lines are annihilation spectra with lower DM mass. Redder lines are spectra from larger DM mass. All spectral models are sourced from the Heavy Dark Matter models [65]. Axes are drawn roughly according to the energy sensitivity of HAWC.

1262 **6.3.2 J Astrophysical Components**

1263 The J-factor profiles for each source are imported from Louis Strigari et al. (referred to with
 1264 \mathcal{LS}) [66]. The \mathcal{LS} catalog fits a Navarro–Frenk–White (NFW) [48] spatial DM distributions to

1265 the dSphs which has a DM density of

$$\rho(r) = \frac{\rho_0}{\frac{r}{R_s} \left(1 + \frac{r}{R_s}\right)^2}. \quad (6.1)$$

1266 ρ_0 and the scale radius, R_s are free parameters fit for each dSph. r is the distance from the center
1267 of the dSph.

1268 Profiles in $\frac{dJ}{d\Omega}(\theta)$ up to an angular separation $\theta = 0.5^\circ$ were provided directly from the authors.

1269 Map generation from these profiles were almost identical to Section 5.3.2 except that a higher order
1270 trapezoidal integral was used for the normalization of the square, uniformly-spaced map:

$$p^2 \cdot \sum_{i=0}^N \sum_{j=0}^M w_{i,j} \frac{dJ}{d\Omega}(\theta_{i,j}, \phi_{i,j}) \quad (6.2)$$

1271 p is the angular side of one pixel in the map. $w_{i,j}$ is a weight assigned the following ways:

1272 $w_{i,j} = 1$ if $(\theta_{i,j}, \phi_{i,j})$ is fully within the region of integration

1273 $w_{i,j} = 1/2$ if $(\theta_{i,j}, \phi_{i,j})$ is on an edge of the region of integration

1274 $w_{i,j} = 1/4$ if $(\theta_{i,j}, \phi_{i,j})$ is on a corner of the region of integration

1275 Figure 6.3 shows the median and $\pm 1\sigma$ maps used as input for this DM annihilation study.

1276 6.3.3 Source Selection and Annihilation Channels

1277 HAWC's sources for this multithreaded analysis include Coma Berenices, Draco, Segue 1, and
1278 Sextans. \mathcal{LS} observed up to 43 sources in its publication, however only 4 of the best fit profiles
1279 were provided at the time this thesis was written. A full description of each source used in this
1280 analysis is found in Table 6.1.

1281 This analysis improves on chapter 5 in the following ways. Previously, the particle physics
1282 model used for gamma-ray spectra from DM annihilation was from the PPPC [44] which missed
1283 important considerations relevant for the neutrino sector. HDM is used to account for this shortfall
1284 [65]. HDM also models DM to the Planck scale which permits HAWC to probe PeV scale DM. For
1285 this study, we sample DM masses: 1 TeV - 10 PeV with 6 mass bins per decade in DM mass. In

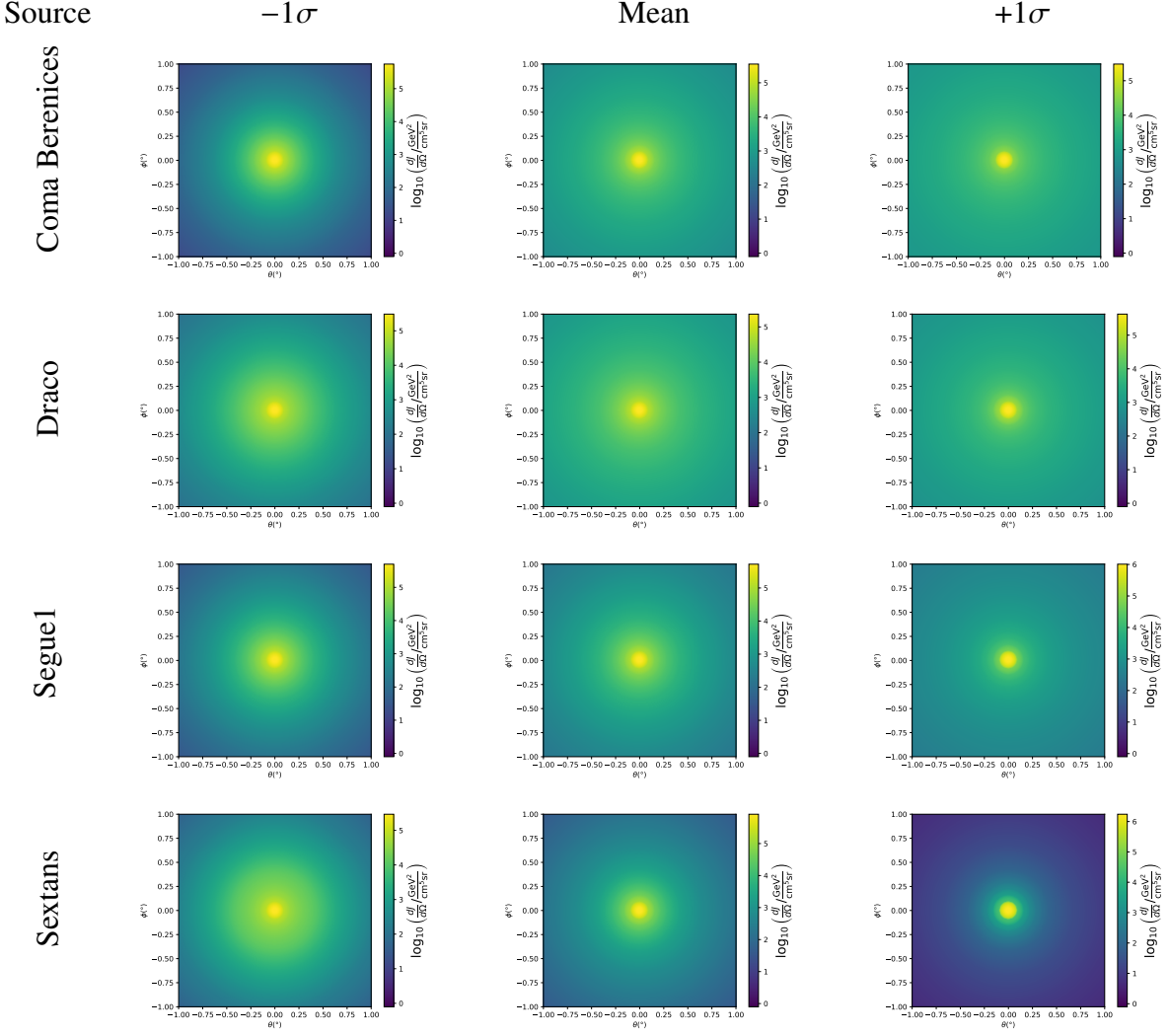


Figure 6.3 $\frac{dJ}{d\Omega}$ maps for Coma Berenices, Draco, Segue1, and Sextans. Columns are divided for the $\pm 1\sigma$ uncertainties in $dJ/d\Omega$ around the mean value from \mathcal{LS} [66]. Origin is centered on the specific dwarf spheroidal galaxies (dSph). θ and ϕ axes are the angular separation from the center of the dwarf. Profiles are truncated at 1° and flattened beyond.

1286 the case of line spectra ($\chi\chi \rightarrow \gamma\gamma$, or ZZ), we double the mass binning to 12 DM mass bins per
 1287 decade in DM mass.

1288 \mathcal{LS} provides 25 sources within HAWC's field of view. Additionally, NFW [48] DM distributions
 1289 have fewer parameters than Zhao [47], so \mathcal{LS} fits ultra-faint dwarves which expands the number of
 1290 sources. However, all sources were not provided by the authors in time for the completion of this
 1291 dissertation. Finally, the gamma-ray ray dataset is much larger. The study performed here analyzes
 1292 2565 days of data compared to 1017 days analyzed in chapter 5.

1293 **6.4 Likelihood Methods**

1294 These are identical to Section 5.4.1 and no additional changes are made to the likelihood. Bins
 1295 in this analysis are expanded to include HAWC’s NN energy estimator.

1296 **6.5 Computational Methods: Multithreading**

1297 Previously, as in Section 5.3, the likelihood was minimized for one model at a time. One model
 1298 in this case representing a DM annihilation channel (CHAN), DM mass (m_χ), and dSph ((SOURCE)).
 1299 In an effort to conserve human and CPU time, jobs submitted for high performance computing
 1300 contained a list of m_χ to iterate over for likelihood fitting. Jobs were then trivially parallelized
 1301 for each permutation of the two lists: CHANS and SOURCES. The lists for CHANS and SOURCES are
 1302 found in Section 6.3.1 and Table 6.1, respectively. Initially, 11 m_χ were serially sampled for one
 1303 job defined by a [CHAN, SOURCE] tuple. Computing the likelihoods would take between 1.5 to 2 hrs,
 1304 stochastically, for a job. We expect to compute likelihoods for data and 300 Poisson background
 1305 trials. The estimated CPU time based on the above for all CHAN (N = 17) and SOURCE (M = 25)
 1306 was estimated to 127,925 jobs. In total, 1,407,175 likelihood fits and profiles would be computed
 1307 for the 11 mass bins we wished to study. The estimated CPU time ranged between 8k CPU days
 1308 to 10k CPU days. Human time is more challenging to estimate as job allocation is stochastic and
 1309 highly dependent on what other users are submitting. Yet, it is unlikely that all jobs would run
 1310 simultaneously. Therefore, we can expect human time to be about as long as was seen in chapter 5

Name	Distance (kpc)	l, b ($^\circ$)	$\log_{10} J$ (\mathcal{LS} set) $\log_{10}(\text{GeV}^2 \text{cm}^{-5} \text{sr})$
Coma Berenices	44	241.89, 83.61	$19.00^{+0.36}_{-0.35}$
Draco	76	86.37, 34.72	$18.83^{+0.12}_{-0.12}$
Segue I	23	220.48, 50.43	$19.12^{+0.49}_{-0.58}$
Sextans	86	243.50, 42.27	$17.73^{+0.13}_{-0.12}$

Table 6.1 Summary of the relevant properties of the dSphs used in the present work. Column 1 lists the dSphs. Columns 2 and 3 present their heliocentric distance and galactic coordinates, respectively. Column 4 reports the J -factors of each source given from the \mathcal{LS} studies and estimated $\pm 1\sigma$ uncertainties. The values $\log_{10} J$ (\mathcal{LS} set) [66] correspond to the mean J -factor values for a source extension truncated at 0.5° .

1311 which was on the order of months to fully compute on a smaller analysis. A visual aid to describe
1312 how jobs were organized is provided in Figure 6.4.

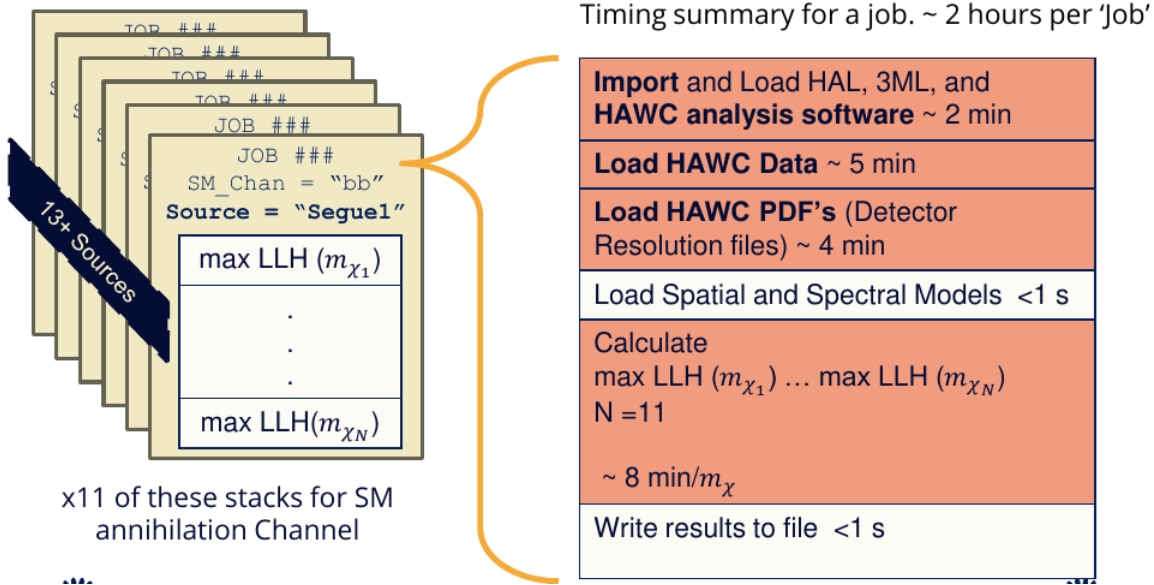


Figure 6.4 Infographic on how jobs and DM computation was organized in Section 5.3. Jobs were built for each permutation of CHANS and SOURCES shown by the left block in the figure. Each job, which took on the order 2 hrs to compute, had the following work flow: 1. Import HAWC analysis software, 2 min to run. 2. Load HAWC count maps, 5 min to run. 3. Load HAWC energy and spatial resolutions, 4 min. 5. Load DM spatial source templates and spectral models, less than 1 s. 6. Perform likelihood fit on data and model, about 8 min per DM mass. 7. Write results to file, less than 1s.

1313 The computational needs for this next generation DM analysis are extreme and is unlike other
1314 analyses performed on HAWC. It became clear that there was a lot to gain from optimizing how
1315 the likelihoods are computed. This section discusses how multi-threading was applied to solve and
1316 reduce HAWC's computing of likelihoods for large parameter spaces like in DM searches.

1317 6.5.1 Relevant Foundational Information

1318 The profiling of the likelihood for HAWC is done via gradient descent where the normalization
1319 of Equation (7.1) (linearly correlated with $\langle \sigma v \rangle$) is rescaled in the descent. Additionally, we sample
1320 the likelihood space for a defined list of $\langle \sigma v \rangle$'s described in Section 5.4.2. The time to compute
1321 these values is not predictable or consistent because many variables can change across the full
1322 model-space. Comprehensively, these variables are:

1323 • m_χ : DM rest mass
 1324 • CHAN : DM annihilation channel in SM.
 1325 • SOURCE : dSph. Involves a spatial template AND coordinate in HAWC data.
 1326 • $\langle\sigma v\rangle$: Effectively the flux normalization and free parameter in the likelihood fit.
 1327 Therefore, we develop an asynchronous, functional-parallel coding pattern. Asynchronous meaning
 1328 the instructions within a function are independent and permitted to be out of sync with sibling
 1329 computations. Functional-parallel meaning that instructions are the subject of parallelization
 1330 rather than threading the likelihood computation. This is close to trivial parallelization seen in
 1331 Figure 6.4 except that we seek to consolidate the loading stages (software, data, and detector
 1332 resolution loading). Multiple asynchronous threads are expected to reduce total serial processing
 1333 time and total overhead across the entire project in addition to saving human time.

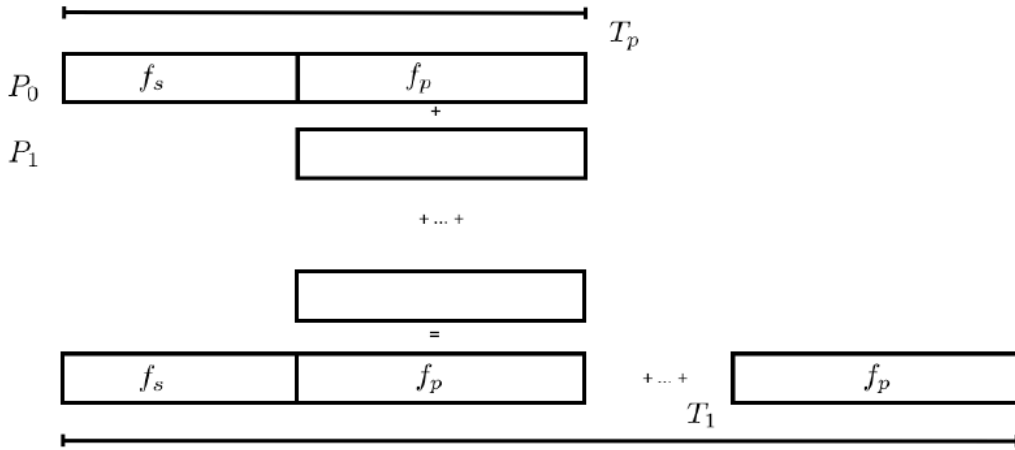


Figure 6.5 Graphic of Gustafson parallel coding pattern. f_s is the fraction of a program, in time, spent on serial computation. f_p is the fraction of computing time that is parallelizable. T_p is the total time for a parallel program to run. T_1 is the total time for a parallel program to run if only 1 processor is allocated. P_N is the N -th processor where it's row is the computation the processor performs. The Gustafson pattern is most similar to what is implemented for this analysis. Figure is pulled from [68].

1334 We need a way to measure and compare the expected speedup and efficiency gain for this
 1335 asynchronous coding pattern. I pull inspiration for timing measurement from [68] and use *Amdahl's*

1336 law with hybrid programming. Hybrid programming meaning that the computation is a mix of
 1337 distributed and shared memory programming. If we assume the code is fully parallelizable over p
 1338 processors and c threads, the ideal speedup is simply pc , and ideal run-time is $T_1/(pc)$. T_1 is the
 1339 total time for a parallel program to run if only 1 processor is allocated. However, the coding pattern
 1340 contains some amount of unavoidable serial computation, as shown in Figure 6.5. In our case, the
 1341 run time, $T_{p,c}$, is estimated to be

$$T_{p,c} = \frac{T_1}{pc} (1 + F_s(c - 1)). \quad (6.3)$$

1342 F_s is the fraction of CPU time dedicated to serial computation. The expected speedup, $S_{p,c}$, is

$$S_{p,c} \equiv \frac{T_1}{T_{p,c}} = \frac{pc}{1 + F_s(c - 1)}. \quad (6.4)$$

1343 From Equation (6.4), we can see that the speed-up scales with p/F_s . We are free to minimize F_s
 1344 asymptotically by enlarging the total models that are submitted to the thread pool, thereby shrinking
 1345 the CPU fraction dedicated to serial operation. We are also free to define exactly how many threads
 1346 and processors we utilize, yet eventually hit a hard cap at the hardware available on our computing
 1347 cluster. HAWC uses Intel Xeon™processors with 48 cores and 96 threads. We see that a successful
 1348 code will scale well as the expected speedup is inversely correlated with F_s . As the total number
 1349 of models sampled grows, the speedup will also.

1350 6.5.2 Implementation

1351 The multithreaded code was written in Python3 and is documented in the `dark_matter_hawc`
 1352 [repository](#) within the script named `mpu_analysis.py`. A version of the script as of April 25
 1353 **TODO: make sure to update on this date** is also provided in Section B.2. It has many dependencies
 1354 including the HAWC analysis software. Figure 6.6 displays the workflow of a job with 3 threads.
 1355 Within a job, SOURCE is kept fixed and CHANS remains 17 elements long. More m_χ are sampled
 1356 from 11 bins up to 49 (for $\gamma\gamma$ and ZZ) and 25 (for remaining CHANS) which amounts to 12 or 6
 1357 mass bins per decade. m_χ and CHANS are permuted into a 473 element list which is split evenly
 1358 across N threads where N is [2, 8, 16]. For each m_χ -CHAN tuple, 1001 $\langle\sigma v\rangle$ values are sampled in

Timing summary for a multi-threaded job.

Import and Load HAL, 3ML, and HAWC analysis software ~ 2 min		
Load HAWC Data ~ 5 min		
Load HAWC PDF's (Detector Resolution files) ~ 4 min		
Load Spatial Model < 1s		
Load Spectra Models <1 s	Load Spectra Models <1 s	Load Spectra Models <1 s
Calculate max LLH (Chan_0, m_{χ_1}) ... max LLH (Chan_?, m_{χ_N}) N = TOTAL/N_THREADS ~ 8 min/Spec_model	Calculate max LLH (Chan_?, m_{χ_1}) ... max LLH (Chan_?, m_{χ_N}) N = TOTAL/N_THREADS ~ 8 min/Spec_model	Calculate max LLH (Chan_?, m_{χ_1}) ... max LLH (Chan_?, m_{χ_N}) N = TOTAL/N_THREADS ~ 8 min/Spec_model
Write results to file <1 s	Write results to file <1 s	Write results to file <1 s
Join Threads and terminate < 1s		

Figure 6.6 Task chart for one multithreaded job developed for this project. Green blocks indicate a shared resource across the threads AND computation performed serially. Red blocks indicate functional parallel processing within each thread. 3 threads are represented here, yet many more can be employed during the full analysis. Jobs are defined by the SOURCE as these require unique maps to be loaded into the likelihood estimator. The m_{χ} , CHAN, and $\langle \sigma v \rangle$ variables are entered into the thread pool and allocated as evenly as possible across the threads.

1359 the likelihood, and the value of $\langle \sigma v \rangle$ that maximizes the likelihood is found. Although rare, fits
1360 that failed are handled on a case by case basis.

1361 6.5.3 Performance

M Tasks	$T_{p,c}$ (hr:min:s)			
	$T_{1,1}$	$T_{1,2}$	$T_{1,8}$	$T_{1,16}$
50	1:40:37.5	0:52:43.7	0:19:13.8	0:13:44.0
74	2:22:30.0	1:15:00.6	0:25:21.3	0:15:49.8
100	(3:07:51.9)	1:40:10.5	0:30:44.4	0:20:01.4
200	(6:02:20.6)	-	1:00:32.0	0:30:35.0
473	(13:58:40.3)	-	2:01:41.4	1:07:53.2

Table 6.2 Timing summaries for analyses for serial and multithreaded processes. M tasks is the number of functional-parallel tasks ran for the computation. $T_{p,c}$ is a single run time in hours:minutes:seconds for runs utilizing p nodes and c threads. Runs are run interactively on the same computer to maximize consistency. Empty entries are indicated with '-'. (·) entries are estimated entries extrapolated from data earlier in the column.

1362 We see a significant reduction to wall time needed for our dSph analyses to run. Table 6.2

1363 shows the timing summaries for analyses of different sizes and thread counts. Additionally, the
 1364 efficiency gained when consolidating the serial loading of data is also apparent in our ability to
 1365 study many more tasks in about the same amount of wall time as a smaller serial computation. Trials
 1366 represented in the table were run on an AMD Opteron® processor 6344 with 48 cores, 2 threads per
 1367 core; 2.6 GHz clock. This is not the same architecture used for analysis on the HAWC computing
 1368 cluster however they are similar enough that results shown here are reasonably representative of
 1369 computing on the HAWC computing cluster. I use Tab. 6.2 for the inferences and conclusions in
 1370 the following paragraphs.

1371 First, we want to find T_s , the time of serial computation. From Fig. 6.5, the timing for our
 1372 coding pattern can be written as

$$T_s + Mt_p = T_{1,1}^M. \quad (6.5)$$

1373 M is the number of functional-parallel tasks (represented as column 1 of Tab. 6.2), and t_p is the
 1374 average time to complete a single parallel task. $T_{1,1}^M$ is the total time for a parallel program to run if
 1375 only 1 processor is allocated for M parallel task. With two runs of different M (M_1 and M_2), we
 1376 can use a system of equations to compute

$$T_s = 803.1\text{s} \text{ and } t_p = 104.6\text{s} \quad (6.6)$$

1377 Now, we have specific estimation for the fraction of serial computing time, F_s :

$$F_s = \frac{803.1}{803.1 + 104.6 \cdot M}. \quad (6.7)$$

1378 The maximum M for this study is 473 which evaluates to: $F_s = 0.016$ or 1.6% of computing time.
 1379 Table 6.3 shows the resulting speedups.

1380 We see a speedup that generally exceeds expectations from Eq. (6.4) for real trail runs. We also
 1381 see that there are diminishing returns as the number of threads increases. For small jobs with large c ,
 1382 both the expected and observed speedup are significantly smaller than c . One thing not considered
 1383 in Eq. (6.4) is the time incurred via communication latency. Communication latency increases
 1384 with the number of threads and contributes to diminishing returns. Additionally, these values are

M Tasks	F_s	$S_{1,2}$	$S_{1,8}$	$S_{1,16}$
50	1.33 E-1	1.90 [1.76]	5.23 [4.14]	6.35 [5.34]
74	9.40 E-2	1.90 [1.83]	5.62 [4.82]	9.00 [6.64]
100	7.13 E-2	1.88 [1.87]	6.11 [5.34]	9.38 [7.73]
200	3.70 E-2	- [1.93]	5.98 [6.36]	11.85 [10.29]
473	1.60 E-2	- [1.97]	6.89 [7.20]	12.35 [12.91]

Table 6.3 Speed up summaries for analyses for serial and multithreaded processes. M tasks is the number of functional-parallel tasks ran for the computation. $S_{p,c}$ is a single speedup comparison for runs utilizing p nodes and c threads. [·] are the estimated speedups calculated from Tab. 6.2, Eq. (6.7), and Eq. (6.4). Empty entries are indicated with '-'.

1385 for single runs and do not consider the stochastic variation expected in a shared high performance
 1386 computing resource. Therefor, these results are not strictly conclusive, yet demonstrate the merits
 1387 of multi-threading. We see very clearly that there is a lot to gain, and this new coding pattern will
 1388 expand HAWC's analysis capabilities.

1389 6.6 Analysis Results

1390 3 of the 43 $\mathcal{L}\mathcal{S}$ dSphs considered for the multithreaded analysis. These dSph are analyzed
 1391 for emission from DM annihilation according to the likelihood method described in Section 5.4.
 1392 The three likelihood profiles are then stacked to synthesize a combined limit on the dark matter
 1393 annihilation cross-section, $\langle\sigma v\rangle$. This combination is done each of the 17 SM annihilation channels.
 1394 Figure 6.7 and Fig. 6.8 show the combined limits for all annihilation channels with HAWC's
 1395 observations. Test statistics of the best fit $\langle\sigma v\rangle$ values for each m_χ and CHAN are shown in Fig. 6.9
 1396 and Fig. 6.10. We also compare these limits to HAWC's Glory Duck limits shown in Section 5.5.
 1397 The comparison to Glory Duck are featured in Fig. 6.11 for all the DM annihilation channels studied
 1398 for Glory Duck. A full comparison is provided in the appendix in Fig. B.2, Fig. B.3, and Fig. B.4.
 1399 Here, we show updated limits for $\chi\chi \rightarrow b\bar{b}, e\bar{e}, \mu\bar{\mu}, \tau\bar{\tau}, t\bar{t}, W^+W^-$, $\gamma\gamma$ and ZZ . For the first time
 1400 ever, we show limits for $\chi\chi \rightarrow c\bar{c}, s\bar{s}, u\bar{u}, d\bar{d}, \nu_e\bar{\nu}_e, \nu_\mu\bar{\nu}_\mu, \nu_\tau\bar{\nu}_\tau, gg$, and hh .

1401 No DM was found in HAWC observations. The largest excess found in HAWC data was for DM
 1402 annihilating to W -bosons or $\nu_e\bar{\nu}_e$ for $m_\chi = 10$ TeV at significance 2.11σ and 2.14σ respectively.
 1403 HAWC's limits and excesses are dominated by Segue1. Coma Berenices shows excesses at higher
 1404 DM mass, yet no similar excesses were observed in Segue1 or Sextans. Sextans did not contribute

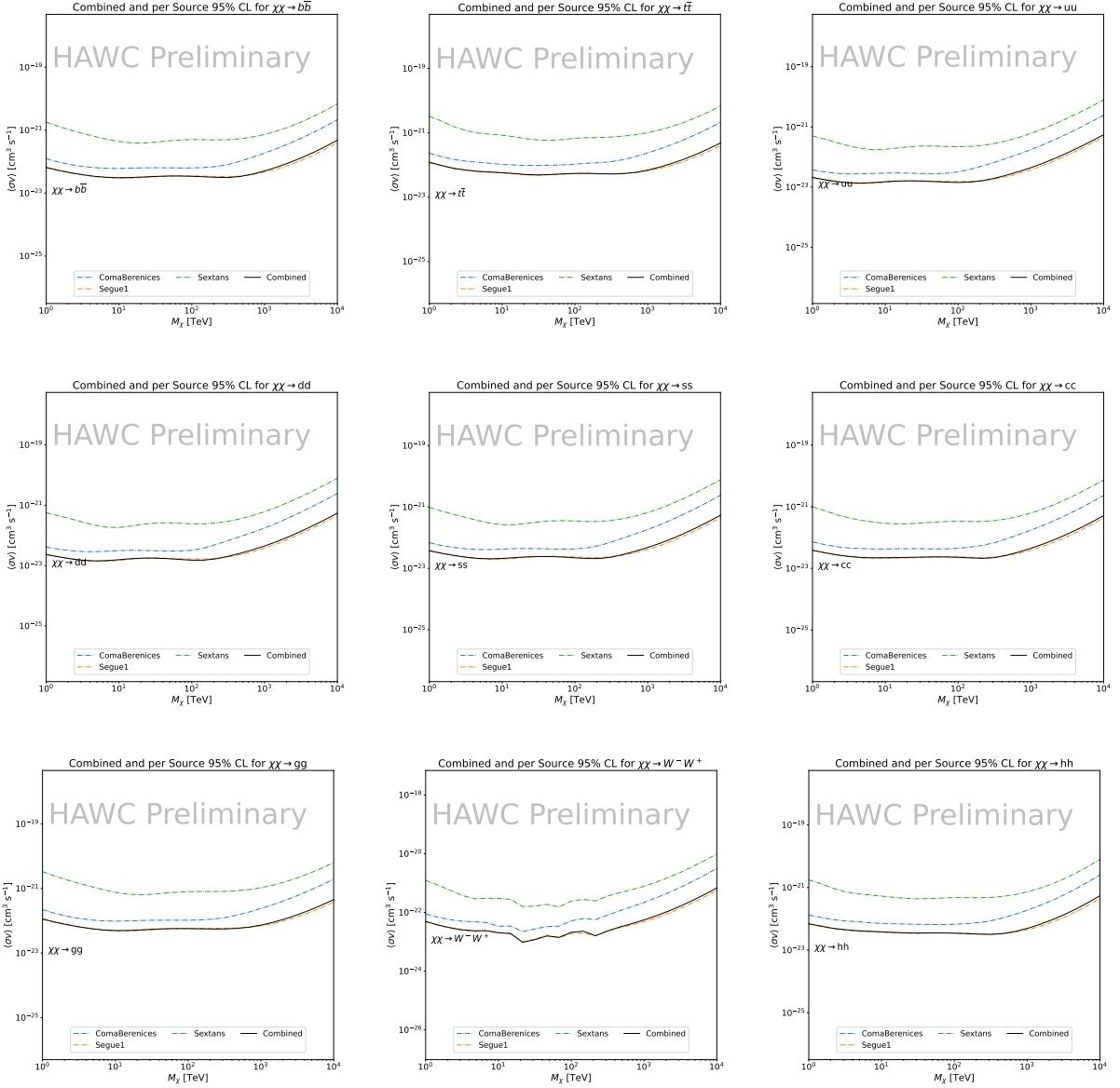


Figure 6.7 HAWC upper limits at 95% confidence level on $\langle\sigma v\rangle$ versus m_χ for $\chi\chi \rightarrow b\bar{b}$, $t\bar{t}$, $u\bar{u}$, $d\bar{d}$, $s\bar{s}$, $c\bar{c}$, gg , W^+W^- , and hh . Limits are with $\mathcal{L}\mathcal{S}$ J -factors [66]. The solid line represents the observed combined limit. Dashed lines represent limits from individual dSphs.

significantly to signal excesses or the combined limit as it is at high zenith. Draco was not included as the PDF of some of our analysis bins were wider than what is reasonable for a point source analysis. Draco is at a high zenith for HAWC, so the effort required to include it was not justified by the benefits.

We did not generate background trials in time of writing this thesis. These are not shown and

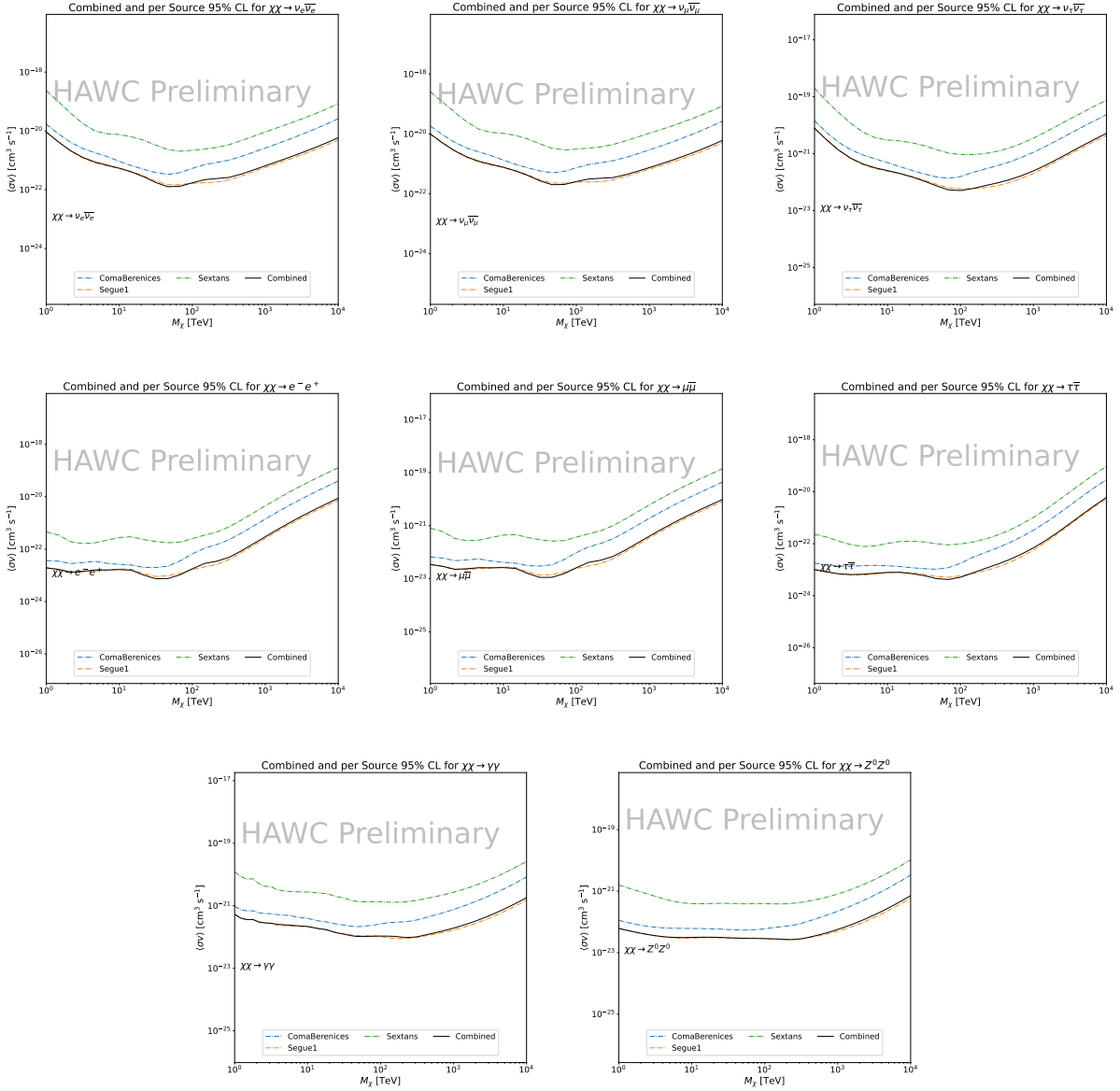


Figure 6.8 HAWC upper limits at 95% confidence level on $\langle\sigma v\rangle$ versus m_χ for $\chi\chi \rightarrow \nu_e \bar{\nu}_e$, $\nu_\mu \bar{\nu}_\mu$, $\nu_\tau \bar{\nu}_\tau$, $e \bar{e}$, $\mu \bar{\mu}$, $\tau \bar{\tau}$, $\gamma\gamma$ and ZZ . Limits use $\mathcal{L}S$ J -factors [66]. The solid line represents the observed combined limit. Dashed lines represent limits from individual dSphs.

1410 are an immediate next step for this analysis before publication.

1411 When comparing these results to Section 5.5, we see an overall decrease to the confidence limit
 1412 therefore improvement to HAWC's expected sensitivity. This improvement is generally stronger
 1413 than a doubling of data, or a factor $\sqrt{2}$ decrease. The comparison is somewhat complex and
 1414 dependent on the dSph and SM annihilation channel. Figure 6.11 shows the comparisons of limits

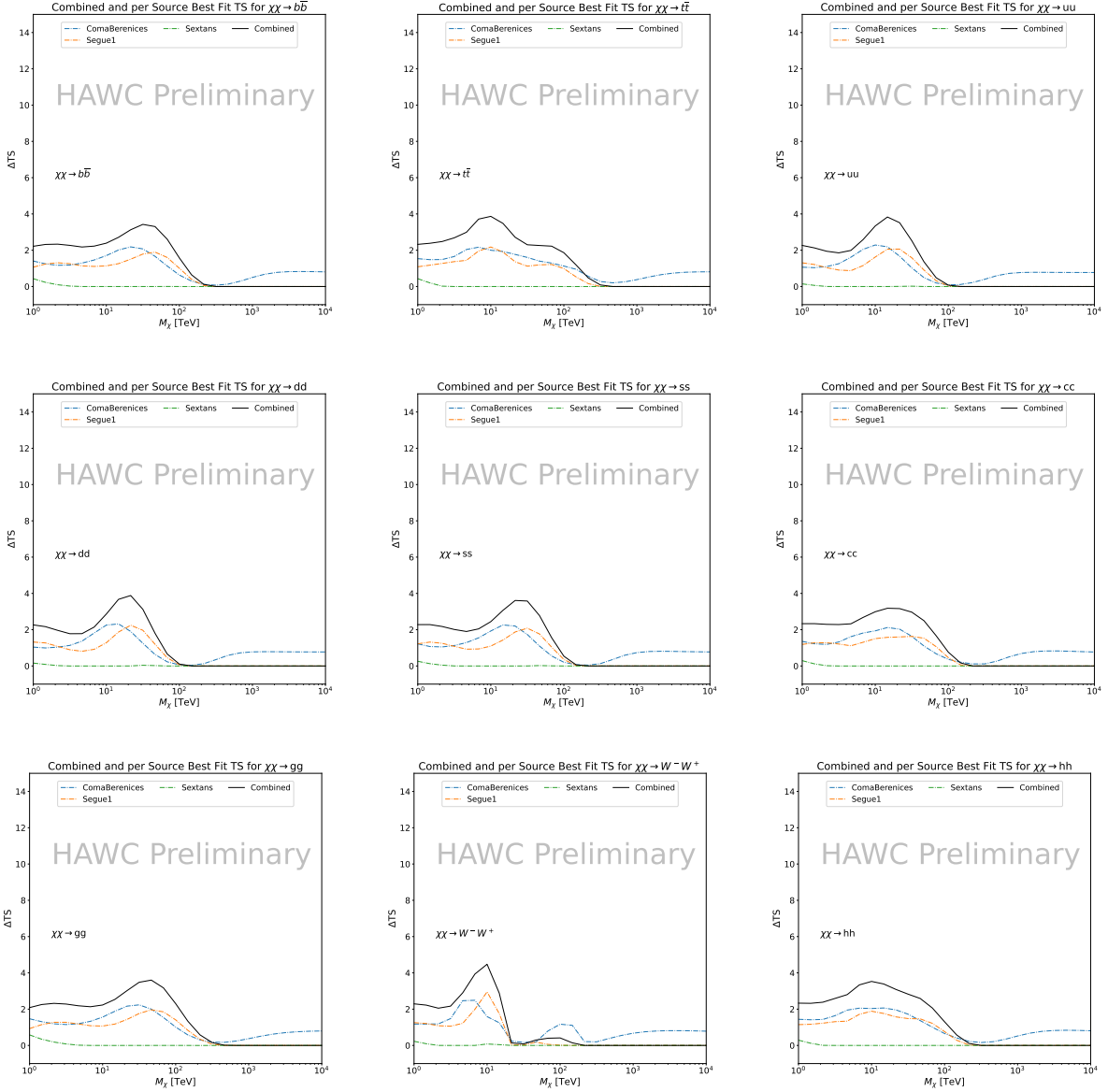


Figure 6.9 HAWC TS values for best fit $\langle\sigma v\rangle$ versus m_χ for SM annihilation channels: $\chi\chi \rightarrow b\bar{b}$, $t\bar{t}$, $u\bar{u}$, $d\bar{d}$, $s\bar{s}$, $c\bar{c}$, gg , W^-W^+ , and hh . Limits use \mathcal{LS} J -factors. The solid black line shows the combined best fit TS values. The colored, dashed lines are the TS values from each dSph.

1415 calculated for this analysis and Glory Duck (Section 5.5). Segue 1 and Coma Berenices are low
 1416 zenith where improvements to HAWC's analysis come only from energy estimation. Differences
 1417 between these two are dominantly from their differences in J -factor, half-light radii of the dSphs,
 1418 and the particle physics inputs. Substantial gains in HAWC's analysis methods (pass 5.F) were
 1419 made at high zenith which is important for sources like Sextans. The HDM particle physics model

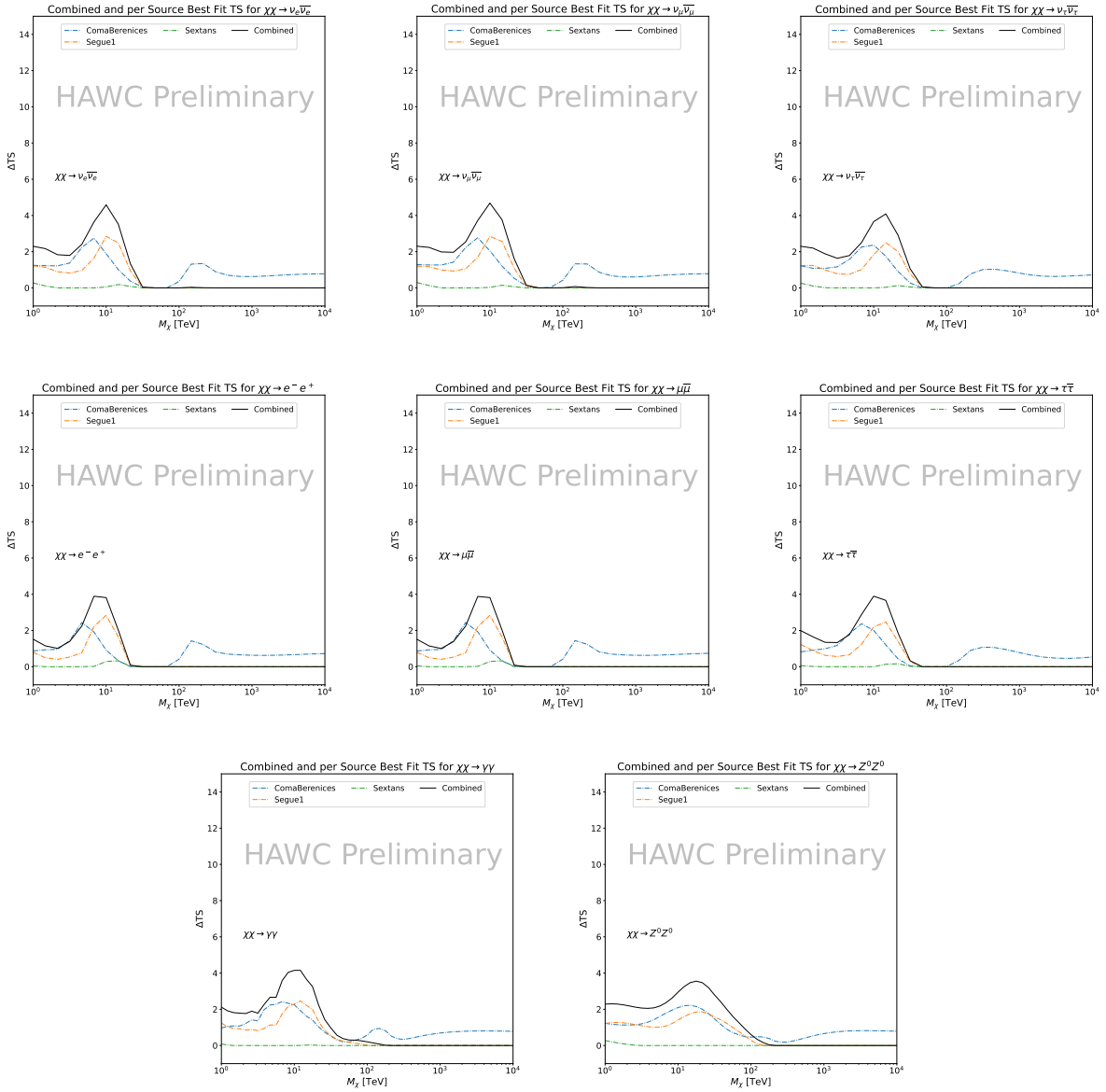


Figure 6.10 HAWC TS values for best fit $\langle\sigma v\rangle$ versus m_χ for SM annihilation channels: $\chi\chi \rightarrow \nu_e \bar{\nu}_e$, $\nu_\mu \bar{\nu}_\mu$, $\nu_\tau \bar{\nu}_\tau$, $e^- e^+$, $\mu \bar{\mu}$, $\tau \bar{\tau}$, $\gamma\gamma$ and ZZ . Limits use \mathcal{LS} J -factors. The solid black line shows the combined best fit TS values. The colored, dashed lines are the TS values from each dSph.

1420 produces almost identical spectra to the PPPC for $\chi\chi \rightarrow e^- e^+$. This channel can be used to
 1421 compare limits between dSph spatial models. Overhead sources see minimal improvement to the
 1422 limits, while high zenith sources see an order of magnitude improvement for all DM masses. Softer
 1423 SM annihilation channels see broad improvements to the limit compared to harder channels.

1424 **6.7 Systematics**

1425 Systematics to this analysis are identical to what was performed earlier in Glory Duck, Sec-
1426 tion 5.7. We are also sensitive to the choice in spatial template, and this was explored in Section 5.7.2
1427 and Section 5.8.2.

1428 **6.8 Conclusion and Discussion**

1429 In this multithreaded analysis, we have used observations of 3 dSphs from HAWC to perform
1430 a collective DM annihilation search towards dSphs. The data were combined across sources
1431 to significantly increase the sensitivity of the search. Advanced computational techniques were
1432 deployed to accelerate wall-time spent analyzing by an order of magnitude. We have observed
1433 no significant deviation from the null, no DM hypothesis, and so present our results in terms of
1434 upper limits on the velocity-weighted cross-section, $\langle\sigma v\rangle$, for seventeen potential DM annihilation
1435 channels across four decades of DM mass.

1436 This analysis serves as a proof of concept for multithreaded HAWC analyses with large parameter
1437 spaces. Larger datasets with fast techniques will be essential to tackling the DM problem. The
1438 models we used for this study include annihilation channels with neutrinos in the final state.
1439 Advanced studies could aim to merge our results with those from neutrino observatories with large
1440 data sets.

1441 A full HAWC analysis will include systematic studies of the J -factor distributions. Additionally,
1442 because of the timing reduction, the study can be doubled in size to include DM decay. We have not
1443 yet received the remaining spatial profiles to the \mathcal{LS} catalog, and limits can be quickly computed
1444 once these are received. Finally, statistical studies with Poisson variation of HAWC's background
1445 are essential to a comprehensive understanding of our observed excesses.

Segue1

Coma Berenices

Sextans

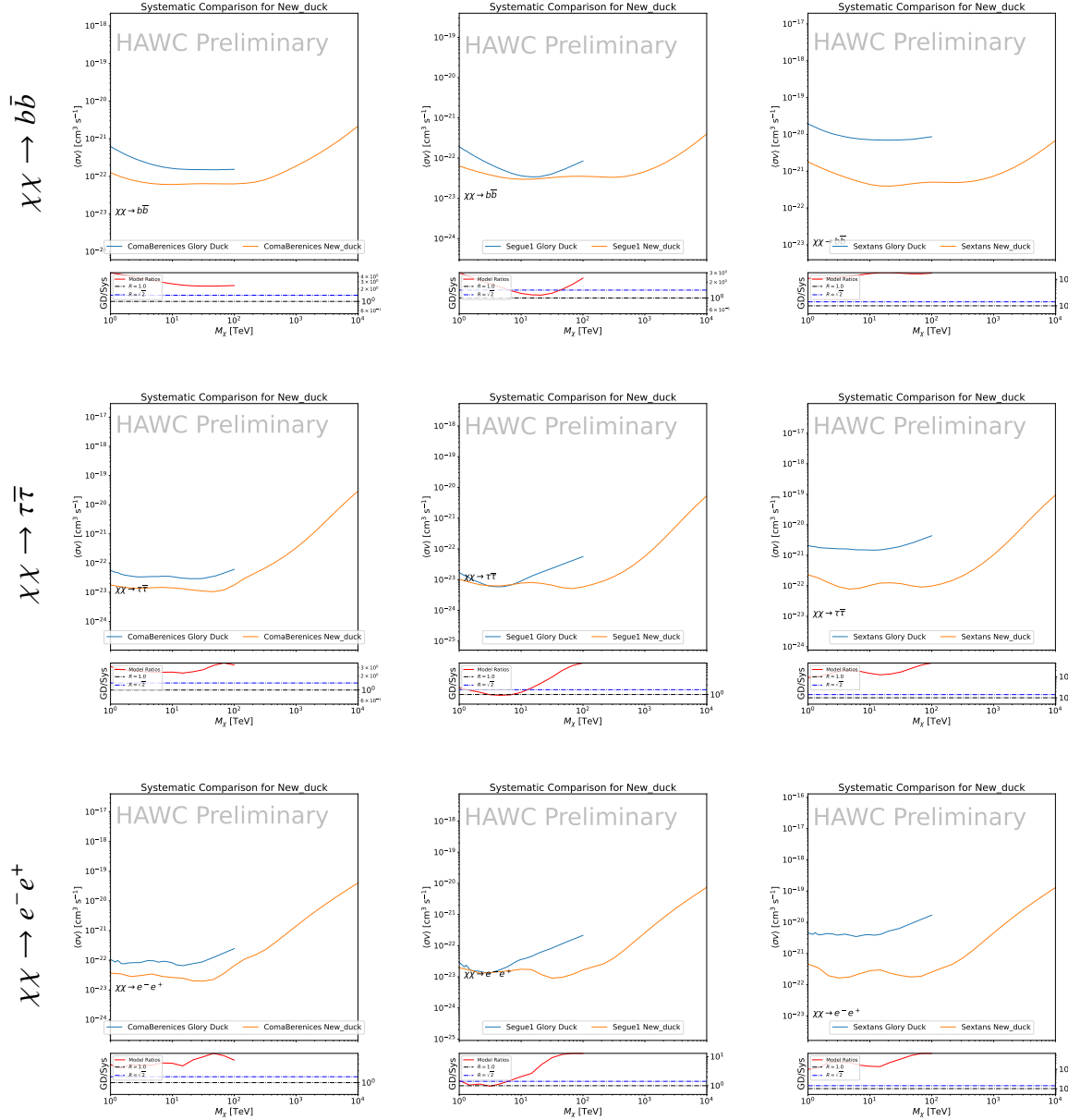


Figure 6.11 Comparison of HAWC limits from this analysis to Glory Duck (Fig. 5.5) for 3 dSphs and 3 DM annihilation channels: $b\bar{b}$, $\tau\bar{\tau}$, and e^-e^+ . Each sector shows the 95% confidence limit from Glory Duck (blue line) and this analysis (orange line) in the top plot. The lower plot features the ratio in log scale of Glory Duck to this analysis in a red solid line. Horizontal dashed lines are for ratios of 1.0 (black) and $\sqrt{2}$ (blue). Ratios larger than 1.0 are for limits smaller, or stricter, than Glory Duck. Ratios larger than $\sqrt{2}$ indicates limits are stricter than a simple doubling of the Glory Duck data.

CHAPTER 7

1446 HEAVY DARK MATTER ANNIHILATION SEARCH WITH ICECUBE'S NORTH SKY 1447 TRACK DATA

1448 7.1 Introduction

1449 Neutrinos are another astrophysical messenger than can travel long distances without significant
1450 attenuation or deflection. Uniquely, they interact less readily than photons especially above PeV
1451 energies. Neutrinos thereofre provide another window through which we can perform dark matter
1452 searches. Neutrinos come in three flavors which triples the multiplicity of the particles we are
1453 searching for.

1454 The previous Icecube DM annihilation analysis towards dwarf galaxies was performed in 2013
1455 [69]. This is in spite of the potentially crucial sensitivity afforded from neutrino spectral lines [70].
1456 A lot has changed in IceCube since its previous DM annihilation search such as, additional strings,
1457 more sophisticated analysis methods, and more accurate theory modeling. It has come time for
1458 IceCube to make a DM dSph contribution.

1459 As I have shown previously in Sec. 5 and Sec. 6, we can build a fast and robust analysis
1460 that shares tools with the field. The hope being that IceCube can eventually combine data with
1461 gamma-ray observatories.

1462 IceCube is sensitive to annihilating DM to the DM ranges above 1 TeV and can produce
1463 competitive results relative to gamma-ray observatories in spectral models that produce sharp
1464 neutrino features. The goal of this analysis is to perform a DM annihilation search using the
1465 Northern Sky Tracks datasets. The search will only be towards dwarf spheroidal galaxies (dSph)
1466 for the strengths mentioned in Section 5.3.3. These sources are treated as point sources for IceCube
1467 with little loss to sensitivity or model dependence on how the DM is distributed. DM masses from
1468 500 GeV to 100 PeV are considered for this analysis. Several DM annihilation channels available
1469 from the HDMspectra are studied in this analysis. This chapter presents the analysis work for IC3
1470 for DM searches toward dSphs.

1471 **7.2 Dataset and Background**

1472 This section enumerates the data and background methods used for IceCube's study of dSphs.

1473 Section 7.2.1 and Section 7.2.2 are most useful for fellow IceCube collaborators looking to replicate

1474 this analysis.

1475 **7.2.1 Itemized IceCube files**

1476 These files are only available withing IceCube's internal documentation and collaborators. They

1477 are not meant for public access, and are presented here so that IceCube collaborators can reproduce

1478 results accurately.

1479 • Software Environment: CVMFS Py3-v4.1.1

1480 • Data Sample: Northern Tracks NY86v5p1

1481 • Analysis Software: csky ([nu_dark_matter](#))

1482 • Analysis wiki: https://wiki.icecube.wisc.edu/index.php/Dark_Matter_Annihilation_Search_towards_dwarf_spheroidals_with_NST_and_DNN_Cascades

1484 • Project repository

1485 **7.2.2 Software Tools and Development**

1486 This analysis was performed inside IceCube's CVMFS (3.4.1.1) software environment using

1487 csky for likelihood calculations. Csky at first did not come with dark matter spectral models

1488 nor could accomodate custom flux models. We developed these capacities for single source and

1489 stacked source studies for this analysis. The analysis code is held in a separate repository from

1490 csky. The [nu_dark_matter branch of csky](#) manages the input of custom dark matter spectra and

1491 accompanied DM astrophysical source then calculates likelihoods with a selected data sample. The

1492 [IceCube Dark Matter dSph repository](#) manages the generation of spectral models for neutrinos,

1493 physics parameter extraction from n_{sig} , J -factor per source inputs, and bookkeeping for the large

1494 parameter space. The project repository required a secondary software environment for neutrino

1495 oscillations. How to launch and run those calculations are documented in the project repository
1496 and the Docker image is additionally saved in Section C.1

1497 7.2.3 Data Set and Background Description

1498 For this analysis, I use the Northern Sky Tracks (NST) Sample (Version V005-P01). The sample
1499 contains up-going track-like events, usually from ν_μ and ν_τ with a superior angular resolution
1500 compared to the cascade dataset. This sample covers 10.4 years of data (IC86_2011-2021). The
1501 accepted neutrino energy range used for the analysis is unique from most other IceCube searches
1502 because DM spectra are hard with large contributions close to $E_\nu = m_\chi$. Therefore the sampled
1503 energy range is $1 < \log(E_\nu/\text{GeV}) < 9.51$ with step size 0.125.

1504 The strength of a dwarf analysis is that there is no additional background consideration beyond
1505 nominal, baseline background estimations (see Section 5.2.3). For NST, the nominal contribu-
1506 tion comes from atmospheric neutrinos and isotropic astrophysical neutrinos. We estimate the
1507 background by scrambling NST data along Right Ascension.

1508 7.3 Analysis

1509 The expected differential neutrino flux from DM-DM annihilation to standard model particles,
1510 $d\Phi_\nu/dE_\nu$, over solid angle, Ω is described by the familiar equation.

$$\frac{d\Phi_\nu}{dE_\nu} = \frac{\langle\sigma v\rangle}{8\pi m_\chi^2} \frac{dN_\nu}{dE_\nu} \times \int_{\text{source}} d\Omega \int_{l.o.s} \rho_\chi^2 dl(r, \theta') \quad (7.1)$$

1511 This is identical to past examples, Eq. (7.1) except that there are 3 neutrino flavors, so there are a
1512 corresponding 3 flux equations. Section 5.3 has a complete description of each term in Eq. (7.1).
1513 Additionally, neutrinos oscillate between flavors which needs to be considered for the expected
1514 neutrino flux at Earth. Section 7.3.1 presents the particle physics model and processing for DM
1515 annihilation. Section 7.3.2 presents the spatial distributions built for each dSph.

1516 7.3.1 $\frac{dN_\nu}{dE_\nu}$ - Particle Physics Component

1517 Neutrino spectra from heavy dark matter annihilation were generated using HDMSSpectra [65]
1518 and χ arrov [71]. HDMSSpectra has tables for the decay and annihilation of heavy dark matter
1519 for different dark matter masses and SM primary annihilation channels. The simulation includes

1520 electroweak radiative corrections and higher order loop corrections with quarks. This publication
1521 also pushes the simulated DM mass to the Plank scale (1 EeV), however this study will not explore
1522 that high.

1523 An important feature in the spectra is that neutrino line channels will be accompanied with
1524 a low energy tail [65]. Thus the earth will not fully attenuate a heavy DM line-like signal from
1525 high declination sources where the neutrino flux must first traverse through the Earth. The DM
1526 annihilation channels that feature lines include all leptonic channels. ($\nu_{e,\mu,\tau}$, e , μ , and τ) We use the
1527 `Xarov` software to propagate and oscillate the neutrinos from the source to Earth. Because these
1528 sources are quite large in absolute terms, and also far (order 10 kpc or more), the resulting flavor
1529 spectra are the averages of the transition probabilities [71]:

$$P(\nu_\alpha \rightarrow \nu_\beta) \approx \begin{bmatrix} 0.55 & 0.18 & 0.27 \\ 0.18 & 0.44 & 0.38 \\ 0.27 & 0.38 & 0.35 \end{bmatrix} \quad (7.2)$$

1530 Examples of the spectra before and after propagation are shown in Fig. 7.1.

1531 When calculating the expected contribution to n_s , only ν_μ , ν_τ are considered as NST's effective
1532 area to ν_e is negligible [72]. Therefore the expected composite neutrino spectrum is sum of the two
1533 flavors: $\nu_\mu + \nu_\tau$. The spectral tables are then converted to splines to condense information, enable
1534 random sampling of the spectra, and reduce computing times. The spectral splines are finally
1535 implemented as a DM class in csky.

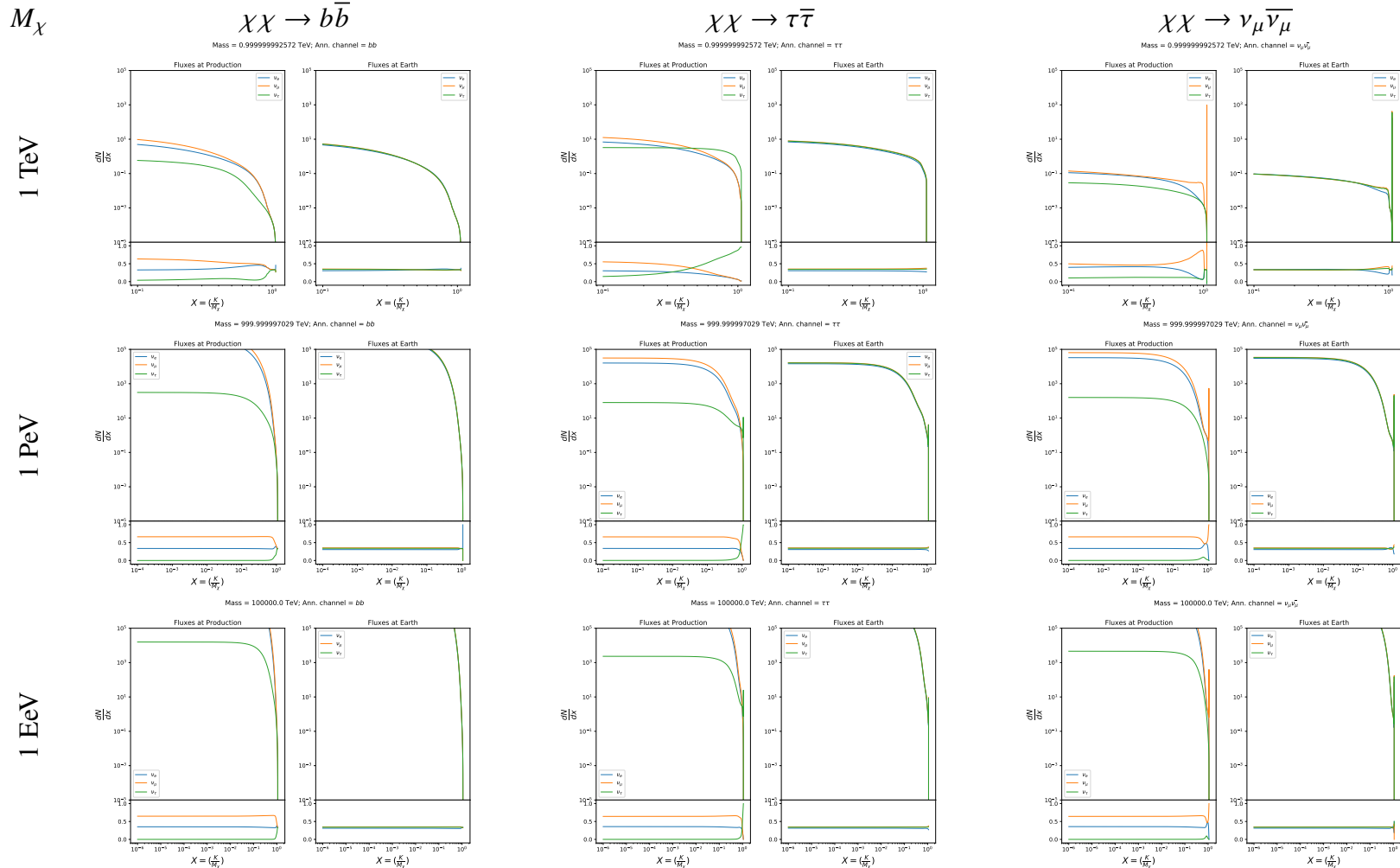


Figure 7.1 Neutrino spectra at production (left panels) and after oscillation at Earth (right panels). Blue, orange, and green lines are the ν_e , ν_μ , and ν_τ spectra respectively. Top panels show the spectra in $\frac{dN}{dE}$. Lower panels plot the flavor ratio to $\nu_e + \nu_\mu + \nu_\tau$. SM annihilation channels $b\bar{b}$, $\tau\bar{\tau}$, and $\nu_\mu\bar{\nu}_\mu$ are shown for $M_\chi = 1$ PeV, TeV, and EeV.

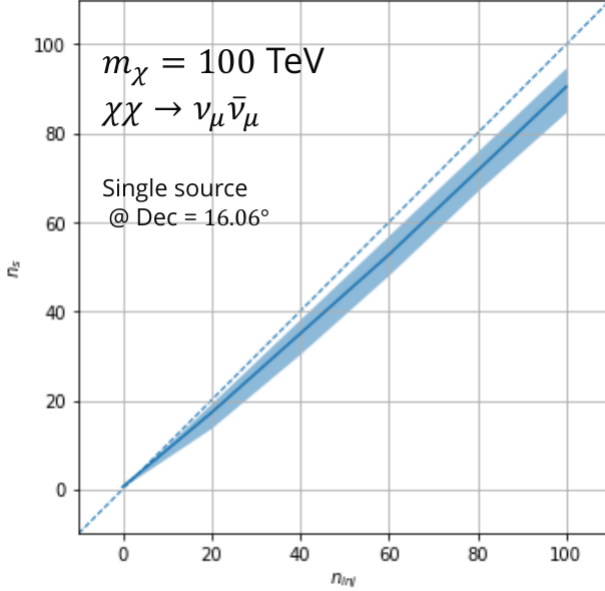


Figure 7.2 Signal recovery for 100 TeV DM annihilation into $\nu_\mu \bar{\nu}_\mu$ for a source at Dec = 16.06°. n_{inj} is the number of injected signal events in simulation. n_s is the number of reconstructed signal events from the simulation. Although the uncertainties are small and tight, the reconstructed n_s are systematically underestimated.

1536 7.3.1.1 Treatment of Neutrino Line Features

1537 All DM annihilation channels into leptons $\chi\chi \rightarrow [\nu_{e,\mu,\tau}, e, \mu, \tau]$ develop a prominent and
 1538 narrow spectral line feature. For all neutrino flavors, this line is visible and prominent in all m_χ
 1539 studied in this analysis. For charged leptons, the feature only really shows up at the larger DM mass
 1540 models and varies between the flavors. Examples for lines in the annihilation spectra with neutrinos
 1541 or charged leptons primary annihilation products are provided in Fig. 7.1.

1542 The neutrino line feature is so narrow relative the sampled energy range that the random
 1543 sampling of the spectra and likelihood fitting rarely capture the line in computation. As a result,
 1544 often the best fit to simulation of background will always floor to TS = 0 and the signal recovery
 1545 systematically underestimates the signal (see Fig. 7.2).

1546 To remedy this, a similar approach to the IceCube's decay analysis [73]. Two smoothing
 1547 kernels were tested (Gaussian, uniform) to widen the line feature. The widths were tuned such that
 1548 the signal recovery approached unity for DM mass 100 TeV to 1 PeV for a source at Segue 1's
 1549 declination, 16.06°. Near horizon was chosen in order to isolate loss in signal recovery from too
 1550 narrow a line versus from Earth's attenuation of very high energy neutrinos. The convolution also

needed to as close as possible preserve the integrated counts of neutrinos. The optimized kernel window for all lines is summarized as:

- Guassian kernel with 2σ width = $3.5E-3 \cdot m_\chi$
- Minimum energy included in convolution = $\text{MIN}[0.995 \cdot m_\chi, E(\nu_{\text{line}}) - 4\sigma]$
- Maximum energy included in convolution = $\text{MAX}[1.005 \cdot m_\chi, E(\nu_{\text{line}}) + 4\sigma]$

where $E(\nu_{\text{line}})$ is the neutrino energy where the neutrino line is at the maximum.

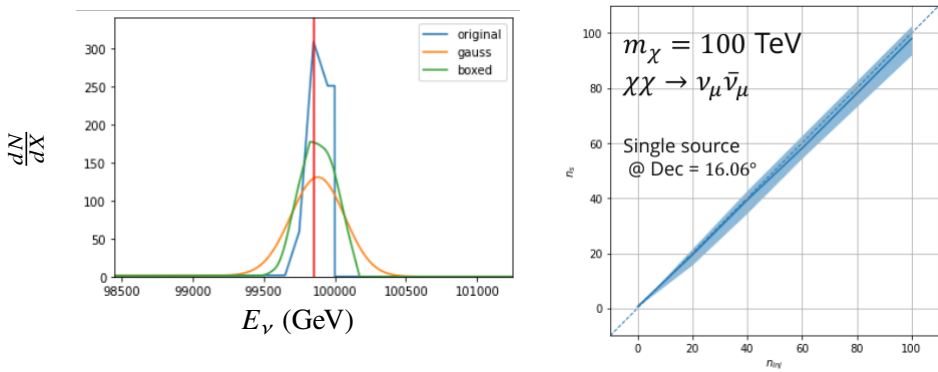


Figure 7.3 Left panel shows the two kernels overlaying the original spectrum from χ aronv after propagation to Earth [71]. The vertical red line indicates where the original neutrino line is maximized. Blue line is the output from χ aronv. Green line is the spectrum after convolution with a flat kernel. Orange line is the spectrum after Gaussian convolution. Right panel shows the signal recovery of the spectral model using the Gaussian kernel with parameters enumerated above.

These parameters broadly improved the signal recovery of the line spectra. An example is in Fig. 7.3. Signal recovery studies for are expanded upon in Section 7.6.

7.3.1.2 Spline Fitting

In an effort to reduce computational work, memory burden, and align with point source methods used for NGC1068 [74], spectral splines were created and adopted for estimating the neutrino flux for the different spectral models. Software was written to generate, book keep, and calculate values on the splines.

When using splines, one has to be careful of the goodness to fit. The spline software used here, Photospline [75], uses the penalized spline technique. Through the penlized technique, poor fits

1566 are penalized according to the accuracy of the nominal value, and the smoothness of the first and
 1567 second derivatives. The B-spline construction however does not penalize on the integral of the fit
 1568 distribution which is critical in low signal studies, such as DM searches. There are additional caveats
 1569 when testing the goodness to fit to the MC generated above for all DM annihilation channels.

- 1570 • The splines must be Log10(*) in Energy and dN/dE to account for the exponential nature of
 1571 the flux.
- 1572 • The fidelity of the fit matters more at $E_\nu \approx m_\chi$ where the model uncertainties are minimal
 1573 and physical considerations (like the cut-off) are most important.
- 1574 • The fidelity of the fit matters less at low E_ν as the model uncertainties are large AND
 1575 IceCube's sensitivity diminishes significantly below 500 GeV.
- 1576 • Total integrated counts should be well preserved.

1577 The resulting cost function was built to evaluate the goodness of spline fits to account for the above
 1578 considerations.

$$e_i = x_i \cdot \left(\frac{dN_i}{dE_i} - 10^{\hat{e}_i} \right) \quad (7.3)$$

1579 Where \hat{e}_i is the spline estimator's value for x_i . $x_i = E_{\nu_i}/m_\chi$. $\frac{dN_i}{dE_i}$ is the flux value from MC. I then
 1580 take the RMS of the error distribution and the resulting value, err, is used to evaluate the fidelity of
 1581 the spectral spline.

$$\text{err} = \sqrt{\frac{1}{x_{\max} - x_{\min}} \int_{x_{\min}}^{x_{\max}} e^2 dx} \quad (7.4)$$

1582 Each SM channel had unique tolerances for 'err'. Channels with very hard cut-offs had looser
 1583 tolerance for err because a significant error would be generated from single counts over/underes-
 1584 timated at the cut-off. Soft channels do not share this issue, so the tolerance is much stricter. All
 1585 annihilation channels from HDM are modeled well below IceCube's NST sensitivity. We do not
 1586 think it is necessary to evaluate the spline fits below 100 GeV [72] and use this value as the default
 1587 lower cut-off. Yet, HDM's model uncertainties at $E_\nu < 10^{-6} \cdot m_\chi$ span an order of magnitude
 1588 [65]. We also choose not to evaluate the splines below this critical value if it is within IceCube's

$\chi\chi \rightarrow$	GOOD	OK	FAIL	Limits of err calc [X_{min}, X_{max}]
$Z^0 Z^0, W^+ W^-$	1.0E-3	1.0E-3, 1.0E-2	1.0E-2	MAX[100GeV/ m_χ , 10^{-6}], 1.0
$t\bar{t}, hh$	1.0E-5	1.0E-5, 1.0E-4	1.0E-4	MAX[100GeV/ m_χ , 10^{-6}], 1.0
$b\bar{b}, d\bar{d}, u\bar{u}$	9.0E-7	9.0E-7, 9.0E-6	9.0E-6	MAX[100GeV/ m_χ , 10^{-6}], 1.0
$\nu\bar{\nu}_{e,\mu,\tau}$	1.0E-3	1.0E-3, 1.0E-2	1.0E-2	MAX[100GeV/ m_χ , 10^{-6}], MIN[0.995, ($E_n(\nu_{line}) - 4\sigma$)/ M_χ]
$e\bar{e}, \mu\bar{\mu}, \tau\bar{\tau}$	1.0E-3	1.0E-3, 1.0E-2	1.0E-2	MAX[100GeV/ m_χ , 10^{-6}], MIN[0.995, ($E_n(\nu_{line}) - 4\sigma$)/ M_χ]

Table 7.1 Spline err tolerances used for input in particle physics component to Eq. (7.1). Column 1 is the DM annihilation channel being fit. Columns 2, 3, and 4 are the tolerances for "GOOD" (pass), "OK" requires inspection, and "FAIL" (tune and refit) respectively. Column 5 has the X ranges over which the error is evaluated. MAX/MIN [·, ·] takes the maximum or minimum of the two enclosed values.

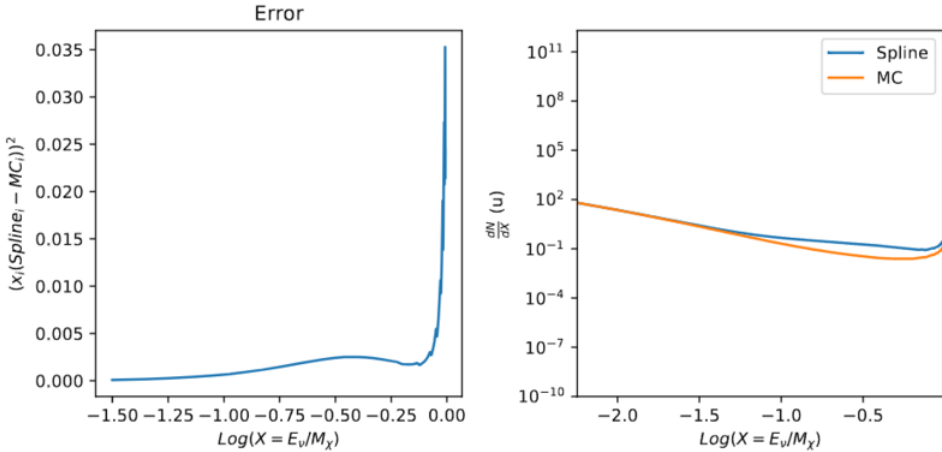


Figure 7.4 Example spline that failed the fit. Failed splines are corrected on a case by case basis unless the SM channel has a systematic problem fitting the splines. In this case, I made a bookkeeping error and loaded the incorrect spectral model

1589 sensitivity. Finally, the smoothing of the spectral lines in leptonic annihilation channels are ignored
 1590 for evaluating the fit. We used the lower limit of the kernel mask as the upper limit of evaluation.
 1591 Table 7.1 summarizes the tolerances for the DM annihilation channels used for this analysis.

1592 The errors are then plotted in two ways. First, FAIL and OK are directly plotted with e_i as a
 1593 function of x, and the full spline and MC. An example of a single failure is provided in Fig. 7.4
 1594 Second, a summary plot of all the splines is plotted and colors coded. Figure C.1 are the spline
 1595 summaries as of writing this thesis. The goal broadly is to eliminate all red and inspect yellow
 1596 statuses.

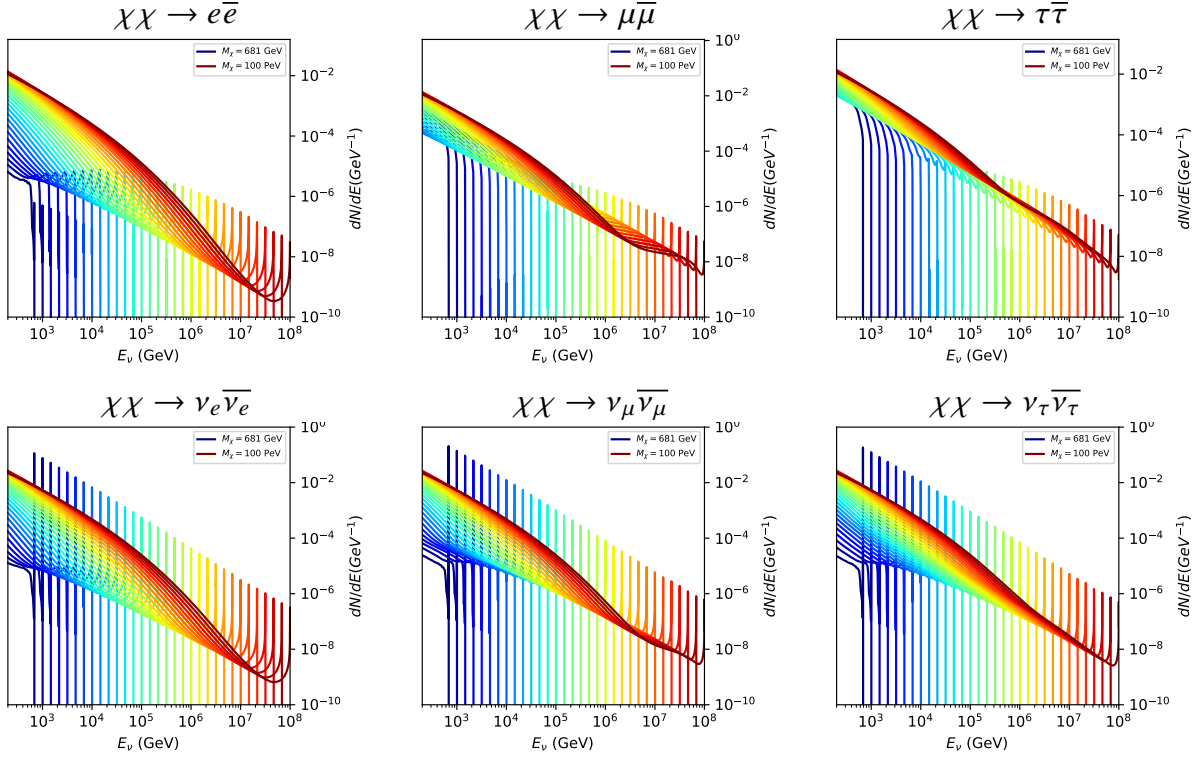


Figure 7.5 Summary of input spectral models that were smoothed with Gaussian kernel. Spectral models are for $\chi\chi \rightarrow e\bar{e}$, $\mu\bar{\mu}\tau\bar{\tau}$, $\nu_e\bar{\nu}_e$, $\nu_\mu\bar{\nu}_\mu$, and $\nu_\tau\bar{\nu}_\tau$. These spectra are the composite ($\nu_\mu + \nu_\tau$) of neutrino flavors. Every spectral model used for this analysis is featured as a colored solid line. Bluer lines are for lower DM mass spectral models. DM masses range from 681 GeV to 100 PeV. HDM [65], χ arov [71], and Photospline [75] are used to generate these spectra. Energy (x-axis) was chosen to roughly represent the energy sensitivity of NST.

1597 The ν_e spectra at Earth are not considered in this analysis, so no work was done to refine the
 1598 spline fits for this flavor. A Final inspection of the splines by eye to verify that the spline fitting did
 1599 not introduce spurious features into the distribution that would corrupt the likelihood fitting.

1600 **7.3.1.3 Composite Neutrino Spectra**

1601 With all of the previously mentioned pieces, we are ready to fully assemble a comprehensive
 1602 description of the particle physics term dN/dE in Eq. (7.1).

$$\frac{dN_\nu}{dE_{\nu_\oplus}} = \left(\frac{dN_{\nu_e}}{dE_{\nu_e}} + \frac{dN_{\nu_\mu}}{dE_{\nu_\mu}} + \frac{dN_{\nu_\tau}}{dE_{\nu_\tau}} \right)_{\text{src}} \cdot \mathbf{P}(\nu_\alpha \rightarrow \nu_\beta) \quad (7.5)$$

1603 Figure 7.5 shows the spectral models that required Gaussian smoothing, the leptonic annihilation
 1604 channels. The remaining models where the only processing was spline fitting are documented in
 1605 Section C.3. Notice that the different neutrino flavors are unique, especially in their low energy

1606 tails. Therefore, this analysis will be sensitive to DM annihilating to the distinct neutrino flavors.

1607 **7.3.2 *J*- Astrophysical Component**

1608 For this analysis, we re-adopt the \mathcal{GS} model used in Sec. 5 for dSph from [45]. These
1609 models are based on a modified Navarro-Frenk-White (NFW) profile where the indices of the NFW
1610 (traditionally 1,3,1) are allowed to float. The angular width of these sources is much smaller than
1611 the angular resolution of IceCube NST [74]. We therefore treat these sources as point sources in
1612 this analysis, and forgo generating maps. These sources and the \mathcal{GS} model have already been
1613 discussed at length in Section 5.3.2 and is not repeated here. IceCube uses identical sources to
1614 Tab. 5.1 except we analyze source with declinations above 0.0 degrees.

1615 **7.3.3 Source Selection and Annihilation Channels**

1616 We use all of the dSphs presented in IceCube’s previous dSph DM search [69]. IceCube’s
1617 sources for these simulation studies include Bootes I, Canes Venatici I, Canes Venatici II, Coma
1618 Berenices, Draco, Hercules, Leo I, Leo II, Leo V, Leo T, Segue 1, Segue 2, Ursa Major I, Ursa
1619 Major II, and Ursa Minor. A full description of all sources used is in Table 5.1. Sources with
1620 declinations less than 0.0 are excluded from this analysis.

1621 This analysis improves on the previous IceCube dSph paper [69] in the following ways. Pre-
1622 viously, the IceCube detector was not yet completed to the 86 string configuration. Many more
1623 dSphs will be observed, from 4 to 15. Previously, the particle physics model used for neutrino-ray
1624 spectra from DM annihilation did not have EW corrections where they are now included [65]. The
1625 spectral models also predict substantial differences between the neutrino flavors, so this analysis
1626 will be the first DM dwarf analysis to discriminate between primary neutrino flavors. The study
1627 performed here studies 10.4 years of data.

1628 The SM annihilation channels probed for this study include $\chi\chi \rightarrow$

1629 $b\bar{b}, t\bar{t}, u\bar{u}, d\bar{d}, e\bar{e}, \mu\bar{\mu}, \tau\bar{\tau}, ZZ, W^+W^-, \nu_e\bar{\nu}_e, \nu_\mu\bar{\nu}_\mu$, and $\nu_\tau\bar{\nu}_\tau$

1630 **7.4 Likelihood Methods**

1631 I use the Point-Source search likelihood which is widely used in IceCube analyses. The
1632 likelihood function is defined as the following:

$$L(n_s) = \prod_{i=1}^N \left[\frac{n_s}{N} S_i + \left(1 - \frac{n_s}{N}\right) B_i \right] \quad (7.6)$$

1633 where i is an event index, S and B are the signal PDF and background PDF respectively. For a joint
1634 analysis where the sources are stacked the likelihood is expanded in the simplified way:

$$L(n_s) = \prod_{i=1}^{N_{\text{sources}}} L_i(n_s) \quad (7.7)$$

1635 Where L_i is the likelihood from the i -th source in the stacked analysis. The Test Statistic (TS)
1636 definition remains the same as Eq. (5.7)

1637 **7.5 Background Simulation**

1638 Before we look at data, we must first analyze background and signal injection to validate our
1639 analysis. This is in part because the TS distributions are not expected to behave according to a
1640 chi-squared distribution with 1 degree of freedom. TS distributions can also vary significantly
1641 between DM mass and annihilation models. Therefor, Wilks' theorem may not be applicable to the
1642 analysis. Instead, a critical value is defined from a large number of background trials. We study the
1643 TS distributions first for each source, then for the stacked analysis. The following sections show
1644 the results of the likelihood fitting for a suite of background trials.

1645 I assume that TS values are physical: $\text{TS} \geq 0$. η denotes the fraction of positive TS values
1646 above the threshold and written in the legend of the TS distributions. $\epsilon[x]$ indicate the fraction
1647 of events where $\text{TS} < x$. For TS plots shown here, the decimal values of x are 1.0e-2 and 1.0e-3.
1648 Each subplot represents a simulation of 100,000 data-scrambled background trials. ?? show the
1649 background TS distributions obtained from Segue 1, a source with little Earth attenuation and
1650 large J -factor, and Ursa Major II, similarly large J -fator but significantly more Earth attenuation,
1651 assuming that dark matter annihilates into $b\bar{b}$, $\tau\bar{\tau}$, and $\nu_\mu\bar{\nu}_\mu$. I show the TS distributions of a
1652 stacked study of 15 sources for all DM annihilation channels.

1653 **7.5.1 TS per Source**

1654 Figure 7.6 to Figure 7.11 present the TS distributions for Segue 1 and Ursa Major II for 100,000
1655 trials. More studies for all annihilation channels and remaining 13 sources were also performed
1656 and are documented in IceCube’s internal wiki.

1657 Although it was not expected, almost every distribution produced follows a χ^2 distribution with
1658 1 degree of freedom. This is important for future assumptions made in Sec. 8 and may justify
1659 statistical calculations assuming Wilk’s theorem is valid.

1660 **7.5.2 Stacked TS**

1661 Figure 7.12 to Figure 7.22 present the TS distributions for a stacked study of 15 sources with
1662 \mathcal{GS} J -factors on 100,000 trials. The presentation of these plots are identical to the single source
1663 distributions in Section 7.5.1.

1664 Each subplot, except the final, is the TS distribution for a specific DM mass listed in the subplot.
1665 The final subplot plots the all DM spectral models used as input for the TS distribution calculations
1666 with bluer lines indicating lower DM mass and redder indicating higher DM mass.

1667 **7.6 Signal Recovery**

1668 We also wish to understand how well the analysis is able to reconstruct signal neutrinos. In
1669 order to test this, we inject neutrinos from our spectral models randomly then attempt to discern the
1670 number of signal neutrinos in the data. Figure 7.23 and Figure 7.24 show this study for $\chi\chi \rightarrow b\bar{b}$,
1671 $t\bar{t}$, and $\nu_\mu\bar{\nu}_\mu$ for a stacked analysis of 15 sources. We see that the analysis is conservative at smaller
1672 m_χ , yet improves at larger m_χ . We also see that the uncertainty around the reconstructed signal
1673 events shrinks for the neutrino annihilation spectra.

1674 **7.6.1 Sensitivities**

1675 In IceCube, we usually define the 90% confidence level (CL), as the minimum number of signal
1676 events (n_s) required to have a Type I error rate smaller than 0.5 and Type II error rate of 0.1. We
1677 compute n_s from the following equation

$$n_s = T_{live} \int_0^{\Delta\Omega} d\Omega \int_{E_{min}}^{E_{max}} dE_\nu A_{eff}(\hat{n}, E_\nu) \frac{d\Phi_\nu}{d\Omega dE_\nu}(\hat{n}, E_\nu), \quad (7.8)$$

1678 to extract the sensitivity on the dark matter annihilation cross-section. T_{live} is the detector livetime,
1679 A_{eff} is the effective area of the detector, and $E_{\text{min}}, E_{\text{max}}$ are the minimum, maximum energies of
1680 the expected neutrinos, respectively.

1681 Sensitivities are calculated for each source individually as if they were the only source and as a
1682 stack over 1000 trials. From Eq. (7.8) and Eq. (7.1) we can compute the $\langle \sigma v \rangle$ at a 90% confidence
1683 level. Figure 7.25 and Fig. 7.26 show the sensitivities for some DM annihilation channels. Not
1684 all channels computed successfully in time for the writing of this dissertation. Among channels
1685 missing include two neutrino flavors: e and τ .

1686 7.7 Systematics

1687 Lol What Systematics. Beside signal recovery we don't have many additional studies for here.
1688 The current analysis plan is to compare these sensitivities to another J -factor catalog such as \mathcal{LS}
1689 [66]. Additionally, we set out to perform a standard suite of IceCube systematic studies which
1690 include: **TODO: THE BIG 4: ICE MODEL ETC** The following section enumerates the impact of
1691 the Earth on our hardest neutrino spectra.

1692 7.7.1 Earth Effects

1693 One systematic I check however is the impact of the Earth on our sensitivity to $\chi\chi \rightarrow \nu_\mu \overline{\nu}_\mu$.
1694 This channel is expected to be significantly impacted because it has a significant contribution at
1695 PeV energies for $m_\chi \geq 1\text{PeV}$. The Earth is expected to attenuate these higher energy neutrinos.
1696 However, these neutrino spectra have significant low energy contributions, so we do not expect to
1697 entirely loose our sensitivity. This motivated a study examining our $\langle \sigma v \rangle$ sensitivity over all DM
1698 masses sampled for a selection of declinations.

1699 For this systematic study, I sample 6 DM masses per decade from 1 TeV to 100 PeV. I select
1700 declinations that are shared with sources in the \mathcal{GS} catalog: Bootes I, Canes Venatici II, Leo V,
1701 Ursa Major I, and Ursa Minor. I study a fake source who's J -factor is shared with Ursa Major II,
1702 but who's coordinates belong to the aformentioned list. The sensitivity studies performed for each
1703 source (Fig. 7.26 and **TODO: refer to appendix ns plots**) provided n_s for 1000 trials which we use
1704 as inputs into Eq. (7.8). We derive $\langle \sigma v \rangle$ using $\log_{10} J = 19.42 \log_{10}(\text{GeV}^2\text{cm}^{-5})$ **TODO: refer to**

1705 **figure** shows the results of these calculations.

1706 **TODO:** refer to **fig** shows that we have significant but diminishing sensitivity to source at high
1707 declination. We see in the worse case, the sensitivity at high declination is up to an order of
1708 magnitude worse than at low declination. However, for $m_\chi < 1$ PeV, the sensitivities are very
1709 similar. Their similar sensitivities imply that a stacking analysis with IceCube is most powerful
1710 in the 1 TeV to 1 PeV region. Above 1 PeV, our limits and sensitivities are dominated by sources
1711 near the horizon. When we additionaly consider the J -factors, we expect Segue 1 to dominate
1712 contributions to sensitivity and limits where $m_\chi > 1$ PeV.

1713 **7.8 Conclusions**

1714 We built many things for this analysis. We utilized advanced computing techniques like
1715 parrallel programming and spline fitting of particle physics Monte Carlo to greatly expand and
1716 refine IceCube's sensitivity to DM annihilation from dSphs. We imported updated astrophysical
1717 and particle physics models that better represent what we beleive neutrino signals from DM
1718 annihilation should look like. We, for the first time, build an analysis that is sensitivty to PeV DM
1719 annihilation.

1720 When we compare to previous IceCube publications of dSphs [69], we see an order of magnitude
1721 improvement to our sensitivity. This analysis has been working group approved within IceCube and
1722 has begun the unblinding process. This processes did not complete in time for this dissertation.
1723 Therefor we do not show data for this thesis and is the clear next step.

1724 The test statistic distributions in this analysis also demonstrate more characteristic behaviour
1725 compared to previous DM analyses. With a 10 year dataset, we finally have enough statistics to
1726 almost trivially combine with other photon obervatories, such as HAWC. The first ground work for
1727 a multi-messenger DM search is provided with concluding remarks in Sec. 8.

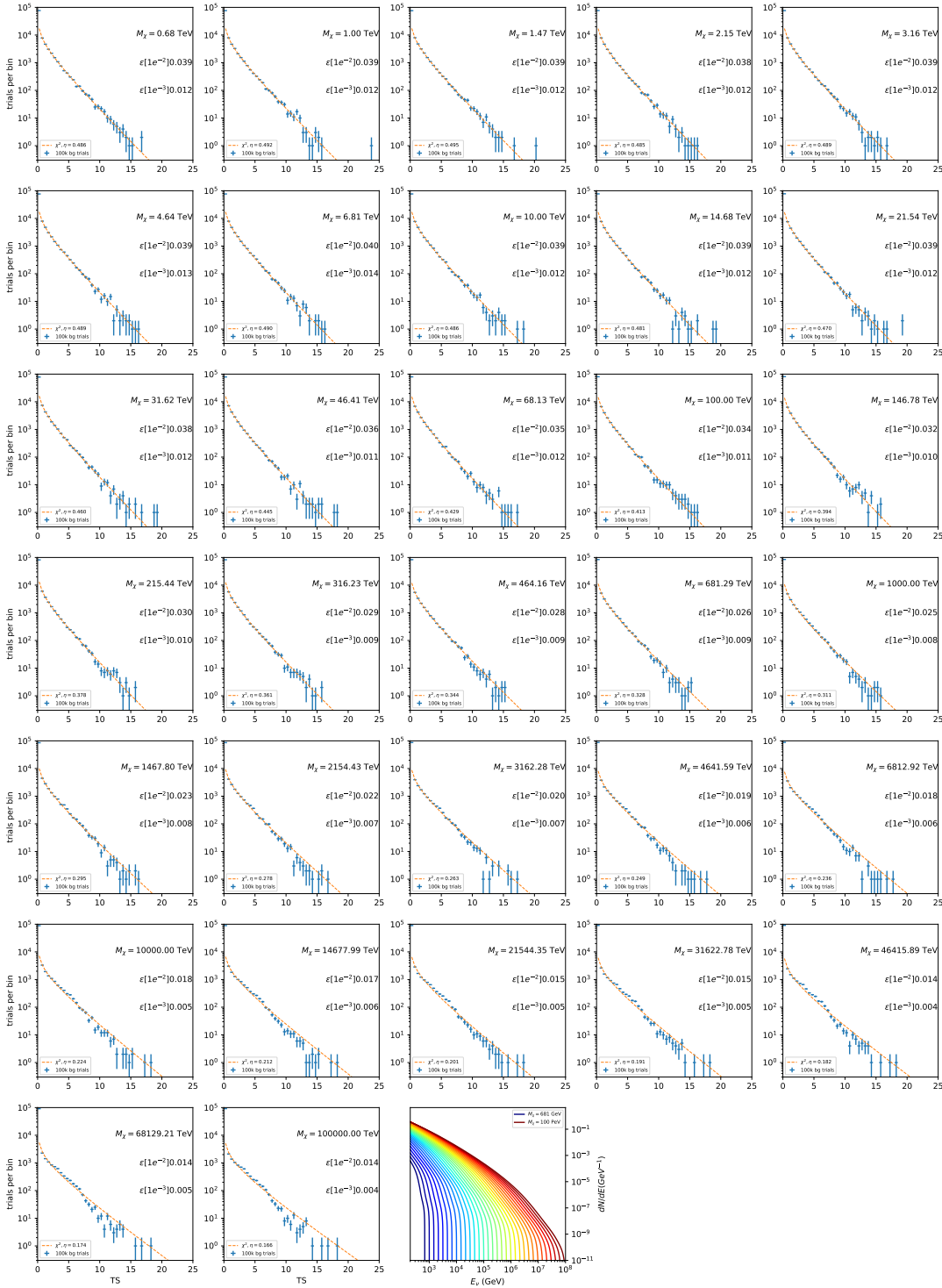


Figure 7.6 Test statistic (TS) distributions for Segue 1 and $\chi\chi \rightarrow b\bar{b}$. Each subplot, except the final, is the TS distribution for a specific DM mass listed in the subplot. Orange dashed lines are the traces for a χ^2 distribution with 1 degree of freedom. $\epsilon[\cdot]$ is the fraction of trials smaller than the bracketed value. The final subplot plots the all DM spectral models, similar to Fig. 7.5, used as input for the TS distributions.

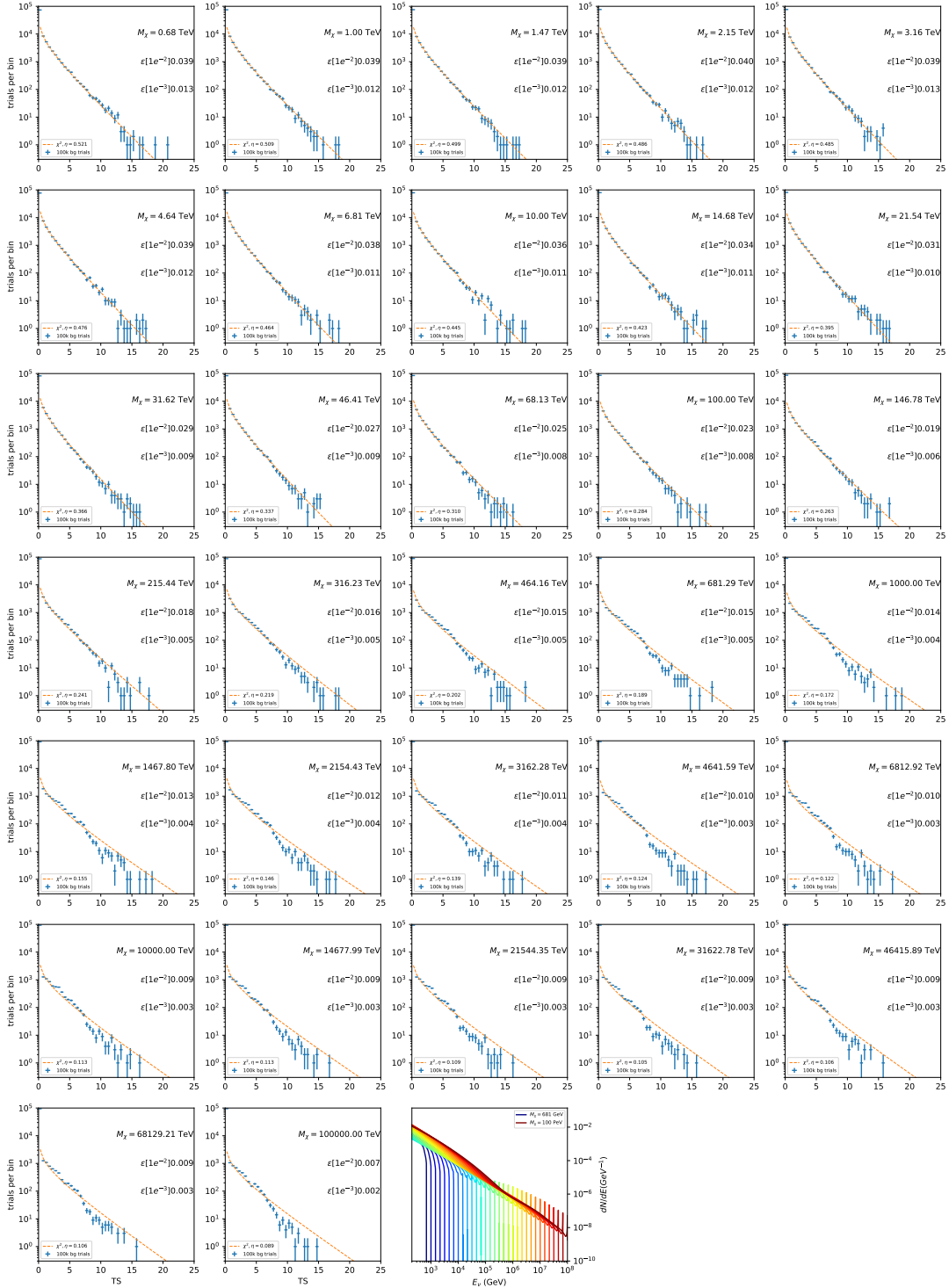


Figure 7.7 Same as Fig. 7.6 for Segue 1 $\chi\chi \rightarrow \tau\bar{\tau}$.

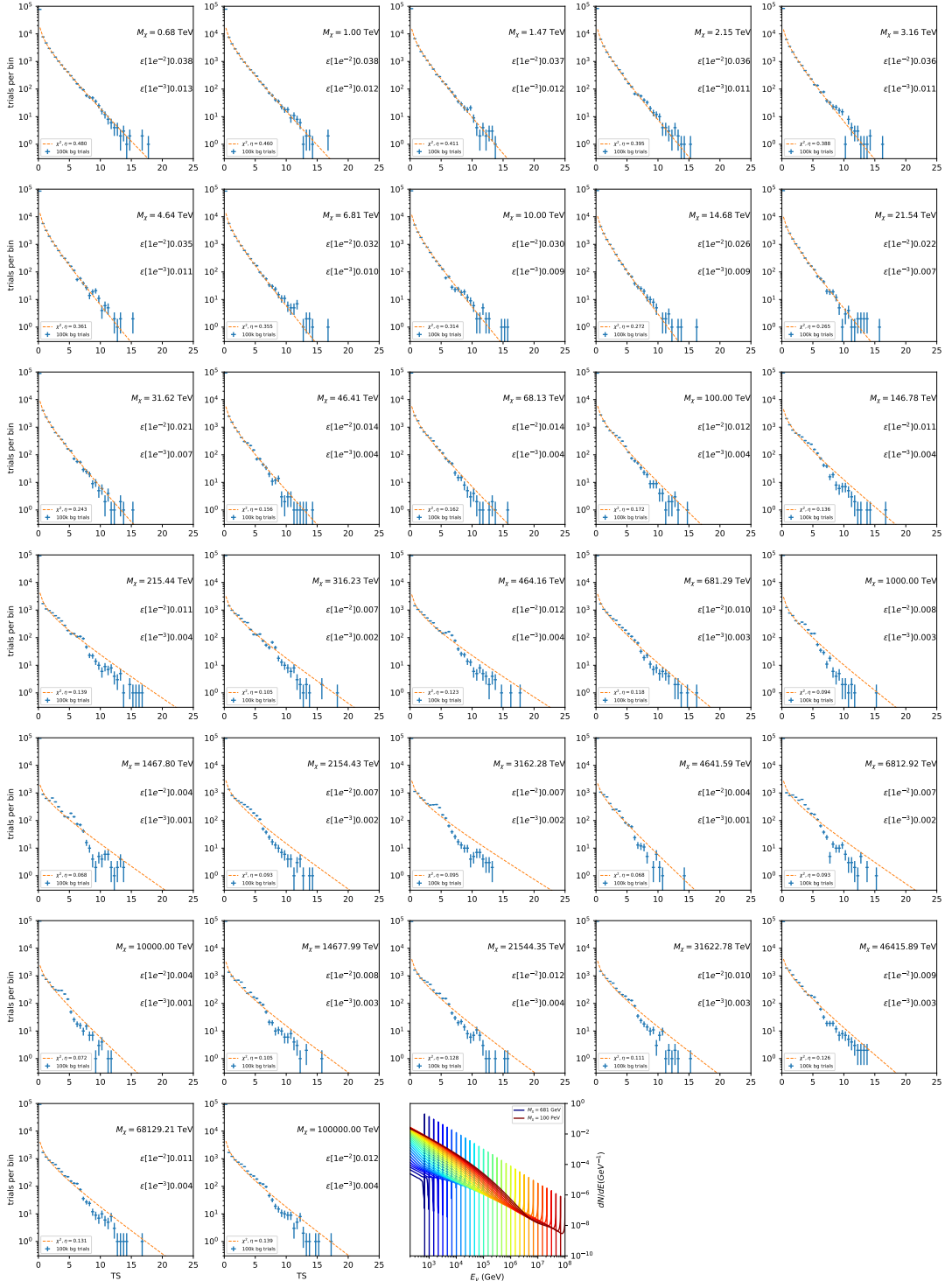


Figure 7.8 Same as Fig. 7.6 for Segue 1 $\chi\chi \rightarrow \nu_\mu \bar{\nu}_\mu$.

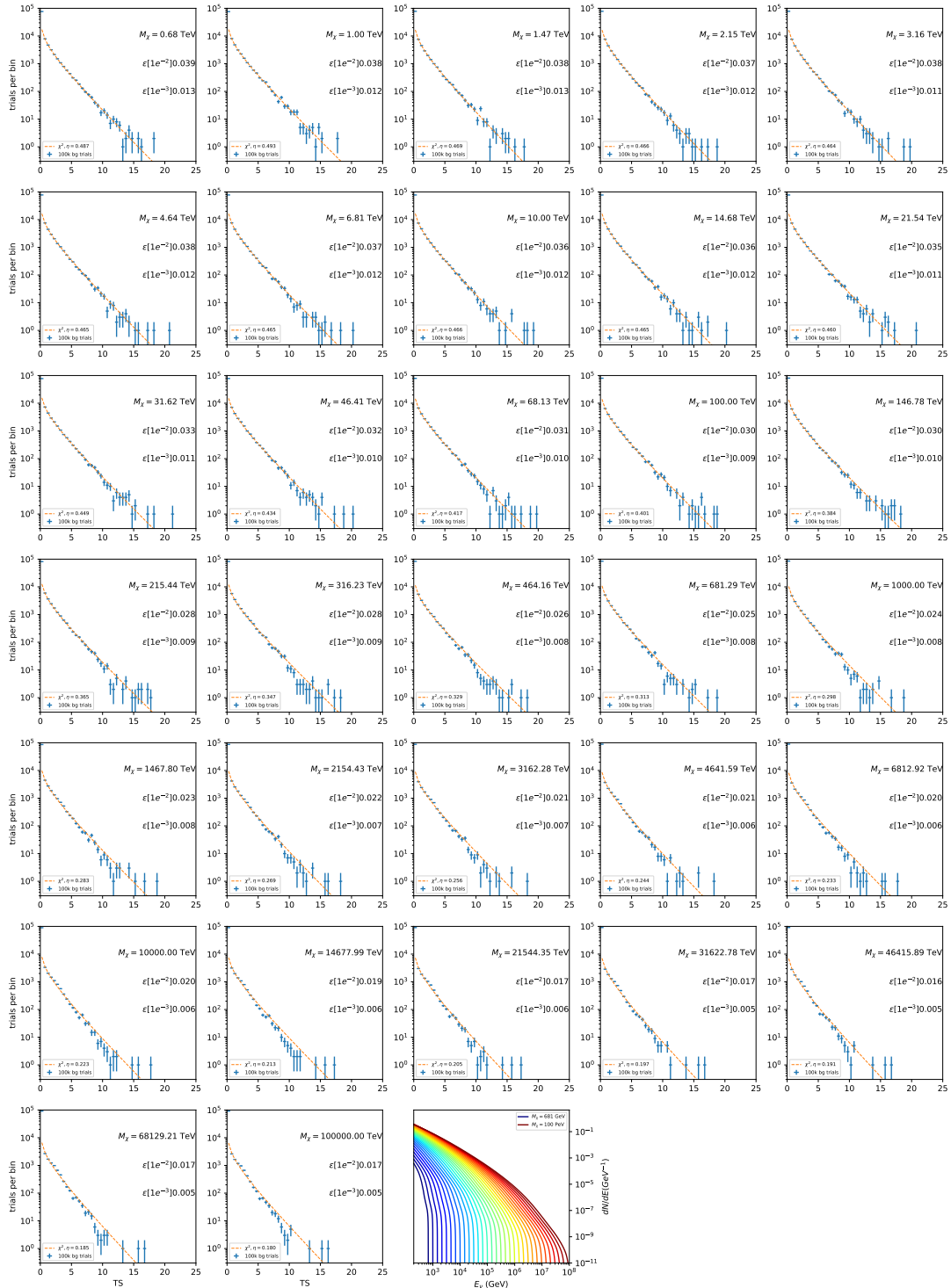


Figure 7.9 Same as Fig. 7.6 for Ursa Major II 1 $\chi\chi \rightarrow b\bar{b}$.

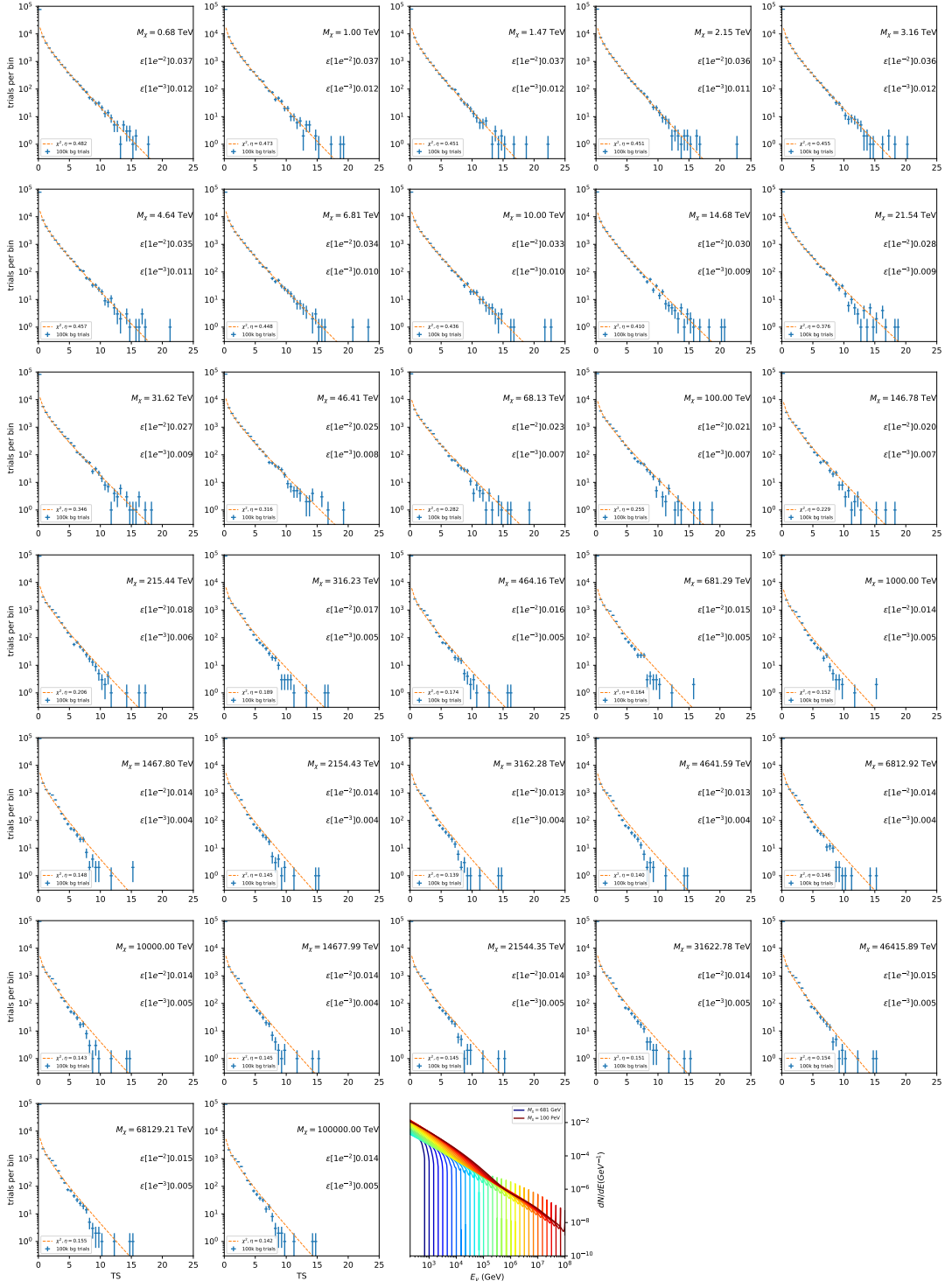


Figure 7.10 Same as Fig. 7.6 for Ursus Major II 1 $\chi\chi \rightarrow \tau\bar{\tau}$.

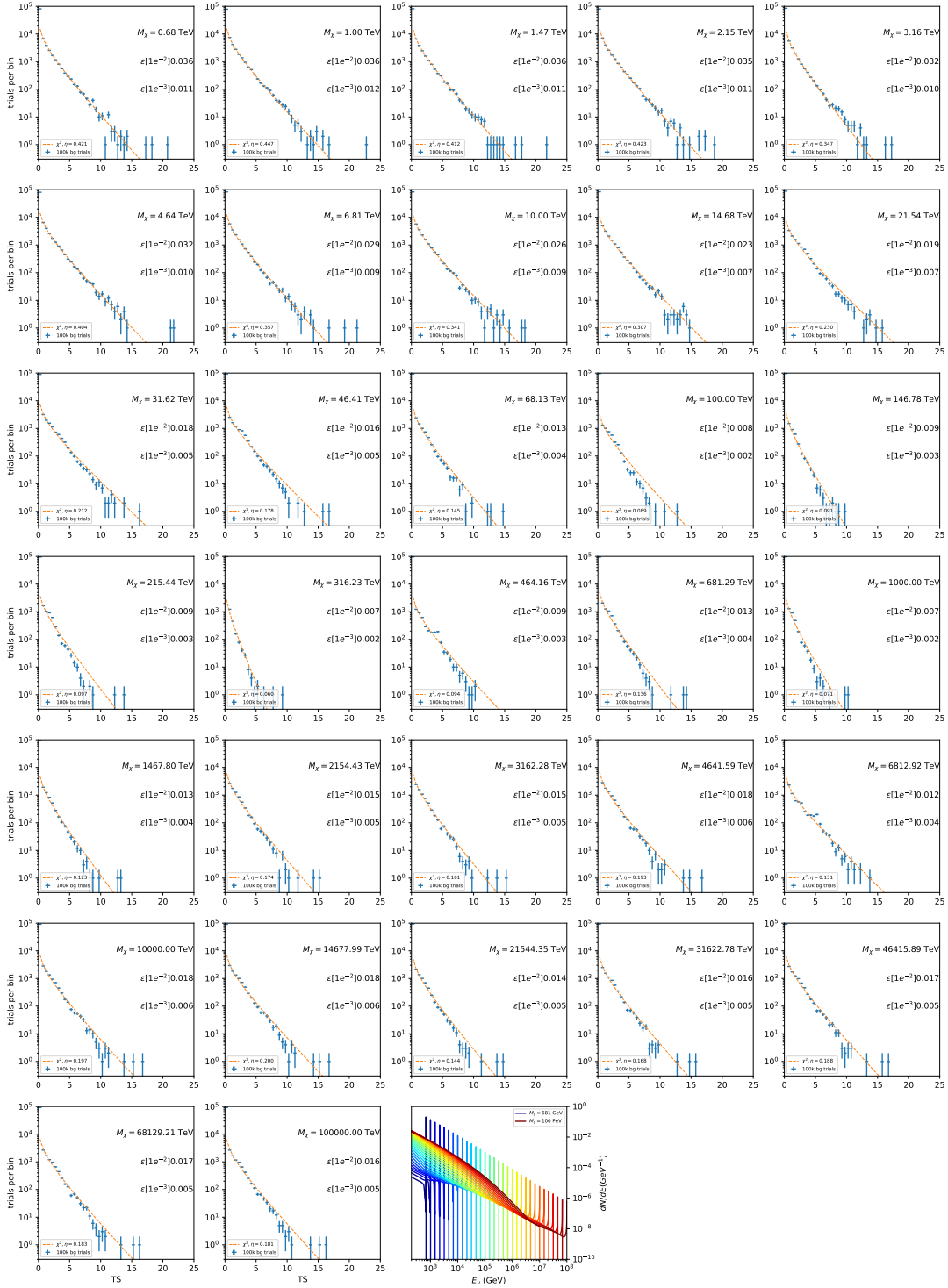


Figure 7.11 Same as Fig. 7.6 for Ursus Major II 1 $\chi\chi \rightarrow \nu_\mu \bar{\nu}_\mu$.

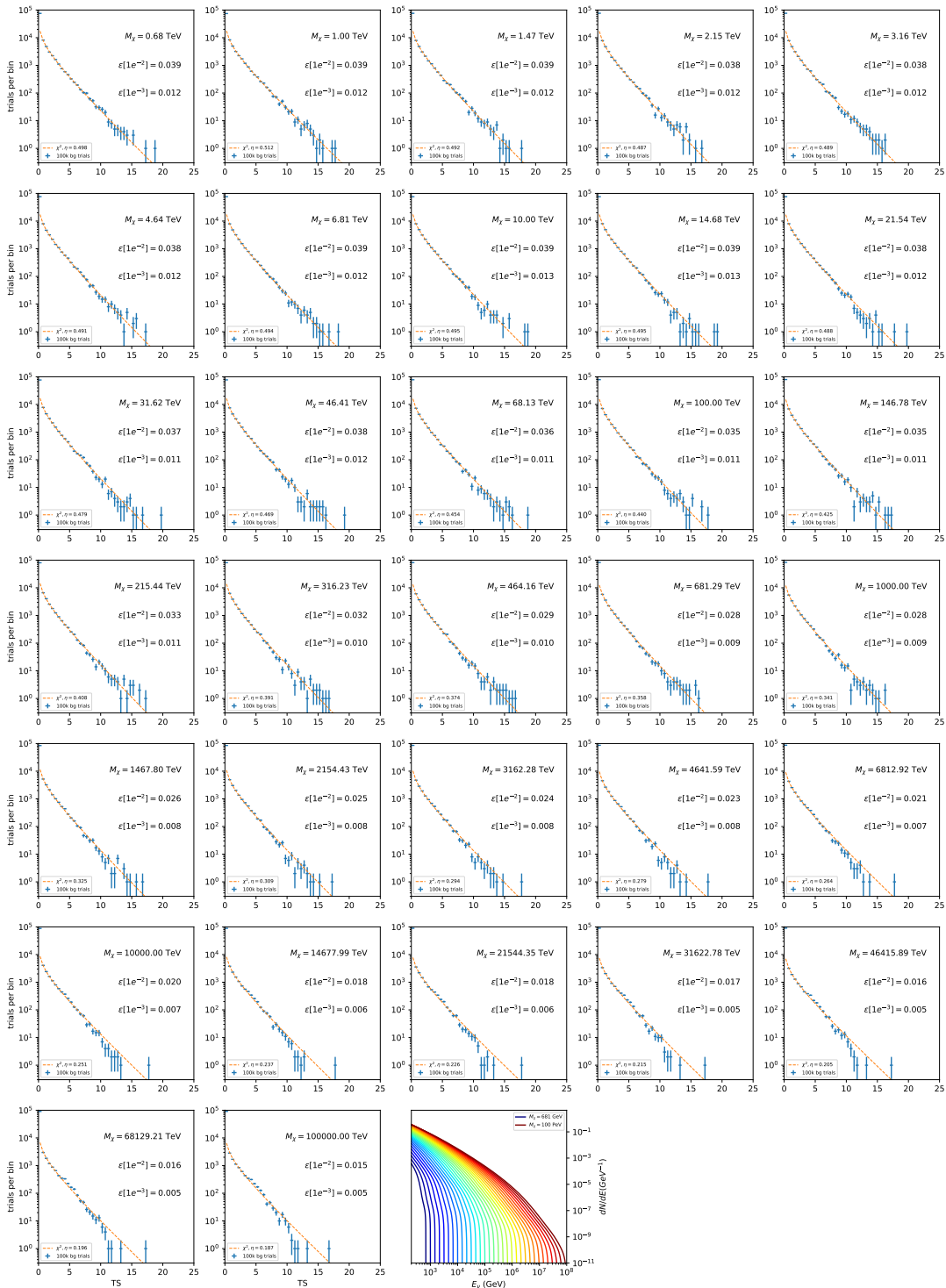


Figure 7.12 Same as Fig. 7.6 for 15, $\mathcal{G}\mathcal{S}$ J-factor, stacked sources and $\chi\chi \rightarrow b\bar{b}$.

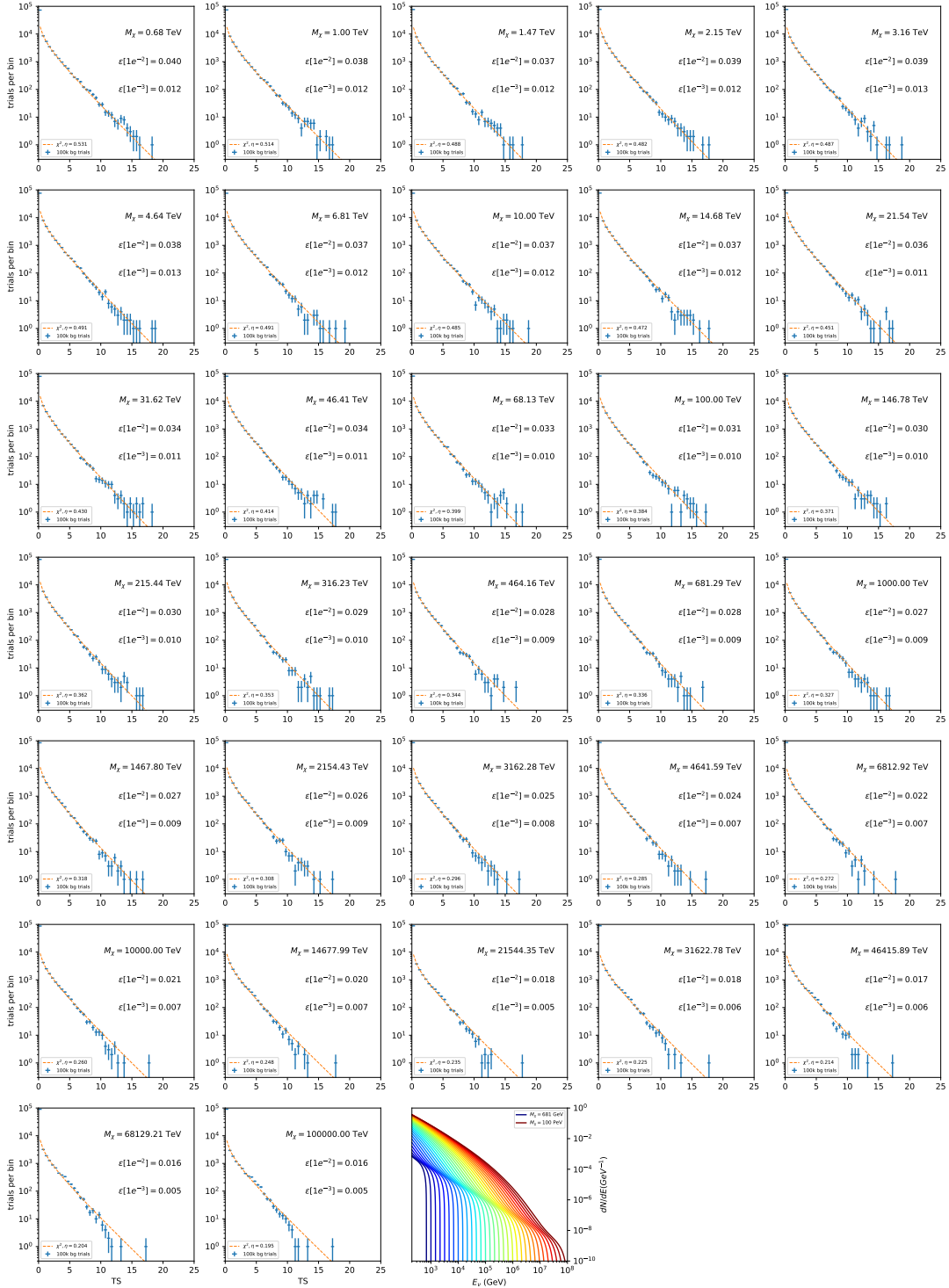


Figure 7.13 Same as Fig. 7.6 for 15, GS J-factor, stacked sources and $\chi\chi \rightarrow t\bar{t}$.

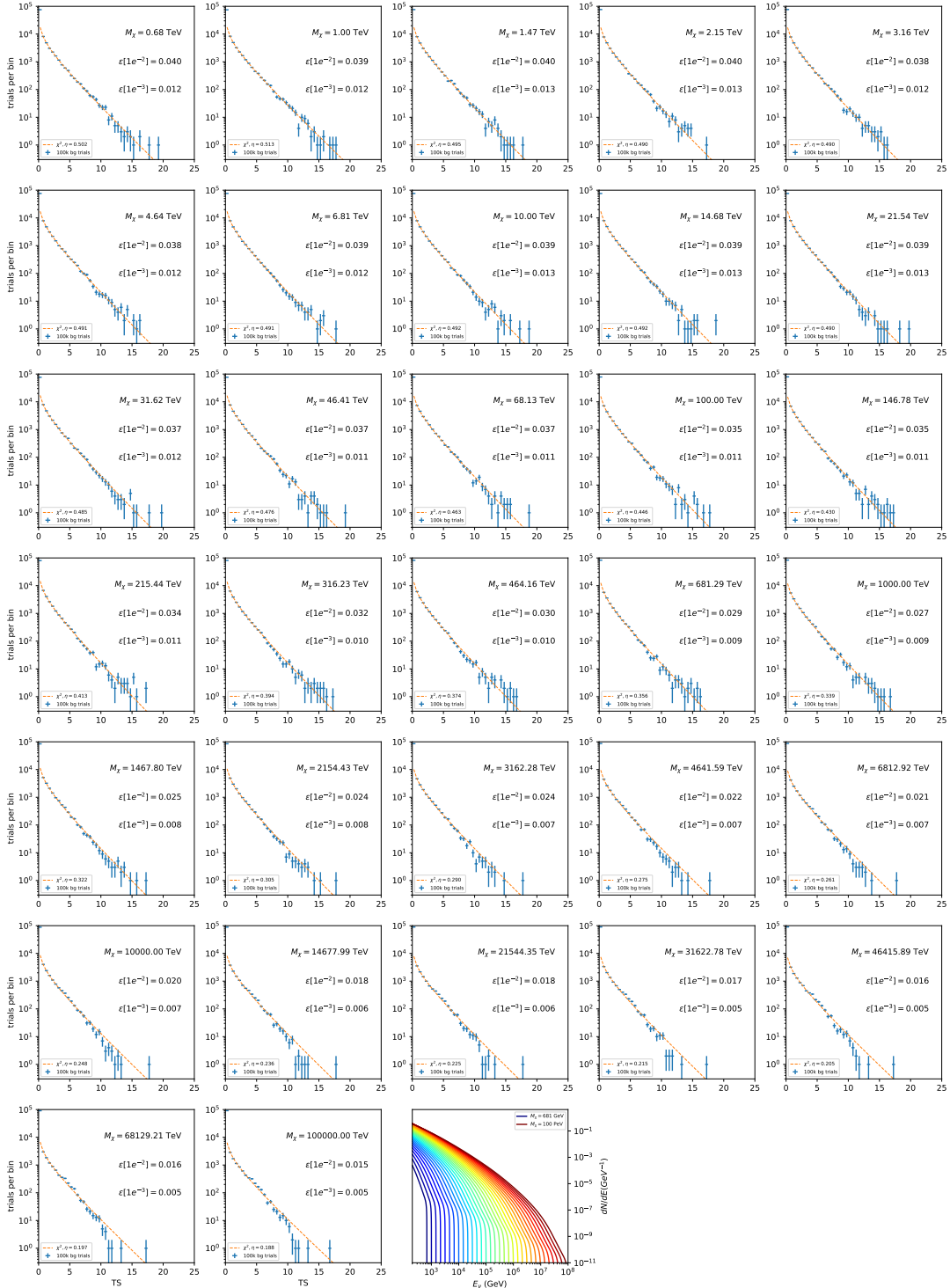


Figure 7.14 Same as Fig. 7.6 for 15, \mathcal{GS} J-factor, stacked sources and $\chi\chi \rightarrow u\bar{u}$.

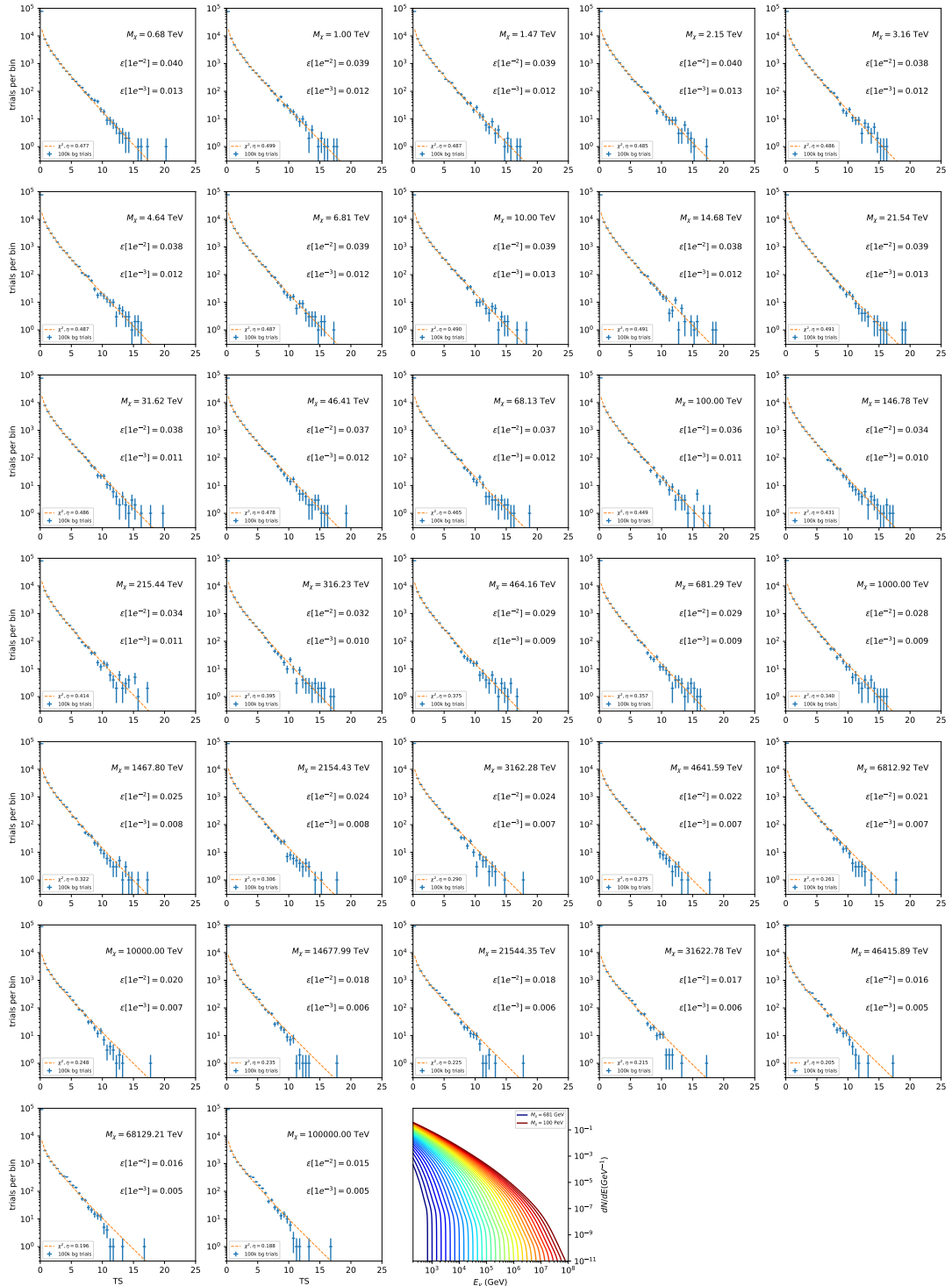


Figure 7.15 Same as Fig. 7.6 for 15, $\mathcal{G}\mathcal{S}$ J-factor, stacked sources and $\chi\chi \rightarrow d\bar{d}$.

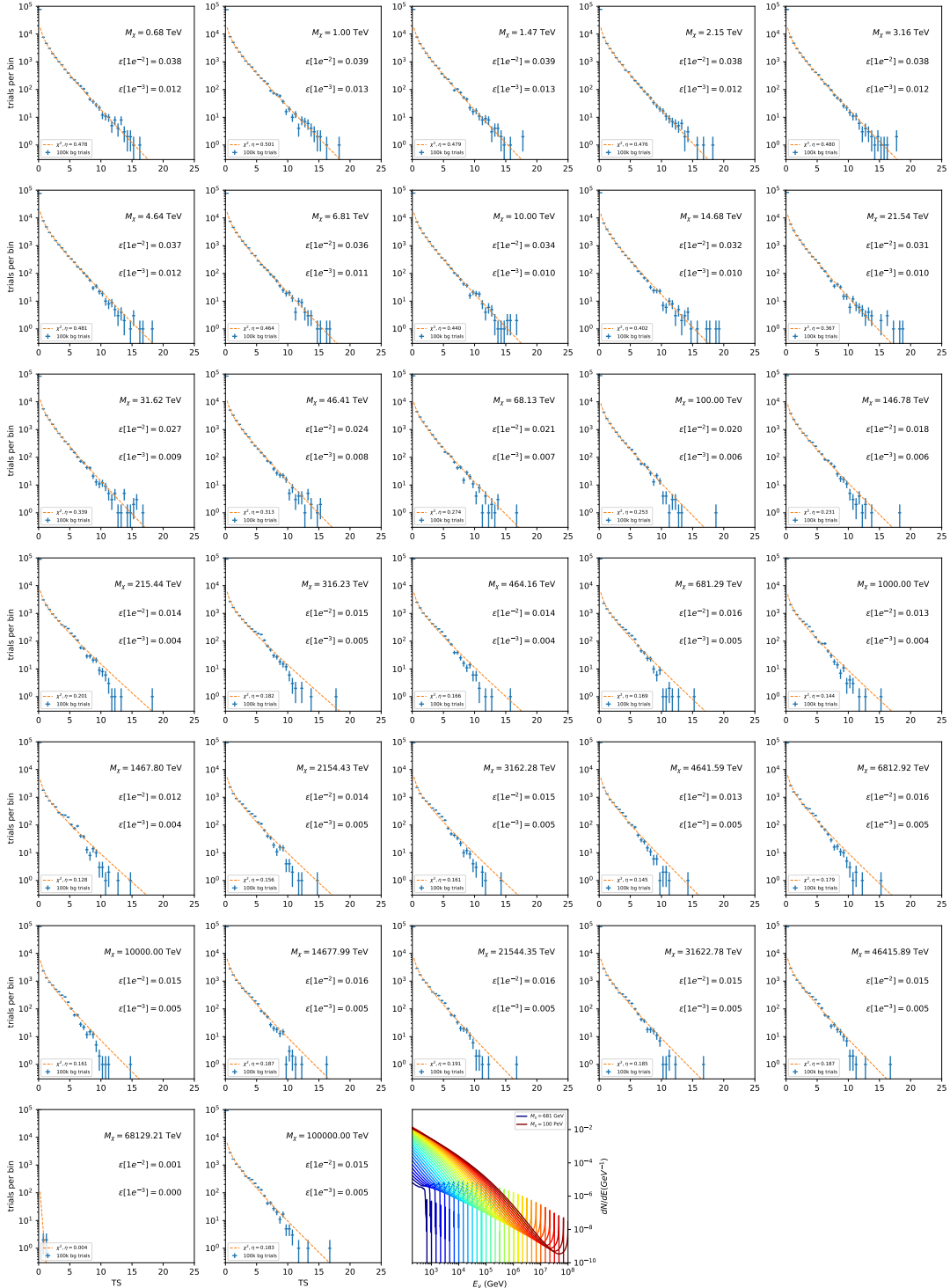


Figure 7.16 Same as Fig. 7.6 for 15, $\mathcal{G}\mathcal{S}$ J-factor, stacked sources and $\chi\chi \rightarrow e\bar{e}$.

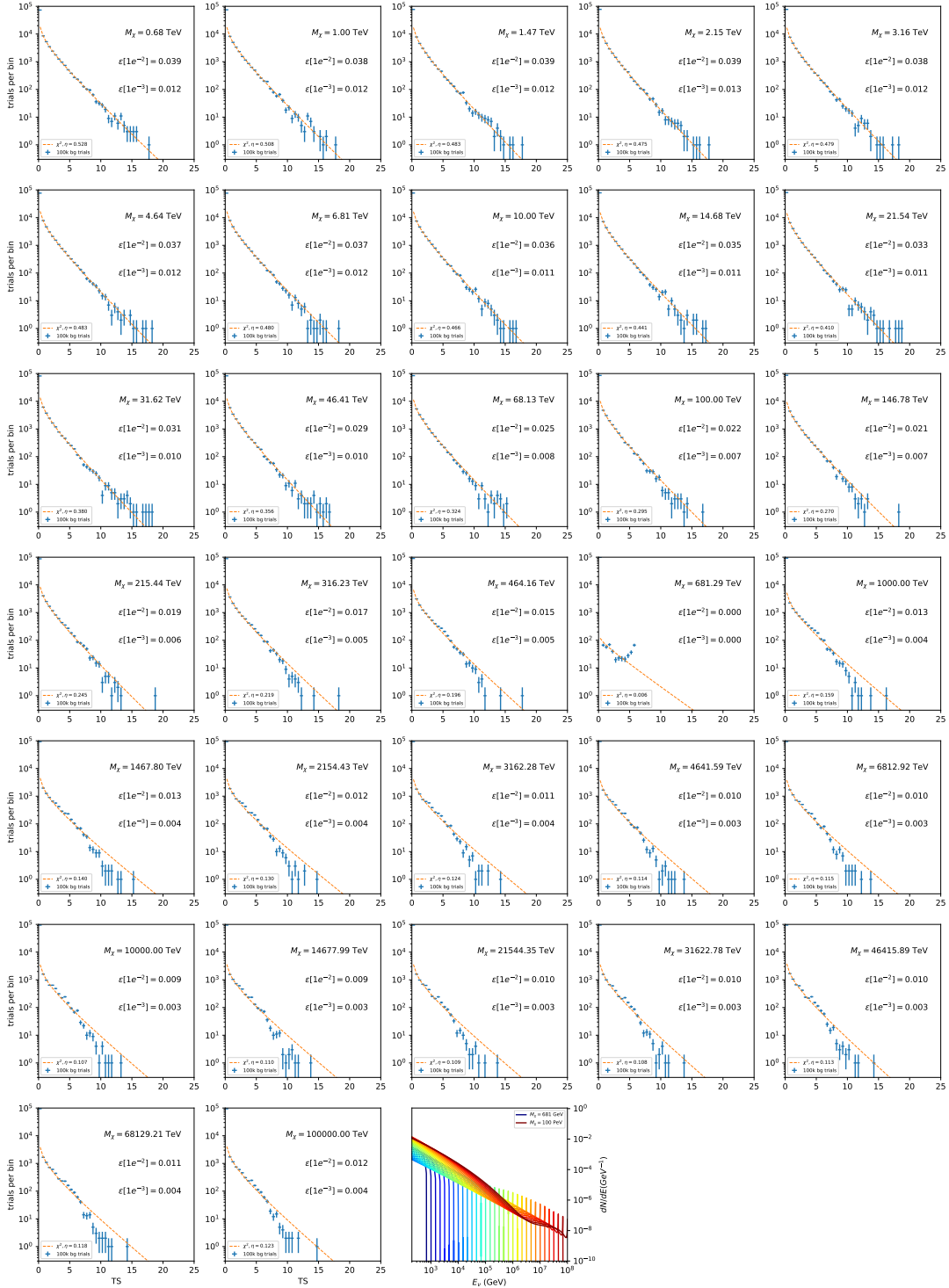


Figure 7.17 Same as Fig. 7.6 for 15, \mathcal{GS} J -factor, stacked sources and $\chi\chi \rightarrow \mu\bar{\mu}$.

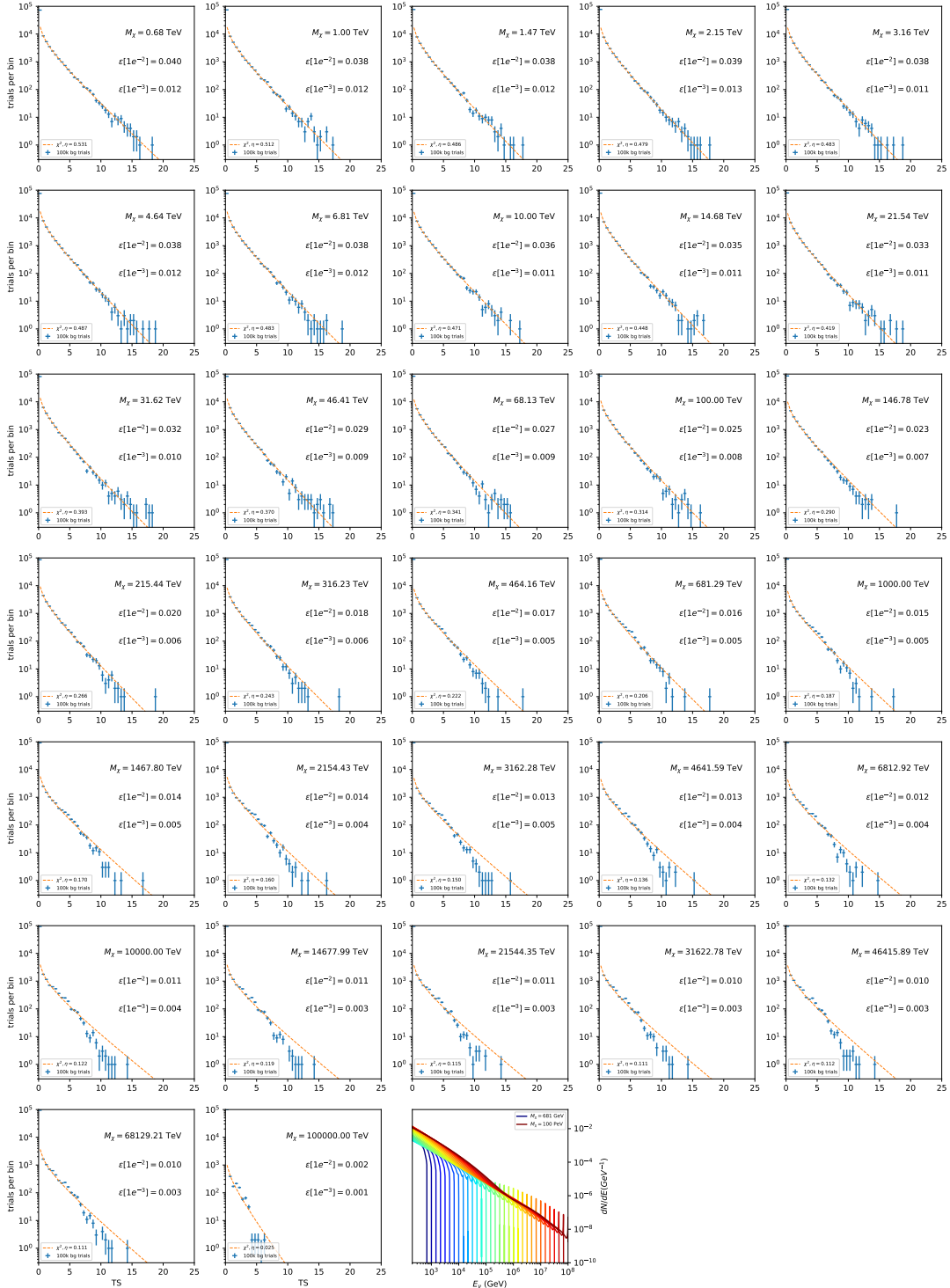


Figure 7.18 Same as Fig. 7.6 for 15, \mathcal{GS} J -factor, stacked sources and $\chi\chi \rightarrow \tau\bar{\tau}$.

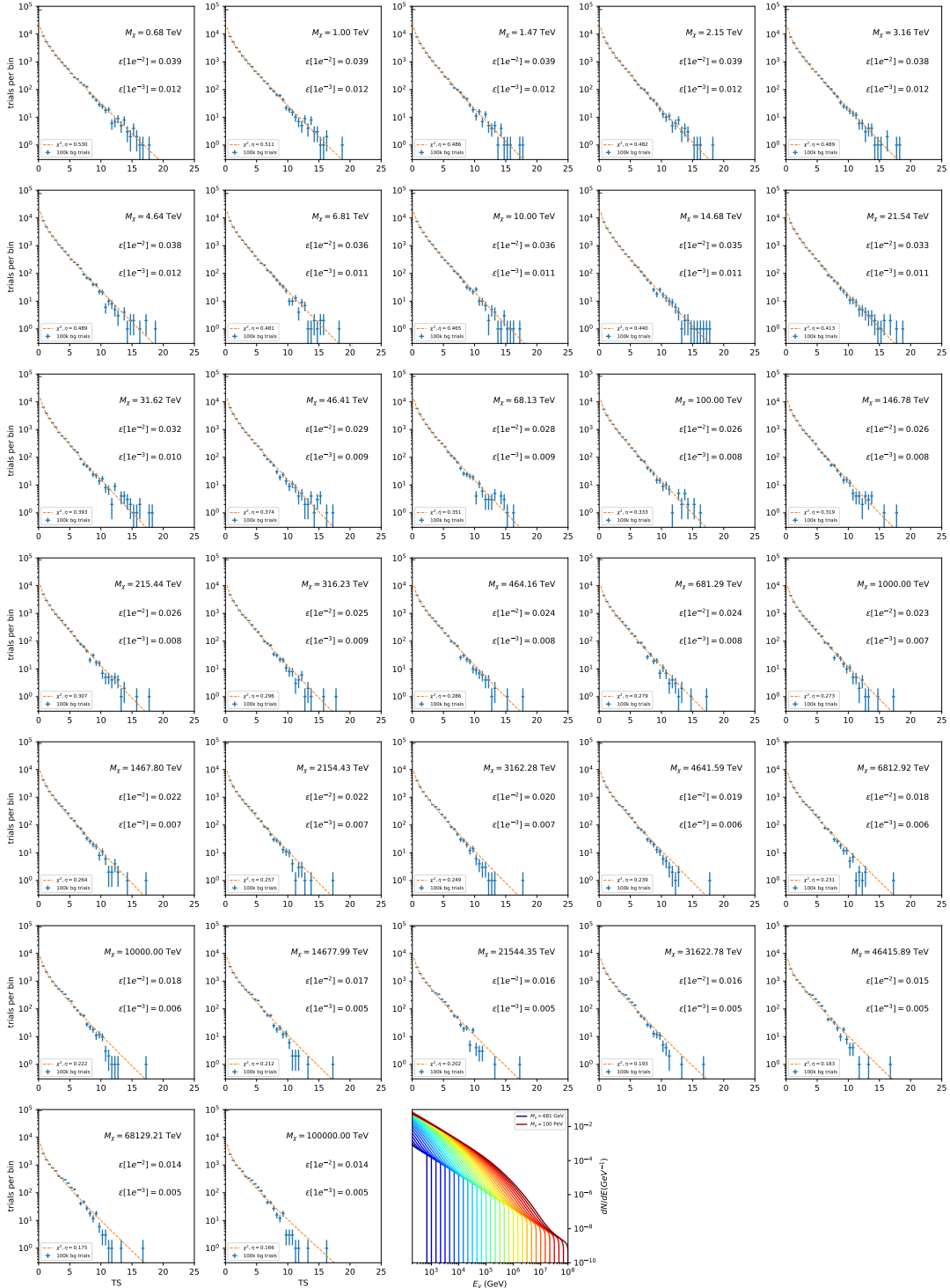


Figure 7.19 Same as Fig. 7.6 for 15, GS J-factor, stacked sources and $\chi\chi \rightarrow W^+W^-$.

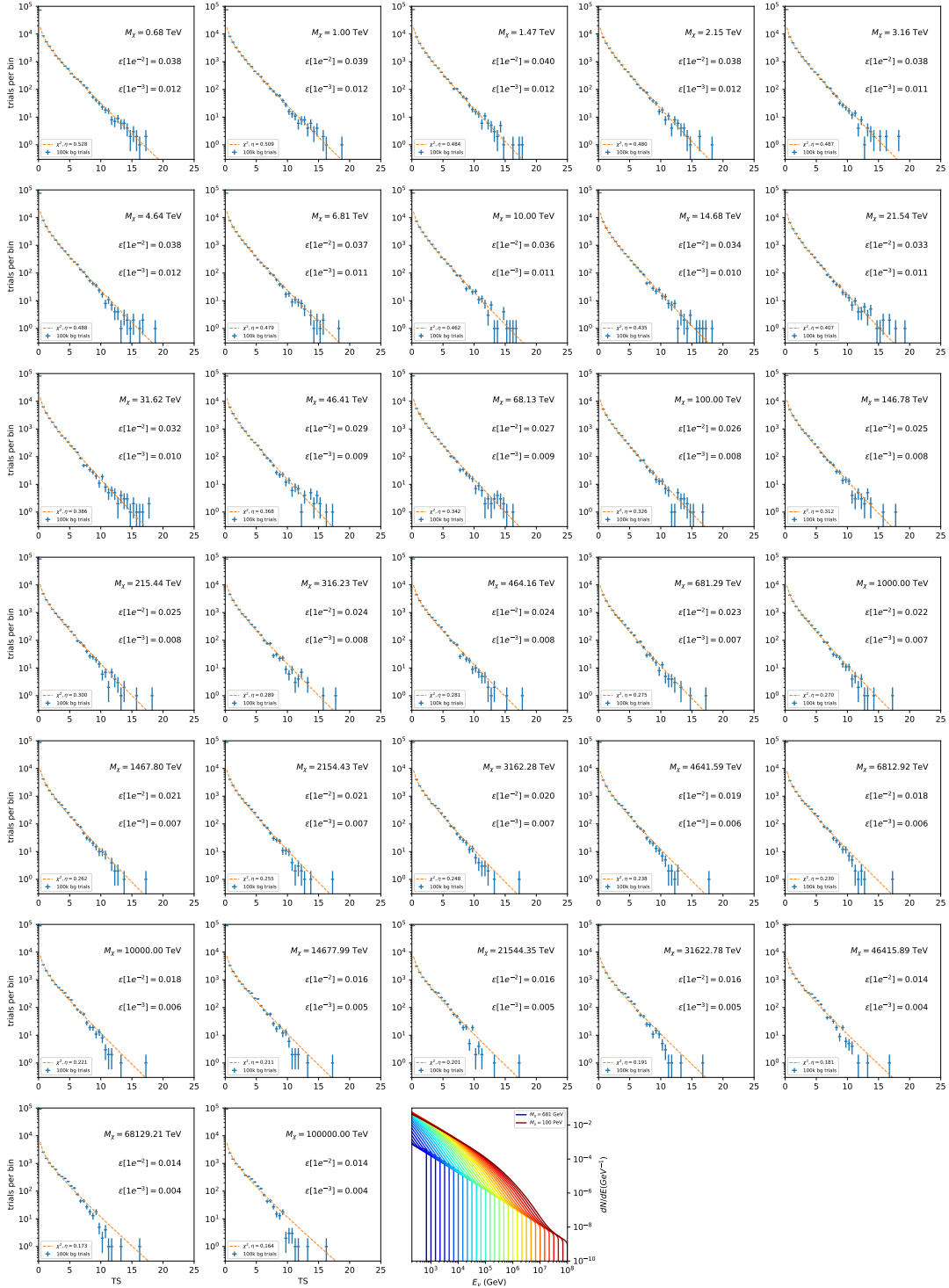


Figure 7.20 Same as Fig. 7.6 for 15, \mathcal{GS} J-factor, stacked sources and $\chi\chi \rightarrow ZZ$.

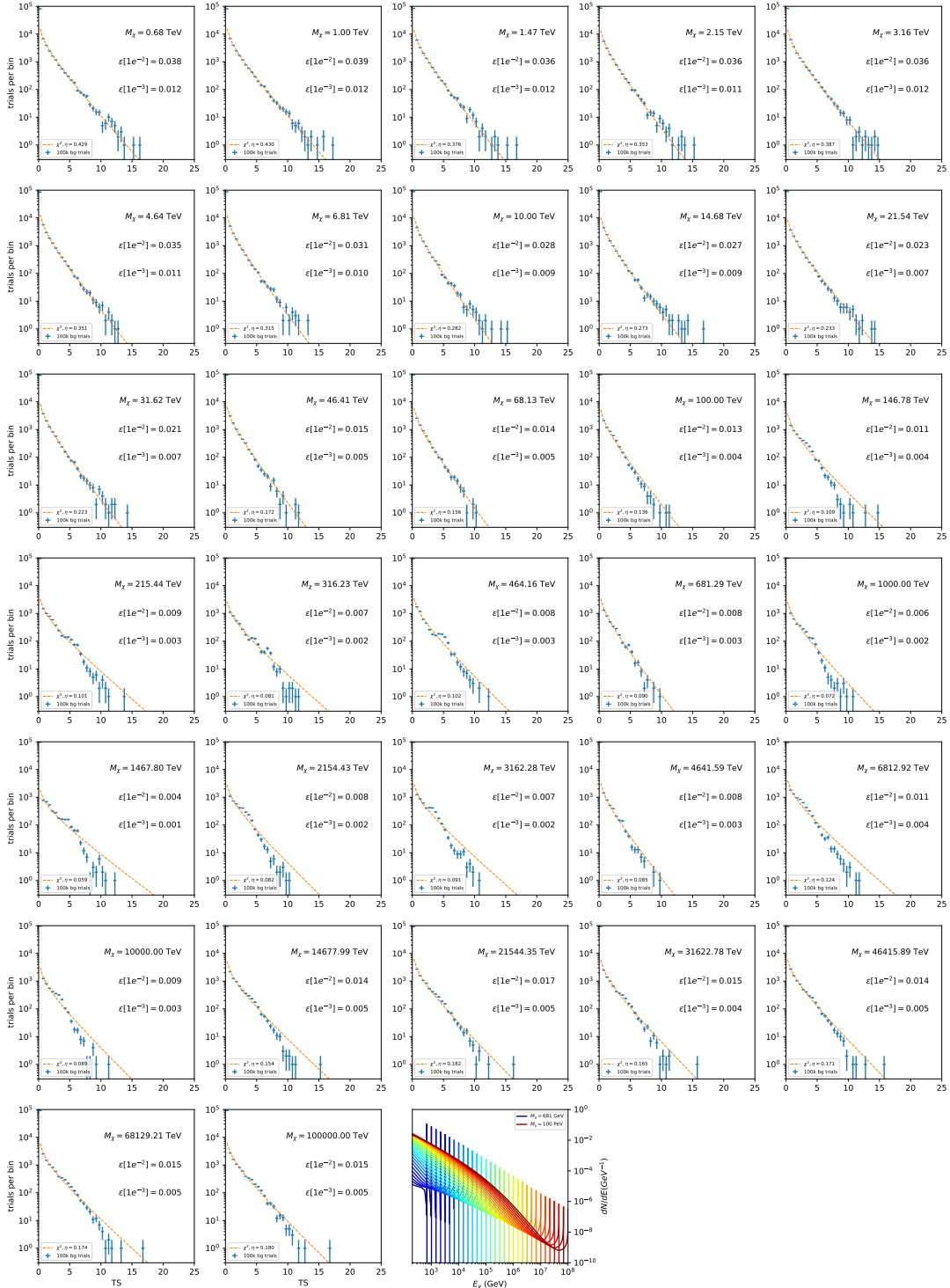


Figure 7.21 Same as Fig. 7.6 for 15, \mathcal{GS} J -factor, stacked sources and $\chi\chi \rightarrow \nu_e \bar{\nu}_e$.

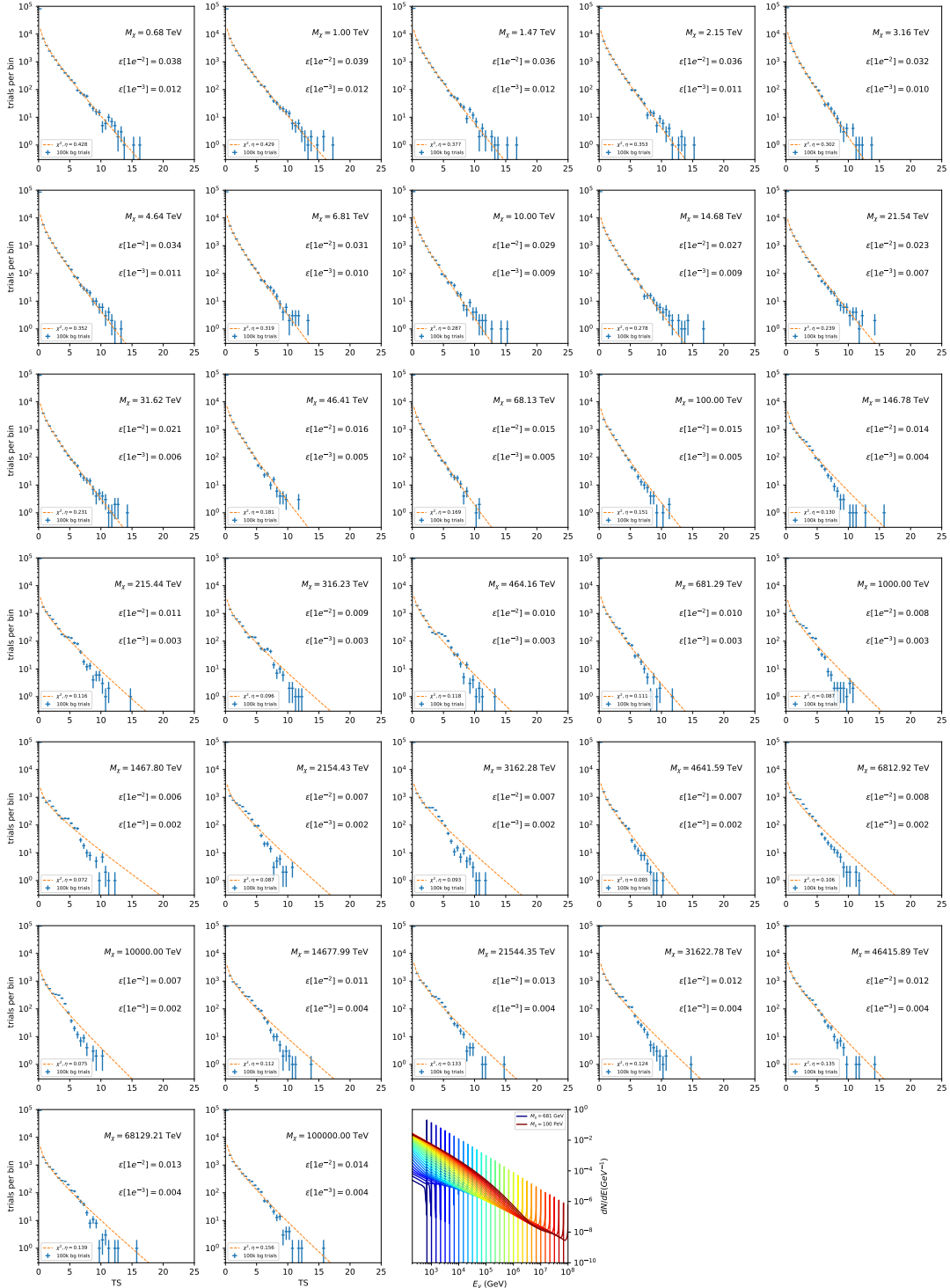


Figure 7.22 Same as Fig. 7.6 for 15, \mathcal{GS} J -factor, stacked sources and $\chi\chi \rightarrow \nu_\mu \bar{\nu}_\mu$.

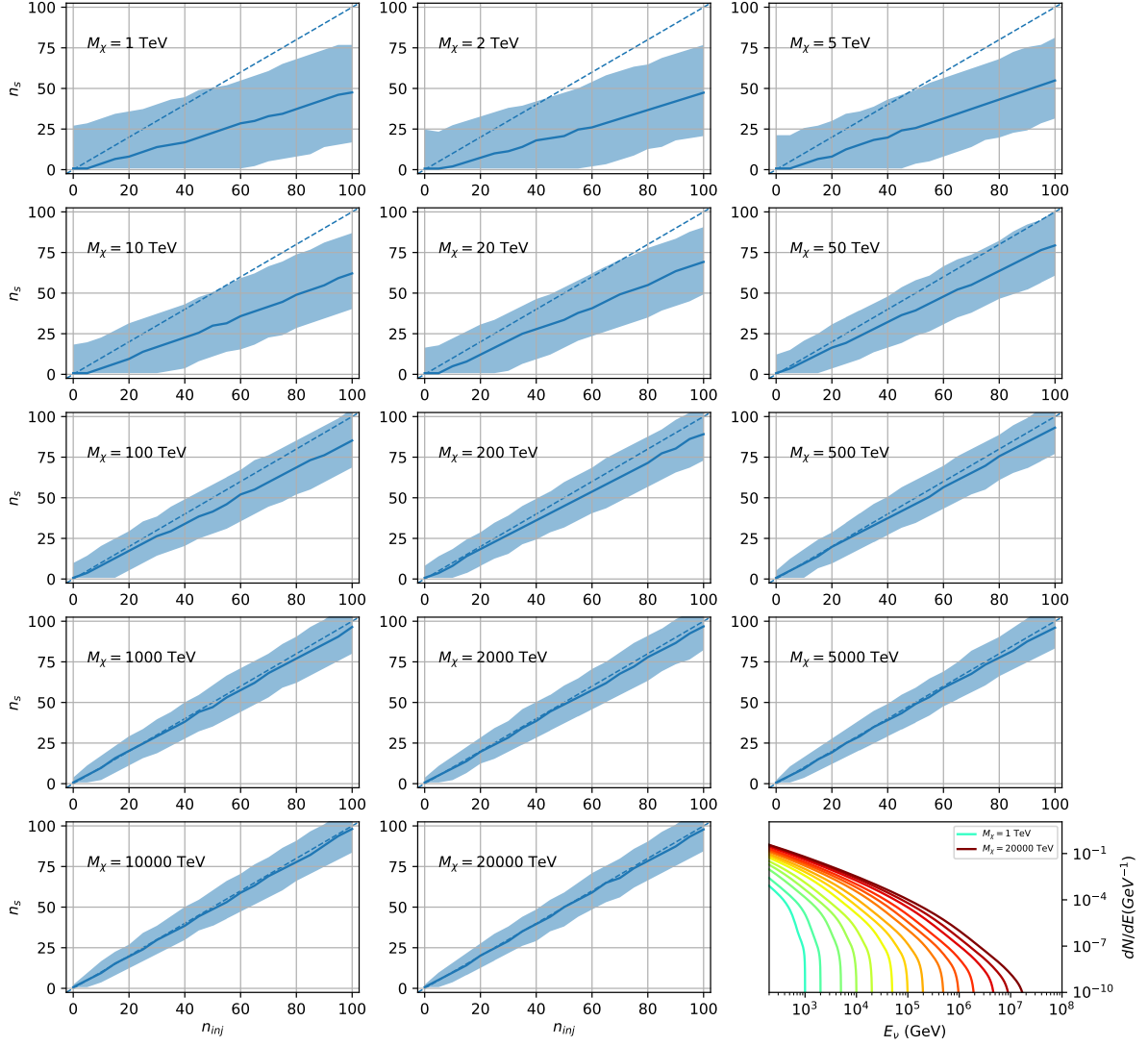


Figure 7.23 Signal Recovery study for an analysis with 15 stacked sources using the \mathcal{GS} J -factors [45]. Each panel block represents 14 studies for DM mass ranging between 1 TeV and 20 PeV and one annihilation channel. Panel block is for $t\bar{t}$. Each panel block features every spectral model used as input in the bottom-right subpanel. The remaining panels show n_{inj} as the number of signal events injected into background simulation. Whereas, n_s is the number of signal events recovered from analyzing the injected simulation. Blue line represents the median values of 100 simulations. Light blue bands show the 1σ statistical uncertainty around the median.

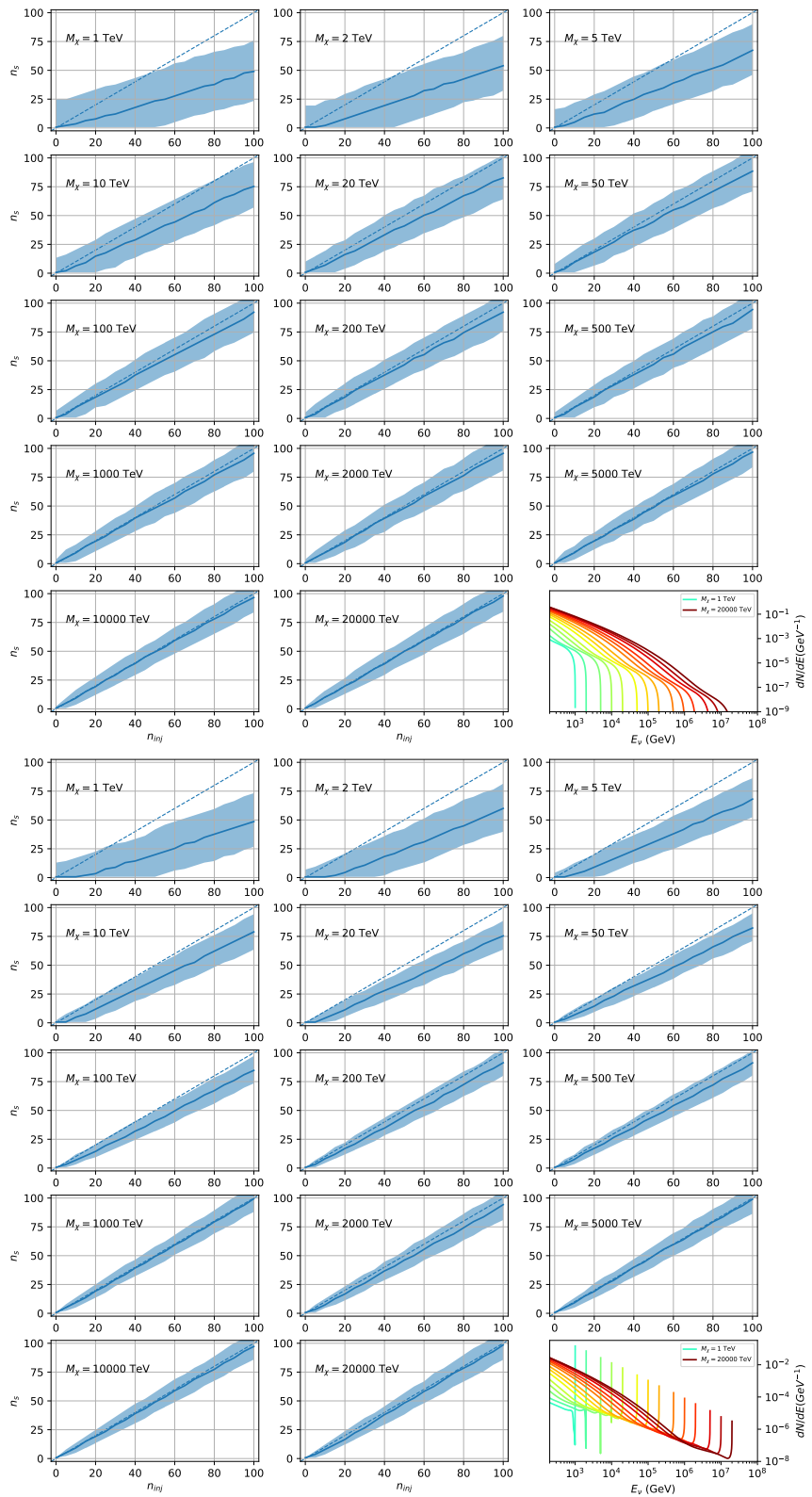


Figure 7.24 Same as Fig. 7.23 but for $\chi\chi \rightarrow b\bar{b}$ (top) and $\nu_\mu\bar{\nu}_\mu$ (bottom).

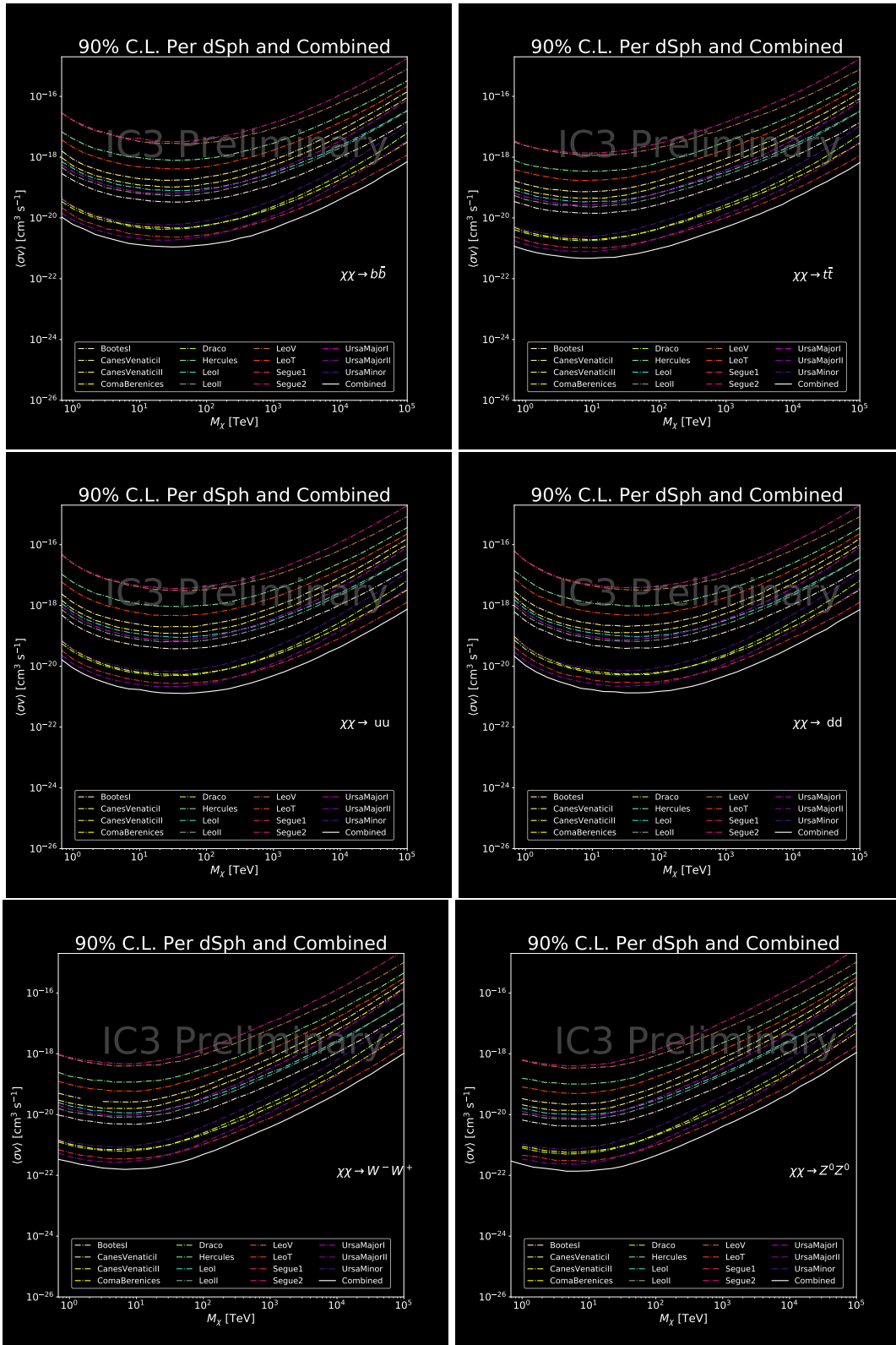


Figure 7.25 Words. I prent Icecibe Sensitivities weeee

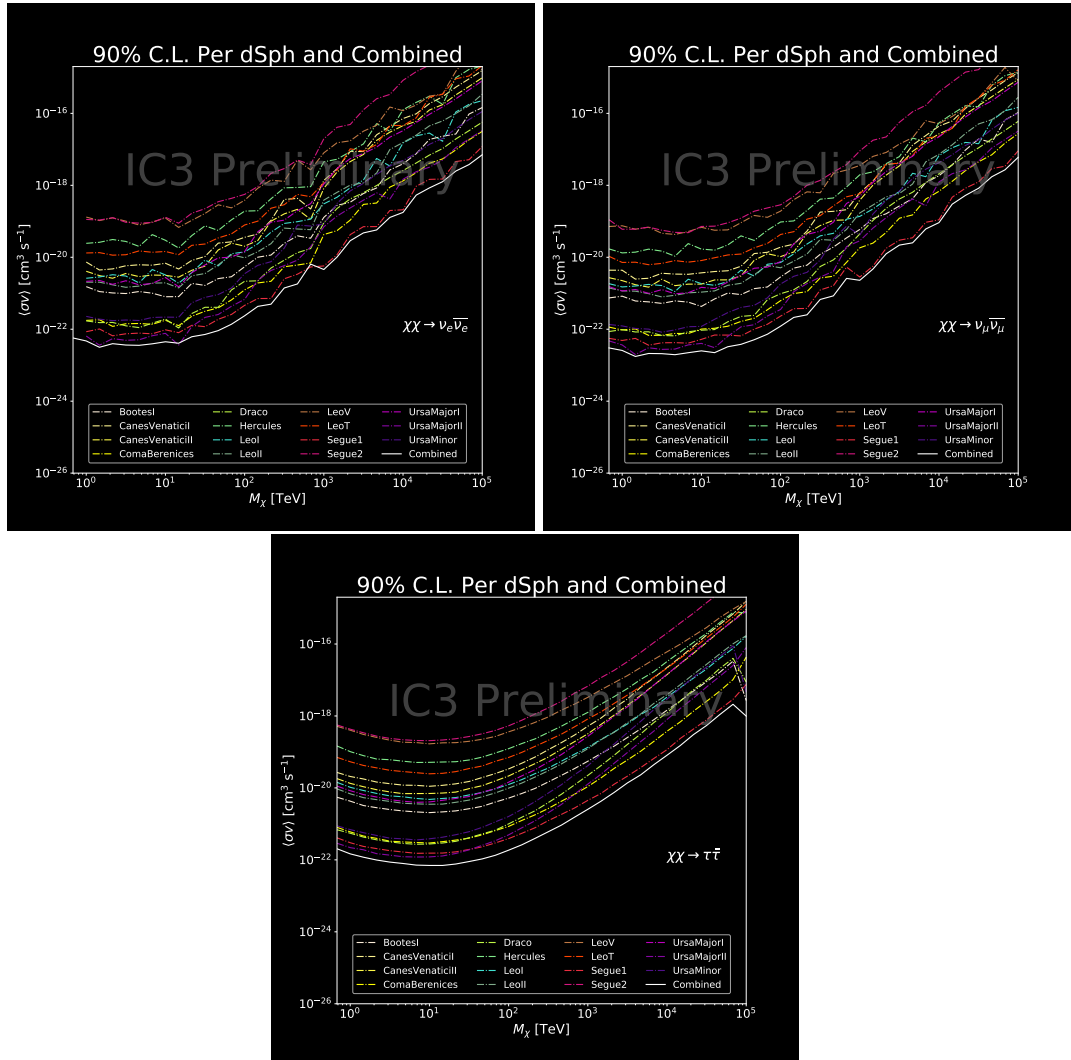


Figure 7.26 Words. I prent Icecibe Sensitivities weeee



Figure 7.27 TODO: Earth attenuation diagram.[NEEDS A SOURCE][FACT CHECK THIS]



Figure 7.28 TODO: Declination sensitivity plot[NEEDS A SOURCE][FACT CHECK THIS]

CHAPTER 8

1728

NU DUCK

MULTI-EXPERIMENT SUPPLEMENTARY FIGURES

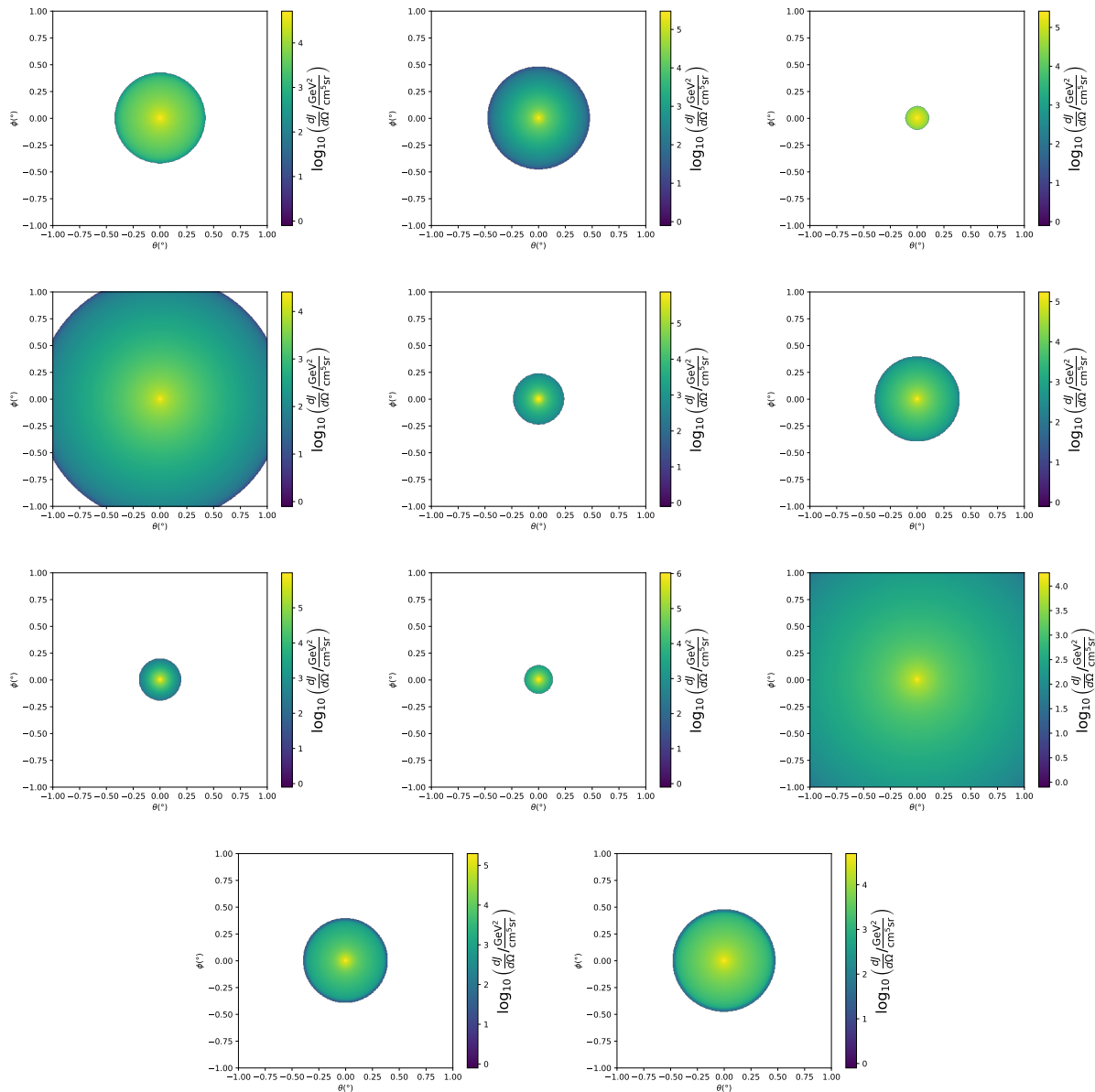


Figure A.1 Sister figure to Figure 5.3. Sources in the first row from left to right: Bootes I, Canes Venatici I, II. In second row: Draco, Hercules, Leo I. In the first row: Leo II, Leo IV, Sextans. In the final row: Ursa Major I, Ursa Major II.

APPENDIX B

1730 MULTITHREADING DARK MATTER ANALYSES SUPPLEMENTARY MATERIAL

1731 B.1 Remaining Spectral Models

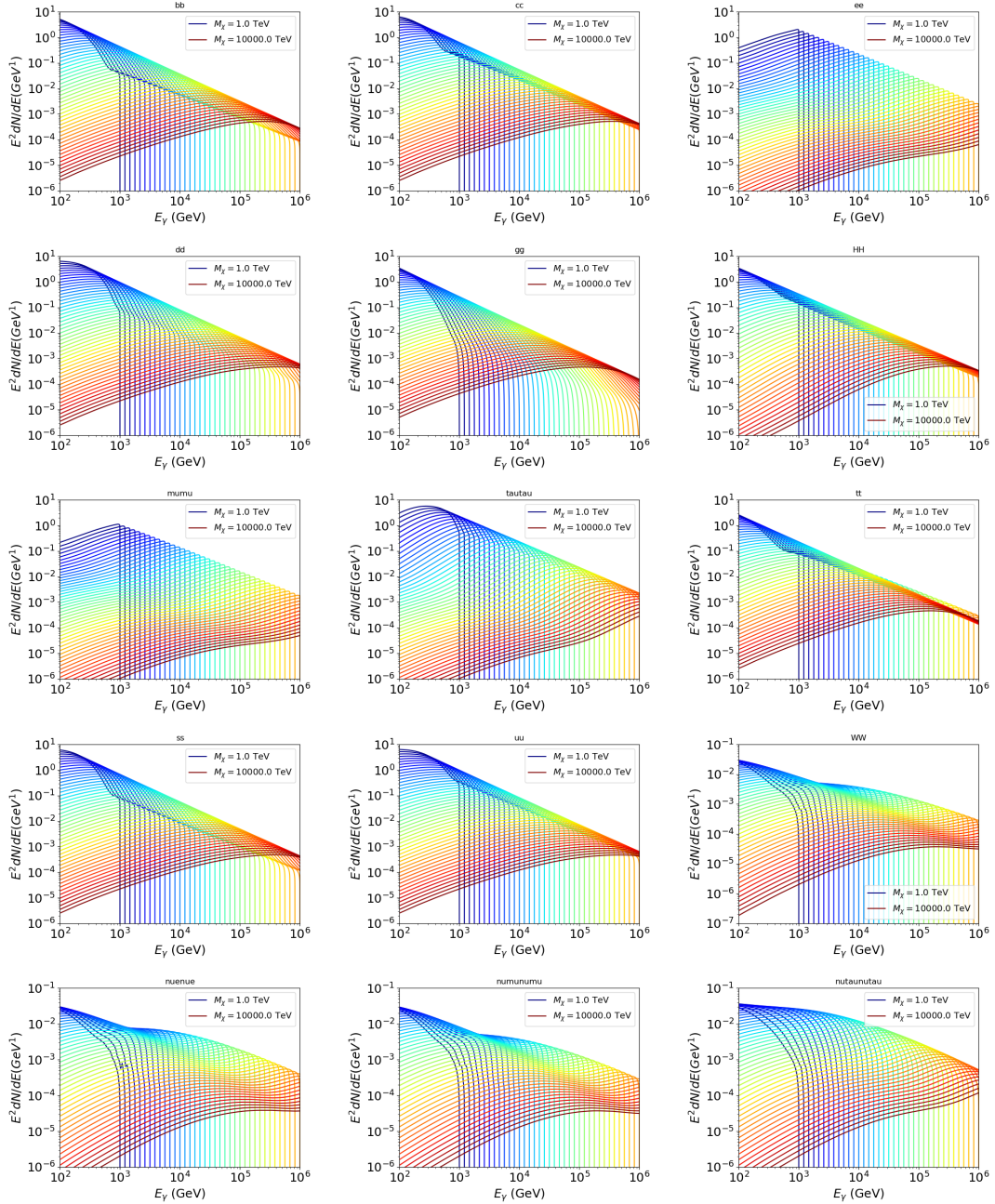


Figure B.1 Sister figure to Figure 6.2 for remaining SM primary annihilation channels studied for this thesis. These did not require any post generation smoothing and so are directly pulled from [65] with a binning scheme most helpful for a HAWC analysis.

1732 B.2 mpu_analysis.py

```
17331 import warnings
17342 with warnings.catch_warnings():
17353     warnings.simplefilter("ignore")
17364 # Python base libraries
17375 import os
17386 import sys
17397 import time
17408 # Import general libraries with namespace
17419 import matplotlib
17420 # Necessary for computing on cluster
17431 matplotlib.use("agg")
17442 import numpy as np
17453 import multiprocessing as mp
17464 # Import HAWC software
17475 sys.path.insert(1, os.path.join(os.environ['HOME'], 'hawc_software', 'threeML-
1748     analysis-scripts', 'fitModel'))
17496 from analysis_modules import *
17507 from threeML import *
17518 from hawc_hal import HAL, HealpixConeROI
17529 from threeML.minimizer.minimization import FitFailed
17530 # Import Dark Matter HAWC Libraries
17541 import analysis_utils as au
17552 import spectra as spec
17563 import sources as srcs
17574
17585 #* READ ONLY PATHS This block will change eventually
17596 MASS_LIST = './plotting/studies/nd/masses.txt'
17607 CHAN_LIST = './plotting/studies/nd/chans.txt'
17618
17629 #* WRITE PATHS, default location is to scratch
17630 OUT_PATH = os.path.join(os.environ["SCRATCH"], os.environ["USER"], 'New_duck')
```

```

17641 print('Our out path is going to be {}'.format(OUT_PATH))
17652
17663 # Define parallel Function. Can also be run serially
17674 def some_mass_fit(sigVs, datalist, shape, dSph, jfactor, mass_chan,
17685                 progress=None, log_file='', queue=None, i_job=0):
17696
17707     if progress is None:
17718         progress = [0]
17729     else: # Create log files for each thread
17730         log_file = log_file.replace('.log', '_ThreadNo_')
17741         log_file = log_file + str(i_job) + ".log"
17752         sys.stdout = open(log_file, "w")
17763
17774     fits = []
17785
17796     try:
17807         for m_c in mass_chan:
17818             print(f'Mass chan tuple: {m_c}')
17829             mass = int(m_c[0])
17830             ch = m_c[1]
17841             # Build path to output files
17852             outPath = os.path.join(OUT_PATH, ch, dSph)
17863             au.ut.ensure_dir(outPath)
17874
17885             if progress[i_job] < 0:
17896                 # If the master gets a Keyboard interrupt, commit suicide.
17907                     break
17918
17929                     ### Start Model Building for DM mass and SM channel #####
17930                     spectrum = spec.DM_models.HDMSpectra()
17941                     spectrum.set_channel(ch)
17952
17963                     myDwarf = ExtendedSource(dSph, spatial_shape=shape,

```

```

17974                     spectral_shape=spectrum)

17985

17996     spectrum.J = jfactor * u.GeV**2 / u.cm**5
18007     spectrum.sigmav = 1e-24 * u.cm**3 / u.s
18018     spectrum.set_dm_mass(mass * u.GeV)

18029

18030     spectrum.sigmav.bounds = (1e-30, 1e-12)
18041     model = Model(myDwarf)
18052     ##### End model Building #####
18063
18074     jl = JointLikelihood(model, datalist, verbose=False)
18085
18096     try:
18107         result, lhdf = jl.fit(compute_covariance=False)
18118         ts = -2.* (jl.minus_log_like_profile(1e-30) - jl.
1812         _current_minimum)
18139         # Also profile the LLH vs sv
18140         ll = jl.get_contours(spectrum.sigmav, sigVs[0],
18151                         sigVs[-1], len(sigVs),
18162                         progress=False, log=['False'])
18173
18184         sigv_ll = au.ut.calc_95_from_profile(ll[0], ll[2])
18195         # Write results to file
18206         outFileLL = outPath+f"/LL_{dSph}_{ch}_mass{int(mass)}_GD.txt"
18217         np.savetxt(outFileLL, (sigVs, ll[2]),
18228                         delimiter='\t', header='sigV\tLL\n')
18239
18240         with open(outPath+f"/results_{dSph}_{ch}_mass{int(mass)}_GD.
1825         txt", "w") as results_file:
18261             results_file.write("mDM [GeV]\tsigV_95\tsigV_B.F.\n")
18272
18283             results_file.write("%i\t%.5E\t%.5E\t%.5E"%(mass, sigv_ll,
18294                                         ts, result.value[0]))

```

```

18305         # End write to file
18316     except FitFailed: # Don't kill all threads if a fit fails
18327         print("Fit failed. Go back and calculate this spectral model
1833    later")
18348         fits.append((ch, mass, -1, -1))
18359         with open(log_file+'.fail', 'w') as f_file:
18360             f_file.write(f'{ch}, {mass}\n')
18371
18382         progress[i_job] += 1
18393         matplotlib.pyplot.close() # Prevent leaky memory
18404
18415         fits.append((ch, mass, result.value[0], ts))
18426         progress[i_job] += 1
18437         matplotlib.pyplot.close()
18448     except KeyboardInterrupt:
18459         progress[i_job] = -1
18460
18471     fits = np.array(fits)
18482     if queue is None:
18493         return fits
18504     else:
18515         queue.put((i_job, fits))
18526
18537 def main(args):
18548     masses = np.loadtxt(MASS_LIST, dtype=int)
18559     chans = np.loadtxt(CHAN_LIST, delimiter=',', dtype=str)
18560     mass_chan = au.ut.permute_lists(chans, masses)
18571
18582     print(f"DM masses for this study are: {masses}")
18593     print(f"SM Channels for this study are XX -> {chans}")
18604     print(mass_chan)
18615
18626 # extract information from input argument

```

```

18637 dSph = args.dSph
18648 data_mngr = au.ut.Data_Selector('P5_NN_2D')
18659 dm_profile = srcts.Spatial_DM(args.catalog, dSph, args.sigma, args.decay)
18660
18671     ### Extract Source Information ####
18682 if dm_profile.get_dec() < -22.0 or dm_profile.get_dec() > 62.0:
18693     raise ValueError("HAWC can't see this source D: Exitting now...")
18704
18715 print(f'{dSph} information')
18726 print(f'jfac: {dm_profile.get_factor()}\tRA: {dm_profile.get_ra()}\tDec: {dm_profile.get_dec()}\n')
1873
18747
18758 shape = SpatialTemplate_2D(fits_file=dm_profile.get_src_fits())
18769     ### Finish Extract Source Information ####
18770
18781     ### LOAD HAWC DATA ####
18792 roi = HealpixConeROI(data_radius=2.0, model_radius=8.0,
18803                         ra=dm_profile.get_ra(), dec=dm_profile.get_dec())
18814 bins = choose_bins.analysis_bins(args, dec=dm_profile.get_dec())
18825
18836 hawc = HAL(dSph, data_mngr.get_datmap(), data_mngr.get_detres(), roi)
18847 hawc.set_active_measurements(bin_list=bins)
18858 datalist = DataList(hawc)
18869     ### FINISH LOAD HAWC DATA ####
18870
18881 # set up SigV sampling. This sample is somewhat standardized
18892 sigVs = np.logspace(-28,-18, 1001, endpoint=True) # NOTE This will change
1890 with HDM
18913
18924 if args.n_threads == 1:
18935     # No need to start || programming just iterate over the masses
18946     kw_arg = dict(sigVs=sigVs, datalist=datalist, shape=shape, dSph=dSph,
18957                 jfactor=dm_profile.get_factor(), mass_chan=mass_chan,

```

```

18968             log_file=args.log)
18979     some_mass_fit(**kw_arg)
18980 else:
18991     # I Really want to suppress TQMD output
19002     from tqdm import tqdm
19013     from functools import partialmethod
19024     tqdm.__init__ = partialmethod(tqdm.__init__, disable=True)
19035
19046     x = np.array_split(mass_chan, args.n_threads)
19057     n_jobs = len(x)
19068
19079     print("Thread jobs summary by mass and SM channel")
19080     for xi in x:
19091         print(f'{xi}')
19102
19113     queue = mp.Queue()
19124     progress = mp.Array('i', np.zeros(n_jobs, dtype=int))
19135
19146     # Define task pool that will be split amongsts threads
19157     kw_args = [dict(sigVs=sigVs, datalist=datalist, shape=shape,
19168                     dSph=dSph, jfactor=dm_profile.get_factor(),
19179                     mass_chan=mass_chan, progress=progress,
19180                     queue=queue, i_job=i, log_file=args.log)
19191         for i, mass_chan in enumerate(x)]
19202
19213     # Define each process
19224     procs = [mp.Process(target=some_mass_fit, kwargs=kw_args[i]) \
19235         for i in range(n_jobs)]
19246
19257     ### Start MASTER Thread only code block ###
19268     # Begin running all child threads
19279     for proc in procs: proc.start()
19280

```

```

19291     try:
19302         # In this case, the master does nothing except monitor progress of
1931         the threads
19323             # In an ideal world, the master thread also does some computation.
19334                 n_complete = np.sum(progress)
19345                     while_count = 0
19356
19367                         while n_complete < len(mass_chan):
19378
19389                             if np.any(np.asarray(progress) < 0):
19390                                 # This was no threads are stranded when killing the script
19401                                     raise KeyboardInterrupt()
19412                                         if while_count%1000 == 0:
19423                                             print(f"{np.sum(progress)} of {len(mass_chan)} finished")
19434
19445                                         n_complete = np.sum(progress)
19456                                         time.sleep(.25)
19467                                         while_count += 1
19478
19489                                         except KeyboardInterrupt:
19490                                             # signal to jobs that it's time to stop
19501                                                 for i in range(n_jobs):
19512                                                     progress[i] = -2
19523                                                     print('\nKeyboardInterrupt: terminating early.')
19534                                         ### End MASTER Thread only code block ###
19545
19556                                         fitss = [queue.get() for proc in procs]
19567                                         print(fitss)
19578                                         print(f'Thread statuses: {progress[:]}')
19589
19590                                         # putting results in a file
19601
19612                                         print("QUACK! All Done!")

```

```

19623
19634
19645 if __name__ == '__main__':
19656     import argparse
19667
19678     p = argparse.ArgumentParser(description="Run a DM annihilation analysis on
1968         a dwarf spheroidal for a specific SM channel for DM masses [1 TeV to 10
1969         PeV]")
19709
19710     # Dwarf spatial modeling arguements
19721     p.add_argument("-ds", "--dSph", type=str,
19722                     help="dwarf spheroidal galaxy to be studied", required=
19723                     True)
19724
19725     p.add_argument("-cat", "--catalog", type=str, choices=['GS15', 'LS20'],
19726                     default='LS20', help="source catalog used")
19727
19728     p.add_argument("-sig", "--sigma", type=int, choices=[-1, 0, 1], default=0,
19729                     help="Spatial model uncertainty. 0 corresponds to the
19730             median. +/-1 correspond to the +/-1sigma uncertainty respectively.")
19731
19732
19733     # Arguements for the energy estimators
19734
19735     p.add_argument("-e", "--estimator", type=str,
19736                     choices=['P5_NHIT', 'P5_NN_2D'],
19737                     default="P5_NN_2D", required=False,
19738                     help="The energy estimator choice. Options are: P5_NHIT,
19739             P5_NN_2D. GP not supported (yet).")
19740
19741     p.add_argument("--use-bins", default=None, nargs="*",
19742                     help="Bins to use for the analysis", dest="use_bins")
19743
19744     p.add_argument('--select_bins_by_energy', default=None, nargs="*",
19745                     help="Does nothing. May fill in later once better
19746             understood")
19747
19748     p.add_argument('--select_bins_by_fhit', default=None, nargs="*",
19749                     help="Also does nothing see above")

```

```

19950         help="Exclude Bins", dest="exclude")

19961

19972 # Computing and logging arguements.

19983 p.add_argument('-nt', '--n_threads', type=int, default=1,
19994                         help='Maximum number of threads spawned by script. Default
2000      is 4')

20015 p.add_argument('-log', '--log', type=str, required=True,
20026                         help='Name for log files. Especially needed for threads')

20037

20048 p.add_argument('--decay', action="store_true",
20059                         help='Set spectral DM hypothesis to decay')

20060

20071 args = p.parse_args()

20082 print(args.decay)

20093 if args.exclude is None: # default exclude bins 0 and 1
20104     args.exclude = ['B0C0Ea', 'B0C0Eb', 'B0C0Ec', 'B0C0Ed', 'B0C0Ee']

20115

20126 if args.decay: OUT_PATH += '_dec'
20137 else: OUT_PATH += '_ann'

20148

20159 OUT_PATH = OUT_PATH + '_' + args.catalog
20160 if args.sigma != 0: OUT_PATH += f'_{args.sigma}sig'

20171

20182 main(args)

```

2019 B.3 Comparison with Glory Duck

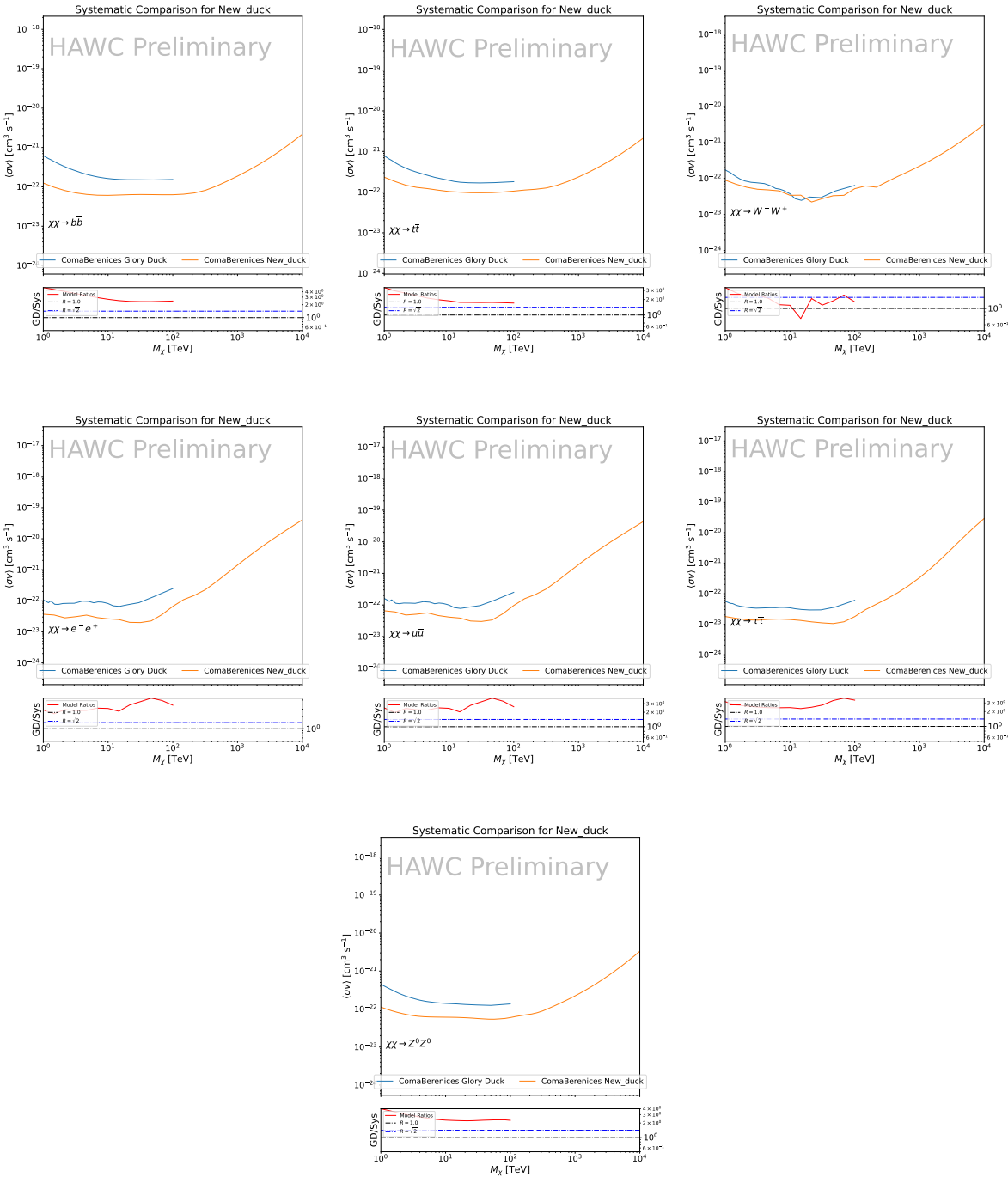


Figure B.2 TODO: fill this out

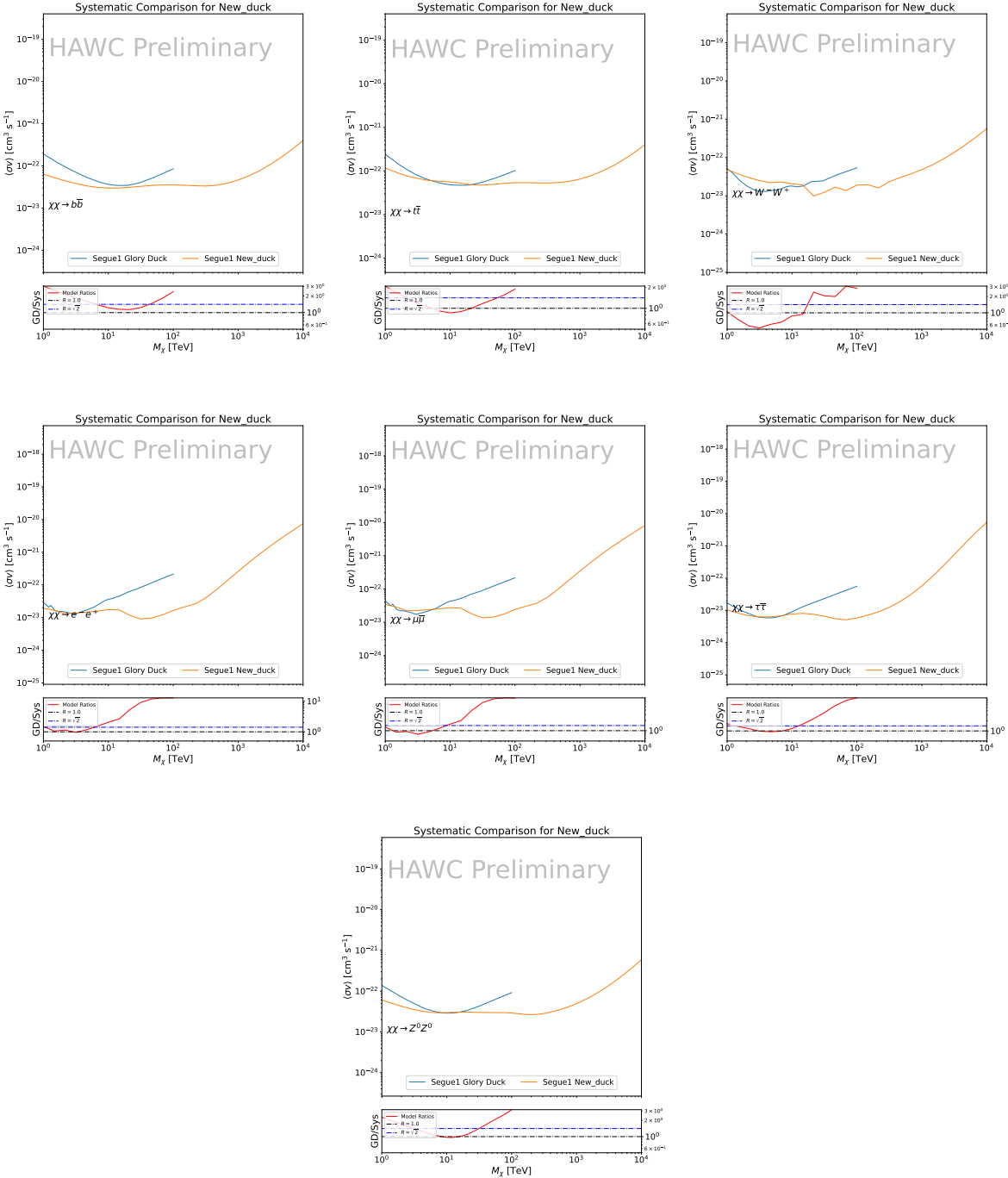


Figure B.3 TODO: fill this out

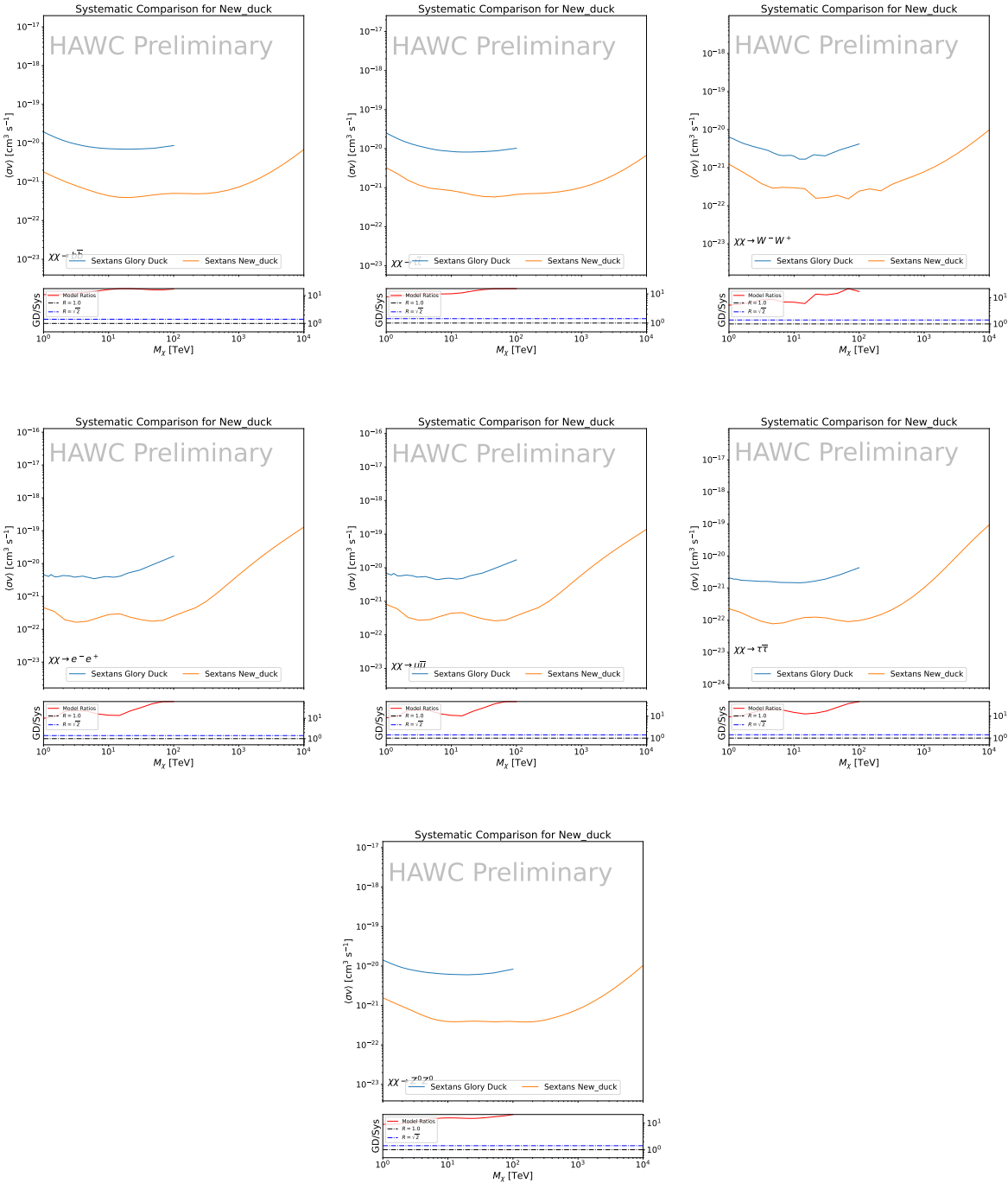


Figure B.4 TODO: fill this out

APPENDIX C

2020 ICECUBE HEAVY DARK MATTER ANALYSIS SUPPLEMENTARY MATERIAL

2021 **C.1 Docker Image for Oscillating Neutrino Spectra**

```
2022 1 FROM ubuntu:18.04
2023 2
2024 3 # Execute commands to install software packages
2025 4 RUN apt -y update
2026 5
2027 6     # Install utility programs
2028 7 RUN apt -y install vim wget git cmake
2029 8
2030 9 ARG DEBIAN_FRONTEND=noninteractive
2031 10
2032 11     # Install python
2033 12 RUN apt -y install python python-dev python-pip libjpeg-dev zlib1g-dev
2034 13
2035 14     # We need Python2 for installing Charon.
2036 15 RUN apt -y install python-numpy python-sympy python-matplotlib \
2037 16             python-sympy python-h5py python-astropy python-ipython
2038 17
2039 18     # Install dependencies of Charon : SQuIDS, NuSQuIDS
2040 19 RUN apt -y install libgsl-dev libgslcblas0 libgsl23 gsl-bin pkg-config
2041 20     # Install SQuIDS
2042 21 RUN mkdir /home/SQuIDS /home/SQuIDS_install
2043 22 WORKDIR /home/SQuIDS
2044 23 RUN git clone https://github.com/jsalvado/SQuIDS.git
2045 24 WORKDIR /home/SQuIDS/SQuIDS
2046 25 RUN git checkout 7ad9ba7c6ad06d1f0fa8418f937ebf1a403fef90
2047 26     # Before executing "make install" an environmental variable has to be set.
2048 27 ENV PKG_CONFIG_PATH=/home/SQuIDS/SQuIDS/lib
2049 28 RUN ./configure --prefix=../SQuIDS_install \
```

```

20509     && make
20510 RUN make install
20521
20532 # Set up an environmental variable that is required to install nuSQuIDS..
20543 ENV SQuIDS=/home/SQuIDS/SQuIDS
20554 ENV LD_LIBRARY_PATH=$SQuIDS/lib:$LD_LIBRARY_PATH
20565
20576 # Install NuSQuIDS
20587 RUN mkdir /home/nuSQuIDS
20598 WORKDIR /home/nuSQuIDS
20609 RUN git clone https://github.com/qrliu/nuSQuIDS.git
20610 WORKDIR /home/nuSQuIDS/nuSQuIDS
20621 RUN git checkout 072d8ef740e2fc7330f1fabaea94f0f4540c46f9
20632 RUN apt -y install libhdf5-dev hdf5-tools
20643 RUN apt -y install libboost1.65-all-dev
20654 RUN ./configure --with-squids=$SQuIDS --with-python-bindings --prefix=../
2066     nuSQuIDS_install \
20675     && make \
20686     && make install
20697
20708 # Set up an environmental variable for nuSQuIDS.
20719 ENV nuSQuIDS=/home/nuSQuIDS/nuSQuIDS
20720 ENV LD_LIBRARY_PATH=$nuSQuIDS/lib:$LD_LIBRARY_PATH
20731
20742 # Build the python bindings
20753 WORKDIR /home/nuSQuIDS/nuSQuIDS/resources/python/src
20764 RUN make
20775
20786 # Set up an environmental variable for the python bindings.
20797 ENV PYTHONPATH=$nuSQuIDS/resources/python/bindings/:$PYTHONPATH
20808
20819 # Install Charon in the /home/Charon/charon directory.
20820 RUN mkdir /home/Charon

```

```
20831 WORKDIR /home/Charon
20842 RUN git clone https://github.com/icecube/charon.git \
20853   && apt -y install unzip python-scipy
20864 WORKDIR charon
20875 RUN git checkout c531efe4e01dc364a60d1c83f950f04526ccd771
20886 RUN unzip ./charon/xsec/xsec.zip -d charon/xsec/ \
20897
20908 # Download neutrino spectra tables in the /home/Charon/charon/data directory
2091 .
20929 && mkdir ./charon/data
20930 WORKDIR ./charon/data
20941 RUN wget --no-check-certificate https://icecube.wisc.edu/~qliu/charon/
2095   SpectraEW.hdf5 \
20962 && wget --no-check-certificate https://icecube.wisc.edu/~qliu/charon/
2097   Spectra_PYTHIA.hdf5 \
20983 && wget --no-check-certificate https://icecube.wisc.edu/~qliu/charon/
2099   Spectra_noEW.hdf5
21004
21015 WORKDIR ../..
21026 RUN python setup.py install
21037 WORKDIR /home
```

2104 C.2 Spline Fitting Statuses

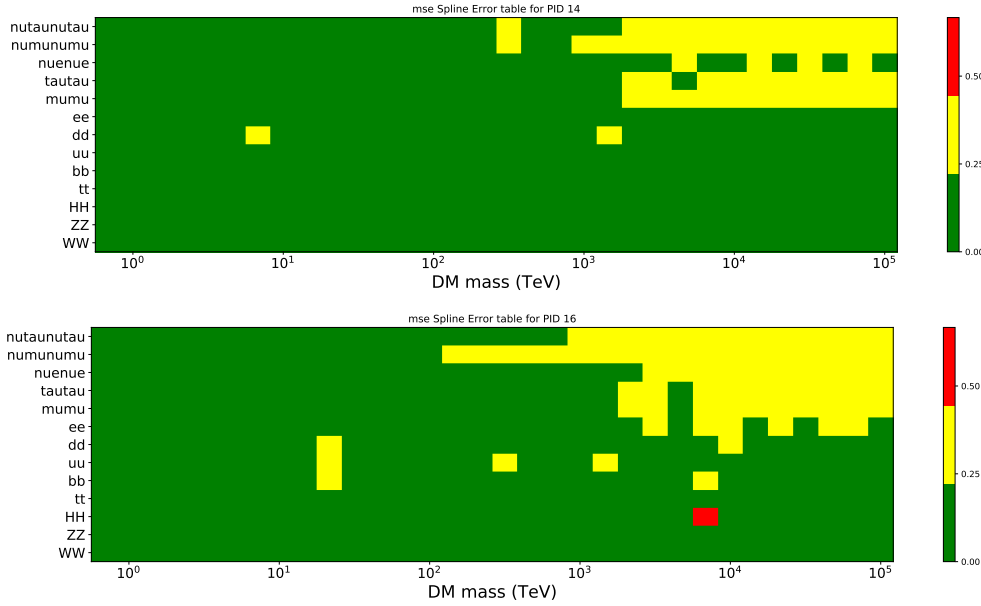


Figure C.1 Current status of spline tables according to constraints defined by Tab. 7.1. Green splines are splines that passed under the GOOD tolerance. Yellow are splines that are OK. Red are splines that FAIL. All yellow splines were inspected individually before running the analysis. Splines were made for the μ (PID 14; top panel) flavor and τ (PID 16; bottom panel) neutrino flavors.

2105 C.3 Neutrino Composite Spectra

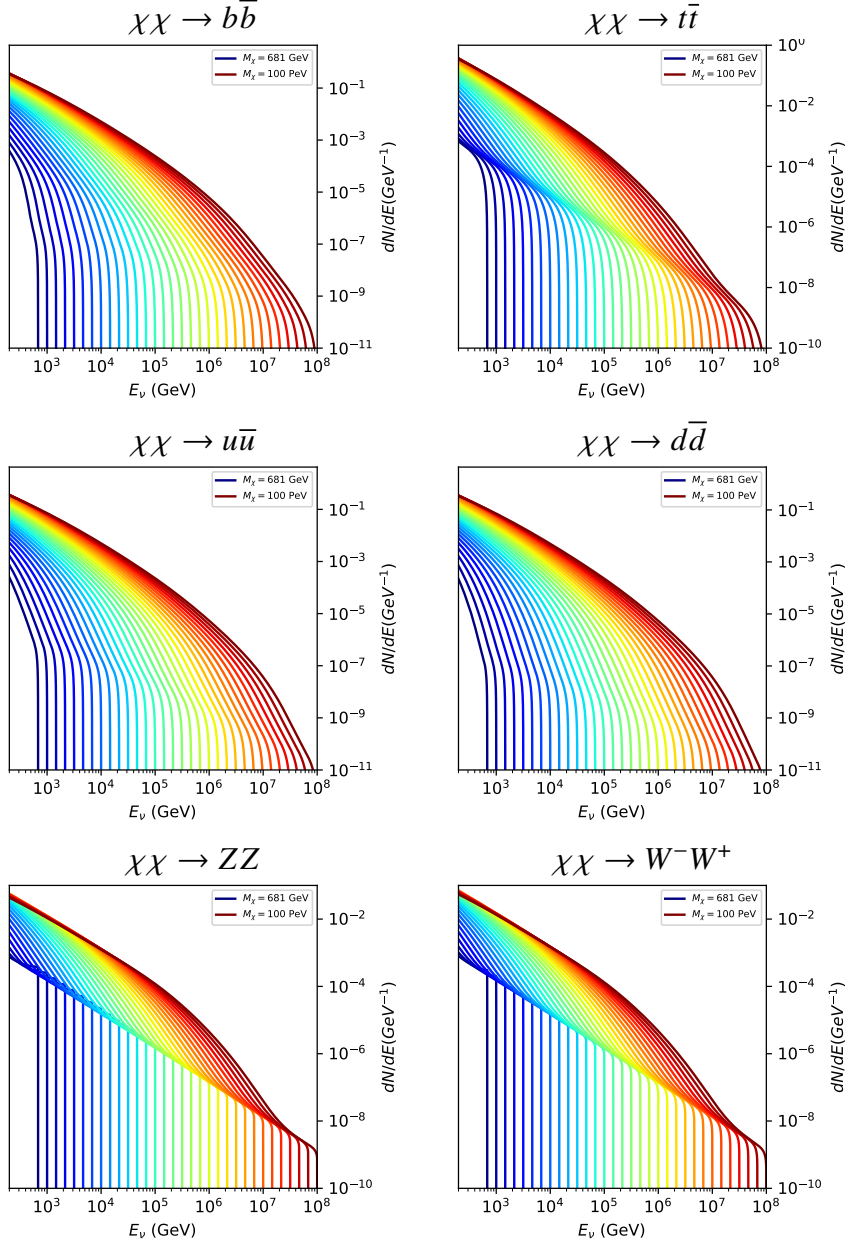


Figure C.2 Sister figure to Fig. 7.5 for annihilation channels that did not require kernel smoothing. These spectra are the composite ($\nu_\mu + \nu_\tau$) of neutrino flavors. Every spectral model used for this analysis is featured as a colored solid line. Bluer lines are for lower DM mass spectral models. DM masses range from 681 GeV to 100 PeV.

2106 C.4 Segue 1 And Ursa Major II Signal Recovery



Figure C.3 TODO: Fill this out eventually. I think I want all the plots generated first[NEEDS A SOURCE][FACT CHECK THIS]

2107

BIBLIOGRAPHY

- 2108 [1] Anne M. Green. “Dark matter in astrophysics/cosmology”. In: *SciPost Phys. Lect.*
 2109 *Notes* (2022), p. 37. doi: [10.21468/SciPostPhysLectNotes.37](https://doi.org/10.21468/SciPostPhysLectNotes.37). URL: <https://scipost.org/10.21468/SciPostPhysLectNotes.37>.
- 2111 [2] Bing-Lin Young. “A survey of dark matter and related topics in cosmology”. In: *Frontiers*
 2112 *of Physics* 12 (Oct. 2016). doi: <https://doi.org/10.1007/s11467-016-0583-4>.
 2113 URL: <https://doi.org/10.1007/s11467-016-0583-4>.
- 2114 [3] Gianfranco Bertone, Dan Hooper, and Joseph Silk. “Particle dark matter: evidence,
 2115 candidates and constraints”. In: *Physics Reports* 405.5 (2005), pp. 279–390. ISSN:
 2116 0370-1573. doi: <https://doi.org/10.1016/j.physrep.2004.08.031>. URL:
 2117 <https://www.sciencedirect.com/science/article/pii/S0370157304003515>.
- 2118 [4] Gianfranco Bertone and Dan Hooper. “History of dark matter”. In: *Rev. Mod. Phys.*
 2119 90 (4 Aug. 2018), p. 045002. doi: [10.1103/RevModPhys.90.045002](https://doi.org/10.1103/RevModPhys.90.045002). URL: <https://link.aps.org/doi/10.1103/RevModPhys.90.045002>.
- 2121 [5] Fritz Zwicky. “The Redshift of Extragalactic Nebulae”. In: *Helvetica Physica Acta* 6.
 2122 (1933), pp. 110–127. doi: [10.5169/seals-110267](https://doi.org/10.5169/seals-110267).
- 2123 [6] Vera C. Rubin and Jr. Ford W. Kent. “Rotation of the Andromeda Nebula from a
 2124 Spectroscopic Survey of Emission Regions”. In: *ApJ* 159 (Feb. 1970), p. 379. doi:
 2125 [10.1086/150317](https://doi.org/10.1086/150317).
- 2126 [7] K. G. Begeman, A. H. Broeils, and R. H. Sanders. “Extended rotation curves of spiral galax-
 2127 ies: dark haloes and modified dynamics”. In: *Monthly Notices of the Royal Astronomical So-*
 2128 *ciety* 249.3 (Apr. 1991), pp. 523–537. ISSN: 0035-8711. doi: [10.1093/mnras/249.3.523](https://doi.org/10.1093/mnras/249.3.523).
 2129 eprint: <https://academic.oup.com/mnras/article-pdf/249/3/523/18160929/mnras249-0523.pdf>. URL: <https://doi.org/10.1093/mnras/249.3.523>.
- 2131 [8] *Different types of gravitational lenses*. website. Feb. 2004. URL: <https://esahubble.org/images/heic0404b/>.
- 2133 [9] Douglas Clowe et al. “A Direct Empirical Proof of the Existence of Dark Matter”. In: *apjl*
 2134 648.2 (Sept. 2006), pp. L109–L113. doi: [10.1086/508162](https://doi.org/10.1086/508162). arXiv: [astro-ph/0608407](https://arxiv.org/abs/astro-ph/0608407)
 2135 [*astro-ph*].
- 2136 [10] Planck Collaboration and N. et. al. Aghanim. “Planck 2018 results I. Overview and the
 2137 cosmological legacy of Planck”. In: *A&A* 641 (2020). doi: [10.1051/0004-6361/201833880](https://doi.org/10.1051/0004-6361/201833880). URL: <https://doi.org/10.1051/0004-6361/201833880>.
- 2139 [11] Wayne Hu. *Matter Density Animation*. web. 2024. URL: <http://background.uchicago.edu/~whu/animbut/anim2.html>.

- 2141 [12] Wenlong Yuan et al. “A First Look at Cepheids in a Type Ia Supernova Host with JWST”. in:
2142 *The Astrophysical Journal Letters* 940.1 (Nov. 2022). doi: [10.3847/2041-8213/ac9b27](https://doi.org/10.3847/2041-8213/ac9b27).
2143 URL: <https://dx.doi.org/10.3847/2041-8213/ac9b27>.
- 2144 [13] Wendy L. Freedman. “Measurements of the Hubble Constant: Tensions in Perspective”. In:
2145 *The Astrophysical Journal* 919.1 (Sept. 2021), p. 16. doi: [10.3847/1538-4357/ac0e95](https://doi.org/10.3847/1538-4357/ac0e95).
2146 URL: <https://dx.doi.org/10.3847/1538-4357/ac0e95>.
- 2147 [14] Jodi Cooley. “Dark Matter direct detection of classical WIMPs”. In: *SciPost Phys. Lect.
2148 Notes* (2022), p. 55. doi: [10.21468/SciPostPhysLectNotes.55](https://doi.org/10.21468/SciPostPhysLectNotes.55). URL: <https://scipost.org/10.21468/SciPostPhysLectNotes.55>.
- 2150 [15] “Search for new phenomena in events with an energetic jet and missing transverse momentum
2151 in pp collisions at $\sqrt{s} = 13$ TeV with the ATLAS detector”. In: *Phys. Rev. D* 103
2152 (11 July 2021), p. 112006. doi: [10.1103/PhysRevD.103.112006](https://doi.org/10.1103/PhysRevD.103.112006). URL: <https://link.aps.org/doi/10.1103/PhysRevD.103.112006>.
- 2154 [16] *Jetting into the dark side: a precision search for dark matter*. website. July 2020. URL:
2155 <https://atlas.cern/updates/briefing/precision-search-dark-matter>.
- 2156 [17] Celine Armand et. al. “Combined dark matter searches towards dwarf spheroidal galaxies
2157 with Fermi-LAT, HAWC, H.E.S.S., MAGIC, and VERITAS”. in: *Proceedings of Science*.
2158 Vol. 395. Mar. 2022. doi: <https://doi.org/10.22323/1.395.0528>.
- 2159 [18] Tracy R. Slatyer. “Les Houches Lectures on Indirect Detection of Dark Matter”. In: *SciPost
2160 Phys. Lect. Notes* (2022), p. 53. doi: [10.21468/SciPostPhysLectNotes.53](https://doi.org/10.21468/SciPostPhysLectNotes.53). URL:
2161 <https://scipost.org/10.21468/SciPostPhysLectNotes.53>.
- 2162 [19] Christian W Bauer, Nicholas L. Rodd, and Bryan R. Webber. “Dark matter spectra from
2163 the electroweak to the Planck scale”. In: *Journal of High Energy Physics* 2021.1029-8479
2164 (June 2021). doi: [https://doi.org/10.1007/JHEP06\(2021\)121](https://doi.org/10.1007/JHEP06(2021)121).
- 2165 [20] Riccardo Catena and Piero Ullio. “A novel determination of the local dark matter density”.
2166 In: *Journal of Cosmology and Astroparticle Physics* 2010.08 (Aug. 2010), p. 004. doi:
2167 [10.1088/1475-7516/2010/08/004](https://doi.org/10.1088/1475-7516/2010/08/004). URL: <https://dx.doi.org/10.1088/1475-7516/2010/08/004>.
- 2169 [21] B. P. Abbott et al. “Observation of Gravitational Waves from a Binary Black Hole Merger”.
2170 In: *Phys. Rev. Lett.* 116 (6 Feb. 2016), p. 061102. doi: [10.1103/PhysRevLett.116.061102](https://doi.org/10.1103/PhysRevLett.116.061102). URL: <https://link.aps.org/doi/10.1103/PhysRevLett.116.061102>.
- 2172 [22] R. Abbasi et. al. “Observation of high-energy neutrinos from the Galactic plane”. In: *Science*
2173 380.6652 (June 2023), pp. 1338–1343.
- 2174 [23] NASA Goddard Space Flight Center. *Fermi’s 12-year view of the gamma-ray sky*. website.

- 2175 2022. URL: <https://svs.gsfc.nasa.gov/14090>.
- 2176 [24] Marco Cirelli et al. “PPPC 4 DM ID: a poor particle physicist cookbook for dark matter
2177 indirect detection”. In: *Journal of Cosmology and Astroparticle Physics* 2011.03 (Mar.
2178 2011), p. 051. doi: [10.1088/1475-7516/2011/03/051](https://doi.org/10.1088/1475-7516/2011/03/051). URL: <https://dx.doi.org/10.1088/1475-7516/2011/03/051>.
- 2180 [25] Javier Rico. “Gamma-Ray Dark Matter Searches in Milky Way Satellites—A Comparative
2181 Review of Data Analysis Methods and Current Results”. In: *Galaxies* 8.1 (Mar. 2020), p. 25.
2182 doi: [10.3390/galaxies8010025](https://doi.org/10.3390/galaxies8010025). arXiv: [2003.13482 \[astro-ph.HE\]](https://arxiv.org/abs/2003.13482).
- 2183 [26] W. B. Atwood et al. “The Large Area Telescope on the Fermi Gamma-Ray Space Telescope
2184 Mission”. In: *apj* 697.2 (June 2009), pp. 1071–1102. doi: [10.1088/0004-637X/697/2/1071](https://doi.org/10.1088/0004-637X/697/2/1071). arXiv: [0902.1089 \[astro-ph.IM\]](https://arxiv.org/abs/0902.1089).
- 2186 [27] M. Ackermann et al. “Searching for Dark Matter Annihilation from Milky Way Dwarf
2187 Spheroidal Galaxies with Six Years of Fermi Large Area Telescope Data”. In: *prl* 115.23,
2188 231301 (Dec. 2015), p. 231301. doi: [10.1103/PhysRevLett.115.231301](https://doi.org/10.1103/PhysRevLett.115.231301). arXiv:
2189 [1503.02641 \[astro-ph.HE\]](https://arxiv.org/abs/1503.02641).
- 2190 [28] Mattia Di Mauro, Martin Stref, and Francesca Calore. “Investigating the effect of Milky
2191 Way dwarf spheroidal galaxies extension on dark matter searches with Fermi-LAT data”.
2192 In: *Phys. Rev. D* 106 (12 Dec. 2022), p. 123032. doi: [10.1103/PhysRevD.106.123032](https://doi.org/10.1103/PhysRevD.106.123032).
2193 URL: <https://link.aps.org/doi/10.1103/PhysRevD.106.123032>.
- 2194 [29] F. et al. Aharonian. “Observations of the Crab Nebula with H.E.S.S.”. In: *Astron. Astrophys.*
2195 457 (2006), pp. 899–915. doi: [10.1051/0004-6361:20065351](https://doi.org/10.1051/0004-6361:20065351). arXiv: [astro-ph/0607333](https://arxiv.org/abs/astro-ph/0607333).
- 2197 [30] J. Albert et al. “VHE γ -Ray Observation of the Crab Nebula and its Pulsar with the MAGIC
2198 Telescope”. In: *The Astrophysical Journal* 674.2 (Feb. 2008), p. 1037. doi: [10.1086/525270](https://doi.org/10.1086/525270). URL: <https://dx.doi.org/10.1086/525270>.
- 2200 [31] N. Park. “Performance of the VERITAS experiment”. In: *Proceedings, 34th International
2201 Cosmic Ray Conference (ICRC2015): The Hague, The Netherlands, July, 30th July - 6th
2202 August*. Vol. 34. 2015, p. 771. arXiv: [1508.07070 \[astro-ph.IM\]](https://arxiv.org/abs/1508.07070).
- 2203 [32] A. Abramowski et al. “H.E.S.S. constraints on Dark Matter annihilations towards the Sculptor
2204 and Carina Dwarf Galaxies”. In: *Astropart. Phys.* 34 (2011), pp. 608–616. doi: [10.1016/j.astropartphys.2010.12.006](https://doi.org/10.1016/j.astropartphys.2010.12.006). arXiv: [1012.5602 \[astro-ph.HE\]](https://arxiv.org/abs/1012.5602).
- 2206 [33] A. Abramowski et al. “Search for dark matter annihilation signatures in H.E.S.S. observations
2207 of Dwarf Spheroidal Galaxies”. In: *Phys. Rev. D* 90 (2014), p. 112012. doi: [10.1103/PhysRevD.90.112012](https://doi.org/10.1103/PhysRevD.90.112012). arXiv: [1410.2589 \[astro-ph.HE\]](https://arxiv.org/abs/1410.2589).

- 2209 [34] H. Abdalla et al. “Searches for gamma-ray lines and ‘pure WIMP’ spectra from Dark
2210 Matter annihilations in dwarf galaxies with H.E.S.S”. in: *JCAP* 11 (2018), p. 037. doi:
2211 [10.1088/1475-7516/2018/11/037](https://doi.org/10.1088/1475-7516/2018/11/037). arXiv: [1810.00995 \[astro-ph.HE\]](https://arxiv.org/abs/1810.00995).
- 2212 [35] J. Aleksić et al. “Optimized dark matter searches in deep observations of Segue 1 with
2213 MAGIC”. in: *JCAP* 1402 (2014), p. 008. doi: [10.1088/1475-7516/2014/02/008](https://doi.org/10.1088/1475-7516/2014/02/008).
2214 arXiv: [1312.1535 \[hep-ph\]](https://arxiv.org/abs/1312.1535).
- 2215 [36] V.A. Acciari et al. “Combined searches for dark matter in dwarf spheroidal galaxies observed
2216 with the MAGIC telescopes, including new data from Coma Berenices and Draco”. In: *Physics of the Dark Universe* (2021), p. 100912. issn: 2212-6864. doi: <https://doi.org/10.1016/j.dark.2021.100912>. URL: <https://www.sciencedirect.com/science/article/pii/S2212686421001370>.
- 2220 [37] M. L. Ahnen et al. “Indirect dark matter searches in the dwarf satellite galaxy Ursa Major II
2221 with the MAGIC Telescopes”. In: *JCAP* 1803.03 (2018), p. 009. doi: [10.1088/1475-7516/2018/03/009](https://doi.org/10.1088/1475-7516/2018/03/009). arXiv: [1712.03095 \[astro-ph.HE\]](https://arxiv.org/abs/1712.03095).
- 2223 [38] S. et al. Archambault. “Dark matter constraints from a joint analysis of dwarf Spheroidal
2224 galaxy observations with VERITAS”. in: *prd* 95.8 (Apr. 2017). doi: [10.1103/PhysRevD.95.082001](https://doi.org/10.1103/PhysRevD.95.082001). arXiv: [1703.04937 \[astro-ph.HE\]](https://arxiv.org/abs/1703.04937).
- 2226 [39] Louise Oakes et al. “Combined Dark Matter searches towards dwarf spheroidal galaxies with
2227 Fermi-LAT, HAWC, HESS, MAGIC and VERITAS”. in: *Proceedings of Science*. 2019.
- 2228 [40] Celine Armand et al. on behalf of the Fermi-LAT, HAWC, HESS, MAGIC, VERITAS.
2229 “Combined Dark Matter searches towards dwarf spheroidal galaxies with Fermi-LAT,
2230 HAWC, HESS, MAGIC and VERITAS”. in: *Proceedings of Science*. 2021.
- 2231 [41] Daniel Kerszberg et al. on behalf of the Fermi-LAT, HAWC, HESS, MAGIC, and VER-
2232 TIAS collaborations. “Search for dark matter annihilation with a combined analysis of
2233 dwarf spheroidal galaxies from Fermi-LAT, HAWC, H.E.S.S., MAGIC and VERITAS”. in:
2234 *Proceedings of Science*. 2023.
- 2235 [42] A. U. Abeysekara et al. “Observation of the Crab Nebula with the HAWC Gamma-Ray
2236 Observatory”. In: *The Astrophysical Journal* 843.1 (June 2017), p. 39. doi: [10.3847/1538-4357/aa7555](https://doi.org/10.3847/1538-4357/aa7555). URL: <https://doi.org/10.3847/1538-4357/aa7555>.
- 2238 [43] Giacomo Vianello et al. *The Multi-Mission Maximum Likelihood framework (3ML)*. 2015.
2239 arXiv: [1507.08343 \[astro-ph.HE\]](https://arxiv.org/abs/1507.08343).
- 2240 [44] Marco Cirelli et al. “PPPC 4 DM ID: a poor particle physicist cookbook for dark matter
2241 indirect detection”. In: *Journal of Cosmology and Astroparticle Physics* 2011.03 (Mar.
2242 2011). issn: 1475-7516. doi: [10.1088/1475-7516/2011/03/051](https://doi.org/10.1088/1475-7516/2011/03/051). URL: <http://dx.doi.org/10.1088/1475-7516/2011/03/051>.

- 2244 [45] Alex Geringer-Sameth, Savvas M. Koushiappas, and Matthew Walker. “DWARF GALAXY
2245 ANNIHILATION AND DECAY EMISSION PROFILES FOR DARK MATTER EXPERI-
2246 MENTS”. In: *The Astrophysical Journal* 801.2 (Mar. 2015), p. 74. ISSN: 1538-4357. doi:
2247 [10.1088/0004-637x/801/2/74](https://doi.org/10.1088/0004-637x/801/2/74). URL: <http://dx.doi.org/10.1088/0004-637X/801/2/74>.
- 2249 [46] A. Albert et al. “Dark Matter Limits from Dwarf Spheroidal Galaxies with the HAWC
2250 Gamma-Ray Observatory”. In: *The Astrophysical Journal* 853.2 (Feb. 2018), p. 154. ISSN:
2251 1538-4357. doi: [10.3847/1538-4357/aaa6d8](https://doi.org/10.3847/1538-4357/aaa6d8). URL: <http://dx.doi.org/10.3847/1538-4357/aaa6d8>.
- 2253 [47] HongSheng Zhao. “Analytical models for galactic nuclei”. In: *Mon. Not. Roy. Astron. Soc.*
2254 278 (1996), pp. 488–496. doi: [10.1093/mnras/278.2.488](https://doi.org/10.1093/mnras/278.2.488). arXiv: [astro-ph/9509122](https://arxiv.org/abs/astro-ph/9509122)
2255 [[astro-ph](#)].
- 2256 [48] Julio F. Navarro, Carlos S. Frenk, and Simon D. M. White. “The Structure of Cold Dark
2257 Matter Halos”. In: *ApJ* 462 (May 1996), p. 563. doi: [10.1086/177173](https://doi.org/10.1086/177173). eprint:
2258 [astro-ph/9508025](https://arxiv.org/abs/astro-ph/9508025) ([astro-ph](#)).
- 2259 [49] V. Bonnivard et al. “Spherical Jeans analysis for dark matter indirect detection in dwarf
2260 spheroidal galaxies - Impact of physical parameters and triaxiality”. In: *Mon. Not. Roy.
2261 Astron. Soc.* 446 (2015), pp. 3002–3021. doi: [10.1093/mnras/stu2296](https://doi.org/10.1093/mnras/stu2296). arXiv:
2262 [1407.7822](https://arxiv.org/abs/1407.7822) [[astro-ph.HE](#)].
- 2263 [50] M. Ackermann et al. “Searching for Dark Matter Annihilation from Milky Way Dwarf
2264 Spheroidal Galaxies with Six Years of Fermi Large Area Telescope Data”. In: *prl* 115.23,
2265 231301 (Dec. 2015), p. 231301. doi: [10.1103/PhysRevLett.115.231301](https://doi.org/10.1103/PhysRevLett.115.231301). arXiv:
2266 [1503.02641](https://arxiv.org/abs/1503.02641) [[astro-ph.HE](#)].
- 2267 [51] M. L. Ahnen et al. “Limits to Dark Matter Annihilation Cross-Section from a Combined
2268 Analysis of MAGIC and Fermi-LAT Observations of Dwarf Satellite Galaxies”. In: *JCAP*
2269 1602.02 (2016), p. 039. doi: [10.1088/1475-7516/2016/02/039](https://doi.org/10.1088/1475-7516/2016/02/039). arXiv: [1601.06590](https://arxiv.org/abs/1601.06590)
2270 [[astro-ph.HE](#)].
- 2271 [52] Javier Rico et al. *gLike: numerical maximization of heterogeneous joint
2272 likelihood functions of a common free parameter plus nuisance parameters*.
2273 <https://doi.org/10.5281/zenodo.4601451>. Version v00.09.03. Mar. 2021. doi: [10.5281/zenodo.4601451](https://doi.org/10.5281/zenodo.4601451). URL: <https://doi.org/10.5281/zenodo.4601451>.
- 2275 [53] Tjark Miener and Daniel Nieto. *LklCom: Combining likelihoods from different experiments*.
2276 <https://doi.org/10.5281/zenodo.4597500>. Version v0.5.3. Mar. 2021. doi: [10.5281/zenodo.4597500](https://doi.org/10.5281/zenodo.4597500). URL: <https://doi.org/10.5281/zenodo.4597500>.
- 2278 [54] T. Miener et al. “Open-source Analysis Tools for Multi-instrument Dark Matter Searches”.
2279 In: *arXiv e-prints*, arXiv:2112.01818 (Dec. 2021), arXiv:2112.01818. arXiv: [2112.01818](https://arxiv.org/abs/2112.01818)

- 2280 [astro-ph.IM].
- 2281 [55] Alex Geringer-Sameth and Matthew Koushiappas Savvas M. and Walker. “Dwarf galaxy
2282 annihilation and decay emission profiles for dark matter experiments”. In: *Astrophys.*
2283 *J.* 801.2 (2015), p. 74. doi: [10.1088/0004-637X/801/2/74](https://doi.org/10.1088/0004-637X/801/2/74). arXiv: [1408.0002](https://arxiv.org/abs/1408.0002)
2284 [astro-ph.CO].
- 2285 [56] Gianfranco Bertone, Dan Hooper, and Joseph Silk. “Particle dark matter: evidence, can-
2286 didates and constraints”. In: *Physics Reports* 405.5-6 (Jan. 2005), pp. 279–390. ISSN:
2287 0370-1573. doi: [10.1016/j.physrep.2004.08.031](https://doi.org/10.1016/j.physrep.2004.08.031). URL: <http://dx.doi.org/10.1016/j.physrep.2004.08.031>.
- 2289 [57] V. Bonnivard et al. “Dark matter annihilation and decay in dwarf spheroidal galaxies: The
2290 classical and ultrafaint dSphs”. In: *Mon. Not. Roy. Astron. Soc.* 453.1 (2015), pp. 849–867.
2291 doi: [10.1093/mnras/stv1601](https://doi.org/10.1093/mnras/stv1601). arXiv: [1504.02048](https://arxiv.org/abs/1504.02048) [astro-ph.HE].
- 2292 [58] A. et al. Albert. “Searching for Dark Matter Annihilation in Recently Discovered Milky Way
2293 Satellites with Fermi-LAT”. in: *Astrophys. J.* 834.2 (2017), p. 110. doi: [10.3847/1538-4357/834/2/110](https://doi.org/10.3847/1538-4357/834/2/110). arXiv: [1611.03184](https://arxiv.org/abs/1611.03184) [astro-ph.HE].
- 2295 [59] Mattia Di Mauro and Martin Wolfgang Winkler. “Multimessenger constraints on the dark
2296 matter interpretation of the Fermi-LAT Galactic Center excess”. In: *prd* 103.12, 123005
2297 (June 2021), p. 123005. doi: [10.1103/PhysRevD.103.123005](https://doi.org/10.1103/PhysRevD.103.123005). arXiv: [2101.11027](https://arxiv.org/abs/2101.11027)
2298 [astro-ph.HE].
- 2299 [60] H. C. Plummer. “On the Problem of Distribution in Globular Star Clusters: (Plate 8.)”
2300 In: *Monthly Notices of the Royal Astronomical Society* 71.5 (Mar. 1911), pp. 460–470.
2301 ISSN: 0035-8711. doi: [10.1093/mnras/71.5.460](https://doi.org/10.1093/mnras/71.5.460). eprint: <https://academic.oup.com/mnras/article-pdf/71/5/460/2937497/mnras71-0460.pdf>. URL:
2303 <https://doi.org/10.1093/mnras/71.5.460>.
- 2304 [61] Daniel R. Hunter. “Derivation of the anisotropy profile, constraints on the local velocity
2305 dispersion, and implications for direct detection”. In: *JCAP* 02 (2014), p. 023. doi:
2306 [10.1088/1475-7516/2014/02/023](https://doi.org/10.1088/1475-7516/2014/02/023). arXiv: [1311.0256](https://arxiv.org/abs/1311.0256) [astro-ph.CO].
- 2307 [62] Barun Kumar Dhar and Liliya L. R. Williams. “Surface mass density of the Einasto family
2308 of dark matter haloes: are they Sersic-like?” In: *Mon. Not. Roy. Astron. Soc.* (2010). doi:
2309 [10.1111/j.1365-2966.2010.16446.x](https://doi.org/10.1111/j.1365-2966.2010.16446.x).
- 2310 [63] M. Baes and E. Van Hese. “Dynamical models with a general anisotropy profile”. In:
2311 *Astron. Astrophys.* 471 (2007), p. 419. doi: [10.1051/0004-6361:20077672](https://doi.org/10.1051/0004-6361:20077672). arXiv:
2312 [0705.4109](https://arxiv.org/abs/0705.4109) [astro-ph].
- 2313 [64] Matthew G. Walker, Edward W. Olszewski, and Mario Mateo. “Bayesian analysis of re-
2314 solved stellar spectra: application to MMT/Hectochelle observations of the Draco dwarf

- 2315 spheroidal”. In: *mnras* 448.3 (Apr. 2015), pp. 2717–2732. doi: [10.1093/mnras/stv099](https://doi.org/10.1093/mnras/stv099).
2316 arXiv: [1503.02589 \[astro-ph.GA\]](https://arxiv.org/abs/1503.02589).
- 2317 [65] Nicholas L. Rodd et al. “Dark matter spectra from the electroweak to the Planck scale”. In:
2318 *J. High Energy Physics* 121.10.1007 (June 2021).
- 2319 [66] Pace, Andrew B and Strigari, Louis E. “Scaling relations for dark matter annihilation and
2320 decay profiles in dwarf spheroidal galaxies”. In: *Monthly Notices of the Royal Astronomical
2321 Society* 482.3 (Oct. 2018), pp. 3480–3496. ISSN: 0035-8711. doi: [10.1093/mnras/sty2839](https://doi.org/10.1093/mnras/sty2839).
- 2323 [67] Albert, A. et al. “Search for gamma-ray spectral lines from dark matter annihilation in
2324 dwarf galaxies with the High-Altitude Water Cherenkov observatory”. In: *Phys. Rev. D* 101 (10 May 2020), p. 103001. doi: [10.1103/PhysRevD.101.103001](https://doi.org/10.1103/PhysRevD.101.103001). URL:
2326 <https://link.aps.org/doi/10.1103/PhysRevD.101.103001>.
- 2327 [68] Victor Eijkhout and Edmund Show and Robert van de Geijn. *The Science of Computing. The Art of High Performance Computing*. Vol. 3. Open Copy published under CC-BY 4.0
2328 license, 2023, pp. 63–66.
- 2330 [69] Aartsen, M. et al. “IceCube search for dark matter annihilation in nearby galaxies and galaxy
2331 clusters”. In: *Phys. Rev. D* 88 (12 Dec. 2013), p. 122001. doi: [10.1103/PhysRevD.88.122001](https://doi.org/10.1103/PhysRevD.88.122001). URL: <https://link.aps.org/doi/10.1103/PhysRevD.88.122001>.
- 2333 [70] Pearl Sandick et al. “Sensitivity of the IceCube neutrino detector to dark matter annihilating
2334 in dwarf galaxies”. In: *Phys. Rev. D* 81 (8 Apr. 2010), p. 083506. doi: [10.1103/PhysRevD.81.083506](https://doi.org/10.1103/PhysRevD.81.083506). URL: <https://link.aps.org/doi/10.1103/PhysRevD.81.083506>.
- 2336 [71] Qinrui Liu and Jeffrey Lazar and Carlos A. Argüelles and Ali Kheirandish. “ χ aro: a tool
2337 for neutrino flux generation from WIMPs”. In: *Journal of Cosmology and Astroparticle
2338 Physics* 2020.10 (Oct. 2020), p. 043. doi: [10.1088/1475-7516/2020/10/043](https://doi.org/10.1088/1475-7516/2020/10/043). URL:
2339 <https://dx.doi.org/10.1088/1475-7516/2020/10/043>.
- 2340 [72] Tessa Cerver. “Time Integrated searches for Astrophysical Neutrino Sources using the
2341 IceCube Detector and Gender in Physics studies for the Genera Project”. In: *UNIVERSITE
2342 DE GEN`EVE* (2019), pp. 57–64.
- 2343 [73] Minjin Jeong on behalf of the IceCube Collaboration. “Search for Dark Matter Decay in
2344 Nearby Galaxy Clusters and Galaxies with IceCube”. In: *Proceedings of Science* 444.38
2345 (2023).
- 2346 [74] IceCube Collaboration. “Evidence for neutrino emission from the nearby active galaxy NGC
2347 1068”. In: *Science* 378.6619 (2022).
- 2348 [75] Nathan Whitehorn and Jakob van Santen. *Photospline*. IceCube: GitHub.